



UMinho | 2021

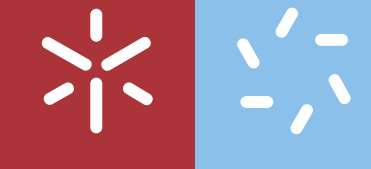
**Search for new interactions
in the top quark sector**

Ana Paula Pereira Peixoto



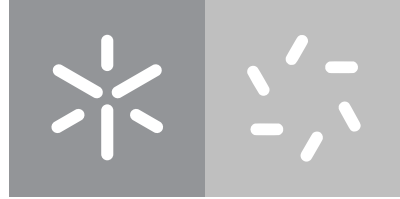
junho de 2021

Universidade do Minho
Escola de Ciências



Ana Paula Pereira Peixoto

**Search for new interactions
in the top quark sector**



Universidade do Minho
Escola de Ciências

Ana Paula Pereira Peixoto

**Search for new interactions
in the top quark sector**

Tese de doutoramento em Física

Trabalho efetuado sob a orientação do
**Professor Doutor Nuno Filipe da Silva
Fernandes de Castro**

DECLARAÇÃO

Nome: Ana Paula Pereira Peixoto

E-mail: ana.peixoto@cern.ch

Telefone: +351969233066

Número de Cartão de Cidadão: 13630865 1 ZX9

Título da Tese: Search for new interactions in the top quark sector

Orientador: Professor Doutor Nuno Filipe da Silva Fernandes de Castro

Ano de Conclusão: 2021

Designação do Doutoramento: Doutoramento em Física

É AUTORIZADA A REPRODUÇÃO INTEGRAL DESTA TESE APENAS PARA EFEITOS DE INVESTIGAÇÃO,
MEDIANTE DECLARAÇÃO ESCRITA DO INTERESSADO, QUE A TAL SE COMPROMETE;

Universidade do Minho, 18 de Junho de 2021

Assinatura:

DECLARAÇÃO DE INTEGRIDADE

Declaro ter atuado com integridade na elaboração do presente trabalho académico e confirmo que não recorri à prática de plágio nem a qualquer forma de utilização indevida ou falsificação de informações ou resultados em nenhuma das etapas conducente à sua elaboração.

Mais declaro que conheço e que respeitei o Código de Conduta Ética da Universidade do Minho.

Universidade do Minho, 18 de Junho de 2021

(Ana Paula Pereira Peixoto)

Acknowledgements

This thesis would not have been possible without the support of all those who surrounded me, both professionally and personally.

First of all, I am deeply grateful to my supervisor, Nuno Castro, for his endless support, invaluable scientific advise and perpetual motivation to grow as a physicist. I appreciate all his time and opportunities given in the past five years as a PhD student.

I also have to thank all the colleagues from the single-top and top+X subgroups in ATLAS for all the important advises to the development of the data analysis, especially to Oliver Kind, Sebastian Mergelmeyer, Lidia Dell'Asta and Archil Durgishvili. I am also thankful to Johannes Erdmann, Michael Chala and Maria Ramos for everything I learned with our collaboration. I would like to thank to the Portuguese ATLAS group for all the interesting physics discussions. A special thanks goes to Patricia Conde Muñoz for her leadership and continuous support along the way. I am also grateful to the whole LIP team for making it a great place to work and welcoming everyone in the best way possible. Thanks to all my colleagues and friends at LIP, especially my close colleagues from LIP-Minho for the help in different areas of this thesis. I also thank to Peter Jenni and the ATLAS group at CERN for the friendship and assistance during my stay at CERN.

To my friends of Paredes de Coura and Braga I express my most sincere thanks for always being a source of joy and laughter. A special thanks goes to my close friend Tiago Vale for the exceptional cooperation, never-ending patience and solid companionship. Finally, I owe my deepest gratitude to my family, especially to my parents Manuela and Carlos, my sister and my nephews for all their patience and emotional support.

This thesis has been supported by the Fundação para a Ciência e Tecnologia grant SFRH/BD/129321/2017 and by different projects within the Laboratório de Instrumentação e Física Experimental de Partículas (LIP): *Collaboration in the ATLAS Experiment at CERN: Data taking and Analysis* with the reference CERN/FIS-PAR/0002/2019, *BigDataHEP: Understanding Big Data in High Energy Physics* with the references PTDC/FIS-PAR/29147/2017 and POCI/01-0145-FEDER-029147 and *Projecto Exploratório* with the reference IF/00050/2013/CP1172/CT0002. This research was also awarded with the prize ATLAS PhD Grant 2019.

Abstract

Search for new interactions in the top quark sector

The top quark is the heaviest elementary particle discovered so far and the study of its unique properties provides not only an essential test of the Standard Model of Particle Physics, but also an important window into physics beyond it. This thesis presents a search for Flavour Changing Neutral Currents processes through the top quark interactions with a neutral Z boson and a light quark, that can be an up or charm quark. The analysis uses a 139 fb^{-1} dataset of proton-proton collisions collected at a center-of-mass of $\sqrt{s} = 13 \text{ TeV}$ with the ATLAS detector, at the Large Hadron Collider between 2015 and 2018. The presented analysis focus on the tZq vertex interactions with a final state composed by three leptons, resulting from the leptonic decays of the top quark and the Z boson. In order to improve the sensitivity of the search, events from both production and decay modes are considered, being split in distinct signal regions according with the number of jets. Methods based on multivariate techniques were developed and applied to dedicated signal regions to discriminate tZq events against background events, which are dominated by top quark pair production in association with a Z boson as well as diboson production. All the analysis' regions were combined in a statistic model using a profile likelihood fit to constrain the background predictions and reduce the systematic uncertainties. Since no evidence for a signal was found, upper limits on the cross-section and branching ratio of these processes at 95% confidence level were evaluated. The observed (expected) limit on the branching ratio of $t \rightarrow uZ$ is $6.16 (4.88) \times 10^{-5}$, while the observed (expected) limit on the branching ratio of $t \rightarrow cZ$ is $13.02 (10.76) \times 10^{-5}$. Additionally, observed (expected) limits excluding cross-sections of $\sigma(pp \rightarrow tZ)$ above $37 (29) \text{ fb}$ and $118 (96) \text{ fb}$ were obtained for the tZu and tZc processes.

Through a phenomenological study, the search for a new pseudo-scalar particle S has also been investigated focusing on several leptonic final states. The sensitivity study of these dedicated analyses allowed to conclude that new physics scales as large as $\Lambda \sim 90 \text{ TeV}$ can be probed with an integrated luminosity of 150 fb^{-1} .

Resumo

Pesquisa de novas interações no sector do quark top

O quark top é a partícula elementar mais pesada descoberta até ao momento e o estudo das suas propriedades únicas proporciona um teste essencial ao Modelo Padrão da Física das Partículas, para além de uma importante janela para novos fenómenos de física. A presente tese descreve a pesquisa de processos de mudança de sabor através de correntes neutras através de interações entre um quark top, um bosão neutro Z e um quark leve, sendo um quark up ou charm. A análise usa um conjunto de dados com uma luminosidade de 139 fb^{-1} referentes a colisões protão-protão colectadas a uma energia de centro de massa de $\sqrt{s} = 13 \text{ TeV}$ pelo detector ATLAS, no Large Hadron Collider entre 2015 e 2018. A análise apresentada tem como foco interações com o vértice tZq com um estado final composto por três leptões, resultando dos decaimentos leptónicos do quark top e do bosão Z . Para melhorar a sensibilidade da pesquisa, eventos originários tanto do modo de produção como do modo de decaimento são considerados, sendo divididos em regiões de sinal distintas, definidas de acordo com o número de jactos. Métodos baseados em técnicas de análise multivariacional foram desenvolvidos e aplicados nas regiões de sinal, de forma a discriminar eventos tZq e eventos de fundo, dominados pela produção de um par de quarks top em associação com um bosão Z , bem como pela produção de dibosões. Todas as regiões definidas na análise foram combinadas num modelo estatístico para restringir as previsões dos processos de fundo e diminuir as incertezas sistemáticas. Não tendo sido observada nenhuma evidência de sinal nos dados analisados, foram obtidos limites superiores na secção eficaz e na probabilidade de decaimento a um nível de confiança de 95%. O limite observado (esperado) na probabilidade de decaimento do processo $t \rightarrow uZ$ é $6.16 (4.88) \times 10^{-5}$, enquanto que o limite observado (esperado) na probabilidade de decaimento do processo $t \rightarrow cZ$ é $13.02 (10.76) \times 10^{-5}$. Adicionalmente, limites a excluir $\sigma(pp \rightarrow tZ)$ abaixo de $37 (29) \text{ fb}$ e $118 (96) \text{ fb}$ foram obtidos para os processos tZu e tZc .

Através de um estudo fenomenológico, a pesquisa por uma nova partícula pseudo-escalar S foi investigada, tendo como foco diferentes estados finais leptónicos. O estudo de sensibilidade destas análises dedicadas permitiu concluir que escalas de nova física da ordem de $\Lambda \sim 90 \text{ TeV}$ podem ser exploradas com uma luminosidade integrada de 150 fb^{-1} .

Contents

List of Figures	x
List of Tables	xv
1 Introduction	1
2 The top quark within the Standard Model of Particle Physics and beyond	4
2.1 The Standard Model of particle physics	4
2.1.1 Standard Model Lagrangian	5
2.1.2 Experimental successes and shortcomings of the Standard Model	12
2.1.3 Measurements in Particle Physics	13
2.2 Top quark physics	15
2.2.1 Flavour Changing Neutral Currents in the top quark sector	17
2.2.2 Interference studies with tZq and $t\gamma q$ FCNC anomalous couplings	21
3 The ATLAS experiment at the Large Hadron Collider	25
3.1 CERN	25
3.2 The Large Hadron Collider	26
3.2.1 Luminosity and pile-up	28
3.3 The ATLAS Experiment	30
3.3.1 ATLAS coordinate system	30
3.3.2 Magnet system	31
3.3.3 Inner detector	32
3.3.4 Calorimeter system	33
3.3.5 Muon spectrometer	34
3.3.6 Trigger and data acquisition system	35
3.3.7 Forward detectors	37
3.4 Worldwide LHC computing grid	42
4 Search for flavour changing neutral currents in the top quark sector	43

4.1	Data sample	43
4.2	Object reconstruction	44
4.3	Signal and background modelling	48
4.3.1	Signal modelling	48
4.3.2	Background modelling	49
4.4	Analysis strategy	53
4.4.1	Common selection	54
4.4.2	Top quarks reconstruction	55
4.4.3	Signal regions selection	57
4.5	Comparison of data and Monte Carlo prediction	62
4.5.1	Fake composition	66
4.6	Boosted decision trees	70
4.6.1	Discriminant definitions	71
4.6.2	Input variables	72
4.6.3	Training and evaluation	79
4.6.4	Performance and overtraining checks	80
4.6.5	Hyper-parameters optimisation	87
4.6.6	Validation regions definition	88
4.7	Systematic uncertainties	91
4.7.1	Acceptance and shape uncertainties	94
4.8	Statistical analysis and results	95
4.8.1	Profile likelihood fit	95
4.8.2	The fit model	96
4.8.3	Fit to data	98
4.8.4	Limits	134
5	Top quark phenomenology as a probe of new interactions with a pseudo-scalar particle	136
5.1	Sensitivity on the search for a new scalar S	136
5.1.1	Interactions and constraints	137
5.1.2	Search for $t \rightarrow Sq, S \rightarrow \mu^+ \mu^-$	140
5.1.3	Search for $t \rightarrow Sq, S \rightarrow \tau^+ \tau^-$	144
5.1.4	Search for $t \rightarrow SSq, S \rightarrow \mu^+ \mu^-$	148
6	Conclusion	151
Bibliography		153

Appendices	172
A Optimisation studies for the multivariate discriminants	172
A.0.1 Study of the BDT in SR1	172
A.0.2 Study of the BDT in SR2 ctZ	174
B Effect of the pruning on the branching ratio upper limits	183

List of Figures

2.1	Example of NNLO parton distribution functions.	15
2.2	Feynman diagrams for top quark pair production.	16
2.3	Feynman diagrams for single-top quark production.	17
2.4	LHC and Tevatron measurements of the top quark pair and single-top quark production cross-sections.	18
2.5	FCNC interactions in the top quark sector.	18
2.6	Feynman diagrams for the production and decay modes with the FCNC tZq vertex.	20
2.7	Feynman diagrams for the production and decay modes with the FCNC tZq and $t\gamma q$ vertices.	22
2.8	Transverse momentum of the photon and Z boson for the different processes at parton level.	24
2.9	Transverse momentum of the photon and Z boson for the different processes at detector level.	24
3.1	CERN accelerators and facilities.	26
3.2	LHC dipole magnet.	27
3.3	Mean number of interactions per crossing during LHC Run-2.	29
3.4	ATLAS detector.	30
3.5	ATLAS inner detector.	32
3.6	ATLAS calorimeter system.	34
3.7	ATLAS muon spectrometer.	35
3.8	ATLAS trigger and data acquisition system.	36
3.9	Total integrated luminosity recorded by ATLAS during Run-2.	36
3.11	Scheme of the AFP sub-detector.	38
3.12	Tracks map for the AFP C-side stations after cut on the slope of x position.	40
3.13	Tracks map for the AFP C-side stations after cut on the slope of x and y positions.	40
3.14	Hits map for the AFP C-side near station after cut on the slope of x and y positions.	41
3.15	Hits map for the AFP C-side far station after cut on the slope of x and y positions.	41
4.1	Electron identification efficiencies as function of p_T and η	45
4.2	Muon reconstruction and identification efficiencies.	46
4.3	Distributions of distinct variables in the SR1 region.	60

4.4	Distributions of distinct variables in the SR2 region.	61
4.5	Expected and observed distributions in the $t\bar{t}$ control region.	64
4.6	Expected and observed distributions in the $t\bar{t}Z$ control region.	65
4.7	Expected and observed distributions in the side-band control region 1.	65
4.8	Expected and observed distributions in the side-band control region 2.	66
4.9	Origin of the three leptons from $t\bar{t}$ events with 1 jet.	67
4.10	Origin of the three leptons from $t\bar{t}$ events with 2 jets.	68
4.11	Classification scheme of the MCTruthClassifier tool.	68
4.12	Origin of the three leptons from $t\bar{t}$ events with 3 jets.	69
4.13	Origin of the three leptons from $t\bar{t}$ events with 4 jets.	69
4.14	Origin of the three leptons from $t\bar{t}$ events with ≥ 5 jets.	69
4.15	Schematic view of a Boosted Decision Tree.	71
4.16	Correlation matrix of the full set input variables for the D_2^u discriminant.	75
4.17	$S_{\text{eff}}/\sqrt{B_{\text{eff}}}$ as a function of the cut on the GBDT output score for the D_2^u discriminant.	76
4.18	Distributions of the input variables used for the D_1 discriminant.	77
4.19	Distributions of the input variables used for the D_2^u and D_2^c discriminants.	78
4.20	ROC integral curves for the D_1 discriminant.	81
4.21	ROC integral curves for the D_2^u discriminant.	82
4.22	ROC integral curves for the D_2^c discriminant.	83
4.23	GBDT output score distributions for signal and background events in the test samples.	84
4.24	Distributions of the D_1 , D_2^u and D_2^c discriminants in the side-band background control regions.	85
4.25	Distributions of the D_1 , D_2^u and D_2^c discriminants in the $t\bar{t}Z$ control region.	86
4.26	$S_{\text{eff}}/\sqrt{B_{\text{eff}}}$ and ROC integral as a function of the BDT hyper-parameters combination for the D_2^u discriminant.	88
4.27	Distributions of the D_1 , D_2^u and D_2^c discriminants in the validation regions.	90
4.28	Pruning of the nuisance parameters for the S+B tZu fit in the SRs+CRs with realistic Asimov data.	100
4.29	Pulls and constraints of the nuisance parameters for the S+B tZu fit in the SRs+CRs with realistic Asimov data.	101
4.30	Correlation matrix of the nuisance parameters for the S+B tZu fit in the SRs+CRs with realistic Asimov data.	102
4.31	Ranking of the nuisance parameters for the S+B tZu fit in the SRs+CRs with realistic Asimov data.	102
4.32	Pre- and post-fit BDTG output distributions in the signal regions for the S+B tZu fit in the SRs+CRs with realistic Asimov data.	103

4.33	Pre- and post-fit BDTG output distributions in the side-band control regions for the S+B tZu fit in the SRs+CRs with realistic Asimov data.	105
4.34	Pre- and post-fit event yield distributions in the $t\bar{t}$ and $t\bar{t}Z$ control regions for the S+B tZu fit in the SRs+CRs with realistic Asimov data.	106
4.35	Pre- and post-fit BDTG output distributions in the validation regions for the S+B tZu fit in the SRs+CRs with realistic Asimov data.	107
4.36	Pruning of the nuisance parameters for the S+B tZc fit in the SRs+CRs with realistic Asimov data.	109
4.37	Pulls and constraints of the nuisance parameters for the S+B tZc fit in the SRs+CRs with realistic Asimov data.	110
4.38	Correlation matrix of the nuisance parameters for the S+B tZc fit in the SRs+CRs with realistic Asimov data.	111
4.39	Ranking of the nuisance parameters for the S+B tZc fit in the SRs+CRs with realistic Asimov data.	111
4.40	Pre- and post-fit BDTG output distributions in the signal regions for the S+B tZc fit in the SRs+CRs with realistic Asimov data.	112
4.41	Pre- and post-fit BDTG output distributions in the side-band control regions for the S+B tZc fit in the SRs+CRs with realistic Asimov data.	114
4.42	Pre- and post-fit BDTG output distributions in the validation regions for the S+B tZc fit in the SRs+CRs with realistic Asimov data.	116
4.43	Pulls and constraints of the nuisance parameters for the S+B tZu fit in the SRs+CRs with real data.	118
4.44	Correlation matrix of the nuisance parameters for the S+B tZu fit in the SRs+CRs with real data.	119
4.45	Pre- and post-fit BDTG output distributions in the signal regions for the S+B tZu fit in the SRs+CRs with real data.	120
4.46	Pre- and post-fit BDTG output distributions in the side-band control regions for the S+B tZu fit in the SRs+CRs with real data.	121
4.47	Pre- and post-fit event yield distributions in the $t\bar{t}$ and $t\bar{t}Z$ control regions for the S+B tZu fit in the SRs+CRs with real data.	122
4.48	Pre- and post-fit BDTG output distributions in the validation regions for the S+B tZu fit in the SRs+CRs with real data.	125
4.49	Pulls and constraints of the nuisance parameters for the S+B tZc fit in the SRs+CRs with real data.	126
4.50	Correlation matrix of the nuisance parameters for the S+B tZc fit in the SRs+CRs with real data.	127

4.51	Pre- and post-fit BDTG output distributions in the signal regions for the S+B tZc fit in the SRs+CRs with real data.	128
4.52	Pre- and post-fit BDTG output distributions in the side-band control regions for the S+B tZc fit in the SRs+CRs with real data.	130
4.53	Pre- and post-fit event yield distributions in the $t\bar{t}$ and $t\bar{t}Z$ regions for the S+B tZc fit in the SRs+CRs with real data.	131
4.54	Pre- and post-fit BDTG output distributions in the validation regions for the S+B tZc fit in the SRs+CRs with real data.	133
5.1	Branching ratios of the top quark as function of m_S and of the scalar as a function of \mathbb{Z}_2	139
5.2	Feynman diagrams of the FCNC interactions via tSq vertex.	140
5.3	Mass distributions of the scalar and top quark for the $t \rightarrow Sq, S \rightarrow \mu^+\mu^-$ case.	142
5.4	Limits on the branching ratio and cross-section for the $t \rightarrow Sq, S \rightarrow \mu^+\mu^-$ case.	142
5.5	Mass distributions of the scalar and total system for the $t \rightarrow Sq, S \rightarrow \tau^+\tau^-$ case.	145
5.6	Limits on the branching ratio and cross-section for the $t \rightarrow Sq, S \rightarrow \tau^+\tau^-$ case.	146
5.7	Mass distributions of the two reconstructed scalars for the $t \rightarrow SSq, S \rightarrow \mu^+\mu^-$ case.	149
5.8	Limits on the branching ratio and cross-section for the $t \rightarrow SSq, S \rightarrow \mu^+\mu^-$ case.	149
A.1	Correlation matrix of the full set input variables for the D_1 discriminant.	174
A.2	Signal GBDT output score distributions using the full set of input variables for the D_1 discriminant.	175
A.3	Background GBDT output score distributions using the full set of input variables for the D_1 discriminant.	175
A.4	Signal GBDT output score distributions using the final set of input variables for the D_1 discriminant.	176
A.5	Background GBDT output score distributions using the final set of input variables for the D_1 discriminant.	176
A.6	$S_{\text{eff}}/\sqrt{B_{\text{eff}}}$ as a function of the cut on the GBDT output score for the D_1 discriminant.	177
A.7	$S_{\text{eff}}/\sqrt{B_{\text{eff}}}$ and ROC integral as a function of the BDT hyper-parameters combination for the D_1 discriminant.	177
A.8	Correlation matrix of the full set input variables for the D_2^c discriminant.	179
A.9	Signal GBDT output score distributions using the full set of input variables for the D_2^c discriminant.	180
A.10	Background GBDT output score distributions using the full set of input variables for the D_2^c discriminant.	180
A.11	Signal GBDT output score distributions using the final set of input variables for the D_2^c discriminant.	181

A.12	Background GBDT output score distributions using the final set of input variables for the D_2^c discriminant	181
A.13	$S_{\text{eff}}/\sqrt{B_{\text{eff}}}$ as a function of the cut on the GBDT output score for the D_2^c discriminant	182
A.14	$S_{\text{eff}}/\sqrt{B_{\text{eff}}}$ and ROC integral as a function of the BDT hyper-parameters combination for the D_2^c discriminant	182
B.1	Pulls and constraints of the instrumental nuisance parameters for the S+B tZu fit with distinct pruning thresholds	184
B.2	Pulls and constraints of the instrumental nuisance parameters for the S+B tZu fit without pruning	185
B.3	Pulls and constraints of the theoretical and modelling nuisance parameters for the S+B tZu fit with distinct pruning thresholds	186
B.4	Pulls and constraints of the theoretical and modelling nuisance parameters for the S+B tZu fit without pruning	187
B.5	Pulls and constraints of the instrumental nuisance parameters for the S+B tZc fit with distinct pruning thresholds	188
B.6	Pulls and constraints of the instrumental nuisance parameters for the S+B tZc fit without pruning	189
B.7	Pulls and constraints of the theoretical and modelling nuisance parameters for the S+B tZc fit with distinct pruning thresholds	190
B.8	Pulls and constraints of the theoretical and modelling nuisance parameters for the S+B tZc fit without pruning	191

List of Tables

2.1	Quarks and leptons of the SM.	6
2.2	Bosons of the SM.	6
2.3	Theoretical predictions and experimental limits of the FCNC top quark decays for the SM and some of its extensions.	19
2.4	Cross-section for the processes with FCNC tZq and tyq vertices.	23
3.1	Sizes and energies reached by the LHC accelerators.	27
3.2	LHC operating parameters.	29
3.3	Event yields for simple selection using L1 AFP triggers.	39
3.4	Summary of the optimisation of the region of acceptance for AFP C-side stations.	42
4.1	Summary of the efficiencies for the DL1r b -tagging algorithm.	47
4.2	Overview of the requirements of the physics objects.	48
4.3	Summary of the generation details for all the signal and background processes.	53
4.4	Event selection of the signal regions.	54
4.5	Summary of the mean values and standard deviations resulting from the top quark reconstructions with simulated signal events.	57
4.6	Event yields for signal and background processes in the signal regions.	59
4.7	Event selection of the control regions.	63
4.8	Event yields for the signal and background processes in the control regions.	64
4.9	Summary of the GBDT discriminant variables and its characteristics.	72
4.10	Separation power of the full set of input variables for the D_2^u discriminant.	74
4.11	Separation power of the final set of input variables for the D_2^u discriminant.	74
4.12	Separation power of the final set of input variables for the tZu and tZc coupling searches.	74
4.13	Summary of the configuration parameters used for the GBDT algorithm.	79
4.14	Importance of the input variables for the D_1 discriminant.	80
4.15	Importance of the input variables for the D_2^u discriminant.	87
4.16	Importance of the input variables for the D_2^c discriminant.	87
4.17	Event selection of the validation regions.	88

4.18	Uncertainties on the fake lepton fractions applied to the $t\bar{t}$ sample.	93
4.19	Rate uncertainties applied on the normalisation of the background processes.	94
4.20	Overview of the variables used in the combined fit for the signal and control regions.	97
4.21	Pre-fit event yields for the S+B tZu fit in the SRs+CRs with realistic Asimov data.	104
4.22	Post-fit event yields for the S+B tZu fit in the SRs+CRs with realistic Asimov data.	104
4.23	Pre- and post-fit event yields of the validation regions for the S+B tZu fit in the SRs+CRs with realistic Asimov data.	108
4.24	Pre-fit event yields for the S+B tZc fit in the SRs+CRs with realistic Asimov data.	113
4.25	Post-fit event yields for the S+B tZc fit in the SRs+CRs with realistic Asimov data.	113
4.26	Pre- and post-fit event yields of the validation regions for the S+B tZc fit in the SRs+CRs with realistic Asimov data.	117
4.27	Pre-fit event yields for the S+B tZu fit in the SRs+CRs with real data.	123
4.28	Post-fit event yields for the S+B tZu fit in the SRs+CRs with real data.	123
4.29	Pre- and post-fit event yields of the validation regions for the S+B tZu fit in the SRs+CRs with real data.	124
4.30	Pre-fit event yields for the S+B tZc fit in the SRs+CRs with real data.	129
4.31	Post-fit event yields for the S+B tZc fit in the SRs+CRs with real data.	129
4.32	Pre- and post-fit event yields of the validation regions for the S+B tZc fit in the SRs+CRs with real data.	132
4.33	Observed and expected upper limits on the branching ratios for the FCNC tZu and tZc vertices.	135
4.34	Observed and expected upper limits on the Wilson coefficients for the FCNC tZu and tZc vertices.	135
4.35	Observed and expected upper limits on the tZ production cross-section for the FCNC tZu and tZc vertices.	135
5.1	Event yields of the benchmark signal points for the $t \rightarrow Su, S \rightarrow \mu^+ \mu^-$ analysis.	143
5.2	Event yields of the benchmark signal points for the $t \rightarrow Sc, S \rightarrow \mu^+ \mu^-$ analysis.	143
5.3	Event yields of the background processes for the $t \rightarrow Sq, S \rightarrow \mu^+ \mu^-$ analysis.	144
5.4	Event yields for the last selection cut of the background processes in the $t \rightarrow Sq, S \rightarrow \mu^+ \mu^-$ analysis.	144
5.5	Event yields of the benchmark signal points for the $t \rightarrow Su, S \rightarrow \tau^+ \tau^-$ analysis.	145
5.6	Event yields of the benchmark signal points for the $t \rightarrow Sc, S \rightarrow \tau^+ \tau^-$ analysis.	146
5.7	Event yields of the background processes for the $t \rightarrow Sq, S \rightarrow \tau^+ \tau^-$ analysis.	146
5.8	Event yields for the last selection cut of the background processes in the $t \rightarrow Sq, S \rightarrow \tau^+ \tau^-$ analysis.	147

5.9	Event yields of the benchmark signal points for the $t \rightarrow SSu, S \rightarrow \mu^+ \mu^-$ analysis.	150
5.10	Event yields of the benchmark signal points for the $t \rightarrow SSc, S \rightarrow \mu^+ \mu^-$ analysis.	150
5.11	Event yields of the background processes for the $t \rightarrow SSu, S \rightarrow \mu^+ \mu^-$ analysis.	150
A.1	Separation power of the full set of input variables for the D_1 discriminant.	173
A.2	Separation power of the final set of input variables for the D_1 discriminant.	173
A.3	Separation power of the full set of input variables for the D_2^c discriminant.	178
A.4	Separation power of the final set of input variables for the D_2^c discriminant.	178
B.1	Summary of all the tested normalisation and shape pruning levels.	183
B.2	Expected limits on the branching ratios of $t \rightarrow Zu$ for the different pruning thresholds considered.	184
B.3	Expected limits on the branching ratios of $t \rightarrow Zu$ for the different pruning thresholds considered.	188

Introduction

The top quark is the heaviest elementary particle discovered so far and the study of its properties provides not only an important test of the Standard Model (SM) of particle physics, but also a window to physics beyond it related to the Yukawa coupling to the Higgs boson and to the sensitivity to new heavy particles. At the Run-1 and Run-2 phases of the Large Hadron Collider (LHC), both ATLAS and CMS collaborations developed an extensive programme devoted to the measurement of the top quark properties. In fact, the LHC is a true top quark factory with several million top quarks being produced every year. This is the perfect scenario to expand our knowledge about the top quark sector both by precision measurements of the SM and by direct and indirect searches for physics beyond it.

With so many top quarks being produced, the top quark couplings can be precisely measured due to the increase of data luminosity collected during the entire Run-2 phase of the LHC. The increase on the luminosity and the center-of-mass energy of the proton-proton (pp) collisions allows us to further pursue top quark studies, namely on the flavour changing neutral couplings to the SM gauge bosons. Within the SM formulation, the top quark decays via Flavour Changing Neutral Currents (FCNC) have extremely small branching ratios but some of its extensions predict a significant enhancement of the probability for such processes.

This thesis presents a highly sensitive way of probing the FCNC tZq coupling through a search for top quark decays with tZq vertex using 139 fb^{-1} of pp collision data at $\sqrt{s} = 13\text{ TeV}$. This data was collected during the Run-2 of the LHC between 2015 and 2018. The analysis targets top quark decays to a Z boson and a light quark, where the production and decay modes contribute to the signal. Events are required to have exactly three leptons from the leptonic decays of the Z boson and the top quark and exclusive analysis categories are defined based on the reconstructed mass of the top quark candidate, the number of jets and the value of a b -tagging discriminant that provides a measure on the likelihood of a jet

containing a b -hadron (i.e. a jet originated from a bottom quark).

Multivariate techniques based on Boosted Decision Trees are used to reconstruct the FCNC signal and to distinguish it from the large diboson background. The adequate and precise estimation of the dominant background arising from diboson production with additional light- and heavy-flavour jets plays a major role in this search. Consequently, the modelling has been studied extensively and a combination of the most up to date theoretical predictions and a sophisticated statistical analysis has been developed to constrain the large background uncertainties. The categories rich in signal are analysed together with the signal-depleted ones in a combined likelihood fit that simultaneously determines the event yields for the signal while constraining the overall background model within the assigned systematic uncertainties. The objective of this search is either the discovery of a process not observed yet or the determination of the most stringent limits obtained so far in the tZq vertex of the FCNC processes as well as the study of the respective phenomenological consequences.

The thesis is structured as follows. The important role of the top quark in the SM and models beyond it is described in Chapter 2. It also details the theoretical formulation of the SM and the correspondent experimental successes and shortcomings. The study of new interactions is also motivated in the second part of Chapter 2 with focus on the FCNC processes involving a top quark. Since FCNC processes can occur in both production and decays modes, it was crucial to quantify the interference effects and conclude if these should be considered in the experimental searches at the LHC or, on the contrary, they can be safely neglected. The last section of Chapter 2 describes the study on the interference effects on the tZq and $t\gamma q$ FCNC anomalous couplings pursued in collaboration with the University of Dortmund (Germany). A meticulous work was performed starting on the generation of Monte Carlo (MC) simulation samples focusing on the different modes followed by a detailed analysis of all the variables of the reconstructed objects.

In Chapter 3, CERN, the LHC, the ATLAS detector and the Worldwide LHC Computing Grid are described. The LHC causes the collision of two bunches of protons travelling in opposite directions in four different interaction points, being one of them the center of the ATLAS detector. Since the colliding bunches are composed by 10^{11} protons, the ones not participating in the primary collisions can travel through the beam pipe. The horizontal roman pots located around two hundred meters from the ATLAS interaction point allows the measure of those remaining protons. Chapter 3 also includes the study and the evaluation of the performance of the pixel silicon detectors that compose such horizontal roman pots.

The main topic of this thesis, the search for flavour changing neutral currents with the tZq coupling, is detailed in Chapter 4. The first part of this chapter summarizes the MC simulations that serve as the theoretical predictions of the signal and background processes and describes the particle reconstruction and identification of the measured objects by the multiple sub-systems within the ATLAS detector. The second part presents the selection criteria applied to events, describes the event categorisation and details the multivariate analysis techniques used to reconstruct the FCNC signal events and to separate them

from the dominant background processes. Finally, the background estimation and the assigned systematic uncertainties are introduced before the explanation of the fit model and the results on the upper limits for the signal processes.

The characteristics of the top quark provide an ideal motivation to search for new physics. Chapter 5 presents a phenomenological study focused on the FCNC processes in the top sector with the particularity of being mediated by a neutral pseudo-scalar at the electroweak scale instead of the Z boson. These processes can easily arise in scenarios of new physics, in particular within composite Higgs models. Such interactions are poorly constrained by current experiments, while they can be searched for at the LHC in rare top decays and, more generally, in the channels $pp \rightarrow tS(S) + j$, with $S \rightarrow l^+l^-$. In collaboration with the University of Granada (Spain), a comprehensive study of the theoretical motivation lead up to the creation of a model with the Universal FeynRules Output in order to enable the MC signal generation. The experimental part of this study comprised the generation of MC samples for both signal and background processes, the implementation and optimisation of the selection for the three different scenarios considered and the extraction of the limits on the cross-section that later were translated into limits on the branching ratios of the signal processes.

The top quark within the Standard Model of Particle Physics and beyond

The SM of particle physics is the theoretical framework that so far better describes the subatomic world. Developed in the 1960's [1], it has been tested and has been successful in describing the experimental observations. This chapter presents an overview of the SM with a brief summary of the elementary particles and their fundamental interactions. The second part of this chapter is focused on the top quark: its properties, production mechanisms and decay modes.

2.1 The Standard Model of particle physics

The matter is made from atoms, which are made from electrons and nuclei. The atomic nucleus is made of neutrons and protons and both of them are made of elementary particles named quarks. The elementary particles interact via four fundamental forces in nature: strong force, weak force, electromagnetic force and gravitational force.

The strong interaction is a very short range force (typically around 10^{-15} m) and it is responsible for the stability of the atomic nuclei by preventing them from fragmenting as a result of the electric repulsion of the protons. The weak force describes the beta decay of unstable atoms and acts at very short distances (typically around 10^{-18} m). The electromagnetic interaction acts over an infinite range and is responsible for the interaction between electric charged particles. The SM does not provide a description of the gravitational force, for which no consistent quantum theory exists up to now. Regardless of that, the gravity acts with a coupling strength far too weak to play any role at high energy physics experiments.

Based on relativistic quantum field theory, the SM describes the particle interactions of the strong, weak

and electromagnetic forces. This model assumes that matter is made from elementary point-like particles with spin 1/2 called fermions, which follow the Fermi-Dirac statistics. On the other hand, the interaction force carriers are integer spin particles that obey Bose-Einstein statistics, being called bosons. There are two types of fermions: quarks and leptons. The leptons are divided in the electrically charged particles with the fundamental charge, e , corresponding to an electric charge of -1.6×10^{-19} C and the electrically neutral particles called neutrinos (ν). Differently, the quarks carry fractional electric charge which can be $+2/3|e|$ or $-1/3|e|$. The quarks are characterised by another variable called colour that have three different types: red, green or blue. Since free coloured particles have not been observed, quarks must be confined into colourless composite particles. These particles are either baryons, composed by three quarks, or mesons, consisting of a quark and an antiquark. Baryons and mesons are called hadrons, which consist of bound states of quarks. Additionally, every particle has an associated anti-particle with the same mass but carrying the opposite quantum numbers to its corresponding particle.

Fermions are subdivided in three families or generations. Generations of quarks and leptons are copies with the same quantum numbers except for their masses, having the first generation the lighter particles and the third the heavier. For the lepton case, each generation contains a charged lepton and its partner neutrino while, for the quark case, it contains a quark with an electric charge of $+2/3|e|$ and a quark with an electric charge of $-1/3|e|$. The fundamental fermions and their characteristics are listed in Table 2.1. The bosonic sector is responsible for the interactions described in the SM. The electromagnetic force carrier is the photon (γ), being a massless and electrically neutral particle. The weak force carriers are the W^\pm and Z bosons. Although these three bosons are massive, the Z boson is electrically neutral and the W^\pm bosons have positive and negative electric charge, respectively. The strong force carriers are the gluons (g) which are massless particles with no electric charge. In total, there are eight different mediators of the strong force since the $SU(3)_c$ group has eight generators representing each a colour exchange and a gauge boson (gluon) in colour space. This characteristic implies that gluons interact among themselves and only couple to the strong charged particles. Consequently, the quarks are the only fermions that can participate in the strong interaction. The gauge bosons of the strong, weak and electromagnetic forces and their characteristics are summarised in Table 2.2. Besides the gauge bosons, the SM contains one scalar spin zero boson with a mass of 124.97 ± 0.24 GeV [3], which is called Higgs boson.

2.1.1 Standard Model Lagrangian

In particle physics, a formulation of classical mechanisms called Lagrangian is used to describe physics systems that can be invariant under different kind of transformations, i.e. they contain a symmetry. The transformations can be either time and space dependent called local gauge transformations, or time and space independent, called global transformations. From the Noether theorem [4], a Lagrangian that contains a symmetry describes a physical system which conserves one or more physical quantities. The

Generation	Symbol	Name	Mass	Electric charge [e]
Quarks				
1 st	<i>u</i>	Up	$2.16^{+0.49}_{-0.26}$ MeV	+2/3
	<i>d</i>	Down	$4.67^{+0.48}_{-0.17}$ MeV	-1/3
2 nd	<i>c</i>	Charm	1.27 ± 0.02 GeV	+2/3
	<i>s</i>	Strange	93^{+11}_{-5} MeV	-1/3
3 rd	<i>t</i>	Top	172.76 ± 0.30 GeV	+2/3
	<i>b</i>	Bottom	$4.18^{+0.03}_{-0.02}$ GeV	-1/3
Leptons				
1 st	<i>e</i>	Electron	~ 0.51 MeV	-1
	ν_e	Electron Neutrino	< 1.1 eV	0
2 nd	μ	Muon	~ 105.66 MeV	-1
	ν_μ	Muon Neutrino	< 1.1 eV	0
3 rd	τ	Tau	~ 1776.86 MeV	-1
	ν_τ	Tau Neutrino	< 1.1 eV	0

Table 2.1: Table of quarks and leptons families in the SM and the corresponding masses and electric charges [2].

Interaction	Mediator	Mass [GeV]	Electric Charge [e]
Strong	Gluon $\times 8$ (g)	0	0
Electromagnetic	Photon (γ)	0	0
Weak	Z	91.188 ± 0.002	0
	W^\pm	80.38 ± 0.01	± 1

Table 2.2: Table of the gauge bosons in the SM with their mass and electric charge [2].

Lagrangian of the Standard Model of particle physics is characterised by the Lorentz invariance and the invariance under the non-abelian special unitary group gauge transformation $SU(3)_c \otimes SU(2)_L \otimes U(1)_Y$, where the strong interaction is described by $SU(3)_c$ transformation group and the combination of electromagnetic and weak forces (i.e. the electroweak force) is described by the $SU(2)_L \otimes U(1)_Y$ term. In order to study the SM Lagrangian, one can proceed by splitting the mathematical expression in two terms: the first describing electroweak interactions and the second one describing quantum chromodynamics as

$$\mathcal{L}_{SM} = \mathcal{L}_{EW} + \mathcal{L}_{QCD}. \quad (2.1)$$

2.1.1.1 Quantum electrodynamics

The classical theory of electromagnetic interactions is well known through the Maxwell equations of the nineteenth century. The theory of Quantum Electrodynamics (QED) unified electrodynamics and quantum mechanics providing a quantum field theory based on the gauge invariance of electrodynamics. The QED theory describes the interactions between electrically charged particles mediated by a quantised electromagnetic field. The free spin 1/2 particles are described in the Dirac Lagrangian

$$\mathcal{L}_{Dirac} = \bar{\psi}(i\gamma^\mu \partial_\mu - m)\psi \quad (2.2)$$

where $\bar{\psi}$ corresponds to $\psi^\dagger \gamma^0$, γ^μ ($\mu = 0, 1, 2, 3$) corresponds to the Dirac matrices, m is the fermion mass and ψ is the Dirac field. The Dirac matrices are defined through the Clifford algebra that follows the anti-commutation relation $\{\gamma^\mu, \gamma^\nu\} = \gamma^\mu \gamma^\nu + \gamma^\nu \gamma^\mu = 2g^{\mu\nu}$, being $g^{\mu\nu}$ the Minkowski metric tensor. The Lagrangian in Equation 2.2 is not invariant under a local $U(1)$ gauge transformation of the form

$$\psi \rightarrow e^{-ie\alpha(x)}\psi \text{ and } \bar{\psi} \rightarrow e^{ie\alpha(x)}\bar{\psi} \quad (2.3)$$

where e is in units of the electric charge of the proton and α is a real number. With this transformation the Dirac Lagrangian acquires an additional term of $\bar{\psi}e\gamma^\mu \partial_\mu \psi$. To obtain a $U(1)$ invariant Lagrangian, another term with the expression $\bar{\psi}e\gamma^\mu A_\mu \psi$ is added, where A_μ is the electromagnetic field. Adding this term and the field dynamics, described by the Maxwell equation, the QED Lagrangian can be obtained:

$$\mathcal{L}_{QED} = -\frac{1}{4}F^{\mu\nu}F_{\mu\nu} + \bar{\psi}[i\gamma^\mu(\partial_\mu - eA_\mu) + m]\psi \quad (2.4)$$

where $F^{\mu\nu} = \partial_\mu A_\nu - \partial_\nu A_\mu$ is the electromagnetic field tensor. Requiring local phase invariance under $U(1)$ applied to the Dirac Lagrangian, it is generated all electrodynamics and introduced a massless field which can be interpreted as the photon.

2.1.1.2 Quantum chromodynamics

The interactions between quarks and gluons are described by a quantum field theory called Quantum Chromodynamics (QCD) [5]. Analogous to the electric charge in QED, each quark has an internal degree of freedom known as colour charge and it can be defined by a triplet of fields represented as:

$$q = \begin{pmatrix} q_R \\ q_G \\ q_B \end{pmatrix} \quad (2.5)$$

where each of these fields is a Dirac spinor associated to a colour state (red (R), green (G) and blue (B)). The QCD theory describes the dynamics of the strong interactions through a gauge theory of a local $SU(3)$ invariance, being the correspondent generators written as:

$$t_a = \frac{1}{2}\lambda_a \quad (2.6)$$

where λ_a denote the Gell-Mann matrices and the colour index a running from 1-8. Similarly to the QED gauge fields, the covariant derivative D_μ and the gluon field strength tensor $G_{\mu\nu}^a$ are introduced:

$$D_\mu = \partial_\mu + ig_s t_a G_\mu^a \quad (2.7)$$

where G_μ^a are the gluon fields, g_s is the QCD gauge coupling constant and t_a correspond to the $SU(3)$ generators. After introducing the covariant derivative, the Lagrangian of QCD theory is given by:

$$\mathcal{L}_{QCD} = \bar{q}(i\gamma^\mu D_\mu - m)q - \frac{1}{4}G_{\mu\nu}^a G_a^{\mu\nu} \quad (2.8)$$

where γ^μ are the Dirac matrices and q is the vector in Equation (2.5). The field tensor $G_{\mu\nu}^a$ is defined by:

$$G_{\mu\nu}^a = \partial_\mu G_\nu^a - \partial_\nu G_\mu^a - g_s f_{abc} G_\mu^b G_\nu^c \quad (2.9)$$

where f_{abc} is the structure constant of $SU(3)_c$ defined by the commutation relation $[t_a, t_b] = if_{abc}t_c$. The third term of the tensor describes the gluon self-interaction and is responsible for the non-abelian nature of QCD. The QCD theory has been very successful in the description of the interactions binding quarks to hadrons. However, there are two important characteristics of this theory: asymptotic freedom and confinement [6, 7]. Asymptotic freedom means, at very high energies and short distances, quarks and gluons interact weakly with each other allowing the computation of observables using the perturbation theory. Confinement means that at very low energy scales which corresponds to large spatial separation, when we try to separate quarks, the energy of the gluon field increases in a way that creates quark and anti-quark pairs and, consequently, free quarks cannot exist. This property has the experimental consequence that coloured partons produced in high-energy interactions will manifest themselves as collimated streams of hadrons referred to as “jets” [8].

2.1.1.3 Electroweak theory

Proposed by Glashow, Salam and Weinberg [9–11], the electroweak theory is a unified theory of electroweak interactions which describe the weak and electromagnetic forces from a single gauge group $SU(2)_L \otimes U(1)_Y$ where Y corresponds to the weak hypercharge. The weak hypercharge is given by the Gell-Mann-Nishijima relation $Y = 2(Q - T_3)$ where T_3 is the third component of the weak isospin operator $\hat{T} = \sigma_i/2$ ($i=1,2,3$) with σ_i corresponding to the three Pauli matrices and Q is the fermion electric charge (in units of $|e|$). The subscript in $SU(2)_L$ refers to the fact that only left-handed fermions interact through the weak force. The electroweak interaction is the interaction responsible for the change of flavour of leptons and quarks. The left-handed and right-handed components of the fermions fields can be obtained via the chirality projectors as:

$$\psi_L = \frac{1}{2}(1 - \gamma^5)\psi \text{ and } \psi_R = \frac{1}{2}(1 + \gamma^5)\psi.$$

Right-handed fermions transform as singlets and left-handed fermions transform as doublets:

$$f_R^i = l_R^i, u_R^i, d_R^i \text{ and } f_L^i = \begin{pmatrix} l_L^i \\ v_L^i \end{pmatrix}, \begin{pmatrix} u_L^i \\ d_L^i \end{pmatrix}$$

with $i = 1, 2, 3$ corresponding to the generation index. The field strength tensors for the weak isospin and weak hypercharge fields $W_{\mu\nu}^i$ and $B_{\mu\nu}$ can be explicitly written as:

$$\begin{aligned} W_{\mu\nu}^i &\equiv \partial_\mu W_\nu^i - \partial_\nu W_\mu^i + g\epsilon^{ijk} W_\mu^j W_\nu^k, \\ B_{\mu\nu} &\equiv \partial_\mu B_\nu - \partial_\nu B_\mu \end{aligned} \quad (2.10)$$

where ϵ^{ijk} corresponds to the totally anti-symmetric Levi-Civita tensor, g corresponds to the $SU(2)_L$ gauge coupling, W_ν^i and B_ν are the gauge bosons of $SU(2)_L$ and $U(1)_Y$ respectively and i take values of 1, 2 or 3. The Lagrangian of the gauge field is defined with the weak field tensors $W_{\mu\nu}^i$ and $B_{\mu\nu}$ through the following relation:

$$\mathcal{L}_{gauge} = -\frac{1}{4} W_{\mu\nu}^i W_i^{\mu\nu} - \frac{1}{4} B_{\mu\nu} B^{\mu\nu}. \quad (2.11)$$

Finally, the theory of electroweak interactions can be described through the Lagrangian:

$$\mathcal{L}_{EW} = \sum_{f=l,q} \bar{f}(i\gamma^\mu D_\mu)f + \mathcal{L}_{gauge} \quad (2.12)$$

where the covariant derivative D_μ is defined by

$$D_\mu \equiv \partial_\mu - ig \vec{T} \cdot \vec{W}_\mu - ig' \frac{Y}{2} B_\mu \quad (2.13)$$

being g and g' the coupling constants of the $SU(2)_L$ and $U(1)_Y$ gauge groups, respectively.

The weak interactions are known to violate parity with the weak charged current interaction only coupling to left-handed chirality state fermions and right-handed chirality state anti-fermions. The electroweak bosons mediating the weak charged current interactions are W^+ and W^- bosons, being the gauge fields written as a linear combination of W_μ^1 and W_μ^2 bosons fields:

$$W_\mu^\pm = \frac{1}{\sqrt{2}}(W_\mu^1 \mp iW_\mu^2). \quad (2.14)$$

The weak neutral current and electromagnetic interactions are carried by neutral bosons, the Z boson and the photon, respectively. Since it is experimentally shown that the Z boson couples to both left-handed and right-handed chirality state fermions, the W_μ^3 boson field can not be directly associated to the Z boson. Moreover, the B_μ field can not be directly associated to the photon since it interacts in the same way with both components of left-handed chirality state fermions, including neutrinos, while the photon does not couple to them. Therefore, the Z boson field Z_μ and photon field A_μ are written as a mixing of W_μ^3 and B_μ fields:

$$\begin{pmatrix} Z_\mu \\ A_\mu \end{pmatrix} = \begin{pmatrix} \cos \theta_W & -\sin \theta_W \\ \sin \theta_W & \cos \theta_W \end{pmatrix} \begin{pmatrix} W_\mu^3 \\ B_\mu \end{pmatrix} \quad (2.15)$$

where θ_W is the weak mixing angle defined from the gauge coupling constants g and g' through the relation $\theta_W = \tan^{-1}(g/g')$. The electric charge e can be also seen as the photon coupling strength, which is related to the gauge coupling constant as $e = g \cdot \sin \theta_W$. Although the electroweak Lagrangian in Equation (2.12) does not contain terms related to the fermion masses, the experiments confirmed the existence of massive fermions and electroweak mediators (W^\pm and Z bosons). By spontaneously breaking the symmetry with the Higgs mechanism, the gauge bosons and the fermions acquire their masses through the interaction with the Higgs field.

2.1.1.4 The Higgs-Englert-Brout mechanism

Proposed by three independent groups [12–14], the Higgs-Englert-Brout mechanism solved the contradiction between massive particles and the requirement of gauge invariance. This mechanism is based in a spontaneous symmetry breaking, where the symmetry group $SU(2)_L \otimes U(1)_Y$ breaks down to $U(1)_{EM}$. The Higgs field is a isospin doublet of complex scalar fields and is defined as

$$\Phi \equiv \begin{pmatrix} \phi^+ \\ \phi^0 \end{pmatrix} \quad (2.16)$$

where ϕ^+ corresponds to a electrically charged field and ϕ^0 to a electrically neutral field. The Lagrangian which describes the Higgs field is defined as

$$\mathcal{L}_\Phi = (D_\mu \Phi)^\dagger (D^\mu \Phi) - V(\Phi) \quad (2.17)$$

with the covariant derivative D_μ given by Equation 2.13 and the $V(\Phi)$ corresponding to the Higgs potential defined as

$$V(\Phi) = \mu^2 \Phi^\dagger \Phi + \lambda (\Phi^\dagger \Phi)^2. \quad (2.18)$$

The Higgs potential depends on the parameters μ^2 and λ . Consider the case where $\mu^2 < 0$ and $\lambda > 0$, the minimum of the potential $V(\Phi)$ is given by

$$\langle \Phi^\dagger \Phi \rangle = -\frac{\mu^2}{2\lambda} \equiv \frac{v^2}{2} \quad (2.19)$$

and the Higgs field has a non-zero vacuum expectation value of $v/\sqrt{2}$ and does not have a unique minimum. In the unitary gauge, the Higgs potential minimum can be obtained in a way that the Higgs field acquiring a vacuum expectation value is the electrically neutral field and the Equation 2.16 can be rewritten as:

$$\Phi(x) = \frac{1}{\sqrt{2}} \begin{pmatrix} 0 \\ v + H(x) \end{pmatrix} \quad (2.20)$$

where $H(x)$ represents the ground state fluctuations around the vacuum state.

The interactions between the Higgs field and the fermions fields can be written as

$$\mathcal{L}_{Yukawa} = \sum_{f=l,q} y_f (\bar{f}_L \Phi f_R + \bar{f}_R \bar{\Phi} f_L) \quad (2.21)$$

where the $f_L(f_R)$ corresponds to the left-handed (right-handed) fermion field, the $\bar{f}_L(\bar{f}_R)$ is the hermitian conjugate of the left-handed (right-handed) fermion field and the matrices y_f describe the Yukawa couplings between the Higgs doublet and the fermions. The Lagrangian in Equation 2.21, denominated the Yukawa Lagrangian, is gauge invariant since the terms $\bar{f}_L \Phi f_R$ and $\bar{f}_R \bar{\Phi} f_L$ are singlets. Through the Yukawa Lagrangian, the Higgs field and the Higgs Lagrangian, the mathematical expressions of the mass of the fermions and the mass of the Higgs boson can be obtained:

$$m_f = y_f \frac{v}{\sqrt{2}}, \quad m_H = \sqrt{2\lambda}v \quad (2.22)$$

where the value of the λ is a free parameter of the theory and, consequently, the mass of the Higgs boson could not be predicted before its discovery. The mass of the electroweak gauge bosons can also be deduced, giving $m_W = \frac{vg}{2}$ and $m_Z = v \frac{\sqrt{g^2+g'^2}}{2}$, while the photon remains massless. The masses of the Z and W^\pm bosons are also related to each other through the weak mixing angle as $M_W/M_Z = \cos \theta_W$.

2.1.1.5 Quark mixing and CKM matrix

The fermions acquire masses through the Yukawa interactions that couple left- and right-handed chirality state fermions to the Higgs field. For the neutrinos, this interaction has no effect due to the absence of right-handed neutrinos in the SM. The masses for the other fermions are generated with the change from flavour states to mass states using unitary matrices V :

$$u'_{L,R} = V_{L,R}^u u_{L,R}, d'_{L,R} = V_{L,R}^d d_{L,R}, l'_{L,R} = V_{L,R}^l l_{L,R}, \quad (2.23)$$

where u , d and l are the fermion fields of up-type quarks, down-type quarks and leptons, respectively. Since left-handed quarks are transformed by different matrices ($V_L^u \neq V_L^d$), the $SU(2)$ left-handed quarks doublets are constructed as:

$$\begin{pmatrix} u \\ d'' \end{pmatrix}_L, \begin{pmatrix} c \\ s'' \end{pmatrix}_L, \begin{pmatrix} t \\ b'' \end{pmatrix}_L \quad (2.24)$$

with

$$\begin{pmatrix} d'' \\ s'' \\ b'' \end{pmatrix} = V_{CKM} \begin{pmatrix} d \\ s \\ b \end{pmatrix} = \begin{pmatrix} V_{ud} & V_{us} & V_{ub} \\ V_{cd} & V_{cs} & V_{cb} \\ V_{td} & V_{ts} & V_{tb} \end{pmatrix} \begin{pmatrix} d \\ s \\ b \end{pmatrix} \quad (2.25)$$

where V_{CKM} corresponds to the unitary matrix that describes the quark mixing called Cabibbo-Kobayashi-Maskawa (CKM) matrix. The quark mixing allows a quark from one doublet to decay into a quark from

another doublet through a change on the coupling of the weak charged currents. The CKM matrix consists in a $n \times n$ unitary matrix which describe n quark families and the single elements $V_{q_1 q_2}$ of the CKM matrix are proportional to the coupling of two quarks q_1 and q_2 to a W boson and can be determined experimentally. The CKM matrix can be obtained through a global fit assuming unitarity and three generations of fermions [2]:

$$V_{CKM} = \begin{pmatrix} 0.97401 \pm 0.00011 & 0.22650 \pm 0.00048 & 0.00361^{+0.00011}_{-0.00009} \\ 0.22636 \pm 0.00048 & 0.97320 \pm 0.00011 & 0.04053^{+0.00083}_{-0.00061} \\ 0.00854^{+0.00023}_{-0.00016} & 0.03978^{+0.00082}_{-0.00060} & 0.999172^{+0.000024}_{-0.000035} \end{pmatrix}. \quad (2.26)$$

2.1.2 Experimental successes and shortcomings of the Standard Model

Since its formulation, the SM has been able to describe accurately most experimental observations and all the discovered particles have been accommodated nicely into the model. Throughout the years, the SM has been tested in multiple experiments and its validity has been confirmed with precision measurements. Except for gravity, the SM explains the fundamental interactions of fermionic fields having free parameters corresponding to [15]: three coupling parameters (g , g' and g_s), two parameters to define the Higgs potential (μ^2 and λ), six masses of the quarks coupling to the Higgs field, four parameters for the CKM matrix corresponding to three mixing angles and one Charge Parity (CP)¹ violating phase, three charged lepton masses, one parameter related with non-perturbative CP violation in QCD and seven parameters related with the neutrinos (three for neutrino masses, three for their mixing angles and one for CP violating phase of the neutrino mixing matrix). The SM as described here has a total of 26 free parameters, being the majority of them related to the flavour physics. The consistency of the SM has been tested through the electroweak fit where the fundamental parameters of the SM were fitted to different data measurements, confirming that all the observations within the correspondent uncertainties can be explained from the SM predictions. Despite the remarkable successes of the SM, there are some theoretical and experimental evidences that can not be accommodated into the framework. These disagreements lead to the general conclusion that the SM needs to be regarded as an effective theory, i.e. the low energy realisation of a more complete theory that would be able to explain the whole range of experimental observations. A brief description of the main open questions in the SM can be found below:

- Gravitational lensing and measurements of the rotation curves of galaxies led to the inference of the existence of a non-luminous matter denominated 'dark matter' in the Universe [16–18]. Dark matter does not interact through the electromagnetic force (i.e. it can not be observed) but its presence is

¹The CP symmetry is a combination of the charge conjugation symmetry and the parity symmetry which states that the laws of physics should be the same if a particle or a system of particles are interchanged with respective anti-particles (C symmetry) and when its spatial coordinates are inverted (P symmetry).

evident through gravitational effects, being expected to compose more than 80% of the total matter in the Universe.

- The universe seems to be completely dominated by matter. To explain the matter/anti-matter asymmetry, the three Sakharov conditions [19] need to be met. One of these conditions requires baryon number violation, which is absent in perturbative descriptions of the SM. Besides that, CP violating processes must be present. The CP violation in the weak interaction (coming from the presence of a phase in the CKM matrix) is not strong enough to justify the current observation. Both conditions indicate that physics beyond the SM accounting for strong CP and baryon number violating effects becomes relevant at higher energy scales than experimentally observed at the moment.
- Although neutrino masses are not measured directly, the measurement of oscillations requires that there is a mass difference between the different neutrinos generations [20]. A mass term for neutrinos is not in the SM but the addition of right-handed neutrinos or alternatives such as Dirac neutrinos can be accommodated. Given the fact that the neutrinos are massive, the SM has seven additional free parameters (three parameters for neutrino masses, three for their mixing angles and one for CP violating phase for the neutrino mixing matrix).
- The hierarchical mass structure of the SM fermions, ranging from ~ 1 MeV for the first generation of fermions to ~ 173 GeV of the top quark [21], is not understood. Additionally, the existence of exactly three families of fermions is not justified. The arbitrariness of parameters in the SM, focusing on the fermion masses, introduces a naturalness problem. This does not create a problem to the theory itself but such significant differences in arbitrary parameters are usually considered as unnatural and a possible indication of unknown principles underlying a more complete theory encompassing the SM.
- An important motivation of new theories beyond the SM is the significant sensitivity of the Higgs potential to a high scale, denominated as the hierarchy problem. Elementary scalars, as the Higgs boson, are not protected by chiral or gauge symmetries against large radiative corrections to their masses. Therefore, the Higgs field receives considerable corrections from the virtual effects of any SM particle it couples to. The largest correction to the Higgs boson mass comes from the top quark due to its high mass suggesting that the top quark might play a special role in the electroweak symmetry breaking mechanism and the mass hierarchy pattern.

2.1.3 Measurements in Particle Physics

The goal of particle physics is the understanding of the elementary particles in nature: how many they are, their masses, their properties and the fundamental forces which govern the interactions between

them. This research can be done through colliding elementary particles and by looking and analysing the outcome. Cosmic particles originated in outer space may collide and produce new particles when penetrating the atmosphere of Earth. These collisions occur randomly all the time in the upper atmosphere and the resulting particles can be detected on the ground providing useful information to the physicists. However, it is difficult to rely on cosmic particles since many of the searched phenomena occur with very small rate. Therefore, particle physicists need to build experiments in which they control most of the experimental aspects, such as the particle type, the energy of the colliding beams of particles and the rate of collisions. These experiments can be fixed-target experiments, where an incident beam of particles is sent to collide with atomic nuclei in a stationary block of matter, or colliding-beam experiments in which two beams of particles travelling in opposite directions collide at predefined points. The latter allows a higher energy available to create new particles. To achieve that, a particle accelerator is needed to deliver energy to accelerate the beams of charged particles which can be leptons such as electrons or hadrons such as protons or antiprotons.

The expected interaction rate between two colliding particles is determined by a quantity called the cross-section (σ), which depends on the coupling strength of the interacting force as well as the energy and momentum of the interacting particles. During an interaction process, the forces couple to the interacting particles and bosons are emitted or reabsorbed. The interactions between particles can be visually described by the Feynman diagrams. Such diagrams can also be translated into a mathematical expression that provides the matrix element, \mathcal{M} , which is needed for the calculation of the differential cross-section or the decay rate of a specific process. Therefore, the cross-section is proportional to the probability that an interaction occurs, measuring the effective surface area seen by the colliding particles and as such is expressed in units of area. In the particle physics field, cross-sections are typically quoted in picobarn, pb, where $1 \text{ pb} = 10^{-40} \text{ m}^2$. Another important physical quantity is the decay width, Γ_i , of an unstable particle decaying into a specific final state i . Similarly to the cross-section, the decay width can be obtained through analogous integration over the partial width, $d\Gamma_i$, related to the specific final state. Since an unstable particle may decay into several other particles, the Branching Ratio (BR) of a specific final state should be defined as well, corresponding to the width of a particle decaying to a specific final state divided by the width of this particle decaying into all possible states as represented in the following example:

$$BR(t \rightarrow Zq) = \frac{\Gamma_{t \rightarrow Zq}}{\Gamma_{t \rightarrow Zq} + \Gamma_{t \rightarrow Wb} + \Gamma_{\text{Other top decays}}} \quad (2.27)$$

Both the cross-section and the decay width can be calculated by considering only leading order from the perturbation expansion, called a leading-order calculation (LO). These calculations can be complemented by taking into account higher order radiative corrections as the next-to-leading-order (NLO) or the next-to-next-to-leading-order (NNLO) calculations, among others.

At hadron colliders as the LHC and Tevatron, it is mandatory the knowledge of the composite nature of the protons. These particles are a bound state of partons with quarks and gluons. Apart from the

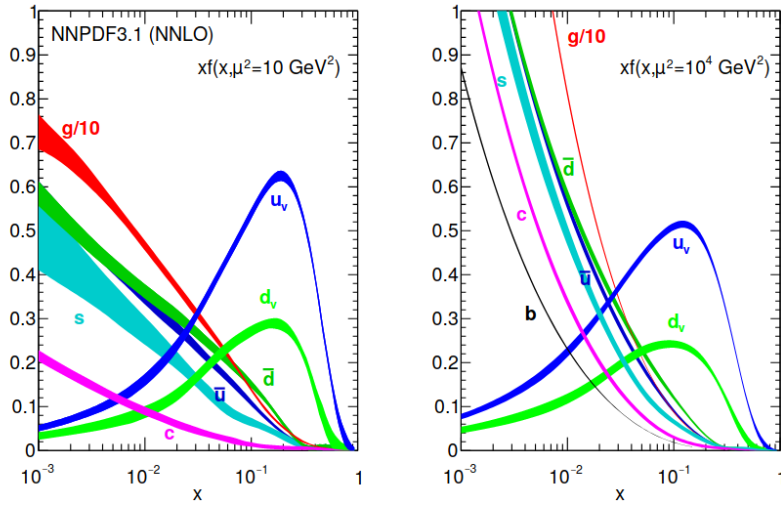


Figure 2.1: Example of NNLO parton distribution functions for various parton flavours as a function of fraction parton momentum x at a scale of 10 GeV^2 (left) and 10^4 GeV^2 (right). Results from NNPDF2.3 set using also data from the LHC obtained by the NNPDF collaboration[25].

quarks of the proton and the valence quarks, the proton has also the so-called sea quarks coming from the gluon splitting into quark-antiquark pairs and the momentum of the proton is divided among all these constituents. The cross-section of the scattering process between two partons requires the knowledge of the initial state of the individual partons. The momentum fraction carried by these partons is described by the Parton Distribution Function (PDF), usually written as $f_i(x_i, Q^2)$. In other words, a PDF can be defined as the probability density for finding a particle, i , with a certain longitudinal momentum fraction, x_i , at Q^2 , where Q^2 is the negative four-momentum transfer squared at the interaction vertex, describing the typical energy scale of the considered interaction. The PDFs are extracted from data obtained at previous collider experiments, as the HERA experiment, since it cannot be obtained from theoretical calculations. An example of the NNPDF2.3 set is shown in Figure 2.1, which is calculated at NNLO accuracy, taking into account terms up to order α_s^3 in the DGLAP (standing for Dokshitzer-Gribov-Kipatov-Altarelli-Parisi) equations [22–24] and includes previous LHC data among another particle physics datasets.

2.2 Top quark physics

Discovered in 1995 by the *CDF* and *DØ* collaborations at Fermilab [26, 27], the top quark was the last quark to be revealed allowing the completion of the third generation of the SM fermions. The top quark was rediscovered also at CERN in 2010 by the ATLAS and CMS collaborations [28, 29]. Its existence opened a new field of particle physics due to its exciting properties. The top quark is the most massive elementary particle known to date, with a mass of $m_{top}=173.34 \pm 0.76 \text{ GeV}$ [21] close to the electroweak symmetry breaking scale of $v = 246 \text{ GeV}$. The large value of the width of the top quark ($1.41 \pm 0.17 \text{ GeV}$ [2]) also causes it to have a very short lifetime of about $5.0 \times 10^{-25} \text{ s}$, being the only quark that decays before

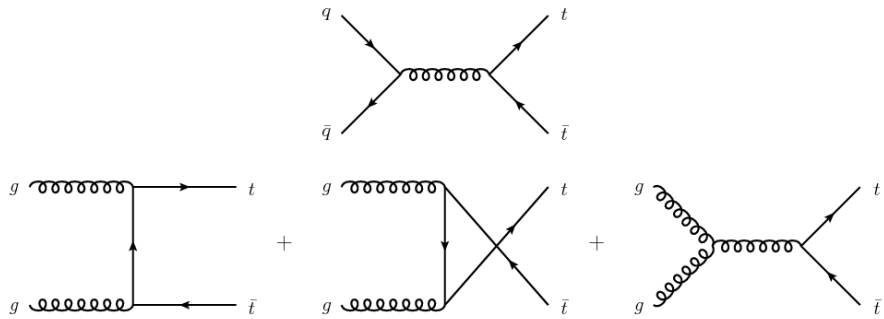


Figure 2.2: Leading-order Feynman diagrams corresponding to the top quark pair production through quark anti-quark annihilation and gluon fusion [31].

hadronising [30]. Such characteristic allows the experiments to directly detect spin information transferred to its decay products undiluted by non-perturbative effects. Moreover, the top quark decay is dominated by the decay channel $t \rightarrow W b$ with a branching ratio close to the unity [2], determined by the V_{tb} element of the CKM matrix. An important consequence of the high mass of the top quark is the strong Yukawa coupling to the Higgs boson, which is very close to 1 according with Equation 2.23:

$$y_t = \sqrt{2} \frac{m_t}{v} \approx 1. \quad (2.28)$$

Being y_t one of the free parameters of the SM, the top quark provides a scientific motivation to test and to understand the SM but also playing a key role in searches for physics beyond it. Through precise measurements of its properties, a deviation from the SM prediction can reveal new physics. Several Beyond the Standard Model (BSM) theories state the top quark as a possible decay product of introduced particles with masses at TeV scale. Besides that, those particles can be too heavy to be produced at the LHC, meaning that the only observable effects may be the indirect ones through the modification of the SM particle properties.

The top quark can be produced in top quark pairs called $t\bar{t}$ production or as a single-top quark associated with other particles called single-top quark production. In hadron colliders, the $t\bar{t}$ production occurs dominantly through the strong interaction. In the $p\bar{p}$ collider LHC, unlike the $p\bar{p}$ collider Tevatron, the top quark pair is produced dominantly, with a fraction of around 85%, through the gluon fusion. The quark anti-quark annihilation and the gluon fusion processes at LO are shown in Figure 2.2. In single-top quark production, the top quark is produced via the electroweak interaction with three different channels: (a) t -channel: W boson and gluon fusion, (b) Wt -channel: associated production of a top quark and a W boson and (c) s -channel: W boson and quark anti-quark annihilation, as shown in Figure 2.3.

The predicted cross-section of the $t\bar{t}$ production considering NNLO with next-to-next-leading-log (NNLL) order at the LHC with $\sqrt{s} = 13$ TeV is 832^{+40}_{-45} pb [32]. For the single-top quark production channels, the values of the cross-section calculated at the LHC with $\sqrt{s} = 13$ TeV are 217 ± 10 pb (NLO with next-to-leading-log (NLL) order) [33], 71.7 ± 3.9 pb (NLO with NNLL) [34] and 10.3 ± 0.4 pb (NLO with NNLL) [35] for t -channel, tW -channel and s -channel, respectively. A comparison between the theoretical and

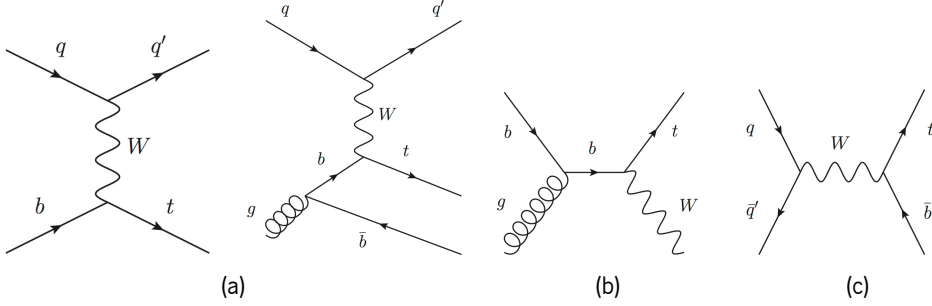


Figure 2.3: Examples of LO Feynman diagrams for single-top quark production: (a) t -channel, (b) tW -channel and (c) s -channel [31].

experimental values for the cross-section of the $t\bar{t}$ production and single-top quark production is presented in Figure 2.4.

2.2.1 Flavour Changing Neutral Currents in the top quark sector

A FCNC process stands for an interaction with a change in the fermion (quark or lepton) flavour through the emission or absorption of a neutral boson. Such processes are not allowed at tree-level in the SM since there is no vertex that directly couples neutral currents (g, Z, γ, H) with two fermions from different generations. On the other hand, the quark flavour may change at higher order correction or loop-level since the CKM mechanism allows the quark flavour change with W^\pm bosons. Figure 2.5(a) shows a forbidden vertex in the SM while Figure 2.5(b) presents a coupling between a top quark and a u or c quark through a loop diagram.

For the evaluation of the amplitude of possible top quark decays through FCNC processes at loop-level, all possible loop diagrams have to be considered. The amplitude suffers from destructive interference since the mass of the top quark is of the order of the electroweak scale and all internal quarks (d, s, b) in the loops have very small masses (i.e. $M_W \gg M_{d, s, b}$). This cancellation is known as the Glashow, Iliopoulos and Maiani (GIM) mechanism [37]. Such effect can also be observed experimentally by the unitarity of the CKM matrix, as predicted by the theory. Therefore, the branching ratio of top quark decay via FCNC suffers from a small decay width as an effect of the GIM mechanism and also the large tree-level rate of the top quark decay to bW . Numerically, an extremely suppressed branching ratio of the order of 10^{-14} is predicted for the top quark decays via FCNC in the SM. Nevertheless, several SM extensions predict an enhanced branching ratio of neutral current top quark decays with respect to the SM which makes these interactions an excellent way to probe new physics. Some examples of BSM theories predicting FCNC processes at higher rates are the two-Higgs doublet model with (FC 2HDM) or without (2HDM) flavour-conservation and the minimal supersymmetric model (MSSM), more commonly known as Supersymmetry (or SUSY). Searches for FCNC interactions in the top sector have already been performed at the Large Electron-Positron collider [38–42], the HERA [43], the Tevatron [44, 45] and the LHC. The current results

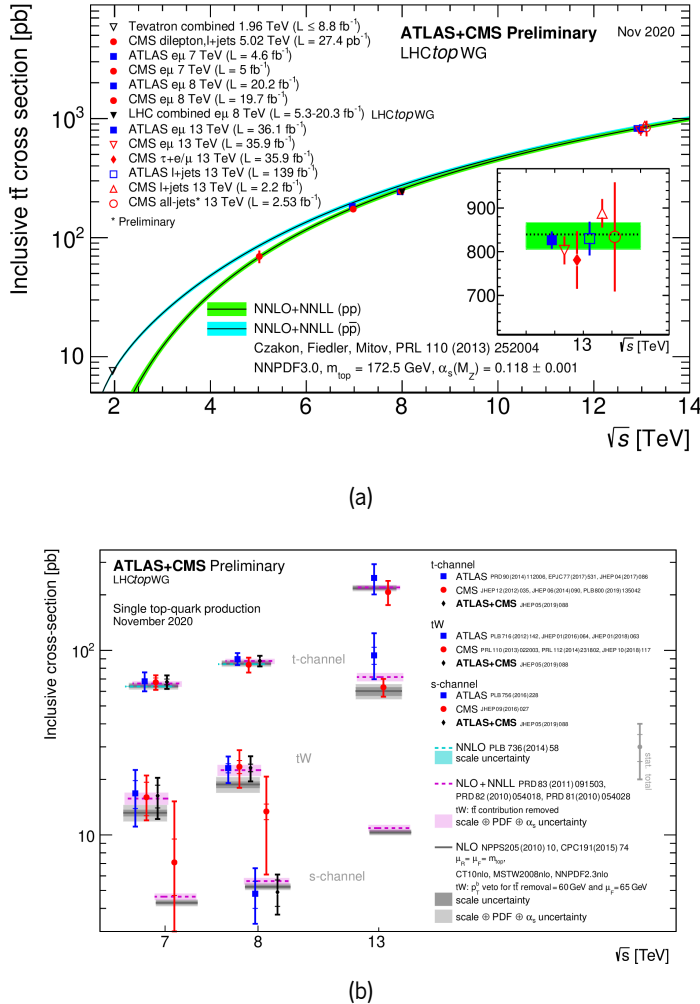


Figure 2.4: (a) Summary of the LHC and Tevatron measurements of the top quark pair production cross-section as a function of the center-of-mass energy compared to the theory prediction [36]. (b) Summary of ATLAS, CMS and combined measurements of the single-top quark production cross-sections in the various channels as a function of the center of mass energy [36]. The theory bands reflect the uncertainties arising from the renormalisation and factorisation scale, parton distribution functions and the strong coupling.

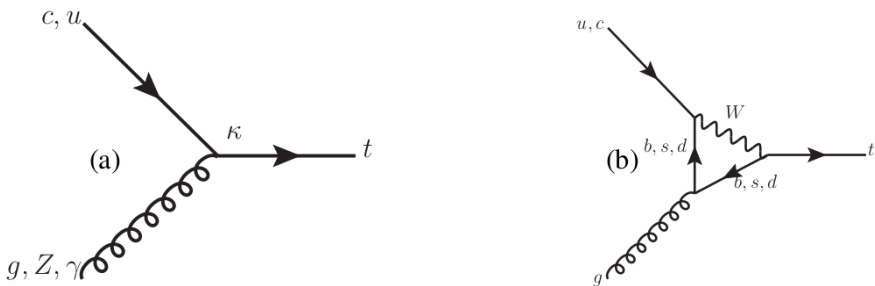


Figure 2.5: Examples of FCNC interactions in the top quark sector: (a) Non-allowed vertex in the SM where up or charm quarks change their flavour to a top quark by interacting with an electrically neutral boson and (b) Allowed FCNC process in the SM through a loop.

from the ATLAS and the CMS collaborations provide the most stringent experimental limits on the BRs of all the FCNC top quark decays. A comparison between SM and BSM models predictions as well as the experimental results from the ATLAS and the CMS collaborations of the branching ratios of the decays of the top quark to an up or a charm quark and a neutral boson are shown in Table 2.3. Focusing on the two Higgs Doublet Models (2HDM), the predictions for the charm quark decays are enhanced in respect with the up quark case since the FCNC couplings are proportional to the masses of the participating quark in the vertex (more specifically to $\sqrt{m_q m_t}$ where m_u is three orders of magnitude smaller than m_c) [46]. In particular, both the two Higgs doublet models with flavour violating and with the flavour conserving Yukawa couplings do not predict the top quark decays through an up quark and a gauge boson since the theoretical framework does not consider a interaction between these bosons and the first generation of quarks. For the MSSM, MSSM with R-parity violation case (RPV) cases, the largest contributions come from gluino exchange diagrams meaning that the $t\bar{t}$ production with a top quark decay via FCNC is the most significant mode for the theoretical prediction (if only the decay mode is considered, the same limits are obtained for up and charm quark since the initial state is composed by gluons instead of a gluon and a quark as in the case of the production).

The analysis presented in this thesis focus on the search for the FCNC tZq anomalous coupling, being q

Process	SM	2HDM (FV/FC)	MSSM	RPV	RS	ATLAS	CMS
$t \rightarrow Zu$	7×10^{-17}	—/—	$\leq 10^{-7}$	$\leq 10^{-6}$	—	1.7×10^{-4} [47]	2.2×10^{-4} [48]
$t \rightarrow Zc$	1×10^{-14}	$\leq 10^{-6}/\leq 10^{-10}$	$\leq 10^{-7}$	$\leq 10^{-6}$	$\leq 10^{-5}$	2.4×10^{-4} [47]	4.5×10^{-4} [49]
$t \rightarrow gu$	4×10^{-14}	—/—	$\leq 10^{-7}$	$\leq 10^{-6}$	—	4×10^{-5} [50]	2×10^{-5} [51]
$t \rightarrow gc$	5×10^{-12}	$\leq 10^{-4}/\leq 10^{-8}$	$\leq 10^{-7}$	$\leq 10^{-6}$	$\leq 10^{-10}$	20×10^{-5} [50]	4.1×10^{-4} [51]
$t \rightarrow \gamma u$	4×10^{-16}	—/—	$\leq 10^{-8}$	$\leq 10^{-9}$	—	2.8×10^{-5} [52]	1.3×10^{-4} [53]
$t \rightarrow \gamma c$	5×10^{-14}	$\leq 10^{-7}/\leq 10^{-9}$	$\leq 10^{-8}$	$\leq 10^{-9}$	$\leq 10^{-9}$	22×10^{-5} [52]	1.7×10^{-3} [53]
$t \rightarrow Hu$	2×10^{-17}	$6 \times 10^{-6}/-$	$\leq 10^{-5}$	$\leq 10^{-9}$	—	1.2×10^{-3} [54]	4.7×10^{-3} [55]
$t \rightarrow Hc$	3×10^{-15}	$2 \times 10^{-3}/\leq 10^{-5}$	$\leq 10^{-5}$	$\leq 10^{-9}$	$\leq 10^{-4}$	1.1×10^{-3} [54]	4×10^{-3} [56]

Table 2.3: Theoretical expectations for the branching ratios of FCNC top decays predicted with the SM, the two Higgs doublet model with flavour violating Yukawa couplings (2HDM (FV)), the flavour-conserving two Higgs doublet model (FC 2HDM), the MSSM, the MSSM for the R-parity violating case (RPV) and warped extra dimensions (RS) [46, 57]. Most stringent experimental limits from the ATLAS and the CMS collaborations are also represented.

an up or a charm quark, where both the decay mode (with gluons in the initial state) and the production mode (with an initial state composed by a light-quark and a gluon) are considered. The corresponding LO Feynman diagrams for decay and production modes are shown in Figure 2.6. The SM predictions of the BR of FCNC $t \rightarrow Zq$ are around 10^{-13} being some orders of magnitude lower than the BSM predictions and experimental sensitivities. Therefore, any measurable BR of such process would be a clear sign of new physics. Even if the FCNC BRs cannot be measured, experimental upper limits can be set and parameters

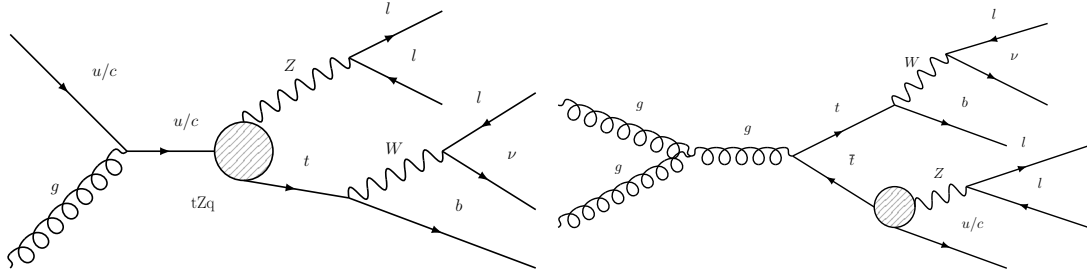


Figure 2.6: Examples of LO Feynman diagrams for tZ production via FCNC (left) and $t\bar{t}$ production with a top quark decaying through the SM and the other via tZq (right). The vertex labelled as tZq corresponds to the coupling responsible for the FCNC interaction.

space of BSM models can be constrained or even models can be excluded. Near the BSM predictions, the most stringent exclusion limits on $\text{BR}(t \rightarrow Zq)$ excluded at 95% confidence level (CL) branching ratios greater than 1.7×10^{-4} and 2.4×10^{-4} for $t \rightarrow Zu$ and $t \rightarrow Zc$ cases, respectively [47]. It should also be mentioned that the same final state can occur in the scenario of an tgq anomalous coupling. In that case, an anomalous coupling between the light quark and the gluon produces a top quark that consequently can decay to a Z boson and a light quark through a tZq anomalous coupling. However, the search for direct top quark production with tgq anomalous coupling established very stringent limits on this coupling, excluding at 95% CL branching ratios of $\text{BR}(t \rightarrow gq)$ greater than 4×10^{-5} and 2×10^{-4} for $t \rightarrow gu$ and $t \rightarrow gc$ cases, respectively [50].

The search for anomalous FCNC couplings in the top quark sector does not imply the creation of a complete new theory. The anomalous couplings can be described model-independently in a so called effective field theory (EFT). In this theory, the SM Lagrangian \mathcal{L}_{SM} is extended by operators in higher-dimensions of the mass suppressed by the scale of new physics Λ_{NP} as shown in Equation (2.29). Dimension-five operators introduce lepton-flavour violating processes and consequently, are not considered in this thesis. Therefore, the anomalous couplings can be approximated with dimension-six operators $O_i^{(6)}$ whose strength is given by the Wilson coefficients $C_i^{(6)}$.

$$\mathcal{L}_{\text{eff}} = \mathcal{L}_{\text{SM}} + \frac{1}{\Lambda_{NP}^2} \sum_i C_i^{(6)} O_i^{(6)} + \dots \quad (2.29)$$

Although more than 80 dimension-six operators exists, not all of them are independent of each other and only a few of them (about 15) have a significant effect on the top quark processes [58]. The relevant operators for an FCNC with a top quark and a Z boson, following the notation in [59], are the operators O_{uB}^{ij} and O_{uW}^{ij} with $i \neq j$ and either $i = 3$ or $j = 3$, respectively, defined as follows:

$$\begin{aligned} O_{uB}^{(ij)} &= (\bar{q}_i \sigma^{\mu\nu} r_j) \tilde{\varphi} B_{\mu\nu}, \\ O_{uW}^{(ij)} &= (\bar{q}_i \sigma^{\mu\nu} \tau^I r_j) \tilde{\varphi} W_{\mu\nu}^I \end{aligned} \quad (2.30)$$

where \bar{q}_i describes the left-handed quark doublet and r_j the right-handed quark singlet, $\sigma^{\mu\nu} = \frac{1}{2}[\gamma^\mu, \gamma^\nu]$ with the gamma matrices, τ^I are the Pauli matrices, $\tilde{\phi}$ is the complex conjugate of the Higgs field doublet and $B_{\mu\nu}$ and $W_{\mu\nu}^I$ are the $U(1)_Y$ and $SU(2)_L$ field tensors, respectively. The indices i and j of the spinors refer to the flavour indices of the quark generations. One index always equals to 3 as a top quark must be involved, while the other one is either 1 or 2 corresponding to an up or charm quark. These operators introduce an FCNC with a tZq vertex. For the generation of the FCNC signal events, the TopFCNC model [60, 61] using these dimension-six operators with calculations at NLO QCD was used where only the tZu or tZc couplings were considered (i.e., assuming that all other couplings are zero) and the assumption on the new physics scale of $\Lambda_{NP} = 1$ TeV. The FCNC operators can be left- or right-handed and both signal hypotheses were considered. Therefore, the search presented in this thesis is performed independently for four different coupling scenarios described by the flavour of the up-type quark, up or charm quark, and by the handedness of coupling, left- or right-handed. The order of the indices i and j in Equation (2.29) defines the chirality of the FCNC operators. For the tZu case, the $C_{uW}^{(13)}$ Wilson coefficient corresponds to the left-handed coupling while the $C_{uW}^{(31)}$ Wilson coefficient corresponds to the right-handed coupling. The tZc couplings are defined by the $C_{uB}^{(23)}$ for the left-handed coupling and $C_{uB}^{(32)}$ for the right-handed coupling. With the TopFCNC UFO model, the Wilson coefficients C_{uW} and C_{uB} are named depending on the indices i and j and its order as discussed in detail in [60, 61]. As an example, the $C_{uW}^{(13)}$ Wilson coefficient corresponds to the model parameter C_{uB} describing the tZu left-handed coupling and the $C_{uW}^{(31)}$ Wilson coefficient corresponds to the model parameter C_{tB} for the tZu right-handed coupling.

2.2.2 Interference studies with tZq and $t\gamma q$ FCNC anomalous couplings

New physics might not only become visible as an excess of measured data over the expected background. An interesting possibility could be a deficit of events due to a destructive interference of a new physics signal with the SM background processes. Another kind of interference could also occur between two modes from a specific model beyond the SM that would modify the expectation for detecting those interactions or particles of the particular model. Interference effects have shown to play an important role in several studies within the top quark sector. In particular, the interference of two SM processes (pair production of top quark and the production of a single-top quark in association with a W boson) enabled the constraint on the interference models for these processes [62]. Searches for FCNC processes through the top quark have focused either on the decay process or on the production process. However, both processes interfere if at least one additional up-type quark is produced in the production process. These interference effects may have an impact on the interpretation of a potential observation of an FCNC signal and on the exclusion limits that are set by the current and future searches. Therefore, it is crucial to quantify whether these interference effects should be considered in the experimental searches at the LHC or, on the contrary, they can be safely neglected, as it has been done to date. The study of interference effects discussed here focus

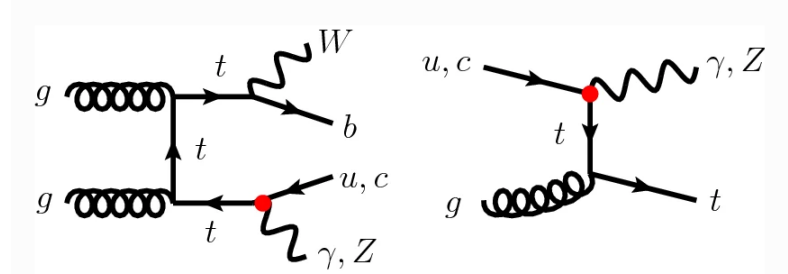


Figure 2.7: Examples of Feynman diagrams for top quark pair production with an FCNC top quark decay to a photon or a Z boson (left) and for the associated production of a single top with a photon or a Z boson via an FCNC interaction (right).

on the top quark FCNC processes with either a photon or a Z boson, as represented in some examples of Feynman diagrams for decay and production modes in Figure 2.7.

Monte Carlo simulated samples were generated for proton-proton collisions at $\sqrt{s} = 13$ TeV with MadGraph5_aMC@NL0 using the TopFCNC [60, 61] UFO [63] model for the production and decay processes. In addition, a sample including both processes and their interference, called "the total process", was generated. The decay process was generated by $pp \rightarrow t\bar{t}$ with $t\bar{t} \rightarrow W^+ b\gamma q$ or $t\bar{t} \rightarrow W^- \bar{b}\gamma q$. The production process was generated by $pp \rightarrow t\gamma$ (or $\bar{t}\gamma$) and adding the processes with an extra quark, anti-quark or gluon, j , i.e. $pp \rightarrow t\gamma j$ (or $\bar{t}\gamma j$). Diagrams with an intermediate \bar{t} (t) were excluded in the case of $t\gamma(j)$ ($\bar{t}\gamma(j)$) production, since these diagrams are considered as part of the decay process. If the extra quark corresponds to the up-type quark that couples via an FCNC to the top quark, interference of the decay and production processes occurs. The total process was generated by $pp \rightarrow t\gamma$ (or $\bar{t}\gamma$) and by adding the processes $pp \rightarrow t\gamma j$ (or $\bar{t}\gamma j$). The same MC simulation for the production, decay and total process was obtained for the Z boson case, where Z was used instead of γ . For all cases, the (anti)-top quarks were decayed to $W^+ b$ ($W^- \bar{b}$) using MadSpin. All W bosons were decayed to an electron or muon and the corresponding neutrino and all Z bosons were decayed to either two electrons or two muons using MadSpin. Pythia8 was used for the parton showering and hadronisation [64]. For all processes, events were matched using the MLM procedure [65] using a k_t value between partons of 30 GeV. Detector effects were simulated with Delphes using the default detector card, tuned to match the CMS detector parameters [66]. As discussed before, the FCNC operators can be left- or right-handed and couple the top quark to the up quark or to the charm quark. The production of the simulated samples was done for each of these four possibilities, with the strength of one operator fixed to a benchmark value, being the other operators set to zero. Uncertainties were evaluated by generating additional samples with fixed renormalisation and factorisation scales set to the top quark mass and by varying the scales by factors of two. Those variations were used as relative uncertainties for the nominal samples, which were generated with a dynamic scale defined as the transverse mass of the system after k_t clustering of the final state particles.

Boson	Production process	Decay process	Total process
γ	$13 \pm 5 \text{ fb}$	$6 \pm 3 \text{ fb}$	$20 \pm 8 \text{ fb}$
Z	$85 \pm 30 \text{ fb}$	$24 \pm 11 \text{ fb}$	$110 \pm 40 \text{ fb}$

Table 2.4: Cross-section of the different processes for the left-handed coupling with the up quark, the top quark and photon/ Z boson, including the uncertainty from scale variations.

The first impact of considering or neglecting interference was evaluated through the comparison of the cross-section for the sum of the decay and production processes with the cross-section of the total process. The results for the left-handed coupling of the top quark to the up quark are presented in Table 2.4, showing that the cross-section for the total process is very close to the cross-section weighted sum of the samples for the production and decay processes. The same conclusions were obtained for the right-handed coupling and for the left- and right-handed couplings to the charm quark. The following test was the study of kinematic distributions of the different final state particles (i.e. the photon/ Z boson, the bottom quark, the top quark, the W boson and the highest- p_T up-type quark) at parton level, where no large effects were observed. The normalised distributions of the transverse momentum of the photon/ Z boson from the total process and the sum of the production and decay processes are shown in Figure 2.8. In the phase space where both the production and the decay process contribute and interference effects can hence appear (in the region of p_T smaller than approximately 300 GeV), the difference between the total process and the sum of the two individual processes is small and covered by the scale uncertainties.

Similarly to the parton level, the transverse momentum of the photon and the Z boson were studied at detector level. With that goal, a simple event selection was applied to mimic the selection of a search: in each event at least one photon or Z boson was required, respectively. The normalised distributions of the transverse momentum of the photon/ Z boson from the total process and from the sum of the production and decay processes are shown in Figure 2.9. The same observations and conclusions hold as for parton level where no large interference effects are seen in the region they could be expected (i.e. $p_T \lesssim 300 \text{ GeV}$).

As a conclusion, interference effects were found to be much smaller than changes from variations of the renormalisation and factorisation scales in the leading order samples used for this phenomenological study [67]. The results both at parton and detector level indicated that the current practice of neglecting interference effects in searches for top quark FCNC interactions at the LHC is a viable strategy also for the future. However, the impact of interference effects on their interpretations should be quantified in the case of observation of FCNC processes in such searches.

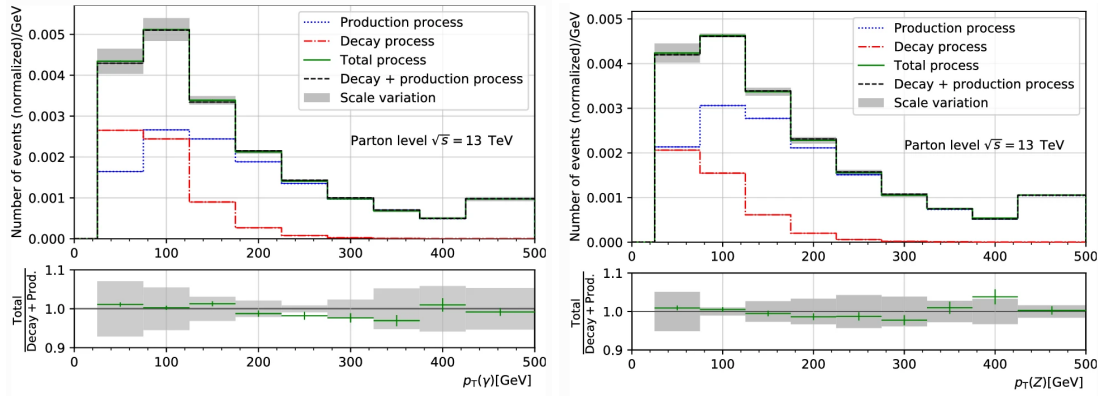


Figure 2.8: The photon (left) and Z boson (right) transverse momentum for the total process compared to the sum of the production and decay processes at parton level. The statistical uncertainty due to the limited size of the samples is shown as a green error bar. The uncertainty in the total process due to variations of the renormalisation and factorisation scales is shown as a band.

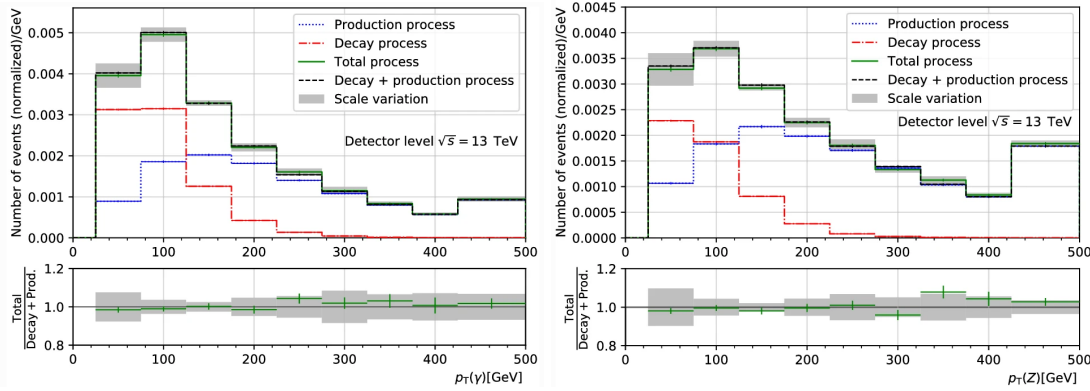


Figure 2.9: The photon (left) and Z boson (right) transverse momentum for the total process compared to the sum of the production and decay processes at detector level. The statistical uncertainty due to the limited size of the samples is shown as a green error bar. The uncertainty in the total process due to variations of the renormalisation and factorisation scales is shown as a band.

The ATLAS experiment at the Large Hadron Collider

The LHC, the main highlight of CERN, is a circular particle accelerator constructed to produce TeV proton-proton and heavy-ion collisions studied by several experiments. The ATLAS detector is one of the four main experiments that benefit from the collisions of particles at the LHC. The following sections present an introduction to the CERN accelerator complex, the LHC and a detailed description of the ATLAS detector, where the data considered in this thesis was collected.

3.1 CERN

Located at the Franco-Swiss border near Geneva, the CERN was founded in September 29th of 1954 with 12 member states and the acronym CERN from the french *Conseil Européen pour la Recherche Nucléaire* was born. The initial goals of this council were the study of atomic nuclei and the congregation of scientists on Europe. Due to the constant progress of the science field, it soon improved to the research in the high energy physics focused on the interaction of subatomic particles.

Several accelerators and detectors with distinct focus in the particle physics field were built at CERN in order to probe the fundamental structure of the Universe. Figure 3.1 shows all the current accelerators as well as the detectors at CERN.

Since its beginning, CERN played a major role in the significant breakthroughs of the particle physics field. Among them are the discovery of neutral currents with the Gargamelle bubble chamber (1973) [69], the discovery of W^\pm and Z bosons with the UA1 and UA2 experiments (1983) [70, 71], the determination of the number of light neutrino families at the Large Electron-Positron Collider (LEP) (1989) [72], the

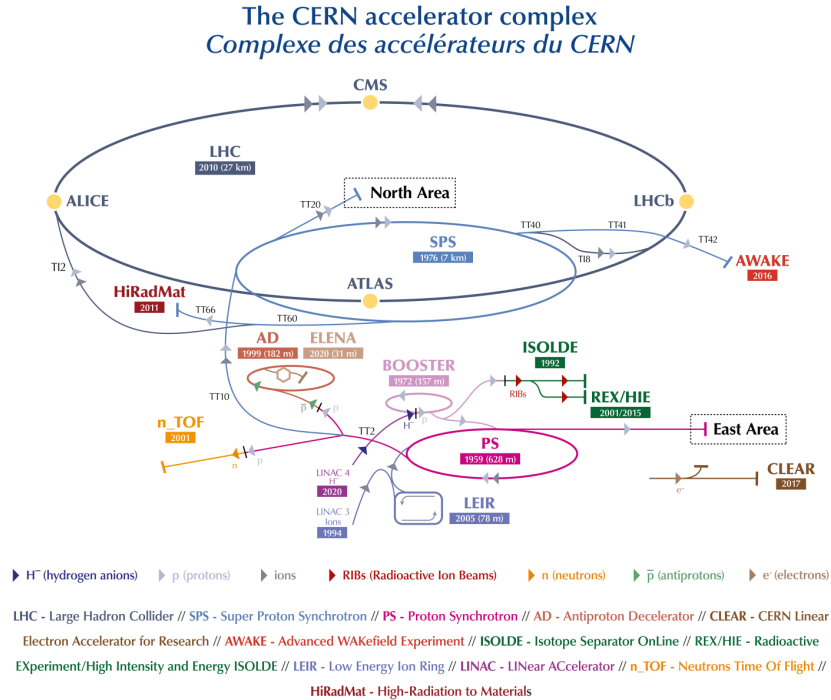


Figure 3.1: Representation of the current CERN accelerator complex with its accelerators, detectors and facilities [68].

discovery of the direct CP violation (1999) [73] and the most recent discovery of the Higgs boson with a mass of 125 GeV observed by the ATLAS and the CMS collaborations (2012) [74, 75].

Throughout the years, the CERN laboratory has become more than an european organisation having today 23 member states as well as associate and observer states represented by more than 17500 scientists from over 70 countries and 600 institutes for their research.

3.2 The Large Hadron Collider

The world largest and most powerful particle accelerator and also one of the most recent addition to the CERN accelerator complex is the LHC. Positioned under France-Swiss boarder between 45 and 70 meters (at 1.4% inclination towards lake Léman), the LHC consists of a ring with a perimeter of 27 kilometers including more than 1000 superconducting magnets and several accelerating structures. An example of the front view of the LHC dipole magnets is represented in Figure 3.2. Inside the 15-meters long dipole magnets, two proton beams travel in opposite directions in separate beam pipes, while being accelerated until reaching a speed close to the speed of light, before they are made to collide at specific points of the tunnel.

Older accelerators as the Proton Synchrotron (PS) and Super Proton Synchroton (SPS) are used to boost the energy of the particles before the injection in the LHC. First, the particles are accelerated at the LINear

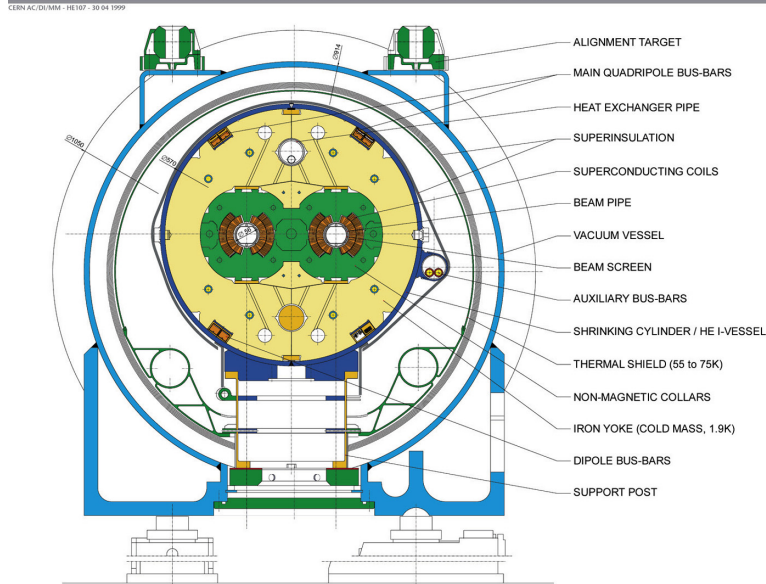
LHC DIPOLE : STANDARD CROSS-SECTION


Figure 3.2: Front view of a LHC dipole [76].

Accelerator	Size	Energy
LINAC2	33 m	90 keV to 50 MeV
BOOSTER	157 m	50 MeV to 1.4 GeV
PS	628 m	1.4 GeV up to 26 GeV
SPS	6.9 km	26 GeV up to 450 GeV
LHC	27 km	450 GeV up to 7000 GeV

Table 3.1: Size and maximum energy reached by the different accelerators currently used at the LHC.

ACcelerator 2 (LINAC 2) reaching an energy of 50 MeV. Subsequently, they are accelerated in the Proton Synchrotron Booster (BOOSTER), PS and SPS before reaching an energy of 1, 26 and 450 GeV, respectively. Finally, the bunches of protons (or heavy ions) are injected in the LHC containing each bunch about 10^{11} protons. Table 3.1 summarises the sizes and the energies reached by the different accelerators at the LHC. The proton beams circulated in the LHC for the first time in September 10th of 2008. From 2010 to 2012, the protons beams had an energy of 3.5 TeV. From 2012 to 2013, the maximum energy was 4 TeV per beam. The first shutdown ended when the LHC started to accelerate beams up to an energy of 6.5 TeV in April 5th of 2015. The LHC had its second run, referred to as Run-2, with proton and also heavy ion collisions at a centre-of-mass energy of 13 TeV from 2015 to 2018. A two year shutdown is currently happening with crucial repairs and upgrades to the LHC and its experiments in anticipation of Run-3. The replacement of the first end-cap station of the New Small Wheel [77] and of the higher-granularity for the existing calorimeter trigger [78] are two flagship upgrade projects of the ATLAS collaboration at the moment.

Being the protons charged particles, a strong magnetic field maintained by electromagnets is needed to curve the proton beams around the circular accelerator. The total of 1232 superconducting electromagnets requires a temperature of 1.9 K (-271.3 C) which is colder than outer space and, consequently, an ultra-high vacuum. This temperature allows the dipole magnets to generate a magnetic field of 8.3 T. Besides these magnets, a total of 392 quadrupole magnets maintain the beams focused and 16 radiofrequency cavities accelerate particles and keep them in controlled bunches with a constant energy.

The beams circulating inside the LHC intersect in four interaction points where distinct particle detector are placed: A Large Ion Collider Experiment (ALICE) [79], A Toroidal LHC ApparatuS (ATLAS) [80], Compact Muon Solenoid (CMS) [81], and Large Hadron Collider beauty (LHCb) [82]. The ATLAS and CMS detectors are two multi-purpose experiments while ALICE and LHCb are focused on the study of heavy-ions collisions and b -physics, respectively. Smaller experiments as LHCf (LHC forward), TOTEM (TOTal Elastic and diffractive cross-section Measurement) and MoEDAL (Monopole and Exotics Detector at the LHC) focus on diffractive physics and the search for magnetic monopoles and profit from the access infrastructures of the major detectors to place its detectors.

3.2.1 Luminosity and pile-up

Luminosity, related with the expected number of events, and pile-up that informs about the number of simultaneous proton interactions are two key factors to characterise any dataset collected at the LHC.

The expected number of events N_i for a specific process (i) with a production cross-section of σ_i is obtained in terms of the instantaneous luminosity (\mathcal{L}) as:

$$N_i = \sigma_i \int \mathcal{L} dt. \quad (3.1)$$

The instantaneous luminosity can be expressed as a function of the rate of pp interactions and in terms of beam parameters as:

$$\mathcal{L} = \frac{N_b^2 n_b f_{rev}}{4\pi\sigma_x\sigma_y} F \quad (3.2)$$

where N_b is the number of protons per bunch, n_b is the number of bunches injected at the LHC per revolution, f_{rev} is the machine revolution frequency (approximately 11 kHz), σ_x and σ_y are the horizontal (x -scan) and vertical (y -scan) Gaussian widths of the colliding beams, and F is the geometric luminosity reduction factor that corresponds to a small correction factor to account for the crossing angle between beams at the interaction point. The LHC design instantaneous luminosity is $\mathcal{L} = 10^{34} \text{ cm}^{-2}\text{s}^{-1}$. Table 3.2 summarises the different parameters of the LHC for each year of the Run-2 data taking.

The high frequency of collisions and the high density of beam bunches culminates in many pp interactions that may occur simultaneously. This process is called pile-up and results in the overlap of the

Parameters	Design	2015	2016	2017	2018
Beam energy (TeV)	7.0	6.5	6.5	6.5	6.5
Bunch spacing (ns)	–	25	25	25/8b4e	25
Maximum number of bunches (n_b)	2808	2232	2208	2544/1909	2544
Protons per bunch ($10^{11} N_b$)	1.15	1.10	1.10	1.10/1.20	1.10
Peak luminosity ($10^{33} \text{ cm}^{-2} \text{ s}^{-1}$)	10	5	13	16	19
Integrated luminosity (fb $^{-1}$)	–	4.0	38.5	50.2	63.4
Mean pile-up	–	16	41	45/60	55

Table 3.2: Operating parameters of the LHC for each data taking period during Run-2 [83].

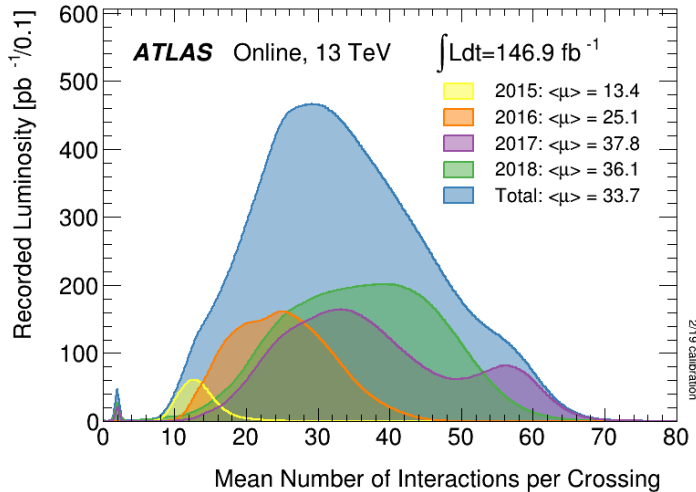


Figure 3.3: Recorded luminosity as a function of mean number of interactions per bunch crossing for the different years of Run-2 data taking [84].

electronic signals from multiple interactions being categorised as *in-time pile-up* or *out-of-time pile-up*. Multiple pp interactions in the same bunch crossing causes *in-time pile-up* while *out-of-time pile-up* occurs when traces from an event in a different bunch crossing are recorded. An increase of N_b or n_b in Equation 3.2 allows a higher luminosity with a raise on the level of pile-up as well. Higher N_b causes more interaction within a given bunch crossing, meaning higher *in-time pile-up*. Higher n_b reduces the space between bunches resulting in the overlap of interactions from different bunch crossing, i.e. *out-of-time pile-up*.

The mean number of interactions per bunch crossing in the Run-2 dataset distribution for each year of the data taking is shown in Figure 3.3.

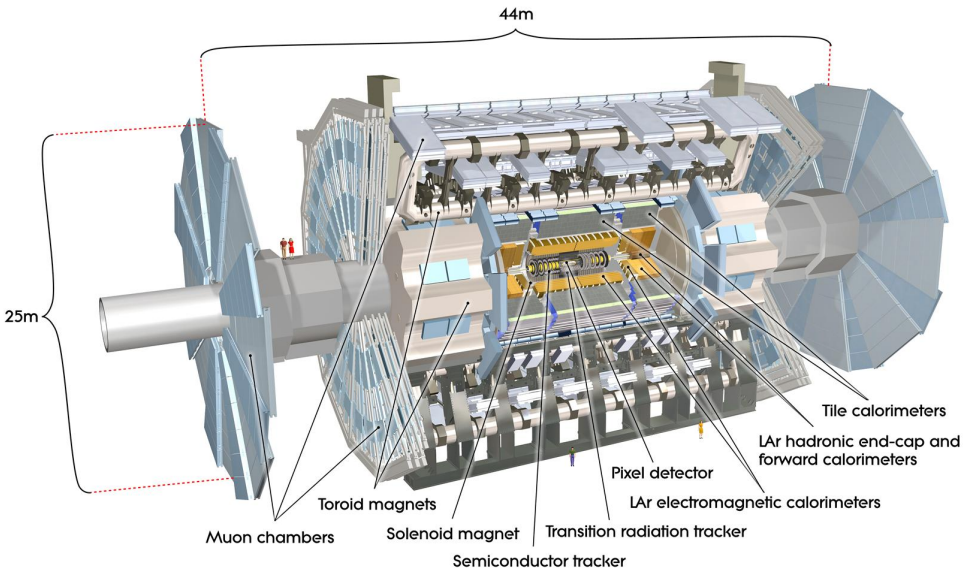


Figure 3.4: Representation of the ATLAS detector with the different subsystems [85].

3.3 The ATLAS Experiment

The ATLAS detector, shown in Figure 3.4, is one of the two general purpose detectors at the LHC that explores a vast range of physics scenarios studying the particles produced in proton-proton collisions at high energies. It is the biggest detector of this kind having 44 meters long, 25 meters wide and weighting around 7000 tones.

The full coverage of the space around the $p\bar{p}$ interaction point allows the detection and the reconstruction of almost all final state objects. This characteristic is possible due to the multilayer structure which consists in many sub-detectors, each of them with a specific purpose. From inside to outside, the sub-detectors are: the inner detector, the electromagnetic calorimeter, the hadronic calorimeter and the muon spectrometer. A brief description of these sub-detectors can be found in the following sections as well as its performance goals.

3.3.1 ATLAS coordinate system

The ATLAS coordinate system is a right-handed cartesian system, with the x -axis towards the center of the LHC ring, the y -axis pointing upwards and the z -axis pointing along the beam pipe. The nominal interaction point is defined as the origin of the coordinate system. The particle momentum p_x , p_y and p_z are defined along the x , y and z -axis, respectively. Since the $x - y$ plane is transverse to the beam direction, the transverse momentum p_T is widely used and defined by the following relation with p_x and p_y :

$$p_T = \sqrt{p_x^2 + p_y^2}. \quad (3.3)$$

To better describe rotational invariant properties, the spherical coordinates (R, ϕ, θ) are used and defined by:

$$R = \sqrt{x^2 + y^2}, \phi = \arctan(y/x), \theta = \arctan(R/z). \quad (3.4)$$

The azimuthal angle ϕ is the angle between the x -axis and the y -axis and the polar angle θ corresponds to the angle between the z -axis and the $x - y$ plane. The azimuthal angle is defined within $\phi \in [-\pi, \pi]$ and the polar angle within $\theta \in [0, \pi]$. The rapidity of the boost of a particle along the beam axis, y , can be obtained by the following mathematical relation:

$$y = \frac{1}{2} \ln \left(\frac{E + p_z}{E - p_z} \right). \quad (3.5)$$

Since a crucial characteristic of hadron collider physics is that the colliding partons carry different longitudinal momentum fractions, the pseudorapidity, η , is defined in terms of the polar angle θ :

$$\eta = -\ln \left[\tan \left(\frac{\theta}{2} \right) \right]. \quad (3.6)$$

The difference in the pseudorapidity of two particles, $\Delta\eta$, is independent of Lorentz boosts along the beam axis. Additionally, the pseudorapidity coincides with the rapidity if the energy of the particle is mainly composed by its momentum. In hadron collider physics, the pseudorapidity is a measure of the longitudinal angle against the beam line being a particle with a large value of η referred to as a forward physics object.

Another important variable is the distance between two particles ΔR defined in terms of the difference in the pseudorapidity and the difference in the azimuthal angle between the two particles:

$$\Delta R = \sqrt{\Delta\eta^2 + \Delta\phi^2}. \quad (3.7)$$

3.3.2 Magnet system

The ATLAS magnet system allows the measurement of the charged particles momentum and it is designed to provide a magnetic field mostly orthogonal to the particle trajectory. It is composed by four large superconducting magnets: one central solenoid, one barrel toroid and two end-cap toroids.

The central solenoid magnet encloses the inner detector and provides a high magnetic field to bend the trajectory of charged particles allowing the momentum measurement by the tracking system.

The toroidal magnet system is divided into three parts with a barrel part placed around the central calorimeter and two end-caps placed at each end of the detector. Each of these toroidal magnets has eight identical coils built radially in a symmetric way around the beam pipe. The toroidal magnet system provides the magnetic field for additional bending of the muon trajectories in order to measure with precision their momentum in the muon barrel and end-cap spectrometers.

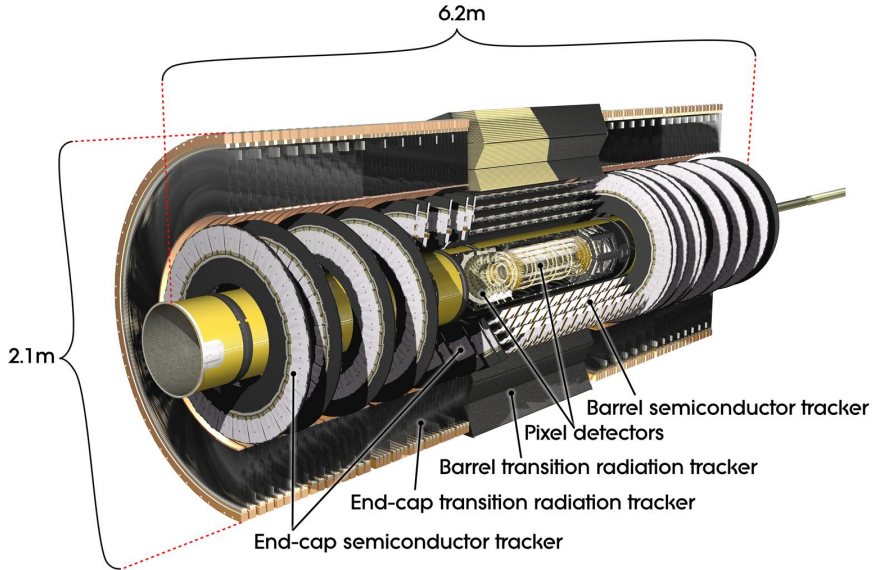


Figure 3.5: Representation of the ATLAS inner detector. The pixel detector refers to the insertable *B*-layer and the pixel detector [86].

In contrast with the central solenoid magnet which produces an uniform magnetic field of approximately 0.5 T, the magnetic field produced by the toroidal magnets varies from 0.15 T to 2.5 T.

3.3.3 Inner detector

The inner detector, shown in Figure 3.5, is a very compact and highly sensitive part of ATLAS and the closest system to the beam pipe allowing the study of the resultant particles from the $p\bar{p}$ collisions. This detector constitutes a tracking system used to the identification and the measurement of the momentum of the charged particles. It also allows the reconstruction of the interaction vertex. It begins a few centimeters close to the proton beam axis and extends to a radius of 2.1 meters and is 6.3 meters in length along the beam pipe. The inner detector have an acceptance in pseudorapidity of $|\eta| < 2.5$ and full coverage in the azimuthal angle ϕ .

Immersed in a 2 T solenoidal magnetic field parallel to the beam axis, it is divided in four different concentric subdetectors named the Insertable *B*-layer (IBL), the Pixel Detector (PD), the Semiconductor Tracker (SCT) and the Transition Radiation Tracker (TRT). The pixel detectors, the components of the IBD and the PD, are the innermost part of the inner detector contributing to the accurate measurement of the particle vertices. The PD uses silicon sensors (pixels) composed by three cylindrical layers in the barrel region and three concentric disks in the end-cap region. The SCT is the middle part of the inner detector and is a silicon microstrip detector composed of a barrel, with four layers of silicon microstrip detectors, and two end-caps, each with nine disks. The TRT is the outermost part of the inner detector and consists of 4 mm diameter gaseous straw tubes interleaved with transition radiation material.

Combining the information from the four subdetectors, the transverse momentum resolution measure in the plane perpendicular to the beam axis is [80]:

$$\frac{\sigma_{p_T}}{p_T} = \frac{0.05\%}{\text{GeV}} p_T \oplus 1\%. \quad (3.8)$$

3.3.4 Calorimeter system

The ATLAS calorimeter system, shown in Figure 3.6, is used to provide an accurate measurement of particles energy by absorb them and measure the shower properties, which eases the particle identification. The calorimeters are designed to stop the majority of the particles, except for muons and neutrinos. Each of the calorimeters are divided into a central barrel part and two symmetric end-caps.

The calorimeter system stops most of the particles from arriving to the muon spectrometer preventing them from being identified as muons. Given the neutrinos do not leave any signatures to be observed and do not interact with the detector material, the missing transverse energy variable, E_T^{miss} , could be obtained since the four-momentum carried by the neutrino implies an unbalance in the total momentum available in the event. The precise measurement of E_T^{miss} is an important mission in the ATLAS calorimeters since this variable is a crucial discriminant for many physics searches.

The electromagnetic calorimeter forces the decay of the particles and then measures the energy of the electromagnetic particles which are leptons or photons. The hadronic calorimeter measures the energy deposition from the hadronic showers of high energy hadrons which are protons and neutrons. The components of the calorimetry system are: the Liquid Argon (LAr) electromagnetic calorimeter, the LAr hadronic end-cap calorimeter (HEC), the LAr forward calorimeter (FCal) and the Tile calorimeter (TileCal). The electromagnetic and the hadronic calorimeters cover a region of $|\eta| < 3.2$ and $|\eta| < 4.9$, respectively.

The LAr electromagnetic calorimeter uses liquid Argon as active material and lead plates as absorber composing a sampling detector of one barrel and two end-caps. The target energy resolution for the electromagnetic calorimeter is [80]:

$$\frac{\sigma_E}{E} = \frac{10\%}{\sqrt{E}} \oplus \frac{17\%}{E} \oplus 0.7\%, \quad (3.9)$$

with E measured in GeV.

The TileCal hadronic calorimeter is also a sampling calorimeter using steel as absorber material and scintillating plastic tiles (as active material) placed in one central barrel and two extended barrels. The target energy resolution for the TileCal hadronic calorimeter is [80]:

$$\frac{\sigma_E}{E} = \frac{50\%}{\sqrt{E}} \oplus 3\%, \quad (3.10)$$

with E measured in GeV.

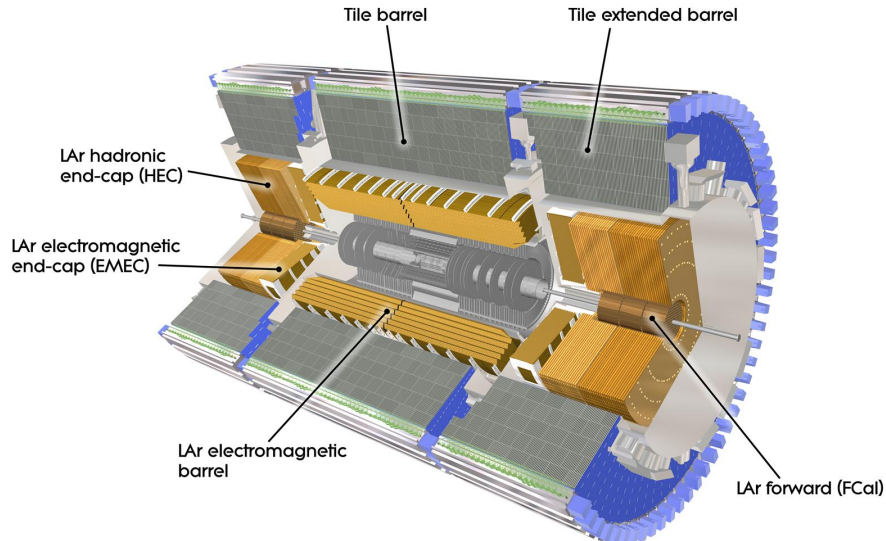


Figure 3.6: ATLAS Calorimeter system [87].

3.3.5 Muon spectrometer

The muon spectrometer, shown in Figure 3.7, is a combination of toroidal superconducting magnets and precision chambers designed to detect and measure the momentum of the muons. As muons minimally interact with the other subdetectors and have long lifetimes, its properties are identified and measured in the outermost detector layer. This system is, by far, the largest tracking system in ATLAS since it extends from a radius of 4.25 m around the calorimeters out to the full radius of the detector (which is 11 m). This detector system covers a region of $|\eta| < 2.7$. It is also designed to trigger the muon in the region of $|\eta| < 2.4$.

It is composed by four distinct chambers: Thin Gap Chambers (TGC), Resistive Plate Chambers (RPC), Monitored Drift Tubes (MDT) and Cathod Strip Chambers (CSC). Due to the magnetic field provided by the toroidal magnets, these subdetectors measure the muons momentum through the curvature of the deflected muon trajectory. The muon spectrometer was designed to provide a transverse momentum resolution of [80]:

$$\frac{\sigma_{p_T}}{p_T} = 10\% \text{ at } p_T = 1 \text{ TeV.} \quad (3.11)$$

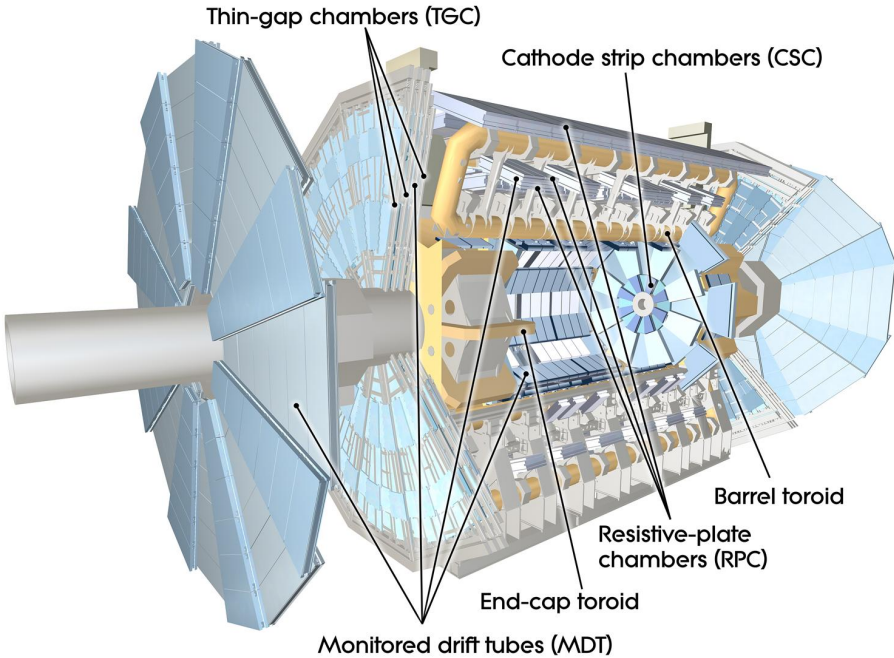


Figure 3.7: Representation of the ATLAS muon spectrometer [88].

3.3.6 Trigger and data acquisition system

The production cross-section of inelastic proton-proton scattering events at the LHC is several orders of magnitude higher than the cross-section of physics signatures. Consequently, millions of uninteresting collisions happen every second. Besides that, the high collision rate of 40 million events per second (i.e., 40 MHz) at the LHC running conditions does not allow the storage and analysis of all amount of data generated.

To reduce the flow of data to acceptable levels, the ATLAS trigger and data acquisition system selects in real time events with different characteristics that make them interesting for physics analyses. The trigger system works in two stages: the level 1 hardware trigger (L1) and the high level software trigger (HLT). In nominal conditions, the L1 and HLT system reduces the event rate to 100 kHz and 1.5 kHz, respectively.

The collision data samples used in the analysis presented in this thesis were collected by the ATLAS detector between 2015 and 2018. The total integrated luminosity delivered by the LHC during this period was 156 fb^{-1} . Each ATLAS subdetector has a record of its performance across the run and only the data collected with all subdetectors working with a certain quality threshold is considered. Therefore, the Good Run Lists (GRL) are created listing, for each luminosity block, the data where the different subdetectors satisfied these requirements. The percentage of data considered as 'good' is 89%, giving a total integrated luminosity of 139 fb^{-1} as represented in Figure 3.9.

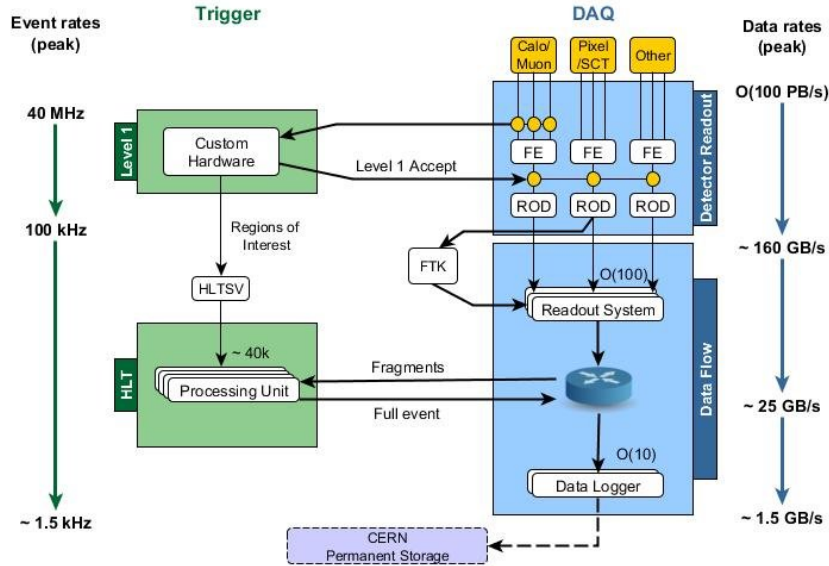


Figure 3.8: Schematic view of the ATLAS trigger and data acquisition system for Run-2 [89].

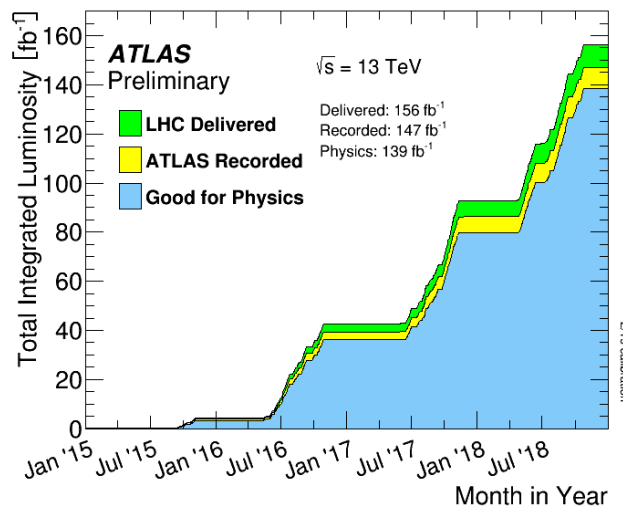


Figure 3.9: The total integrated luminosity delivered, recorded and labeled as good for physics with the ATLAS detector between the years of 2015 and 2018 as a function of time [90].

3.3.7 Forward detectors

The ATLAS detector is not only composed by the central detector, where the muon spectrometer is the outer sub-detector, but also by additional forward sub-detectors located at the LHC tunnel. The ATLAS Forward Proton (AFP) is one of these sub-detectors and explores a significant extension to the physics reach of ATLAS by tagging and measuring the momentum and the emission angle of very forward protons. Such measurements enable the observation and measurement of a range of processes where one or both protons remain intact, that otherwise would be difficult or impossible to study. These processes are typically associated with elastic and diffractive scattering, where the proton radiates a virtual colorless object called Pomeron, often thought of as a non-perturbative collection of soft gluons. Protons suffering a moderate energy loss and emitted at very small angles (around μrad) with respect to the beams will remain inside the beam pipe but separated from the beam axis because of the accumulated dispersion in the beam elements. At 200 meters from the ATLAS interaction point, those protons will be sufficiently separated from the nominal beam orbit so that they can be intercepted by the roman pots inserted into the beam pipe aperture. Commissioned in 2015, the AFP detector is composed by roman pots that combine a silicon pixel tracker and a high resolution time-of-flight detector to achieve high precision measurements of the forward protons and their interaction vertex (despite the fact that the time-of-flight detector are not fully functioning until 2018). Four stations are placed at 205 and 217 meters from the interaction point on both sides of the ATLAS central detector, as represented in Figure 3.10. A model of the roman pot of an AFP station and a picture of the silicon pixel tracker and the time-of-flight detectors assembled can also be found in Figure 3.11. To measure these forward protons, the detectors have to be placed very close to the beam center, so the radiation at the AFP stations is higher than at the first layer of the ATLAS inner tracker. Because of this characteristic, the AFP tracking device in each station is the 3D silicon pixel tracker (also used for the ATLAS Insertable B-Layer) since it accommodates uneven irradiation without degradation, among others advantages. Each station contains one silicon tracker with four layers separated by 9 mm along the z -axis and rotated by 14 degrees around the y -axis. Each plane has a silicon pixel sensor with thickness of 230 μm containing an array of 336×80 pixels of size $50(x) \times 250(y) \mu\text{m}^2$.

In order to evaluate the AFP L1 trigger efficiency, data collected with the AFP sub-detector during special low- μ runs in 2016, where only the C-side was assembled, was used. The first successful run of the AFP sub-detector (in August of 2016 with the run number 305359) was the starting point of this study. The data collected by the AFP sub-detector in 2016 only considered the information from the AFP C-side sub-detectors, since only one arm was installed at the time. The second arm (on the A-side) was commissioned in the summer of 2017. The location of both arms with respect to the ATLAS central detector can be found in Figure 3.10. All the hardware triggers implemented in the AFP sub-detector require at least two hits in two different planes to increase the purity of the selection of the events with a reconstructed track in a specific station. Therefore, a track passing by each station can be reconstructed using at least

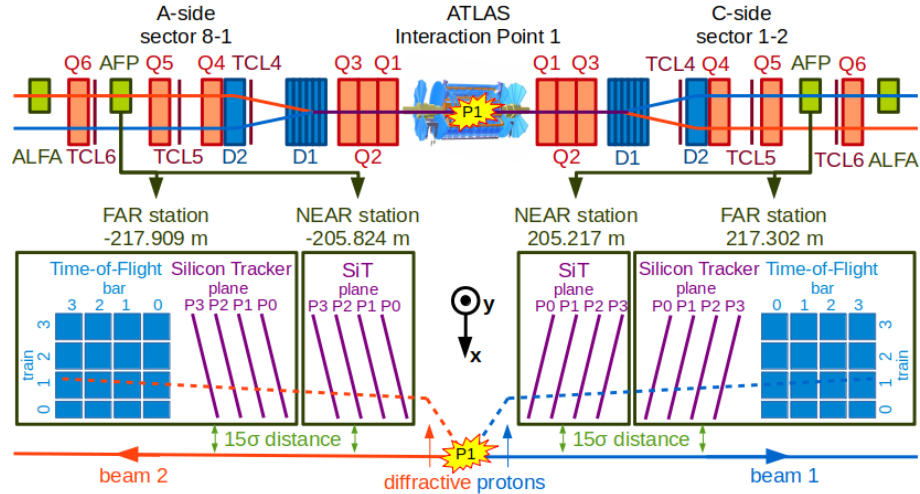


Figure 3.10: Representation of the ATLAS Forward Proton sub-detector [91].

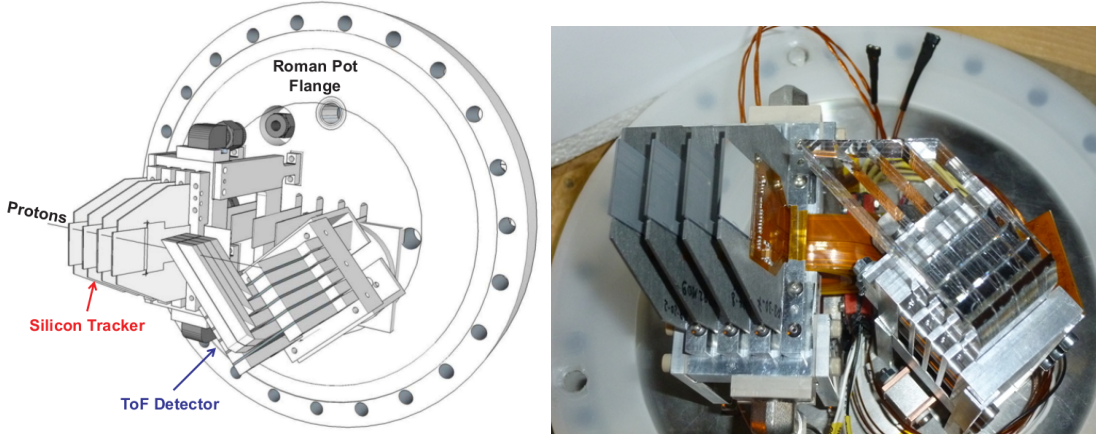


Figure 3.11: The model of the roman pot of an AFP station (left) and the AFP silicon tracking and time-of-flight detector (right) [92].

two hits in two out of four planes of the silicon tracker. In the context of this analysis, the following four L1 triggers were studied:

- L1_AFP_NSC: track reconstructed in the AFP C-side near station;
- L1_AFP_FSC: track reconstructed in the AFP C-side far station;
- L1_AFP_C_ANY: track reconstructed in one of the AFP C-side stations;
- L1_AFP_C_AND: track reconstructed in both AFP C-side stations.

The first step of the analysis consisted in gaining some knowledge on the trigger efficiencies relying only on the information from the trigger itself. In order to do so, the numbers of events passing each of the L1 triggers considered in this analysis together with the reference HLT trigger with empty second level logic (HLT_noalg_L1_AFP_C_ANY) were investigated and summarised in Table 3.3. The simple calculation done by comparing the number of events passing the HLT_noalg_L1_AFP_C_ANY and the L1_AFP_FSC triggers results on an efficiency of the silicon tracker for the AFP C-side far station of 92.6 %.

Selection	Number of events
No cuts	1.5047555e+08
HLT_noalg_L1_AFP_C_ANY	48764
L1_AFP_NSC	24451
L1_AFP_FSC	45165
L1_AFP_C_AND	21378
L1_AFP_C_ANY	48764

Table 3.3: Number of events that passed the selection of the different L1 AFP triggers considered.

The trigger performance is expected to be highly correlated with tracks, meaning that the track reconstruction efficiency should also be considered for studies of the different triggers. The detection of a particle passing by a pixel detector of the silicon tracker is considered a hit, while the combination of two or three hits in the total of the four silicon pixel detectors is considered a track. Taking this condition into account, a detailed study about the correlation between the position of the hits detected by the different layers of the silicon detector and the position of the tracks reconstructed by the silicon tracker was performed for both stations. Moreover, a correlation between the position of the hits detected in the near station and far station was done in order to validate the 2016 data obtained by the AFP detector. Being a recent installed sub-detector at the time, it was crucial to estimate the performance of the hardware trigger as well as the definitions considered for the implemented triggers. Most of the analyses using the AFP data require events passing a trigger selection or an offline track in the near and far station since it provides a better measurement of the path of the forward proton. Besides that, the pattern of the fractional momentum loss evolves with the travelled distance of the involved proton. On average the energy of the protons from non-diffractive processes is much smaller than the typical energy of diffractive protons. The fractional momentum loss has a crucial significance since the diffractive protons have much higher values than the typical energy of the intact protons (as the final state of non-diffractive processes) reaching the AFP sub-detector. The correlation between the position of the tracks reconstructed by the silicon tracker in both stations was also considered.

If a single-number track efficiency for a given AFP station, or to that matter any kind of efficiency of any detector component, is to carry any import, it cannot be interpreted or derived without the knowledge of the acceptance of such a component as well as the precise definition of the object measured. According with the algorithm for the tracking implemented in the dataset analised, only the tracks with a slope of the x position between -0.005 and 0.005 are considered real tracks. After the implementation of the cut on the slope of the x position, a smaller region of acceptance was obtained according with the track maps shown in Figure 3.12. An additional cut on the slope of the y position between -0.05 and 0.05 results in a narrower region with respect to the scenario where only a cut on the slope of the x position is applied. The track maps for each station with the cuts on the slope of the x and y position are shown in Figure 3.13. Such

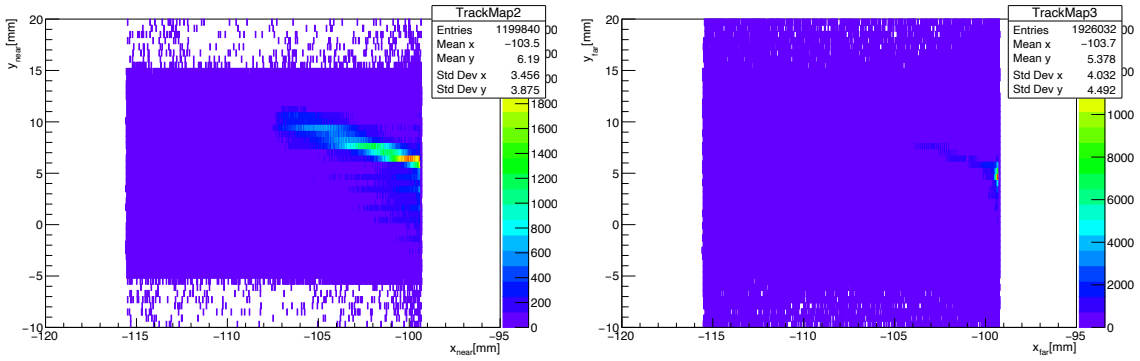


Figure 3.12: Tracks map for the AFP C-side near (left) and the far (right) station after the requirement on the slope of the x position.

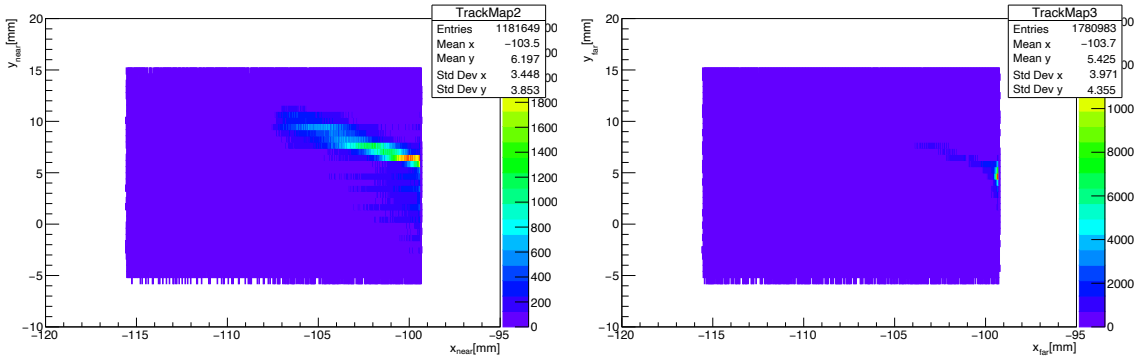


Figure 3.13: Tracks map for the AFP C-side near (left) and the far (right) station after the requirement on the slope of the x and y positions.

requirements are motivated by the geometry of each station, i.e. the limited dimension and the inclination of the silicon planes. The spatial cuts defining the regions of acceptance for each station are summarised in Table 3.4. The distributions of the position of hits in both stations after the requirement on the slope of the x and y positions are presented in Figures 3.14 to 3.15. Although the silicon trackers of both near and far stations are composed by four planes, the data considered in this study only had three silicon planes correctly working for the near station as can be confirmed by the Figure 3.14 and Figure 3.15. The conditions of the silicon plane with high-voltage issues were improved for the following data taking runs. Finally, the combination of the common region of acceptance for hits and tracks for both stations and the requirement of different combinations of tracks and hits multiplicities gave the possibility to achieve a promising efficiency for the L1_AFP_FSC trigger related with the silicon detectors. The optimisation consisted in a total of twelve distinct scenarios for the AFP C-side near and far station. Besides different requirements of hits and tracks in these stations, an analysis with a combination of the triggers passed by the selection was performed. These studies have shown a difference of the trigger efficiency of around 14%, between 85.7% without any cut and 99.5% for the L1_AFP_FSC trigger with all the selection conditions being considered.

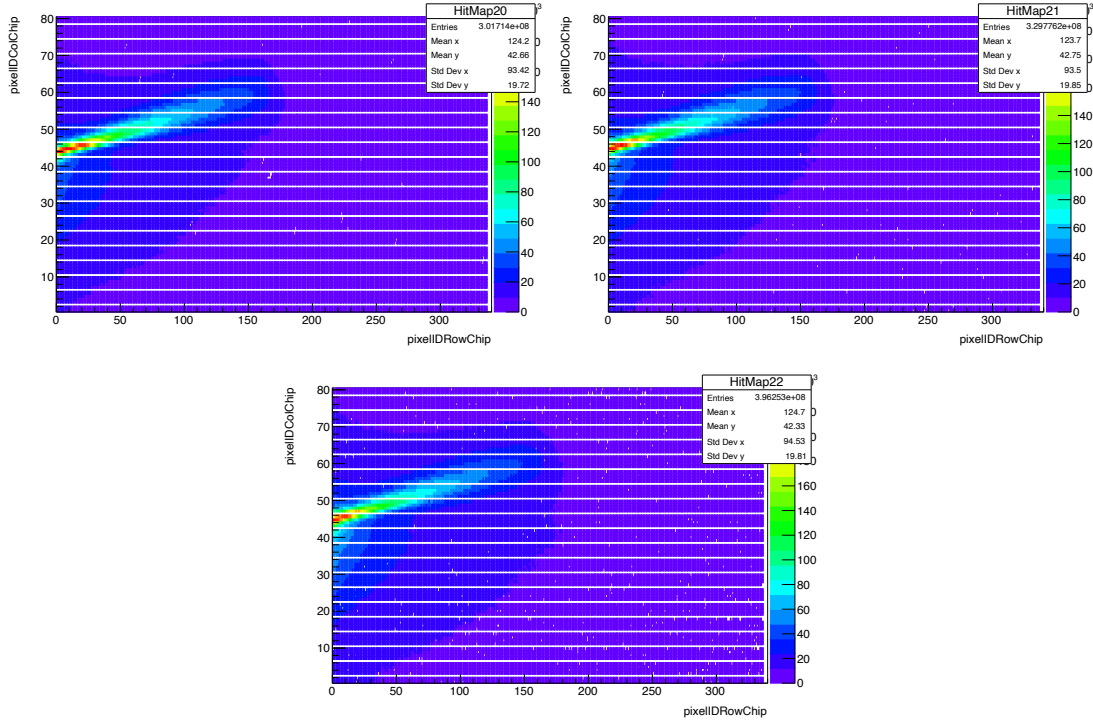


Figure 3.14: Hits map in the AFP C-side near station after the cuts on the slope of the x and y position.

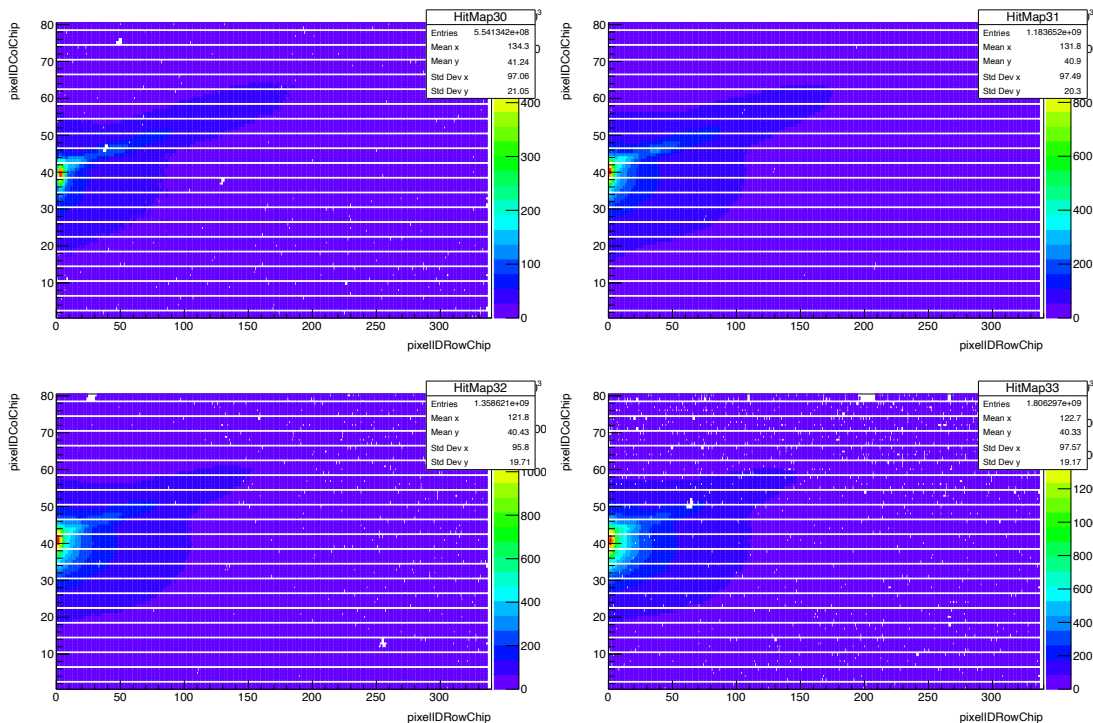


Figure 3.15: Hits map in the AFP C-side far station after the cuts on the slope of the x and y position.

[mm]	Cut on xSlope		Cuts on xSlope and ySlope		
	Near	Far	Near	Far	Difference
Minimum x	-115.567	-115.579	-115.567	-115.579	12 μm
Maximum x	-99.312	-99.212	-99.312	-99.212	100 μm
Minimum y	-5.290	-5.400	-5.286	-5.380	94 μm
Maximum y	14.765	14.786	14.750	14.786	36 μm

Table 3.4: Definition of the region of acceptance of the tracks in the AFP C-side near and far stations.

3.4 Worldwide LHC computing grid

The Worldwide LHC Computer GRID (WLCG) is a global network of more than 170 computing centers in 42 countries. Focusing on the distribution of data from the LHC experiments around the globe, the WLCG is linking up national and international grid infrastructures. This worldwide network is designed to store, organise and analyse the ~ 30 Petabytes of data annually generated at the LHC. The WLCG is divided in different layers, called tiers, each one with distinct purposes.

The Tier 0 is the CERN data centre located in Geneva and also at the Wigner Research Centre for Physics in Budapest. The two sites are connected by two dedicated 100 Gigabit/s data links. The Tier 0 is responsible for the safe-keeping of raw data, first pass reconstruction, distribution of raw data and reconstruction output to the Tier 1.

The Tier 1 is composed by 13 large computer centres. They are responsible for the safe-keeping of a proportional share of raw and reconstructed data, large-scale reprocessing and safe-keeping of a share of simulated data produced at these Tier 2.

The Tier 2 is composed by around 160 sites typically located at universities and other scientific institutes. These sites can store data and provide computing power for specific analysis tasks. The individual scientists can access and process the data through the Tier 3 computing resources consisting of local clusters. The Portuguese contribution at CERN has a strong focus on the Grid computing activities demonstrated by the existence of a WLCG Tier 2 in Lisbon (Portugal).

Search for flavour changing neutral currents in the top quark sector

This chapter presents an overview of the search for flavour-changing neutral current couplings between the top quark and the Z boson in pp collisions at $\sqrt{s} = 13$ TeV at the LHC with the ATLAS detector. The search is performed both for single-top quark production in association with a Z boson and for top quark pair-production events with one top quark decaying through the $t \rightarrow qZ$ ($q = u, c$) channel. Only Z boson and W boson decays to charged leptons (electrons and muons including those coming from leptonic τ lepton decays) are considered as signal, considering that other final states were found to have smaller sensitivity in comparison with the trileptonic one [93]. Consequently, the final state topology for the tZ production mode is characterised by the presence of three isolated charged leptons, exactly one or two jets, with exactly one resulting from a bottom quark hadronisation, and missing transverse momentum from the undetected neutrino. The requirement of at least two jets constitutes the main difference between the tZ production and the $t\bar{t}$ decay modes. Although a similar analysis strategy is applied for both FCNC tZu and tZc cases, two independent analyses are performed in order to search for the two specific signal hypotheses, culminating on the setting of the upper limits on the branching ratio of these processes.

4.1 Data sample

The analysis described in this thesis analysed data collected from 2015 to 2018 by the ATLAS detector. The complete sample includes all data periods from 2015, as well as the whole 2016–2018 datasets, corresponding to the total integrated luminosity of 139 fb^{-1} with an uncertainty of 1.7% [94]. The selected data periods were collected during stable beam LHC operations and with the ATLAS detector fully

functioning.

Single-lepton triggers with distinct p_T thresholds are combined to increase the overall efficiency. The electron triggers select a calorimeter energy cluster matched to a track. Electrons must satisfy identification criteria based on a multivariate technique using a likelihood-based (LH) discriminant, being referred to as the electron likelihood identification [95]. In 2015, electrons had to satisfy a medium identification and have $p_T > 24 \text{ GeV}$. In 2016–2018, electrons had to satisfy a tight identification together with an isolation criteria and have $p_T > 26 \text{ GeV}$. During the four years, to avoid efficiency losses due to identification and isolation at high p_T , two other triggers were also available, selecting medium electrons with $p_T > 60 \text{ GeV}$ and selecting loose electrons with $p_T > 120 \text{ GeV}$ (140 GeV in 2016–2018) [95]. Muons are triggered on by matching tracks reconstructed in the muon spectrometer and in the inner detector. In 2015, muons had to satisfy a loose isolation requirement and have $p_T > 20 \text{ GeV}$. Similarly to the electrons, the p_T threshold increased to $p_T > 26 \text{ GeV}$ for the data collected between 2016 and 2018 with the goal of avoiding efficiency losses due to isolation at high p_T . Another muon trigger without any isolation requirement was available, selecting muons with $p_T > 50 \text{ GeV}$ [96]. The trigger efficiencies for electrons and muons are estimated using a data-driven tag-and-probe method with simulated samples of enriched $Z \rightarrow \ell\ell$ being ℓ an electron or a muon. A tag lepton is characterised as an offline lepton, reconstructed using the full detector information, that has a $\Delta R < 0.1$ with respect to a lepton passing the unprescaled single lepton trigger with $p_T > 26 \text{ GeV}$. A probe lepton is defined as a lepton with opposite charge for which the invariant mass of $|m_{(\text{tag},\text{probe})} - m_Z| < 10 \text{ GeV}$ (requiring also $\Delta\phi_{(\text{tag},\text{probe})} > 2$ for muons). Finally, the fraction of probe leptons matching an associated online lepton defines the lepton trigger efficiency [97, 98].

4.2 Object reconstruction

The physics objects used in this analysis are electrons, muons, jets (including b -tagged jets) and missing transverse momentum. This section describes the main reconstruction and identification criteria applied for each physics object considered.

Electron candidates are reconstructed from energy clusters in the electromagnetic (EM) calorimeter that match a reconstructed track in the inner detector (ID) [99–102]. The clusters are required to be within the range $|\eta| < 2.47$, excluding the transition region between the barrel and endcap calorimeters at $1.37 < |\eta| < 1.52$. Electron candidates must also satisfy a transverse energy requirement of $E_T > 15 \text{ GeV}$. Further requirements on the electromagnetic shower shape, calorimeter energy to tracker momentum ratio, and other discriminating variables are combined into a likelihood-based object quality cut, optimised for strong background rejection. All electron candidates in this analysis must pass the MediumLH selection. Electron tracks are also required to be consistent with the main interaction vertex applying the following requirements: $|d_0^{\text{BL}} \text{ significance}| < 5$ and $|\Delta z_0^{\text{BL}} \sin \theta| < 0.5 \text{ mm}$. Electrons are further required to

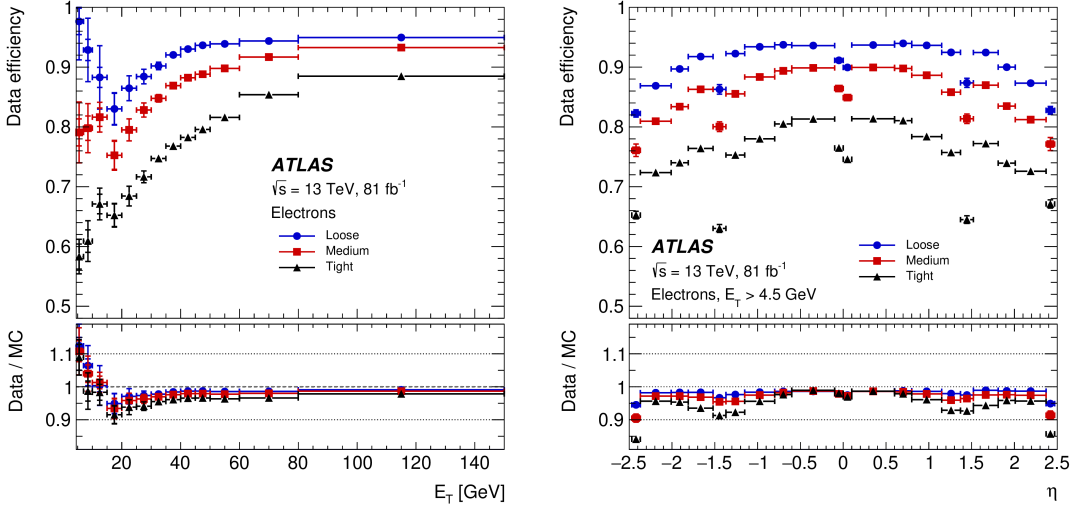


Figure 4.1: Electron identification efficiencies using tag-and-probe method on $Z \rightarrow e^+e^-$ events for the various operating points as function of (a) transverse energy integrated over the full pseudo-rapidity range and (b) pseudo-rapidity for electrons with $E_T > 4.5$ GeV [102].

be isolated, to reject hadronic background but also contributions coming from other sources than prompt W or Z boson decays (hadrons faking an electron signature, heavy-flavour decays or photon conversions). The isolation working point used in this analysis is PLVTight. The Prompt Lepton Veto (PLV) tool combines isolation information and lifetime information to veto non-prompt leptons¹ from heavy flavour decays. Such improvement is possible due to the implementation of a machine learning algorithm called Boosted Decision Trees using several kinematic and angular variables of jets and leptons. Different isolation working points were studied where the PLVTight provided the best results, most specifically on the separation of prompt and non-prompt leptons. For the specific case of the electrons, a reduction of 35% on the contribution coming from the $t\bar{t}$ background was observed while a reduction of only 5% was perceived. Correction factors are applied to simulated electrons to take into account the small differences in reconstruction, identification and isolation efficiencies between data and MC simulation. The identification efficiency is defined as the ratio of the number of leptons (electrons or muons in the case of this thesis) that pass the identification requirements to the total number of truth lepton candidates. For the electrons, the identification efficiency is measured using the tag-and-probe method on $Z \rightarrow e^+e^-$ and $J/\Psi \rightarrow e^+e^-$ simulated events. The performance of the LH identification algorithm is illustrated in Figure 4.1. Depending on the operating point, the identification efficiencies for electrons with $E_T = 25$ GeV are between 68% to 86% and increase with E_T .

Muon candidates are reconstructed by combining a reconstructed track from the ID with one from the muon spectrometer (MS) [103], and are required to have $p_T > 15$ GeV and $|\eta| < 2.5$ [104]. To reject misidentified muon candidates, primarily originating from pion and kaon decays, several quality

¹Non-prompt leptons are real leptons coming from decays-in-flight of pions/kaons, semi-leptonic decays of heavy b -/ c -hadrons or photon conversions.

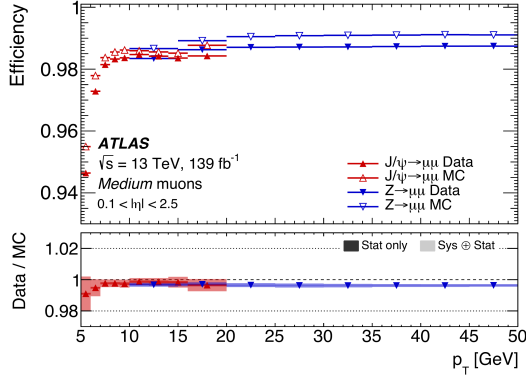


Figure 4.2: Muon reconstruction and identification efficiencies for the Medium criteria measured in $J/\Psi \rightarrow \mu^+\mu^-$ and $Z \rightarrow \mu^+\mu^-$ events as a function of p_T for muons with $0.1 < |\eta| < 2.5$ [104].

requirements are imposed on the muon candidate. The muon candidates in this analysis must pass the Medium identification definition, based, for muons with $|\eta| < 2.5$, on requirements of hits in MS subsystems, and on the compatibility between ID and MS momentum measurements. Muon tracks are also required to be consistent with the beam line applying the requirements: $|d_0^{\text{BL}} \text{ significance}| < 3$ and $|\Delta z_0^{\text{BL}} \sin \theta| < 0.5 \text{ mm}$. Muons are further required to be isolated. The isolation working point used for muons is PLVTight, after similar studies with respect to the electrons on the reduction of the background contribution from non-prompt leptons. Like for electrons, correction factors are applied to simulated muons to account for the small differences between data and simulation. Reconstruction, isolation and identification efficiencies of the muons are measured in data and simulation using the tag-and-probe method on $Z \rightarrow \mu^+\mu^-$ for $p_T(\mu) > 15 \text{ GeV}$, and $J/\Psi \rightarrow \mu^+\mu^-$ for $5 < p_T(\mu) < 15 \text{ GeV}$ simulated events. The reconstruction and identification efficiencies of the muons respecting the Medium criteria are shown in Figure 4.2.

Jets are reconstructed from the particle flow objects [8] using the anti- k_t algorithm [105] with a radius parameter $\Delta R = 0.4$. All jets considered in this analysis should have a transverse momentum $p_T > 25 \text{ GeV}$ and a pseudo-rapidity of $|\eta| < 2.5$. To suppress jets from in-time pile-up, the Jet Vertex Tagger (JVT) discriminant, which is based on a two-dimensional likelihood method, is used [106]. A JVT value of at least 0.59 is required for jets with $p_T < 60 \text{ GeV}$ and $|\eta| < 2.4$, corresponding to an efficiency of 92%.

Jets originating from bottom quarks (called b -jets) are identified by reconstructing secondary vertices from the tracks associated to the jets and by combining their spatial parameters with life-time related information. The performance of the b -tagging algorithms is measured by their ability to correctly identify jets coming from a real b -quark compared to the probability of mistakenly tagging a jet coming from a gluon, a c -quark or a light-flavour parton as a b -jet. The b -tagging efficiencies and c -, τ - and light-jets rejections of the four different operating points of the DL1r tagger are summarised in Table 4.1. A detailed study on the signal acceptance and the background rejection was performed for all the available operating points. For

the tZu case, both 70 % and 77 % b -tag efficiency operating points provided the best results presenting a high signal acceptance and minor background rejection with a signal to the square root of background (S/\sqrt{B}) ratio of 3.21 ± 0.54 and 3.07 ± 0.48 , respectively. The same conclusions were obtained for the tZc case with a S/\sqrt{B} of 1.53 ± 0.26 and 1.51 ± 0.24 for 70 % and 77 % b -tag efficiency operating points, respectively. However, the DL1r b -tagging algorithm with the 77 % of b -tag efficiency operation point is used since it gives a better MC statistics, which will be important for the multivariate analysis and for the consequent signal to background discrimination. Finally, all b -tagged jets considered in this analysis should have a transverse momentum $p_T > 25$ GeV and a pseudo-rapidity of $|\eta| < 2.5$.

b -jet efficiency [%]	c -jet rejection	τ -jet rejection	Light-jet rejection
60	27	220	1300
70	9.4	43	390
77	4.9	14	130
85	2.6	3.9	29

Table 4.1: Summary of the four operating points for the DL1r b -tagging algorithm including benchmark numbers for the efficiency and the correspondent rejection rates [107].

The missing transverse momentum, E_T^{miss} , is a measure of the momentum imbalance, usually due to escaping neutrinos. It is calculated as the magnitude of the negative vector sum of the momenta in the transverse plane of all selected calibrated physics objects in the event [108, 109]. To account for the soft hadronic activity, a soft term built from tracks that are associated to the hard-scatter vertex but are not associated to any of the reconstructed objects. The soft term is included in order to account for low-momentum particles that are not identified among the final state objects [110–112]. It also includes an extra term to account energy losses due to the detector inefficiencies and resolution leading to the mis-measurement of the true transverse energy of the final interacting objects.

In order to avoid double counting of single final state objects, like e.g. an isolated electron being reconstructed both as an electron and as a jet with the requirements above, a procedure is followed to remove overlaps between final state objects. The following sequence of operation steps is performed to solve these ambiguities:

- Electron candidates which share a track with a muon candidate are removed.
- If the distance in ΔR between a jet and an electron candidate is $\Delta R < 0.2$, then the jet is dropped.
If multiple jets are found with this requirement, only the closest one is dropped.
- If the distance in ΔR between a jet and a baseline electron is $0.4 < \Delta R < 0.2$, then the electron is dropped.

- If the distance in ΔR between a jet and a muon candidate is $\Delta R < 0.4$, then: if the jet has more than 2 associated tracks then the muon is dropped, otherwise the jet is removed.

A summary of the selection of the physics objects considered in this analysis can be found in Table 4.2.

Objects	p_T	$ \eta $	ID	Isolation	Additional cuts
Electrons	$> 15 \text{ GeV}$	< 2.47	MediumLH	PLVTight	$ d_0^{\text{BL}} \text{ significance} < 5$ $ \Delta z_0^{\text{BL}} \sin \theta < 0.5 \text{ mm}$
Muons	$> 15 \text{ GeV}$	< 2.5	Medium	PLVTight	$ d_0^{\text{BL}} \text{ significance} < 3$ $ \Delta z_0^{\text{BL}} \sin \theta < 0.5 \text{ mm}$
Jets	$> 25 \text{ GeV}$	< 2.5	PFlow	-	JVT
b -jets	$> 25 \text{ GeV}$	< 2.5	DL1r @77 %	-	-

Table 4.2: Overview of the requirements of the physics objects used in this analysis.

4.3 Signal and background modelling

Monte Carlo simulation samples are used to model the signal and distinct background processes. The generated MC samples containing top quarks are produced with the top quark mass, m_t , parameter set to 172.5 GeV. The detector response to stable particles is emulated by a dedicated simulation [113] based on GEANT4 [114]. Detailed or fast simulation of the detector and the trigger system were performed with standard ATLAS software using GEANT4 [113, 114] or ATLFASTII [113], respectively. The same offline reconstruction methods used on data are also applied to the simulation samples. Additionally, simulated events are corrected so that the object identification, reconstruction and trigger efficiencies; the energy scales; and the energy resolution match those determined from data control samples. A set of minimum-bias interactions were overlaid on the hard-scattering event to account for additional pp collisions in the same or nearby bunch crossings (pile-up). Simulated samples were reweighted to match the different pile-up conditions in data during the Run-2 data taking.

4.3.1 Signal modelling

The MC simulation samples for signal were generated at NLO with MadGraph5_aMC@NLO [115] interfaced to the Pythia8 [64] with the A14 tune [116] and NNPDF2.3LO PDF set. Only decays of the W and Z bosons involving charged leptons were generated at the matrix element level ($Z \rightarrow e^+e^-$, $\mu^+\mu^-$, $\tau^+\tau^-$ and $W \rightarrow e\nu, \mu\nu, \tau\nu$). For the matrix element, PDF set NNPDF3.0NL0 is used. The Universal FeynRules Output (UFO) model [63] is used for computation at the NLO in QCD. Top quark FCNC decay is done by

TopFCNC model [60, 61]. The TopFCNC UFO model includes the effects of new physics at a energy scale Λ by adding effective terms to the SM Lagrangian (as described in Chapter 2). For the signal samples with $t\bar{t}$ production, it is considered that one of the top quarks decays through FCNC to qZ ($q=u,c$) and the other according to the SM to Wb (as represented in Figure 2.6). For the tZ production, a top quark and a Z boson are generated where the top quark decays according to the SM (since the tZq anomalous coupling is assumed in the primary vertex). Taking into account that both production and decay modes are considered in this analysis, separated samples for each mode and tZu/tZc anomalous couplings were generated. In order to allow the study of the chirality of these couplings, samples with left-handed or right-handed couplings were obtained as well. The number of signal events is normalised to a branching ratio of $BR(t \rightarrow uZ) = 1.7 \times 10^{-4}$ and $BR(t \rightarrow cZ) = 2.4 \times 10^{-4}$, constraining $BR(t \rightarrow bW) = 1 - BR(t \rightarrow uZ/cZ)$ for the decay mode samples. Considered $t \rightarrow qZ$ branching ratio values are observed limits obtained from the previous analysis at a center-of-mass energy of 13 TeV with 36 fb^{-1} [47]. The FCNC $t\bar{t}$ decay signal is normalised using the $t\bar{t}$ cross-section prediction at NNLO in QCD including the resummation of NNLL soft-gluon terms calculated using Top++2.0 [117–123]. For pp collisions at a centre-of-mass energy of $\sqrt{s} = 13 \text{ TeV}$, this cross-section corresponds to $\sigma(t\bar{t})_{\text{NNLO+NNLL}} = 832 \pm 51 \text{ pb}$ using a top quark mass of $m_t = 172.5 \text{ GeV}$. The uncertainties on the cross-section due to PDF and α_s are calculated using the PDF4LHC prescription [124] with the MSTW2008 68% CL NNLO [125, 126], CT10 NNLO [127, 128] and NNPDF2.3 5f FFN [129] PDF sets, and are added in quadrature to the scale uncertainty. The FCNC single-top quark production signal cross-section is calculated at NLO using the TopFCNC model as implemented in the MadGraph5_aMC@NLO. For a branching ratio $BR(t \rightarrow uZ)$ of 1.7×10^{-4} , a cross-section of $\sigma(tZ)_{\text{NLO}} = 0.378 \pm 0.001 \text{ pb}$ is calculated. For the tZc case, a cross-section of $\sigma(tZ)_{\text{NLO}} = 0.064 \pm 0.001 \text{ pb}$ is calculated for the scenario where a branching ratio $BR(t \rightarrow cZ)$ of 2.4×10^{-4} is considered.

4.3.2 Background modelling

Several background processes with distinct characteristics were considered in this analysis. Being the final state defined by exactly three leptons, processes with three real leptons, as $t\bar{t}V$, tZq or diboson production play a major role on the event yields of the different regions optimised in this search. However, there are other processes that can have an important fraction of events surviving the selection due to non-prompt or fake leptons, as the $t\bar{t}$, $Z+jets$, Wt and $t\bar{t}H$ processes, among others. The details of the MC simulation of all the studied background processes is described below.

$t\bar{t}$ production The production of $t\bar{t}$ events is modelled using the PowhegBox [130–133] v2 generator at NLO with the NNPDF3.0NLO [134] PDF and the h_{damp} parameter set to $1.5 m_t$ [135]. The h_{damp} parameter is a resummation damping factor and one of the parameters that controls the matching of

Powheg matrix elements to the parton shower and thus effectively regulates the high- p_T radiation against which the $t\bar{t}$ system recoils. The events are interfaced to `Pythia8.230` [136] to model the parton shower, hadronisation, and underlying event, with parameters set according to the A14 tune [137] and using the NNPDF2.3L0 set of PDFs [129]. The decays of bottom and charm hadrons are performed by `EvtGen v1.6.0` [138]. In the sample used, it is required that both the W bosons from the top quarks decay leptonically. The Var3c A14 tune variation [137], that largely corresponds to the variation of α_S for initial state radiation in the A14 tune, is considered as an uncertainty. The impact of final-state-radiation is evaluated using PS weights which vary the renormalisation scale for QCD emission in the FSR by a factor of 0.5 and 2.0, respectively. Additionally, the uncertainty associated to the h_{damp} parameter is evaluated using the alternative sample with the h_{damp} value increased to 3.0 m_t . The impact of the parton shower and hadronisation model is evaluated by comparing the nominal generator setup with a sample produced with the `PowhegBox v2` [130–133] generator using the NNPDF3.0NLO [134] PDF. The events are interfaced with `Herwig7.13` [139, 140], using the `Herwig7.1` default set of tuned parameters [140, 141] and the MMHT2014L0 PDF set [142]. The decays of bottom and charm hadrons are simulated using the `EvtGen v1.6.0` program [138].

$t\bar{t}V$ production The production of $t\bar{t}V$ events is modelled using the `MadGraph5_aMC@NLO v2.3.3` [115] generator at NLO with the NNPDF3.0NLO [134] PDF. The events are interfaced to `Pythia8.210` [136] using the A14 tune [137] and the NNPDF2.3L0 [134] PDF set. The decays of bottom and charm hadrons are simulated using the `EvtGen v1.2.0` program [138]. The uncertainty due to initial-state-radiation is estimated by comparing the nominal $t\bar{t}V$ sample with two additional samples, which have the same setting as the nominal one, but with the Var3 up or down variation of the A14 tune. The Var3c A14 tune variation corresponds to the variation of α_S for initial state radiation in the A14 tune. Another alternative $t\bar{t}Z$ sample is generated with the same `MadGraph5_aMC@NLO` version as the nominal sample, but interfaced to `Herwig7` [139, 140] for the simulation of the parton shower and hadronisation and H7UE [140] for the underlying event model.

tZq production The production of tZq events is modelled using the `MadGraph5_aMC@NLO v2.3.3` [115] generator at NLO with the NNPDF3.0NLO [134] PDF. The events are interfaced with `Pythia8.230` [136] using the A14 tune [137] and the NNPDF2.3L0 [134] PDF set. The uncertainty due to initial-state-radiation is estimated by comparing the nominal tZq sample with two additional samples, which have the same setting as the nominal one, but with the Var3 up and down variations of the A14 tune. The predicted cross-section was calculated with `MadGraph5_aMC@NLO 2.6.0`, using the five-flavour scheme with the `NNPDF30_nlo_as_0118` PDF set and with the renormalisation and factorisation scales, μ_r and μ_f , set to $\mu_r = \mu_f = (m_t + m_Z)/4 = 66$ GeV. The SM tZq cross-section at NLO in QCD, including non-resonant contributions with $m_{\ell^+\ell^-} > 30$ GeV, is 102 fb.

tW production Although having a very low contribution, single-top quark production in the tW -channel is also considered. The contribution from the single-top quark production through t -channel and s -channel were proven to be even less relevant than the tW -channel and consequently not included in the analysis. The associated production of top quarks with W bosons (tW) is modelled using the PowhegBox [131–133, 143] v2 generator at NLO in QCD using the five-flavour scheme and the NNPDF3.0NLO set of PDFs [134]. The diagram removal (DR) scheme [144] is used to remove interference and overlap with $t\bar{t}$ production. The events are interfaced to Pythia8.230 [136] using the A14 tune [137] and the NNPDF2.3L0 set of PDFs [129]. In the samples used, it is required that both W bosons in the event decay leptonically.

tWZ production The production of tWZ events is modelled using the MadGraph5_aMC@NLO v2.3.3 [115] generator at NLO with the NNPDF3.0NLO [134] PDF. The events are interfaced with Pythia8.212 [136] using the A14 tune [137] and the NNPDF2.3L0 [134] PDF set. The decays of bottom and charm hadrons are simulated using the EvtGen v1.2.0 program [138]. In the sample used, it is required that the Z boson decays leptonically. An additional tWZ sample is used to estimate the uncertainty connected with the description of the interference between $t\bar{t}Z$ and tWZ . The nominal sample is generated with the DR1 scheme, while the alternative sample is generated using the DR2 scheme.

Diboson production The samples simulating WW , WZ and ZZ events with at least two charged leptons in the final state are considered. In the trilepton topology, WZ production is the process that significantly contributes to the background and consequently included in the analysis.

Samples of diboson final states (VV) are simulated with the Sherpa v2.2.1 or v2.2.2 [145] generator depending on the process, including off-shell effects and Higgs-boson contributions, where appropriate. Fully leptonic final states and semileptonic final states, where one boson decays leptonically and the other hadronically, are generated using matrix elements at NLO accuracy in QCD for up to one additional parton and at LO accuracy for up to three additional parton emissions. Samples for the loop-induced processes $gg \rightarrow VV$ are generated using LO-accurate matrix elements for up to one additional parton emission for both cases of fully leptonic and semileptonic final states. The matrix element calculations are matched and merged with the Sherpa parton shower based on Catani-Seymour dipole [146, 147] using the MEPSNLO prescription [148–151]. The virtual QCD correction are provided by the OpenLoops library [152, 153]. The NNPDF3.0nnlo set of PDFs is used [134], along with the dedicated set of tuned parton-shower parameters developed by the Sherpa authors [145].

Electroweak production of diboson in association with two jets ($VVjj$) is simulated with the Sherpa v2.2.2 [145] generator. The LO-accurate matrix elements are matched to a parton shower based on Catani-Seymour dipoles [146, 147] using the MEPSLO prescription [148–151]. Samples are generated using the NNPDF3.0nnlo set [134], along with the dedicated set of tuned parton-shower parameters developed by the Sherpa authors.

To assess the uncertainty from the generator, alternative samples are used. The `PowhegBox v2` [131–133] generator is used to generate these alternative WW , WZ and ZZ samples [154] processes at NLO accuracy in QCD. The effect of singly resonant amplitudes as well as the interference effects due to Z/γ^* and identical leptons in the final state is included, where appropriate. Interference effects between WW and ZZ for same-flavor charged leptons and neutrinos are ignored. Events are interfaced to `Pythia8.186` [64] for the modelling of the parton shower, hadronisation, and underlying event, with parameters set according to the `AZNLO` tune [155]. The `CT10` PDF set [127] is used for the hard-scattering processes, whereas the `CTEQ6L1` PDF set [156] is used for the parton shower. The `EvtGen v1.2.0` program [138] is used to decay bottom and charm hadrons.

$Z+jets$ production The `PowhegBox v1` MC generator [131–133, 157] is used for the simulation at NLO accuracy of the hard-scattering processes of Z -boson production and decay in the electron, muon, and tau channels. It is interfaced to `Pythia8.186` [64] for the modelling of the parton shower, hadronisation, and underlying event, with parameters set according to the `AZNLO` tune [155]. The `CT10` PDF set [127] is used for the hard-scattering processes, whereas the `CTEQ6L1` PDF set [156] is used for the parton shower. The effect of QED final-state radiation is simulated with `Photos++` (v3.52) [158, 159]. The `EvtGen v1.2.0` program [138] is used to decay bottom and charm hadrons.

$t\bar{t}H$ production The production of $t\bar{t}H$ events is modelled using the `PowhegBox v2` [130–133, 160] generator which provides matrix elements at NLO in the strong coupling constant α_s in the five-flavour scheme with the `NNPDF3.0nlo` [134] PDF set. The functional form of the renormalisation and factorisation scale is set to $\sqrt[3]{m_T(t) \cdot m_T(\bar{t}) \cdot m_T(H)}$ [161]. The events are interfaced to `Pythia8.230` [136] using the `A14` tune [137] and the `NNPDF2.3L0` [134] PDF set. The decays of bottom and charm hadrons are performed by `EvtGen v1.6.0` [138].

Other rare backgrounds The production of triboson (VVV) events is simulated with the `Sherpa v2.2.2` [145] generator using factorised gauge boson decays. Matrix elements, accurate at NLO for the inclusive process and at LO for up to two additional parton emissions, are matched and merged with the `Sherpa` parton shower based on Catani-Seymour dipole factorisation [146, 147] using the `MEPS@NLO` prescription [148–151]. The virtual QCD correction for matrix elements at NLO accuracy are provided by the `OpenLoops` library [152, 153, 162]. Samples are generated using the `NNPDF3.0nnlo` set [134], along with the dedicated set of tuned parton-shower parameters developed by the `Sherpa` authors. The production of $t\bar{t}t\bar{t}$ events is modelled using the `MadGraph5_aMC@NLO v2.3.3` [115] generator at NLO with the `NNPDF3.1nlo` [134] PDF set. The events are interfaced with `Pythia8.230` [136] using the `A14` tune [137] and the `NNPDF2.3L0` [134] PDF set. The decays of bottom and charm hadrons are simulated using the `EvtGen v1.6.0` program [138]. The other rare top quark processes namely the production

Sample	Generator	Parton shower	ME PDF	PS PDF	Tune parameters
$t\bar{t}$ FCNC	MadGraph5_aMC@NLO [115]	Pythia8 [64]	NNPDF3.0NLO [134]	NNPDF2.3L0	A14 [116]
tZ FCNC	MadGraph5_aMC@NLO	Pythia8	NNPDF3.0NLO	NNPDF2.3L0	A14
$t\bar{t}V$	PowhegBox [130–133]	Pythia8	NNPDF3.0NLO	NNPDF2.3L0	A14
tZq	MadGraph5_aMC@NLO	Pythia8	NNPDF3.0NLO	NNPDF2.3L0	A14
tW	PowhegBox	Pythia8	NNPDF3.0NLO	NNPDF2.3L0	A14
tWZ	MadGraph5_aMC@NLO	Pythia8	NNPDF3.0NLO	NNPDF2.3L0	A14
VV	Sherpa [145]	Sherpa	NNPDF3.0nnlo	NNPDF3.0nnlo	Sherpa default
$VVjj$	Sherpa	Sherpa	NNPDF3.0nnlo	NNPDF3.0nnlo	Sherpa default
$Z+jets$	PowhegBox	Pythia8	CT10 [127]	CTEQ6L1 [156]	AZNLO [155]
$t\bar{t}H$	PowhegBox	Pythia8	NNPDF3.0nlo	NNPDF2.3L0	A14
VVV	Sherpa	Sherpa	CT10	CT10	Sherpa default
$t\bar{t}\bar{t}$	MadGraph5_aMC@NLO	Pythia8	NNPDF3.1nlo	NNPDF2.3L0	A14
$t\bar{t}WW$	MadGraph5_aMC@NLO	Pythia8	NNPDF3.1nlo	NNPDF2.3L0	A14
$t\bar{t}t$	MadGraph5_aMC@NLO	Pythia8	NNPDF3.1nlo	NNPDF2.3L0	A14

Table 4.3: Generators, parton shower simulation, parton distribution functions and tune parameters used to the generation of the MC simulation samples for this analysis. The acronyms ME and PS stand for matrix element and parton shower, respectively.

of $t\bar{t}WW$ and $t\bar{t}t$ are all modeled using the MadGraph5_aMC@NLO generator at LO interfaced with Pythia8 using the A14 tune.

A summary of the generation details of signal and background simulated samples considered in this analysis can be found in Table 4.3.

4.4 Analysis strategy

The search for a particular source of new physics, such as new interactions with the top quark, begins with the thorough understanding of the signatures that the new physics scenario will leave in the detector. This generally requires a strict definition of the final state of the new interaction chosen: for example, deciding between a leptonic decay of the Z boson on the search for FCNC tZq vertex instead of a hadronic decay. With the simulation of the signal processes, the knowledge of both the signal final state and its kinematics therein informs about the specific SM background processes that are likely to be relevant to the analysis. Thereafter, the knowledge of the dominant SM background processes allows to determine how the phenomenology and kinematics of the signal differ with respect to those of the relevant backgrounds. Besides that, it also allows the definition of a basis of kinematic observables that enables the discrimination between the signal and background. Finally, one can define regions of phase space in which the signal-to-background ratio is large, where the likelihood of observing the presence of the signal is ideally maximal. Such regions of large signal purity (i.e. an increased signal-to-background ratio) are commonly referred to as signal regions (SRs). The predictions on the signal and background processes in the signal regions can then be compared to the data (recorded by the ATLAS detector in the case of this thesis). Therefore, the understanding and precise estimation of the backgrounds is a crucial step in all physics analyses. In order

to achieve such understanding, the analysis presented in the present thesis makes use of the so-called control region method. This method is characterised by the definition of a region (or more) in which there is (are) high purities of the dominant background process(es). These regions are referred to as control regions and are ideally obtained using the same basis of observables used to define the signal regions. The control regions (CRs) are defined to be orthogonal to the signal regions, which means that no events satisfying the requirements of the signal regions populate the control regions. The observed data in the control regions (enriched in a specific background process) are then used to derive factors that correct the cross-section predictions of the MC estimates of the dominant background processes targeted by the specific control region. In addition to the signal and control regions, so-called validation regions (VRs) are also defined. The validation regions are typically kinematically more similar to the signal regions than the control regions, while maintaining orthogonality between the control and signal regions. The validation is done by comparing the corrected MC prediction of the backgrounds to the observed data in the validation regions, confirming that both the overall normalisation of the backgrounds agrees with the data as well as the overall shape of the relevant observables used in the definition of the signal regions.

For the search for FCNC interactions with the tZq vertex, the strategy chosen when developing and optimising the analysis relies on a set of requirements which are valid for both production and decay modes being the different features considered with minor variations in the selection. The event selection of the signal regions described in detail in this section is represented in Table 4.4.

Signal regions definition		
Common selections		
Exactly 3 leptons with $ \eta < 2.5$ and $p_T(\ell_1) > 27 \text{ GeV}$, $p_T(\ell_2) > 15 \text{ GeV}$, $p_T(\ell_3) > 15 \text{ GeV}$ ≥ 1 Opposite-Sign Same-Flavour (OSSF) lepton pair, with $ m_{\ell\ell} - 91.19 \text{ GeV} < 15 \text{ GeV}$		
Decay channel - Full SR1	Production channel - Full SR2	
≥ 2 jets with $ \eta < 2.5$ $= 1$ b -jet $-$ $ m_t^{\text{FCNC}} - 172.5 \text{ GeV} < 2\sigma^{\text{FCNC}}$ $-$	$= 1$ jet with $ \eta < 2.5$ $= 1$ b -jet $m_T(\ell_W, v) > 40 \text{ GeV}$ $-$ $-$	$= 2$ jets with $ \eta < 2.5$ $= 1$ b -jet $m_T(\ell_W, v) > 40 \text{ GeV}$ $ m_t^{\text{FCNC}} - 172.5 \text{ GeV} > 2\sigma^{\text{FCNC}}$ $ m_t^{\text{SM}} - 172.5 \text{ GeV} < 2\sigma^{\text{SM}}$

Table 4.4: Overview of the requirements applied for selecting events in the signal regions.

4.4.1 Common selection

Being the analysis focused on the search for the FCNC tZq coupling, the main requirement for both production and decay modes is the reconstruction of a Z boson candidate. The Z boson candidate is

reconstructed with a pair of leptons (electrons or muons) with the same flavour and opposite sign characterised by an invariant mass that satisfy $|m_{\ell\ell} - m_Z| < 15 \text{ GeV}$, where m_Z is set to 91.19 GeV [72]. For both production and decay modes, the analysis considers the leptonic decay of the Z boson and of the top quark resulting in a common final state with exactly three leptons.

Besides the number of leptons and the presence of the Z boson, another common feature is the presence of a top quark decaying to a W boson and a bottom quark, denominated a SM top quark. The reconstruction of the SM top quark considers a jet tagged as coming from a bottom quark (i.e. a b -tagged jet) and the leptonic decay of the W boson to a lepton (electron or muon) and missing transverse energy (coming from the neutrino). Only for the decay signal hypothesis, a top quark decaying to a Z boson and a light quark (up or charm quark) is also produced, being named as FCNC top quark. The reconstruction of the top quarks allow the orthogonality of the signal regions through distinct requirements on their masses.

Taking into account that a Z boson and at least one top quark is always reconstructed, this analysis requires exactly three leptons (electrons or muons) for all regions defined. Another common selection for all the signal and control regions of the search is the requirement on the transverse momentum of the three leptons. A study considering seven different combinations of cuts for these three objects was performed, concluding that the scenario where the leading lepton is required to have transverse momentum of at least 27 GeV and the remaining ones of at least 15 GeV provides the best results with a good signal to background ratio of 0.1436. While the case of the requirements of $p_T(\ell_1) > 27 \text{ GeV}$, $p_T(\ell_2) > 25 \text{ GeV}$ and $p_T(\ell_3) > 15 \text{ GeV}$ gives the best signal to background ratio (0.1464), it also presents a significant reduction of the background contribution which is not ideal for the creation of control regions and the implementation of multivariate techniques. In the extreme case of cutting on $p_T(\ell_1) > 27 \text{ GeV}$, $p_T(\ell_2) > 10 \text{ GeV}$ and $p_T(\ell_3) > 10 \text{ GeV}$, the signal to background ratio reaches the minimum (with 0.1329) while the background, especially from processes with fake leptons, gains an excessive contribution with around 100 additional background events and only 9 additional signal events for both signal regions.

4.4.2 Top quarks reconstruction

In the events having at least two jets with one of them being b -tagged, two top quarks (FCNC and SM tops) candidates are reconstructed under the FCNC $t\bar{t}$ decay signal hypothesis. The kinematics of the top quark candidates can be reconstructed from the corresponding decay particles. The reconstructed Z boson is assumed to come from the FCNC top decay ($t \rightarrow qZ$), while the b -tagged jet from SM top decay ($t \rightarrow bW$). In order to reconstruct both top quarks, it is also needed to associate a reconstructed jet to the q -quark from FCNC top decay, and reconstruct the W boson from the SM top decay. This can be done by assuming the lepton not used to reconstruct the Z boson to be the one coming from the W boson decay (ℓ_W), the missing transverse momentum to be the transverse momentum of the neutrino from W boson

decay and determining the longitudinal component of the neutrino momentum (p_z^ν) using the minimisation of the following expression for each jet combination:

$$\chi_{t\bar{t}}^2 = \frac{(m_{j_a\ell\ell}^{\text{reco}} - m_{t\text{FCNC}})^2}{\sigma_{t\text{FCNC}}^2} + \frac{(m_{j_b\ell_W\nu}^{\text{reco}} - m_{t\text{SM}})^2}{\sigma_{t\text{SM}}^2} + \frac{(m_{\ell_W\nu}^{\text{reco}} - m_W)^2}{\sigma_W^2}, \quad (4.1)$$

where $m_{j_a\ell\ell}^{\text{reco}}$, $m_{j_b\ell_W\nu}^{\text{reco}}$, and $m_{\ell_W\nu}^{\text{reco}}$ are the reconstructed masses of the qZ , bW , and $\ell_W\nu$ systems, respectively. For each jet combination, where any jet can be assigned to j_a , while j_b must correspond to a b -tagged jet, the $\chi_{t\bar{t}}^2$ minimisation gives the most probable value for p_z^ν . From all combinations, the one with the minimum χ^2 is chosen. This procedure assigns a reconstructed jet to the q -quark from FCNC top decay and determines the p_z^ν value, completing all ingredients to reconstruct the four-momenta of the top quark candidates. In Equation (4.1), the central value for the masses ($m_{t\text{FCNC}}$, $m_{t\text{SM}}$ and m_W) and the widths of the top quarks and W boson ($\sigma_{t\text{FCNC}}$, $\sigma_{t\text{SM}}$ and σ_W) are taken from reconstructed FCNC $t\bar{t}$ decays from simulated signal events. This is done by matching the true q - and b -quarks in the simulated events to the reconstructed ones, setting the longitudinal momentum of the neutrino to the p_z of the true simulated neutrino and then performing Bukin fits [163] to the masses of the reconstructed top quarks and W boson. The Bukin fits use a piecewise function with a Gaussian function in the center and two asymmetric tails. Five parameters determine the overall normalisation: the peak position, the width of the core, the asymmetry, the size of the lower tail, and the size of the higher tail. From these parameters, only the peak position and the width enter the χ^2 . The obtained values are $m_{t\text{FCNC}} = 171.0$ GeV, $m_{t\text{SM}} = 166.5$ GeV, $m_W = 80.5$ GeV, $\sigma_{t\text{FCNC}} = 11.1$ GeV, $\sigma_{t\text{SM}} = 23.2$ GeV and $\sigma_W = 15.4$ GeV. These values are extracted from the Bukin fits to the masses of the top quarks and W boson reconstructed by matching the true generated q - and b -quarks to the reconstructed jets within the $\Delta R < 0.4$, assuming the missing transverse momentum to be the neutrino transverse momentum, and setting the longitudinal momentum of the neutrino to the p_z of the true generated particle. The Z boson is reconstructed from the opposite-sign same-flavour lepton pair. If more than one such lepton pair is present then the one with the invariant mass closest to the mass of the Z boson is considered, while the remaining lepton is assumed to come from the W boson. Therefore, the fitted values represent the optimal resolution of the reconstructed top quarks and W boson masses in the FCNC $t\bar{t}$ decay signal events. The mean value is lower and the standard deviation is larger for the SM top than for the top quark with the FCNC decay. This is mainly due to the scale and resolution of the missing transverse momentum that is assumed to be the transverse momentum of the neutrino from the SM top decay.

The SM top quark candidate is reconstructed under the FCNC single-top quark production hypothesis in the events having one or two jets with exactly one being b -tagged, which is assumed to come from the top quark decay ($t \rightarrow bW$). The lepton not used to reconstruct the Z boson is assumed to be the one coming from W boson decay and the missing transverse momentum is assumed to be the transverse momentum

of the neutrino from W boson decay, while the most probable value for the longitudinal component of the neutrino momentum is determined using the minimisation of the following expression:

$$\chi^2_{tZ} = \frac{(m_{b\ell_W\nu}^{\text{reco}} - m_{t\bar{t}\text{SM}})^2}{\sigma_{t\bar{t}\text{SM}}^2} + \frac{(m_{\ell_W\nu}^{\text{reco}} - m_W)^2}{\sigma_W^2}, \quad (4.2)$$

where $m_{b\ell_W\nu}^{\text{reco}}$ and $m_{\ell_W\nu}^{\text{reco}}$ are the reconstructed masses of the bW and $\ell_W\nu$ systems, respectively. The W boson and SM top quark mass resolutions have been checked in the simulated FCNC tZ production signal samples as well. The values obtained from the FCNC $t\bar{t}$ decay and FCNC tZ production signal samples with left-handed and right-handed couplings are summarised in Table 4.5. Given that the values are compatible within uncertainties between different signal types, for simplicity, values extracted from the FCNC $t\bar{t}$ decay samples are used to reconstruct the SM top quark and the W boson under both FCNC $t\bar{t}$ decay (eq. (4.1)) and FCNC tZ production (eq. (4.2)) hypotheses. However, values for the SM top quark and the W boson from the FCNC tZ production samples were tested to evaluate the effect on the expected limits with no significant impact observed. In fact, the central value for the masses and the widths of the top quark and W boson from Equation (4.2) are the same as in Equation (4.1). Therefore, in the events with two jets, the four-momentum of SM top quark candidate reconstructed under the FCNC single-top quark production signal hypothesis is the same as the one reconstructed under the FCNC $t\bar{t}$ decay signal hypothesis.

Sample	FCNC top		SM top		W	
	μ [GeV]	σ [GeV]	μ [GeV]	σ [GeV]	μ [GeV]	σ [GeV]
LH FCNC $t\bar{t}$ decay	171.0 ± 1.7	11.1 ± 1.4	166.5 ± 1.5	23.2 ± 1.6	80.5 ± 0.8	15.4 ± 0.7
LH FCNC tZ production	-	-	167.6 ± 0.8	20.0 ± 1.0	80.6 ± 0.8	12.9 ± 0.9
RH FCNC $t\bar{t}$ decay	171.0 ± 1.4	11.2 ± 1.2	166.0 ± 0.5	22.9 ± 0.8	80.5 ± 0.8	15.4 ± 0.7
RH FCNC tZ production	-	-	166.5 ± 0.8	23.1 ± 0.6	79.6 ± 0.8	15.6 ± 0.8

Table 4.5: Summary of the mean values (μ) and standard deviations (σ) of the top quarks and W boson invariant mass distributions, obtained from the Bukin fits using the FCNC $t\bar{t}$ decay and FCNC tZ production signal samples with left-handed (LH) and right-handed (RH) couplings. Both tZu and tZc samples are combined. Fit uncertainties are shown.

4.4.3 Signal regions selection

Similarly to the reconstruction of the top quarks, the transverse mass of the W boson can be obtained taking into account the physics objects resulting from its decay. The transverse mass of the W boson, $m_T(\ell_W, \nu)$, is computed from the transverse momentum, $p_T(\ell)$, of the lepton coming from the W boson decay (i.e. the lepton not used for the Z boson reconstruction) and the difference of the azimuth, $\Delta\varphi$,

between that lepton and the missing transverse momentum as

$$m_T(\ell_W, \nu) = \sqrt{2E_T^{\text{miss}} p_T(\ell) \left(1 - \cos(\Delta\phi(E_T^{\text{miss}}, p_T(\ell)))\right)}. \quad (4.3)$$

The selection of larger values of the transverse mass of the W boson is particularly useful for the production channel since it allows a considerable decrease of the contribution of background processes as $Z+\text{jets}$ production.

The main difference between the production and decay modes is the multiplicity of jets. While the production channel is characterised mainly by one or two jets in the final state, the final state of the decay channel contains at least two jets. It should be noticed that the signal region focused on the production mode considers the events with one and two jets while the signal region for the decay mode takes the events with at least two jets, complemented by further cuts on the masses of the reconstructed FCNC top quark. From the study of the distribution of the different variables, the production mode has the main contribution from the events with exactly one jet but still has an important fraction from the events with two jets, as can be seen in Figure 4.4(c). Therefore, the separation of the events with one or two jets (SR2) and at least two jets (SR1) was pursued for the signal regions in order to take the best advantages from the two modes. Along with the top quark masses requirements, these signatures of the jet multiplicity enable the separation of the FCNC signal hypotheses into two orthogonal signal regions. The multiplicity of the b -tagged jets is the same for the two signal regions since exactly one bottom quark coming from the decay of the SM top quark is expected for both channels.

Following the implementation of the selection of the signal events, the event yields in the two signal regions indicated that the main background for the signal region focused on the decay mode, denominated as SR1, are $t\bar{t}Z$ and diboson processes while for the signal region targeting the production mode, called SR2, are the SM tZq and diboson production, as shown in Table 4.6. The event yields in Table 4.6 presents the contribution from the diboson production separated into light-flavour (LF) and heavy-flavour (HF) depending on the type of jets associated. Several distributions of important variables for both signal regions after the event selection are shown in Figure 4.3 and Figure 4.4. In the plots and tables of this thesis, some background sources are grouped together due to its small contribution to the event yields for all regions. In particular, the label *Other fakes* represents $Z+\text{jets}$, VV (2ℓ) and $t\bar{t}Z$ (2ℓ) processes, while the label *Other* corresponds to VH , $t\bar{t}WW$, VVV , $t\bar{t}t$ and $t\bar{t}t\bar{t}$ processes. For the SR1 case in Figure 4.3, the distributions of the transverse momentum of the leading lepton, b -tagged jet and Z boson candidate and the transverse mass of the W boson are shown, in which the signal kinematics are similar to the considered background processes. However, the distributions of the jet multiplicity and the mass of the SM top quark present the different characteristics between the signal and the background. In specific for the jet multiplicity, it can be seen that the distinct background processes have more jets than the FCNC tZu and tZc signals. As expected, the major contribution from signal comes from the $t\bar{t}$ decay processes compared with the amount of signal events of the production mode. Concerning the SR2 case in

Figure 4.4, significant differences between the signal and background can be seen in all the distributions. The transverse momentum of the leading lepton, b -tagged jet and Z boson candidate are found to have larger values than the background processes. The mass of the SM top quark, transverse mass of the W boson and the jet multiplicity have a similar distribution for signal and background. It should be noticed that, for this specific signal region (SR2), the fraction of events from the FCNC tZu production mode is significantly larger than the one from FCNC tZc production signal. Such result arises from the difference of an order of magnitude on the cross-sections of both signal hypotheses.

An established strategy on particle physics denominated *blinding strategy* is implemented on data analyses to not bias the selection and consequently the final result. In this approach, the data measurements (in the distributions and in the yields count) are not represented in the regions dominated by the signal until the background prediction is well modelled and understood. The blinded regions considered in this analysis were the signal regions for both production and decay modes. The data measurements were considered in the blinded region in order to test the signal hypothesis only after the background prediction was completely understood in the unblinded regions (validation and control regions).

Process	Decay signal region (SR1)	Production signal region (SR2)
$t\bar{t}Z$	169 ± 22	25 ± 5
tWZ	35 ± 13	10 ± 4
$t\bar{t}W$	6.7 ± 3.4	3.6 ± 1.8
$t\bar{t}H$	7.7 ± 1.2	0.95 ± 0.18
$VV+LF$	29 ± 13	33 ± 12
$VV+HF$	150 ± 70	160 ± 70
tZq	50 ± 8	113 ± 19
$t\bar{t}$	21.2 ± 3.1	33 ± 11
Wt	0.50 ± 0.27	0.4 ± 1.2
$Z+jets$	11 ± 11	9 ± 9
VH	1.2 ± 0.9	2.4 ± 2.9
$t\bar{t}WW$	0.46 ± 0.25	0.03 ± 0.05
VVV	0.8 ± 0.4	0.58 ± 0.30
$t\bar{t}t\bar{t}$	0.22 ± 0.11	0.0021 ± 0.0022
$t\bar{t}t$	0.030 ± 0.016	0.0019 ± 0.0015
$t\bar{t}Z (2\ell)$	0.05 ± 0.06	0.021 ± 0.026
$VV (2\ell)$	0.5 ± 0.5	0.13 ± 0.19
FCNC (u) tZ	13.2 ± 2.1	52.5 ± 2.8
FCNC $t\bar{t}$ (uZ)	63 ± 5	10.6 ± 1.5
FCNC (c) tZ	3.6 ± 0.6	12.2 ± 0.9
FCNC $t\bar{t}$ (cZ)	76 ± 6	18.5 ± 1.9
Total background	480 ± 80	390 ± 70

Table 4.6: Event yields for signal and background processes in the signal regions. The error corresponds to the statistical uncertainties from the MC simulation.

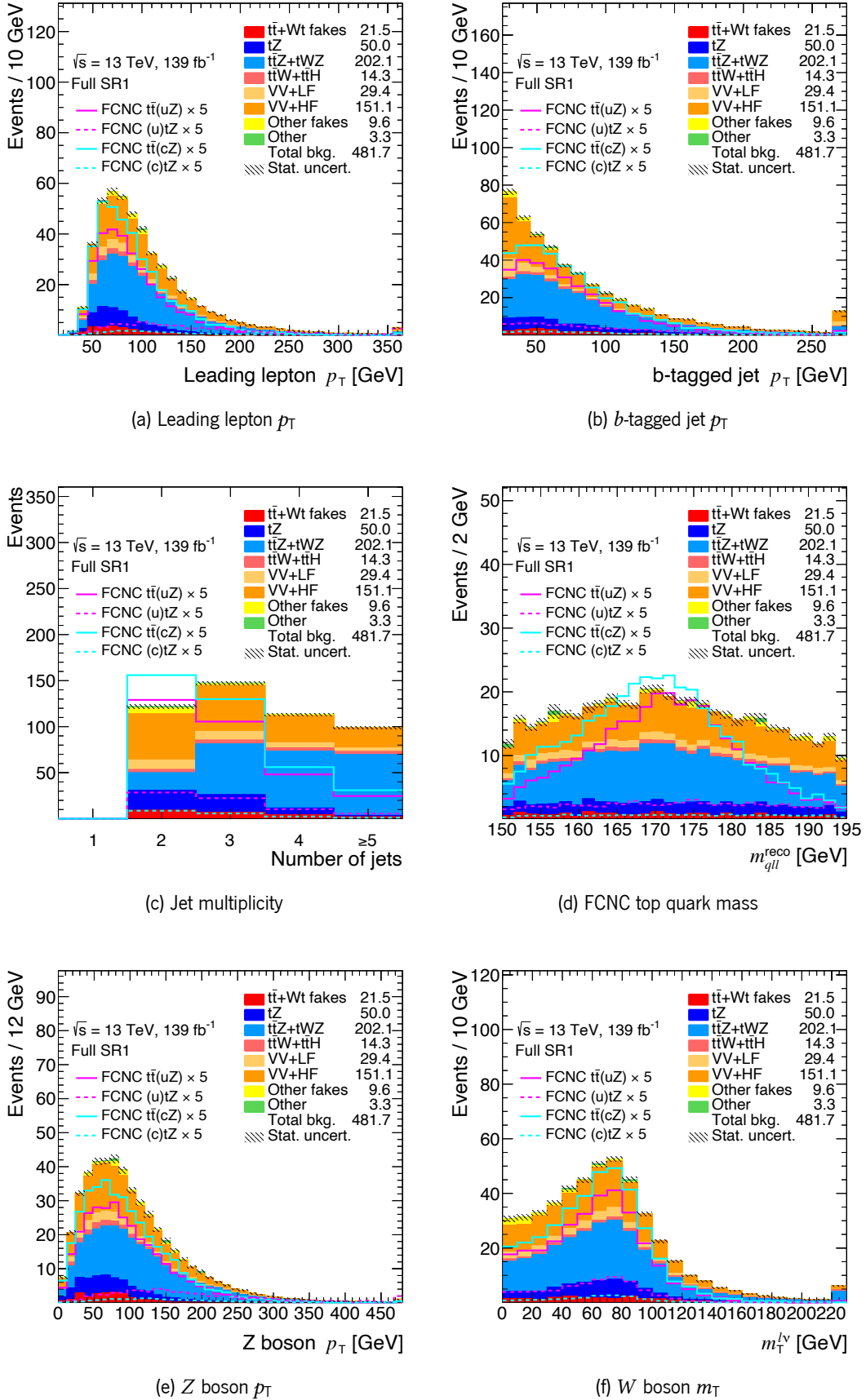


Figure 4.3: Distributions of distinct variables in the SR1 region. The uncertainty band includes only the statistical uncertainty from the MC simulation.

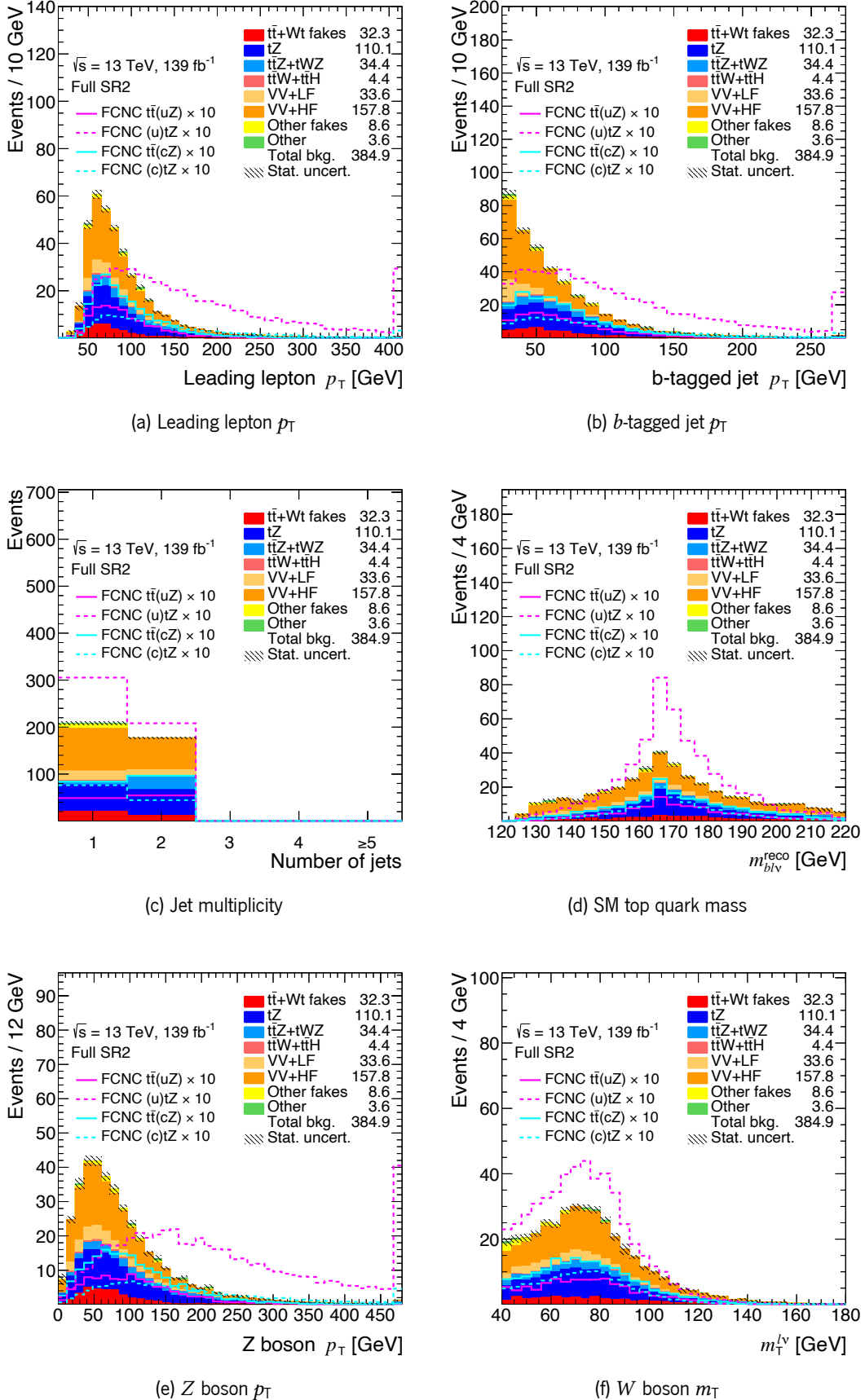


Figure 4.4: Distributions of distinct variables in the SR2 region. The uncertainty band includes only the statistical uncertainty from the MC simulation.

4.5 Comparison of data and Monte Carlo prediction

The detailed study of the level of agreement between the signal and background prediction and the data is crucial in particle physics analyses. The background processes considered in this search are the processes containing three reconstructed leptons in the final state, which can be real or fake leptons.

The main background sources after the signal regions selection are: $t\bar{t}Z$, diboson and SM tZq production processes. The $t\bar{t}Z$ process enters the event selection because of the presence of a SM top quark and of a Z boson in the final state. The only difference to the signal topology, for the semileptonic $t\bar{t}$ decay, is the presence of additional jets in the event. The diboson background (mainly WZ and ZZ production) enters the selection because of the presence of a Z boson and of additional jets, that can come from heavy quarks. As briefly discussed in the previous section, the diboson background is split into $VV+HF$ (heavy flavour) and $VV+LF$ (light flavour) based on the types of jets associated: if one of the associated jets originated from b -quark or c -quark then it is considered as $VV+HF$, otherwise it is considered as $VV+LF$. The jet type is determined using the `jet_truthflav` variable, the result of an algorithm which starts by defining a cone of $\Delta R < 0.3$ associated with each jet. If a b -hadron, with $p_T > 5 \text{ GeV}$, is found within this cone the jet is identified as a b -jet. If no b -hadrons are found, the algorithm searches for c -hadrons, then τ leptons. If none of these identifiers are found the jet is labeled as a light jet. Besides the requirement of the number of leptons, the jet multiplicity plays a major role in the selection since the different background processes can be split in the control regions introduced below. Therefore, the main distinction of the targetted selections are the number of jets and b -tagged jets and, simultaneously, it should be closer enough to the signal regions in order to correctly evaluate the kinematics of the various reconstructed objects. With that goal, two control regions focused on the $t\bar{t}$ and $t\bar{t}Z$ backgrounds with different jet multiplicity while the remaining take the events with the reconstructed top quark masses not considered in the signal regions.

The estimation of the main background processes for both signal regions was done through the definition of several control and validation regions. The data and MC prediction of different distributions and yields from the control regions are compared and later used in the combined fit with the signal region. Therefore, the addition of control regions to the event selection allows a tighter constraint of background expectations and systematic uncertainties for the statistical analysis. An important check is the definition of validation regions that are not included in the fit having the goal of validating the fit procedure in an independent way. The analysis described in this thesis is characterised by four control regions, discussed in this chapter, and two validations regions, obtained by cutting on the output of the multivariate analysis discriminants on the full signal regions and described in detail later in Section 4.6. The selection requirements applied in the control regions defined are summarised in Table 4.7. The expected and observed event yields in the control regions can be found in Table 4.8.

Control regions definition			
Common selections			
Exactly 3 leptons with $ \eta < 2.5$ and $p_T(\ell_1) > 27 \text{ GeV}$, $p_T(\ell_2) > 15 \text{ GeV}$, $p_T(\ell_3) > 15 \text{ GeV}$			
$t\bar{t}$ CR	$t\bar{t}Z$ CR	Side-band CR1	Side-band CR2
≥ 1 OS pair, no OSSF	≥ 1 OSSF pair $ m_{e\ell} - 91.2 \text{ GeV} < 15 \text{ GeV}$	≥ 1 OSSF pair $ m_{e\ell} - 91.2 \text{ GeV} < 15 \text{ GeV}$	≥ 1 OSSF pair $ m_{e\ell} - 91.2 \text{ GeV} < 15 \text{ GeV}$
-	-	-	$m_T(\ell_W, v) > 40 \text{ GeV}$
≥ 1 jet with $ \eta < 2.5$ = 1 b -jet	≥ 4 jets with $ \eta < 2.5$ = 2 b -jets	≥ 2 jets with $ \eta < 2.5$ = 1 b -jet	= 1 jet with $ \eta < 2.5$ = 1 b -jet
-	-	$ m_t^{\text{FCNC}} - 172.5 \text{ GeV} > 2\sigma^{\text{FCNC}}$ $ m_t^{\text{SM}} - 172.5 \text{ GeV} > 2\sigma^{\text{SM}}$	-
-	-	$ m_t^{\text{SM}} - 172.5 \text{ GeV} > 2\sigma^{\text{SM}}$	-

Table 4.7: Overview of the requirements applied for selecting events in the control regions.

Control region for $t\bar{t}$ background: Region designed to control the minor $t\bar{t}$ background. The $t\bar{t}$ production enters the selection due to the presence of a fake lepton. While the normalisation is taken from data, the definition of a control region focused on the $t\bar{t}$ production allows a more consistent evaluation of this background process. The $t\bar{t}$ CR is defined by requiring, as for all regions, three leptons and at least one pair of opposite-sign but different-flavour leptons in the event. Therefore, no cut on the invariant mass of the opposite-sign leptons is applied. Concerning the jet multiplicity, there should be at least one jet in the event, of which exactly one should be b -tagged. The distributions of the transverse momentum of the leading lepton and the jet multiplicity can be found in Figure 4.5.

Control region for $t\bar{t}Z$ background: Region defined to control the main background of the decay signal region (SR1): the $t\bar{t}Z$ production. The selection is constructed by requiring the presence of more jets with respect to the jet multiplicity required in the signal regions. The $t\bar{t}Z$ CR is defined by requiring the presence of at least four jets and exactly two b -tagged jets. The distributions of the transverse momentum of the leading lepton and the transverse momentum of the b -tagged jet can be found in Figure 4.6.

Side-band control regions: Control regions designed to contain a mixture of the main background sources ($t\bar{t}Z$ and diboson production). Two distinct selections are performed reverting the mass cuts for both signal regions described in Table 4.4. The mass side-band CR1 is defined with the same event selection as the SR1 with the only difference being that the mass of the FCNC top quark candidate, m_t^{FCNC} , must be outside $2\sigma^{\text{FCNC}}$ from 172.5 GeV, and the mass of the SM top quark candidate, m_t^{SM} , must be also outside $2\sigma^{\text{SM}}$ from 172.5 GeV. The distributions of the transverse momentum of the b -tagged jet and the mass of the FCNC top quark candidate can be found in Figure 4.7. The mass side-band CR2 is defined with the same event selection as the SR2 with the only difference being that the mass of the SM top quark candidate, m_t^{SM} , must be also outside $2\sigma^{\text{SM}}$ from 172.5 GeV. The distributions of the transverse momentum of the b -tagged jet and the mass of the SM top quark candidate can be found in Figure 4.8.

Process	Side-band CR1	Side-band CR2	$t\bar{t}Z$ CR	$t\bar{t}$ CR
$t\bar{t}Z + tWZ$	96 ± 16	7.6 ± 1.3	227 ± 31	14.8 ± 2.0
$t\bar{t}W$	4.6 ± 2.3	2.2 ± 1.1	3.1 ± 1.6	27 ± 13
$t\bar{t}H$	2.5 ± 0.4	0.31 ± 0.07	7.5 ± 1.2	13.8 ± 2.2
$VV+LF$	27 ± 12	12 ± 4	0.25 ± 0.21	0.39 ± 0.29
$VV+HF$	130 ± 60	51 ± 17	18 ± 12	2.3 ± 1.0
tZq	20 ± 4	6.2 ± 1.3	20 ± 5	0.89 ± 0.18
$t\bar{t} + Wt$	10.2 ± 2.2	7.7 ± 2.0	4.8 ± 1.3	103 ± 17
Other fakes	4 ± 5	2.8 ± 3.5	0.24 ± 0.32	0.12 ± 0.14
Other	3.2 ± 2.8	0.7 ± 0.6	1.8 ± 1.0	2.9 ± 1.5
FCNC (u) tZ	5.0 ± 0.6	2.26 ± 0.27	1.2 ± 0.4	0.65 ± 0.10
FCNC $t\bar{t}$ (uZ)	1.8 ± 0.5	0.44 ± 0.20	1.41 ± 0.25	0.23 ± 0.05
Total background	300 ± 70	90 ± 18	280 ± 40	165 ± 22
Data	340	104	285	156
Data / Bkg.	1.13 ± 0.27	1.15 ± 0.26	1.01 ± 0.14	0.94 ± 0.15

Table 4.8: The expected and observed event yields in the background control regions. The error includes the uncertainty associated with the statistics.

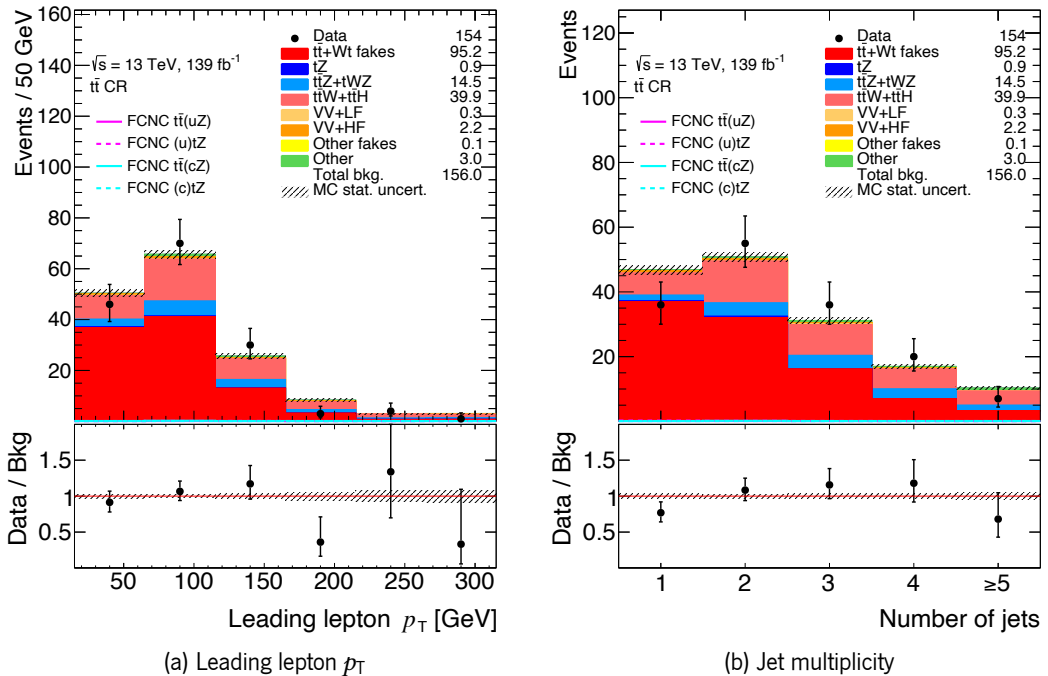


Figure 4.5: Expected and observed distributions in the $t\bar{t}$ control region for (a) leading lepton transverse momentum and (b) jet multiplicity.

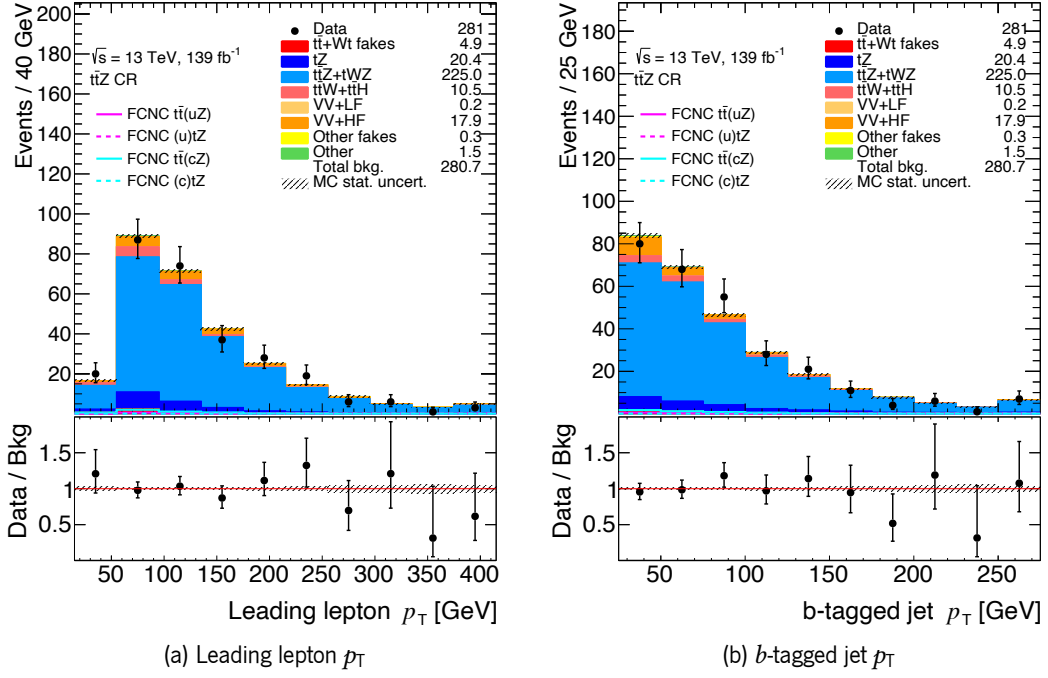


Figure 4.6: Expected and observed distributions in the $t\bar{t}Z$ control region for (a) leading lepton transverse momentum and (b) b -tagged jet transverse momentum.

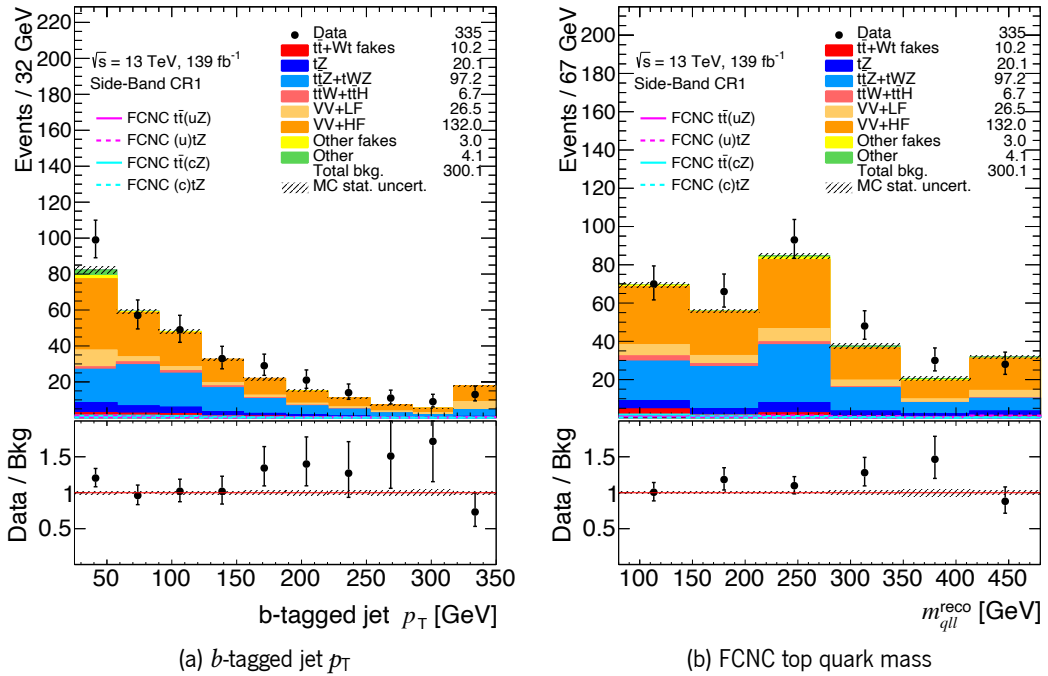


Figure 4.7: Expected and observed distributions in the side-band control region 1 for (a) b -tagged jet transverse momentum and (b) reconstructed FCNC top quark mass.

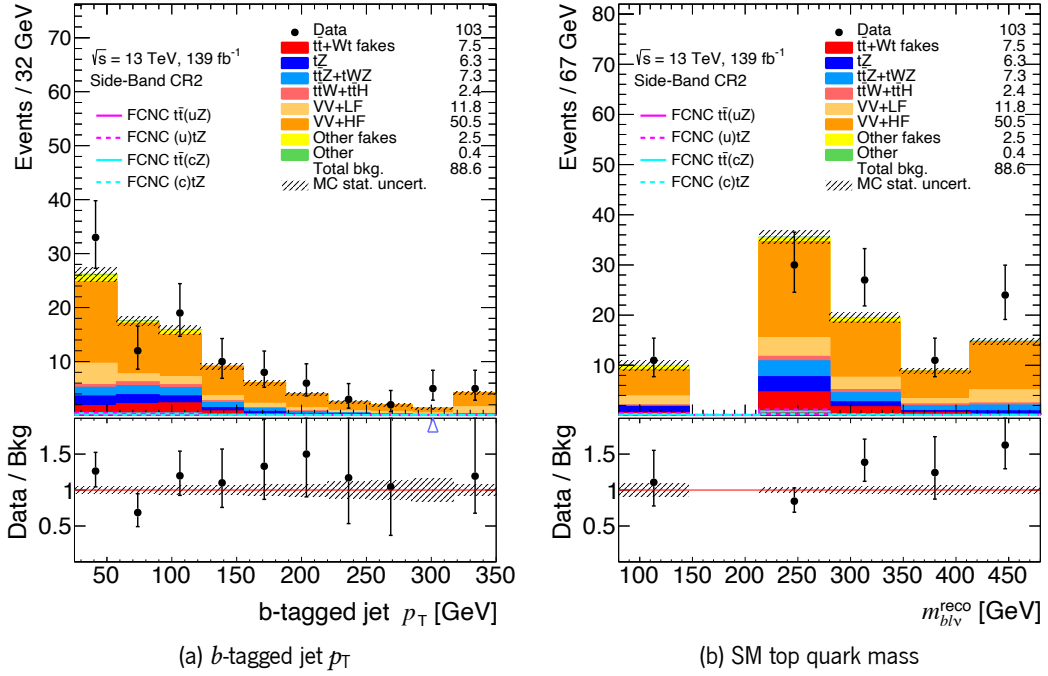


Figure 4.8: Expected and observed distributions in the side-band control region 2 for (a) b -tagged jet transverse momentum and (b) reconstructed SM top quark mass.

4.5.1 Fake composition

Despite the high levels of accuracy achieved by the ATLAS simulation and the lepton reconstruction and identification algorithms, sources of misidentified reconstructed leptons still exist and can lead to an additional source of backgrounds to the analysis. These leptons can arise from the decay of a bottom or charm hadron, an electron from a photon conversion, a jet misidentified as an electron or a muon produced from an in-flight decay of a pion or kaon and can be split into two categories:

- **Non-prompt leptons**

Genuine leptons are identified but such leptons are not originated from the primary pp hard-scattering interaction process;

- **Fake leptons**

Cases in which signal in the ATLAS detector are selected as being leptons when in fact there is no real lepton present. An example would be a jet leaving an energy cluster in the electromagnetic calorimeter and then misidentified as a lepton.

The estimation of the fakes contribution is a crucial step for all the analyses since the contribution from these fake background processes can lead to an incorrect expectation of the remaining background rates. Since this analysis considers a final state with exactly three leptons, the fakes processes come mainly

from $t\bar{t}$ and Z +jets production where only two leptons should be expected. The estimation for the various sources of background relies on MC simulations, for both the normalisation and the shape, while for the $t\bar{t}$ fake-lepton background the shapes are taken from MC but the normalisation is extracted from data. Contrarily, an estimation on the Z +jets is not needed since its contribution is minimal after the requirement on the transverse mass of the W boson applied in the production signal region (SR2).

Therefore, the focus of the fakes estimation was the $t\bar{t}$ background. The origin of the three leptons from $t\bar{t}$ events was studied through the `MCTruthClassifier` tool [164], in order to estimate the contribution from the fake leptons and eventually define an uncertainty to take into account the different sources in the signal and control regions. Using information from the truth particles of the MC simulation samples available, the origin of the different particles of the final state can be studied in detail. Several categories of origin and types of particles can be identified with this tool, being an overview of the flowchart represented in Figure 4.11. For the case of this search, the origin of the leptons from $t\bar{t}$ events in different jet multiplicities is shown in Figures 4.9 to 4.14. As it can be seen, apart from the leptons for which the particle mother is the top quark (66 % of the leptons in each event), the fake leptons come either from photon conversions (around 5-10 %, depending on the region) or from b -hadrons (around 20-30 %, depending on the region and jet multiplicity). A few differences can be noticed for the photon conversion and b -hadron fractions in the signal regions with respect to the $t\bar{t}$ control region where the $t\bar{t}$ background is controlled. To take into account these differences, a systematic uncertainty with values varying for the different jet multiplicities was considered.

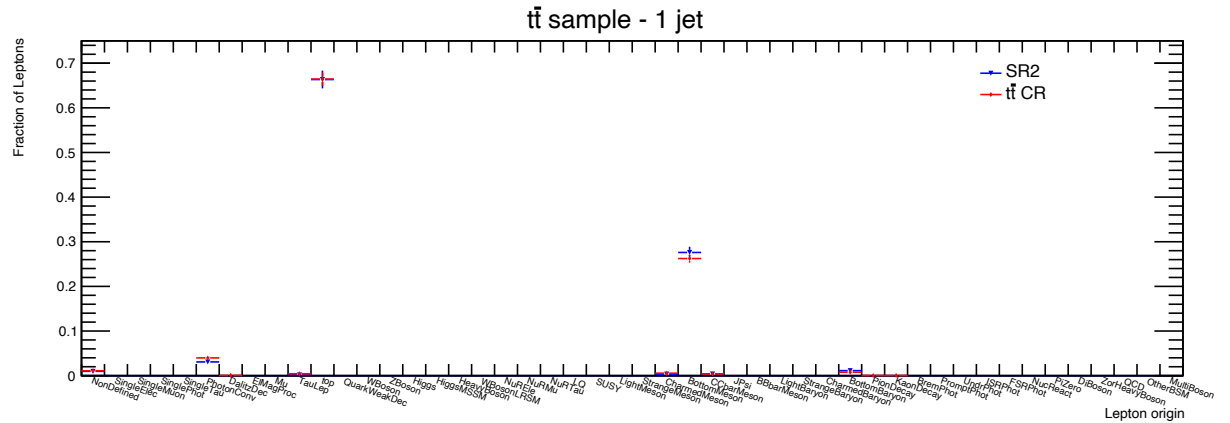


Figure 4.9: Origin of the three leptons from $t\bar{t}$ events with 1 jet in the SR2 and $t\bar{t}$ CR.

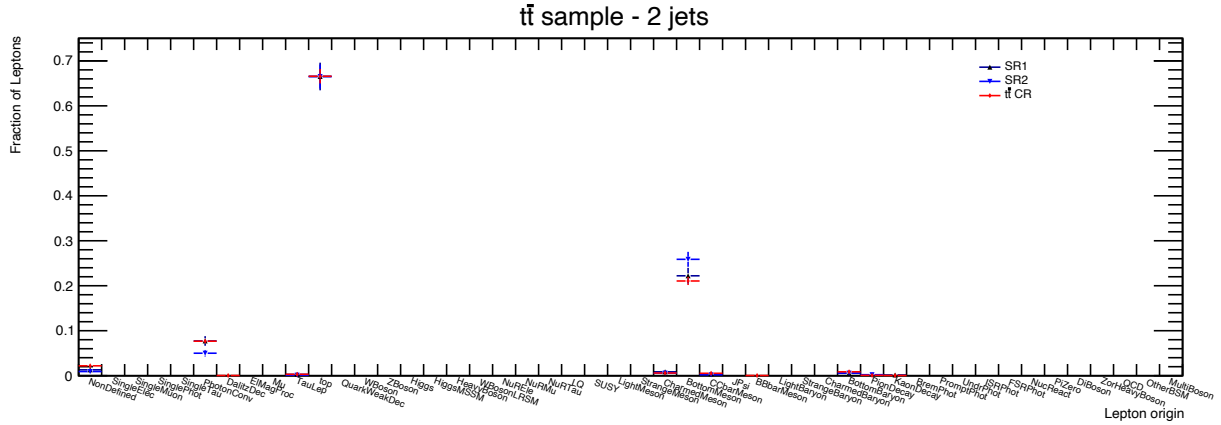
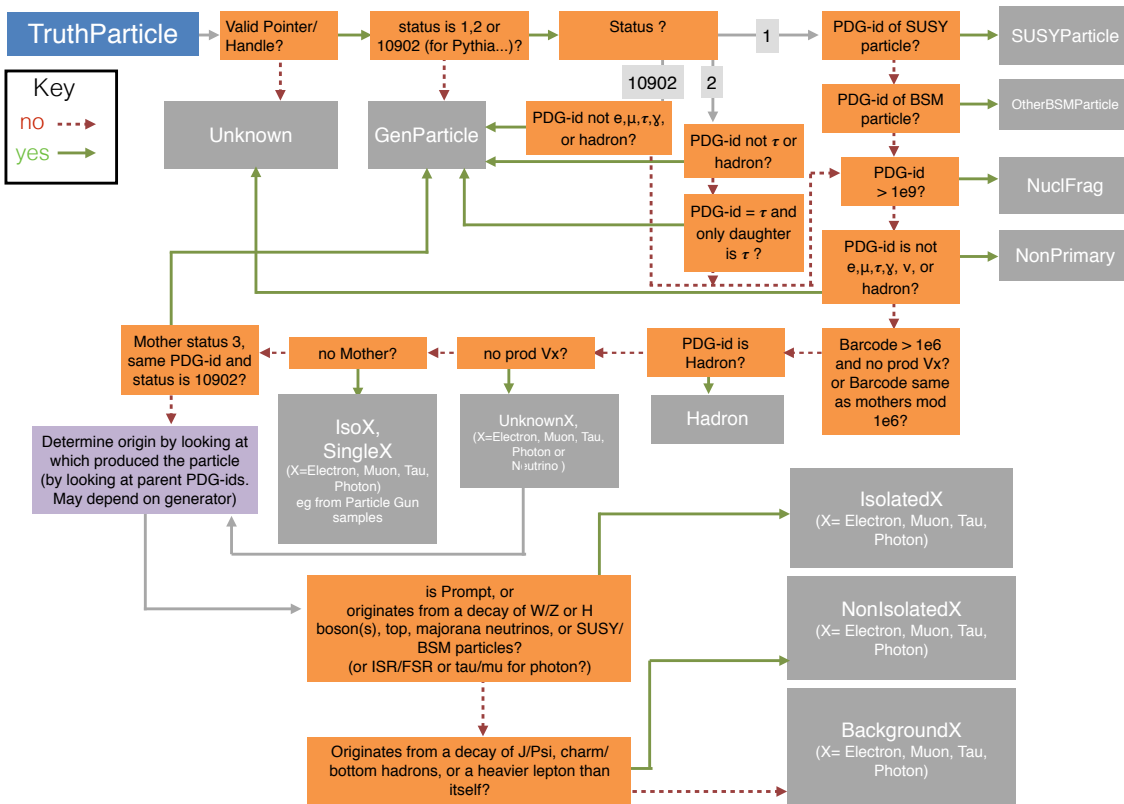

 Figure 4.10: Origin of the three leptons from $t\bar{t}$ events with 2 jets in the SR1, SR2 and $t\bar{t}$ CR.


Figure 4.11: Overview of the classification scheme of the MCTruthClassifier tool [164].

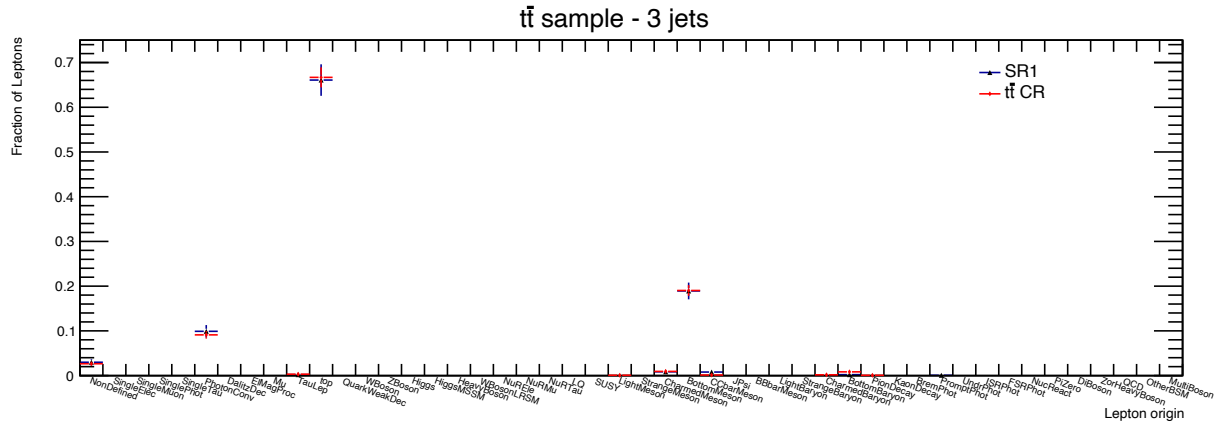


Figure 4.12: Origin of the three leptons from $t\bar{t}$ events with 3 jets in the SR1 and $t\bar{t}$ CR.

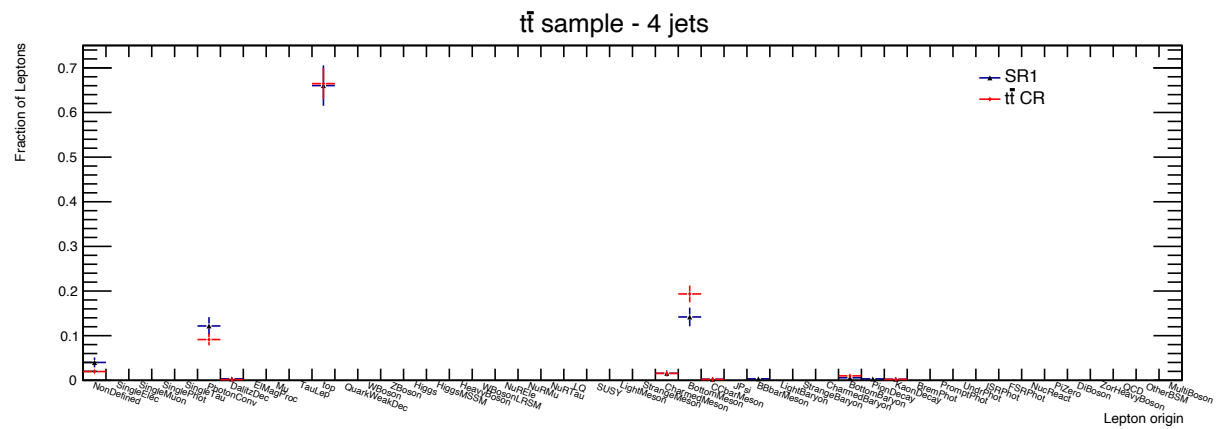


Figure 4.13: Origin of the three leptons from $t\bar{t}$ events with 4 jets in the SR1 and $t\bar{t}$ CR.

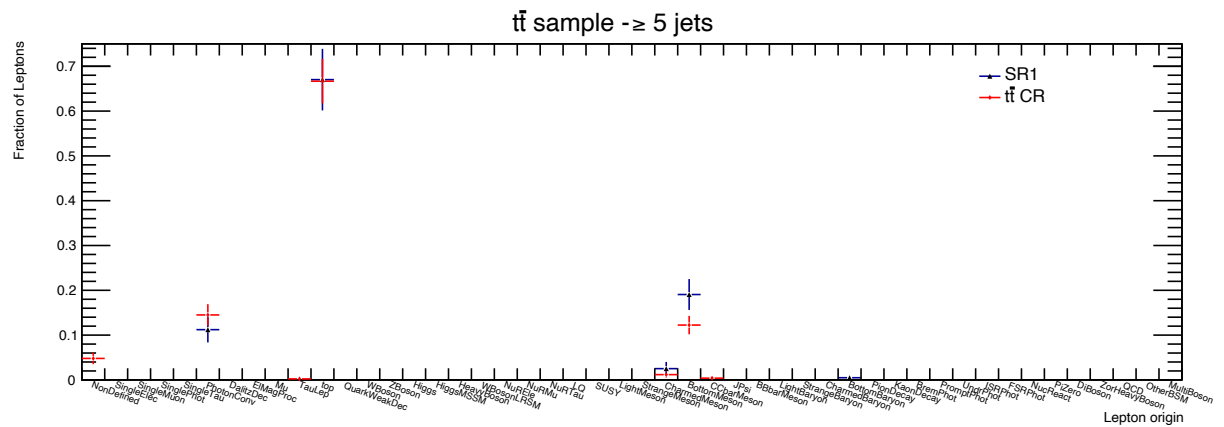


Figure 4.14: Origin of the three leptons from $t\bar{t}$ events with ≥ 5 jets in the SR1 and $t\bar{t}$ CR.

4.6 Boosted decision trees

A good signal to background discrimination allows the fit to correctly characterise the signal kinematics and also to better estimate the main backgrounds contributions. The choice of a single variable exhibiting a clear separation power among signal and background events can be a demanding part of a analysis since several performance studies should be performed for the different variables considered as the discriminant one. Since the search for small signals in large data sets is an important characteristic of the high energy physics, it is essential to extract the maximum of the available information from the data. Taking this into account, multivariate (MVA) classification methods based on machine learning techniques have become a fundamental ingredient to most analyses in this field. The use of MVA aims to take the most out of the input while exploring correlations among different variables to distinguish sinal events from background ones. Boosted Decision Trees (BDT) are a set of binary structured decision trees that use the *boosting* technique, being among the most used machine learning techniques in physics. Decision trees were formalised and developed by Breiman [165] in the context of pattern recognition and data mining. They extend a simple cut-based analysis into a multivariate technique by continuing to analyse events that fail a particular criteria until they satisfy a termination condition as follows. BDTs are trained using decision trees, which are binary tree networks for data categorisation that classify events between signal and background. The decision tree starts from a root node that contains all the events and grows successive layers formed by binary nodes. At each node, a cut on a particular discriminating variable, x_i , is applied to split the data. When a node is generated, the variable and the cut value that can achieve the best separation among signal and background is selected. Each event starts from the root node and goes down the decision tree. The output of the decision tree classifies the events more signal-like or more background-like based on the distributions of signal and background for all the observables given as input. The *boosting* technique is a way of enhancing the classification and regression performance of tipically weak MVA methods, while increasing the stability with respect to statistical fluctuations in the training sample. Such improvement is possible by sequentially applying an MVA algorithm to reweighted versions of the training data and afterwards taking a weighted majority vote of the sequence of MVA algorithms thus produced. Boosting stabilises the response of the decision trees with respect to fluctuations in the training sample and is able to considerably enhance the performance w.r.t. a single tree. An option of boosting method is the gradient boosting [166, 167], which adjusts weights of the decision trees to minimise the deviation between the model response $F(x)$ and the true value y obtained from the training sample. The Gradient Boosted Decision Trees (GBDT) method with TMVA software package is exploited in this study [166, 167]. Due to its simplicity and less susceptibility to overtraining, GBDT is chosen over the other more sophisticated classifiers (like neural networks). The GBDT output score is in the range between -1 and 1. The most signal-like events have scores near 1 while the most background-like events have scores near -1.

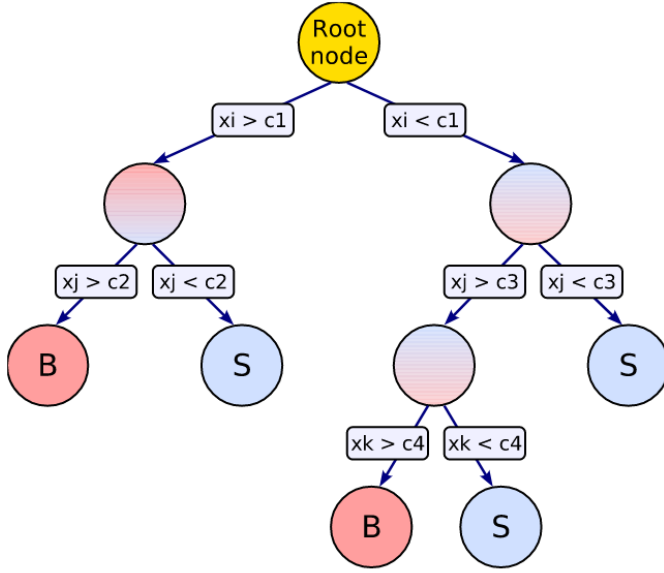


Figure 4.15: Schematic view of a decision tree where, starting from the root node, a sequence of binary splits using the discriminant variables (x) are split into smaller regions. The leaf nodes at the bottom end of the tree are labeled as S for signal and B for background depending on the majority of events that end up in the respective nodes [167].

4.6.1 Discriminant definitions

The goal of a multivariate technique such as the GDBT method is the definition of a discriminant built as result of the combination of several variables obtained from a specific selection. Since this search aims both the production and decay modes with the FCNC tZq anomalous coupling, the initial idea was to build two distinct discriminants, one for each case, due to the differences on the kinematics of the reconstructed objects. However, the final strategy was to have three discriminants: one for the decay mode, another for the production mode with tZu and the final one for the production mode with tZc . Taking this separation into account, the events passing the signal regions are considered in the training of the discriminants. In the decay signal region (SR1), for both tZu and tZc coupling search, the expected contribution from FCNC $t\bar{t}$ decay signal is significantly higher than the one from FCNC tZ production signal. Given the kinematics difference between FCNC tZq decay and production signals, the GBDT is trained with only FCNC $t\bar{t}$ decay signal against backgrounds. Since the kinematics of FCNC $t\bar{t}$ decay events for tZu and tZc couplings are similar, the decay signal samples with both couplings are combined to train the GBDT. The signal processes not entering as signal in the different discriminants are not considered in the training. Consequently, a single MVA discriminant, D_1 , is built for both tZu and tZc coupling searches in SR1. The production signal region (SR2) is particularly sensitive to the tZu coupling in FCNC tZ production events. Therefore, the corresponding MVA discriminant, D_2^u , is built using the GBDT trained with FCNC tZu in single-top production events against backgrounds. Despite the lower sensitivity to the tZc coupling in SR2, it is used in combination with SR1 in the search for tZc coupling. In the total expected tZc signal

yield, the contributions from FCNC $t\bar{t}$ decay and from tZc production signal events are comparable. Taking this into account, the MVA discriminant for tZc coupling, D_2^C , is built using the GBDT trained with the total tZc signal events against backgrounds. Table 4.9 summarises built GBDT discriminant variables, corresponding training regions, signal samples and couplings that are searched using each discriminant.

GBDT discriminant	Training Region	Training signal	Search coupling
D_1	Full SR1	FCNC tZu and tZc in $t\bar{t}$ decays	tZu, tZc
D_2^U	Full SR2	FCNC tZu in tZ production	tZu
D_2^C	Full SR2	FCNC tZc in $t\bar{t}$ decays and tZ production	tZc

Table 4.9: Summary of the GBDT discriminant variables with their training regions, signal samples and search coupling.

4.6.2 Input variables

The GBDT method uses the distributions of a set of variables from the events passing each signal region. The definition of the most important variables to be considered represents an essential step for the construction of the discriminants. After the definition for each discriminant, a set of variables is used as the input to train and test the GBDT method on the events in each signal region. Many input variables can be considered to train the BDT. However, the ones that do not have significant impact on the BDT performance should be removed since they could introduce instability in the BDT output when considering systematic uncertainties. The strategy is to remove variables that have relatively low values of separation and strong correlations with other variables, without significant loss of the BDT performance. As a starting point, all the variables of the final objects (reconstructed top quarks, Z boson, b -tagged jet, among others) are considered as input of the discriminant, which enables the evaluation of the power of separation from each variable to the final result. The separation power of a variable is defined by, as in [167],

$$\langle s^2 \rangle = \frac{1}{2} \int \frac{[p_s(y) - p_b(y)]^2}{p_s(y) + p_b(y)} dy$$

where $p_s(y)$ and $p_b(y)$ are the signal and background PDFs of the classifier y . The separation is 0 (1) for identical (non-overlapping) signal and background shapes. The separation of the full set of variables to built the D_2^U discriminant used in SR2 tZu signal region is shown in Table 4.10, concluding that the best separation power comes from a set of seven variables characterised by a separation higher than 0.1. In any case, the correlation between the different variables in the full set should be considered. If two variables highly correlated are included as input to the GBDT, similar information will be used to construct the discriminant while twice the computational usage will remain. The second step to the definition of the final set of input variables consist of a closer investigation of the correlation matrix of the full set of variables for signal and background events. Figure 4.16 shows the correlation matrices for signal and

background events considered in the training in SR2 to built the D_2^u discriminant used in tZu coupling search. The $p_T^{\ell_1}$, $p_T^{\ell_2}$, $p_T^{\ell_3}$ and p_T^W variables have high correlations with p_T^Z which has better separation value, so that they are removed as well as E_T^{miss} which is highly correlated with p_T^W and having lower separation value. Finally, the impact on the GBDT performance is studied through a comparison on the $S_{\text{eff}}/\sqrt{B_{\text{eff}}}$ ratio between the full set and the final set of variables. Figure 4.17 represent the $S_{\text{eff}}/\sqrt{B_{\text{eff}}}$ ratio for the full set and the final set of variables as a function of the cut on the GBDT output score. After a thorough study of several possibilities for the final set of input variables, the goal of having a minimal difference on the maximum $S_{\text{eff}}/\sqrt{B_{\text{eff}}}$ with a minimal set of used variables was reached. The maximum value of $S_{\text{eff}}/\sqrt{B_{\text{eff}}}$ is 2.531 ± 0.091 for the "full set" of input variables, while 2.205 ± 0.145 for the final set of input variables. Based on the separation values, correlations and impact on the BDT performance, a final set of input variables is defined with a total of 6 variables: transverse momentum of the b -quark and Z boson candidates, mass of the SM top quark, χ^2 from the kinematic fit under the tZ production signal hypothesis and ΔR between the b -quark and Z boson candidates and between the W boson lepton and Z boson candidate. Similar studies on the separation, correlation and GBDT performance for the full set and final set of variables were performed for the discriminants used in SR1 (to built D_1) and in SR2 with tZc coupling (to built D_2^c), being documented in Appendix A. The final set of input variables for each discriminant are listed in Table 4.12, ordered by the separation value. The distributions of the final set of input variables for the three discriminants in the signal regions are presented in Figure 4.18 and Figure 4.19.

Variable	$\langle s^2 \rangle$	Definition
p_T^Z	0.3104	Z boson candidate transverse momentum
$p_T^{\ell 1}$	0.2603	Leading lepton p_T
$H_T(l, j)$	0.1899	Scalar sum of p_T of leptons and jets
p_T^b	0.175	b -quark candidate transverse momentum
p_T^W	0.1234	W boson candidate transverse momentum
$p_T^{\ell 2}$	0.1192	Sub-leading lepton p_T
E_T^{miss}	0.1086	Missing transverse energy
$\Delta R(b, Z)$	0.08017	ΔR between b -quark and Z boson candidates
$p_T^{\ell 3}$	0.05949	Third lepton p_T
$m_{b\ell\nu}$	0.04636	SM top-quark candidate mass
χ_{tZ}^2	0.03171	χ^2 from the kinematic fit under the tZ production signal hypothesis
$\Delta R(\ell, Z)$	0.024	ΔR between W boson lepton and Z boson candidates
$m_{\ell\nu}$	0.01949	W boson candidate mass
$\eta^{\ell 1}$	0.009613	Leading lepton η
η^b	0.004479	b -quark candidate pseudorapidity
$\eta^{\ell 2}$	0.002749	Sub-leading lepton η
$\eta^{\ell 3}$	0.002044	Third lepton η

Table 4.10: Full set of variables considered in the training of the GBDT in SR2 to built the D_2^u discriminant used in tZu coupling search. Variables are ordered by the separation $\langle s^2 \rangle$ value.

Variable	$\langle s^2 \rangle$	Definition
p_T^Z	0.3104	Z boson candidate transverse momentum
p_T^b	0.175	b -quark candidate transverse momentum
$\Delta R(b, Z)$	0.08017	ΔR between b -quark and Z boson candidates
$m_{b\ell\nu}$	0.04636	SM top-quark candidate mass
χ_{tZ}^2	0.03171	χ^2 from the kinematic fit under the tZ production signal hypothesis
$\Delta R(\ell, Z)$	0.024	ΔR between W boson lepton and Z boson candidates

Table 4.11: Final set of input variables considered in the training of the GBDT in SR2 to built the D_2^u discriminant used in tZu coupling search. Variables are ordered by the separation $\langle s^2 \rangle$ value.

SR1 Variable	$\langle s^2 \rangle$	SR2 tZu		SR2 tZc	
		Variable	$\langle s^2 \rangle$	Variable	$\langle s^2 \rangle$
$m_{b\ell\nu}$	0.1364	p_T^Z	0.3104	p_T^Z	0.07408
p_T^q	0.07345	p_T^b	0.175	p_T^b	0.05261
N_{jets}	0.05747	$\Delta R(b, Z)$	0.08017	$m_{b\ell\nu}$	0.02282
$m_{q\ell\ell}$	0.04173	$m_{b\ell\nu}$	0.04636	$\Delta R(b, Z)$	0.02143
$\Delta R(t_{\text{SM}}, t_{\text{FCNC}})$	0.0410	χ_{tZ}^2	0.03171	χ_{tZ}^2	0.01561
$\Delta R(\ell, Z)$	0.02441	$\Delta R(\ell, Z)$	0.024	$\Delta R(\ell, Z)$	0.008783

Table 4.12: Set of variables used in the training of the GBDT in the signal regions to built the discriminants used in the tZu and tZc coupling searches. Variables are ordered by the separation $\langle s^2 \rangle$ value.

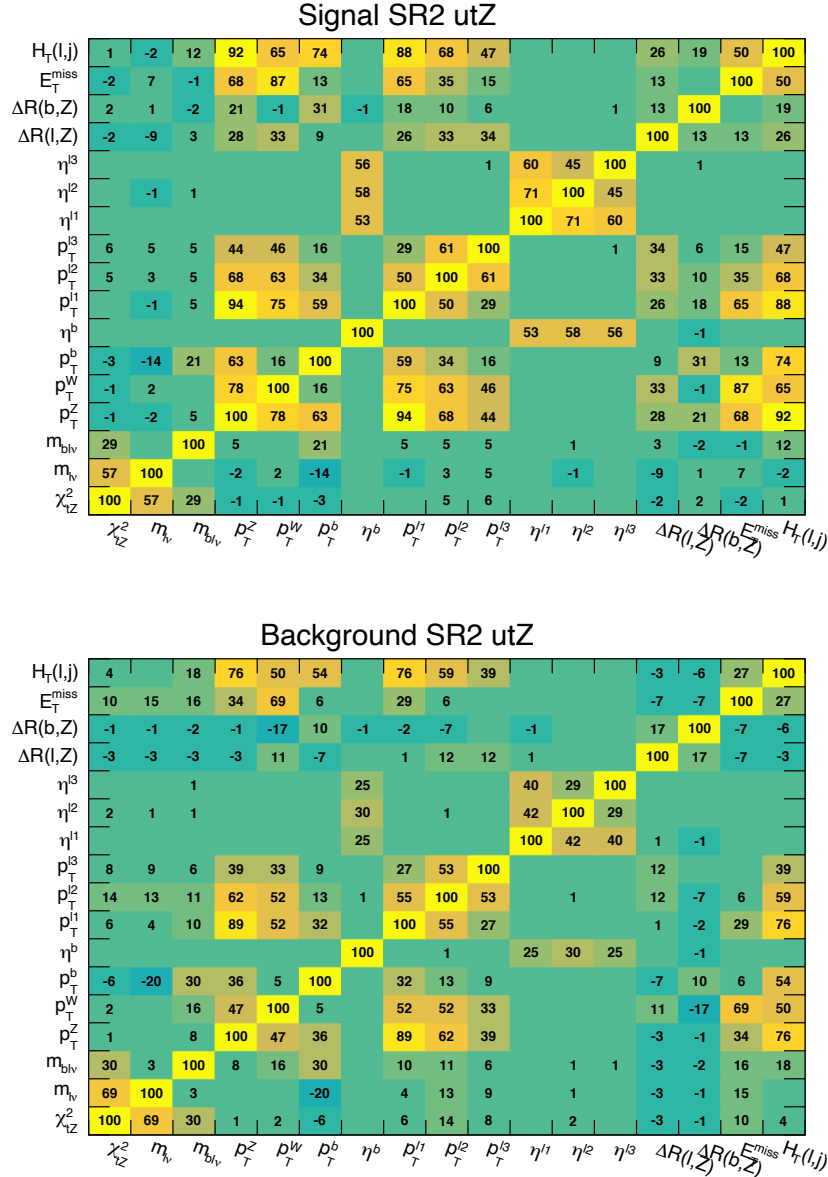


Figure 4.16: Correlation matrix of the input variables from signal (top) and background (bottom) samples considered in the training of the GBDT in SR2 to built the D^u_Z discriminant used in tZu coupling search.

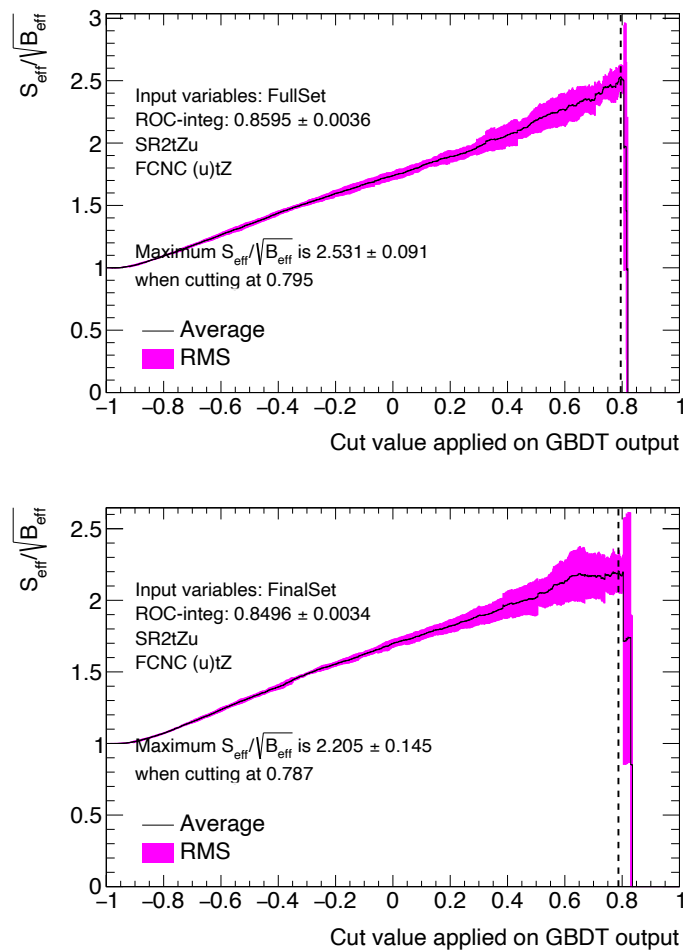


Figure 4.17: The $S_{\text{eff}}/\sqrt{B_{\text{eff}}}$ value averaged over the validation folds as a function of the cut on the BDT output score with "full set" (top) and final set (bottom) of input variables in the SR2 utZ . Values are calculated only if S_{eff} and B_{eff} are above 1% to avoid statistically unstable results.

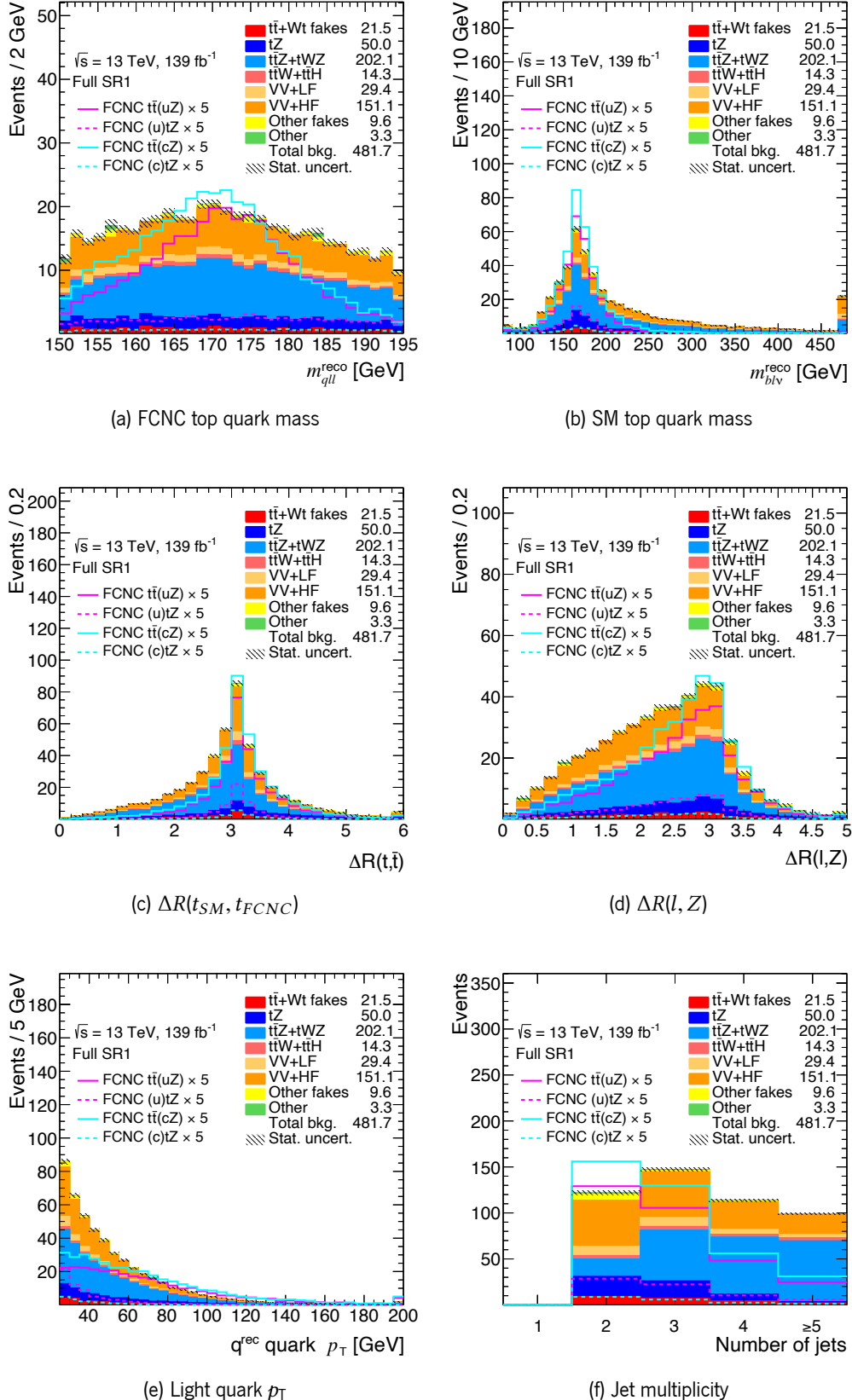


Figure 4.18: Pre-fit distributions of the input variables used in the training of the GBDT in full SR1 to built the D_1 discriminant. Number of signal events are normalised to the current observed branching ratio limits and scaled by factor 5.

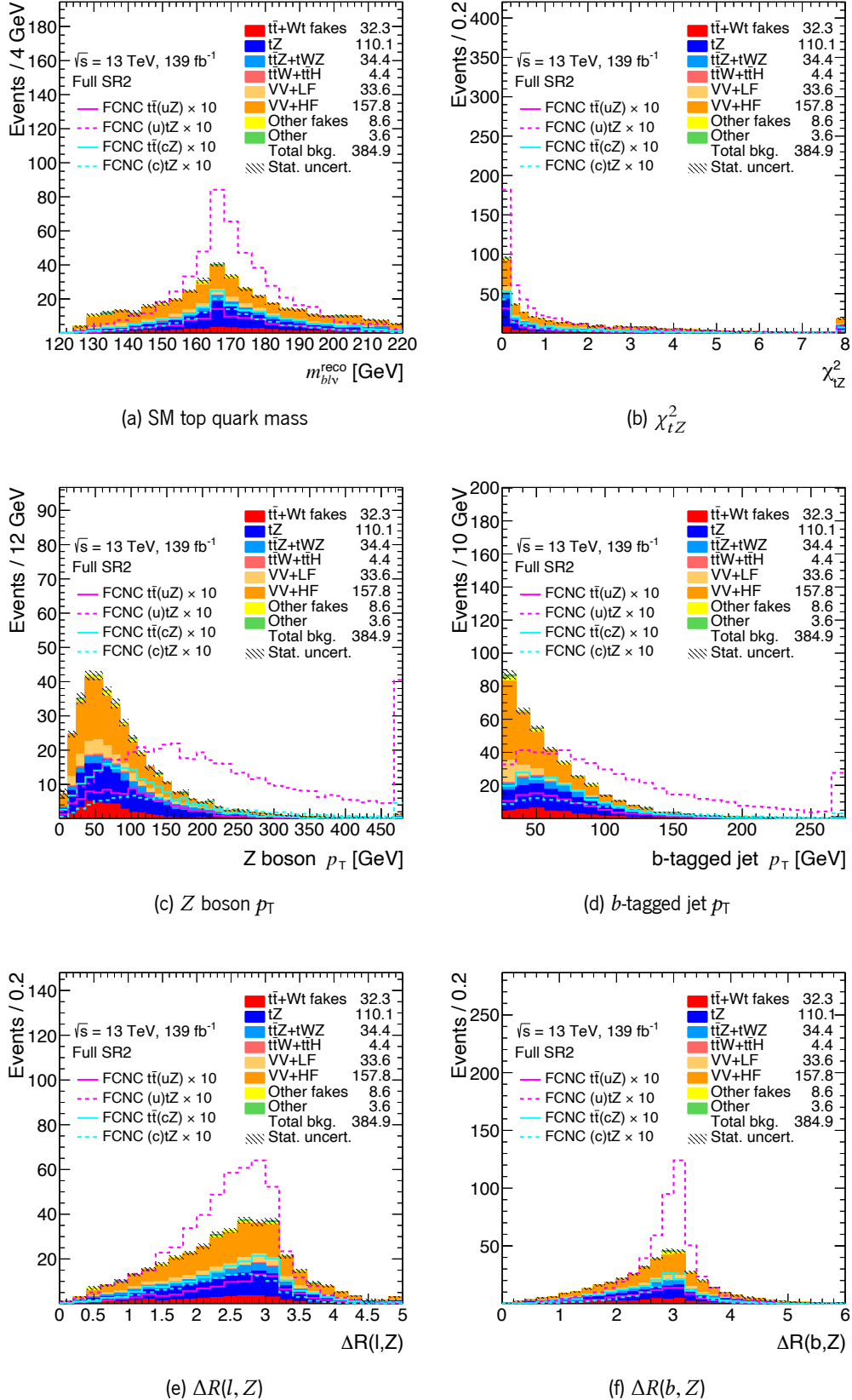


Figure 4.19: Pre-fit distributions of the input variables used in the training of the GBDT in full SR2 to built the D_2^u and D_2^c discriminants. Number of signal events are normalised to the current observed branching ratio limits and scaled by factor 10.

4.6.3 Training and evaluation

In order to train the GBDT algorithm and have a reliable model with a good performance, it is better to use as much statistics as possible from the available signal and background MC samples. On the other hand, to check the performance and validate the model, the trained GBDT model must be applied on the test sample (events that are not used in the training phase) that has sufficiently large statistics. Overtraining is a major concern for the BDT training. If it occurs, the BDT describes statistical fluctuations in the data set used for the training leading to a performance that does not hold if data sets are changed. In order to avoid this, the training sample of MC simulated data is split in two sets of statistically independent samples, with 80 % of available MC statistics being used for the training while 20 % for the testing. All samples, including MC samples of systematic variations and data, are divided into five approximately equal size groups using the pseudo-random numbers², which ensures that the same event in nominal and systematics samples (as the sample with varied jet energy resolution) is assigned in the same group. All events in each group have assigned the same integer pseudo-random number from 1 to 5. In each signal region, five equivalent GBDT models are trained using four groups of nominal MC samples. Each training uses different combination of four groups out of five. The remaining group is used as a test sample. Each of five GBDTs is evaluated on events with the assigned pseudo-random number that is not assigned to the training events of that GBDT. Different parameters can be used in the construction of the discriminants where the best separation between signal and background can be obtained with distinct combinations of such specifications. The BDTs used here are constructed from 800 individual trees, with a maximum depth of 2 nodes for the discriminants for decay and production with tZu coupling. For the specific case of the discriminant for production with tZc coupling, the BDT is constructed from 1000 individual trees and a maximum depth of 1 node. Table 4.13 shows the values used for all the configuration options of the BDT method. They are chosen to counteract overtraining and have an optimal performance.

Option	Value for D_1	Value for D_2^u	Value for D_2^c
NTrees	800	800	1000
MinNodeSize		2%	
BoostType		Grad	
Shrinkage	0.05	0.05	0.025
UseBaggedBoost		True	
BaggedSampleFraction		0.6	
nCuts		200	
MaxDepth	2	2	1
NegWeightTreatment		IgnoreNegWeightsInTraining	

Table 4.13: Used values for configuration options of the TMVA method Boosted Decision Trees [167].

²A pseudo-random number is generated for each event using the C++ `srand` generator with the sum of the dataset `RunNumber`, `DSID` and `EventNumber` as seed.

4.6.4 Performance and overtraining checks

Overtraining leads to a seeming increase in the classification performance over the objectively achievable one, if measured on the training sample, and to an effective performance decrease when measured with an independent test sample. A convenient way to detect overtraining and to measure its impact is therefore to compare the performance results between training and test samples. The evaluation of the performance of each trained BDT is obtained through the Receiver Operating Characteristic (ROC) curves. These curves illustrate background rejection versus signal efficiency caused by a variation of the threshold on the GBDT score. The signal efficiency is defined as the proportion of signal events above a particular threshold on the BDT score to all signal levels, while the background rejection is defined by the proportion of rejected background by the same threshold, being also commonly represented as (1 - background efficiency). A better BDT performance means higher background rejection at similar signal efficiency, resulting in a more convex ROC curve. Figures 4.20 to 4.22 present the ROC curves from the testing and training samples for each GBDT output score in the training signal regions for all the discriminants. The mean value of the ROC integral for the D_1 , D_2^u and D_2^c discriminants is 0.80, 0.85 and 0.69, respectively. No significant overtraining is detected for all the discriminants. The GBDT output score for signal and background from each of five GBDTs used to built the three discriminant variables are compared in Figure 4.23. Results of five GBDTs are in agreement within the statistical uncertainties indicating a good stability of the trained BDTs.

The variable importance is evaluated as the total separation gain that a specific variable had in the decision trees (weighted by the number of events). It is normalised to all variables together, which have an importance of 1. Input variables importance for each of five GBDTs of the three discriminants are presented in Tables 4.14 to 4.16. For most of the variables of the three defined discriminants, the standard deviation divided by the mean of the importance values across the five GBDTs is below 3% indicating a good stability of trained BDTs. The GBDT output score distributions in data and MC events are compared in the background control regions. Figure 4.24 and Figure 4.25 show the pre-fit distributions of discriminant variables in the side-band background control regions and $t\bar{t}Z$ control region, respectively. There is a good agreement between the shapes from data and pre-fit backgrounds.

Variable	GBDT #1	GBDT #2	GBDT #3	GBDT #4	GBDT #5
$m_{q\ell\ell}$	0.1886	0.1899	0.1929	0.1821	0.1825
$\Delta R(t_{\text{SM}}, t_{\text{FCNC}})$	0.179	0.1728	0.17	0.1768	0.1723
$m_{b\ell\nu}$	0.1755	0.1687	0.1571	0.1729	0.1646
$\Delta R(\ell, Z)$	0.1656	0.18	0.1775	0.173	0.1891
p_T^q	0.1637	0.1626	0.1678	0.1614	0.1592
N_{jets}	0.1277	0.126	0.1346	0.1338	0.1322

Table 4.14: Importance of the input variables in each GBDT used to built the D_1 discriminant.

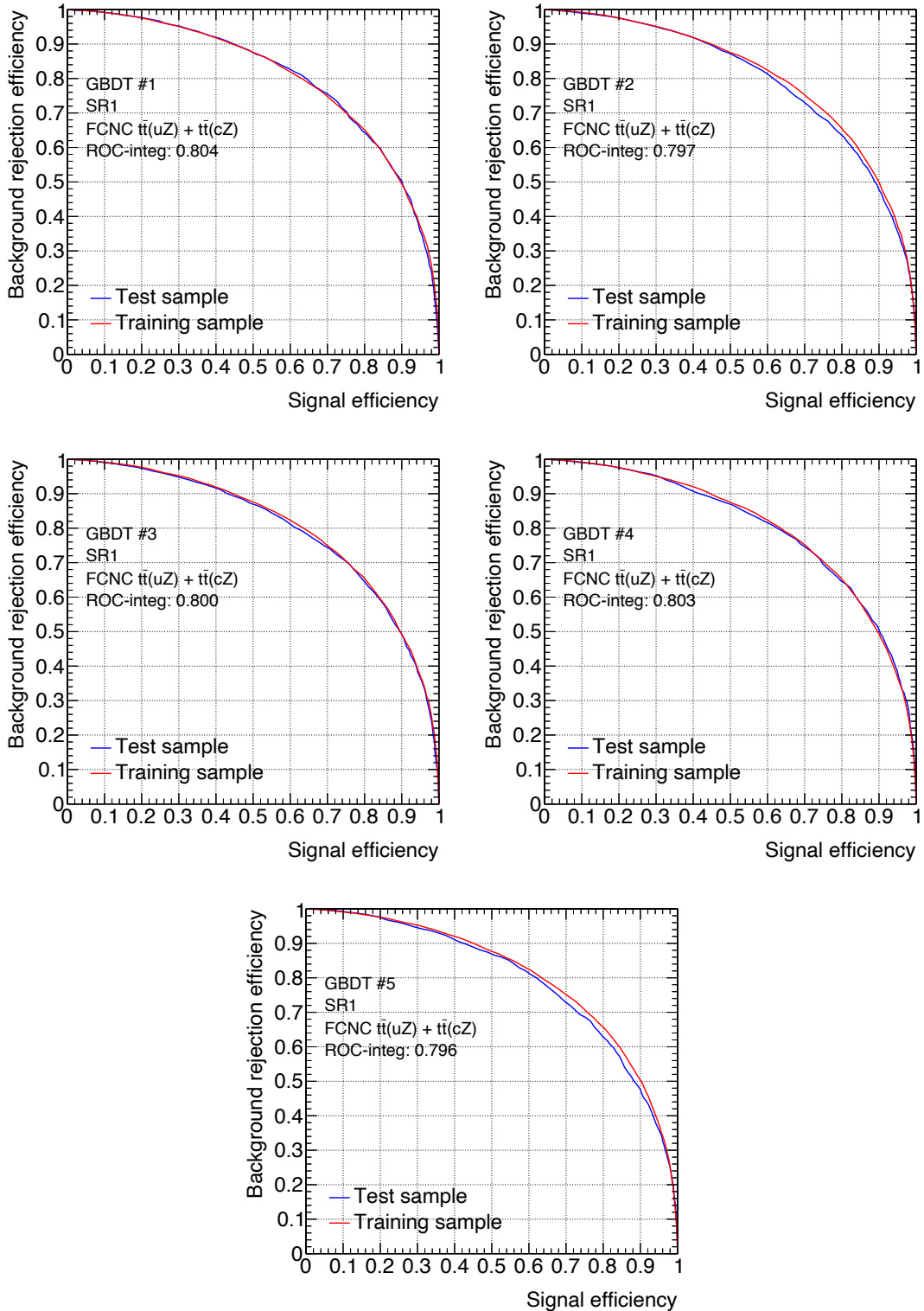


Figure 4.20: The ROC integral curve for each of five GBDTs trained in full SR1 to built the D_1 discriminant. Comparison of the final results between training and test samples.

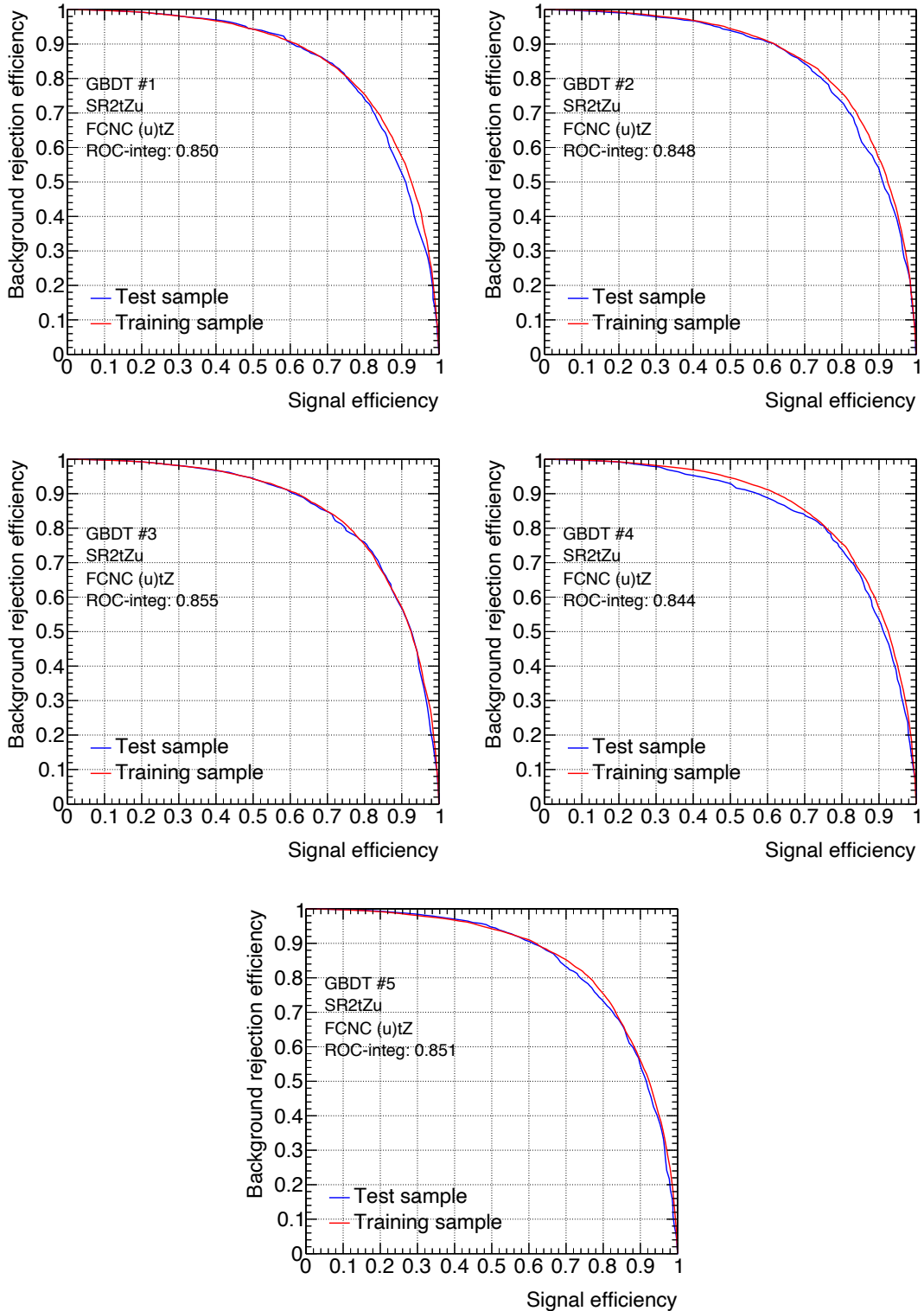


Figure 4.21: The ROC integral curve for each of five GBDTs trained in full SR2 to built the D_2^u discriminant. Comparison of the final results between training and test samples.

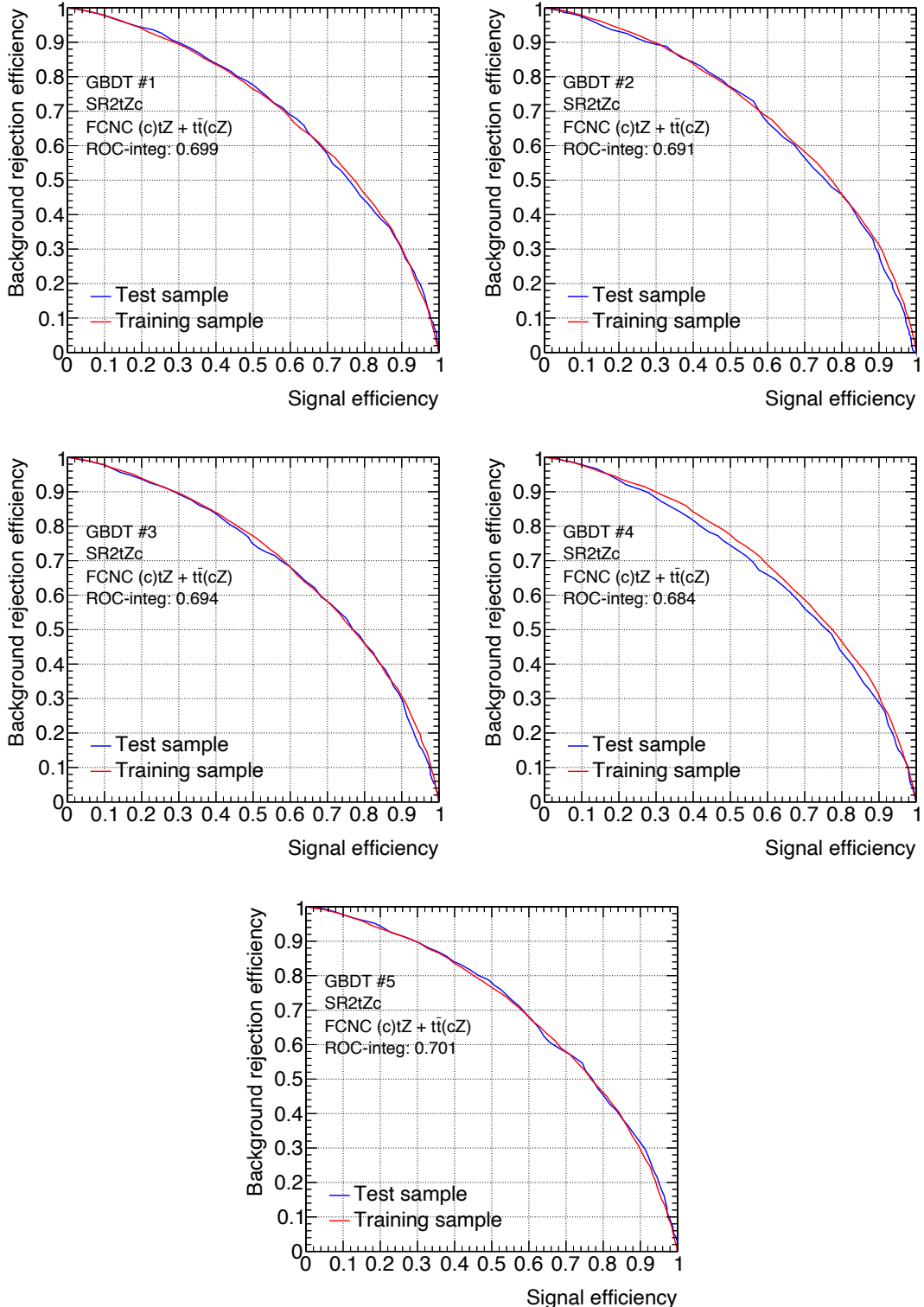


Figure 4.22: The ROC integral curve for each of five GBDTs trained in full SR2 to built the D_2^c discriminant. Comparison of the final results between training and test samples.

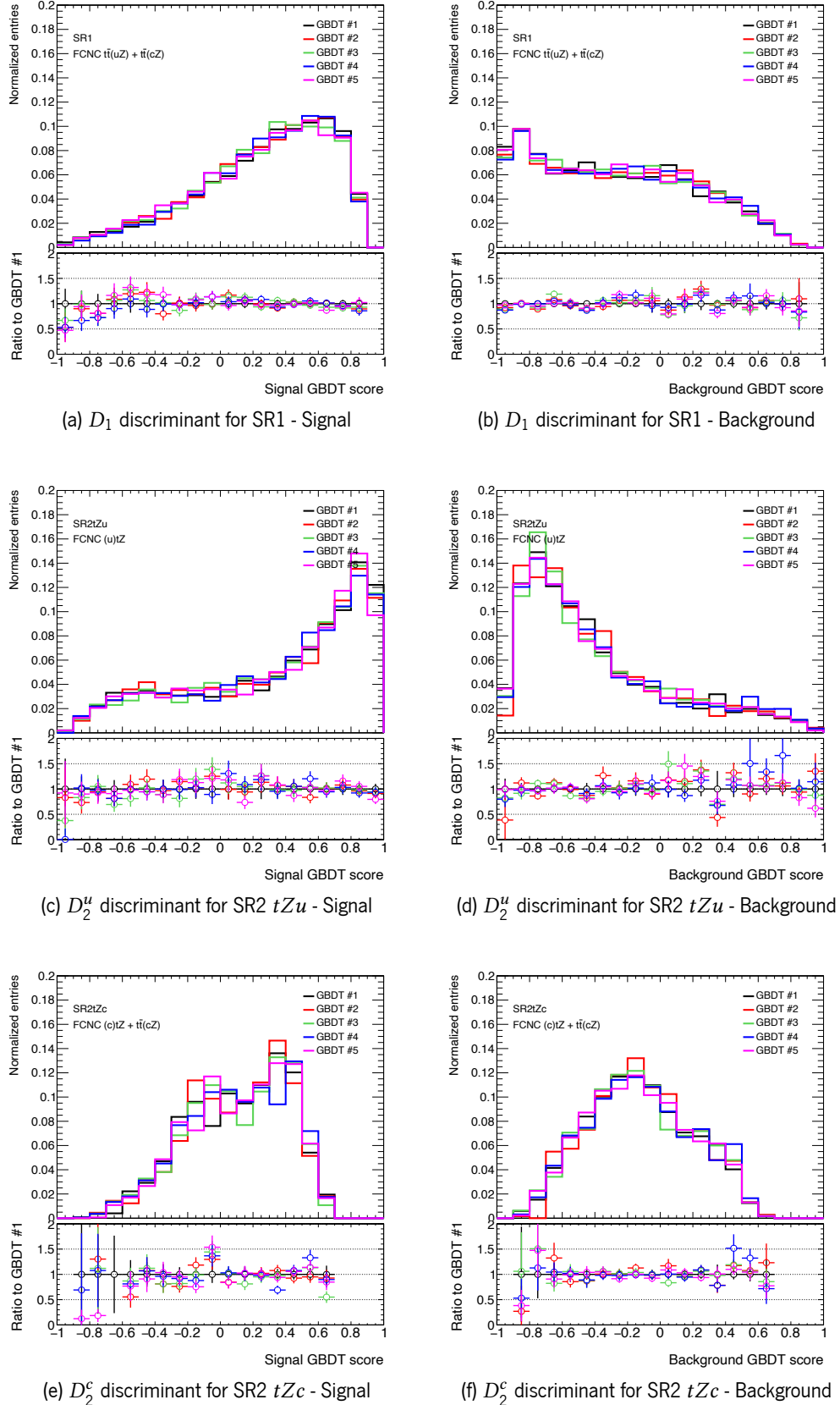


Figure 4.23: The GBDT output score distributions for signal and background events in the test samples. Trained five GBDTs are compared in each signal region.

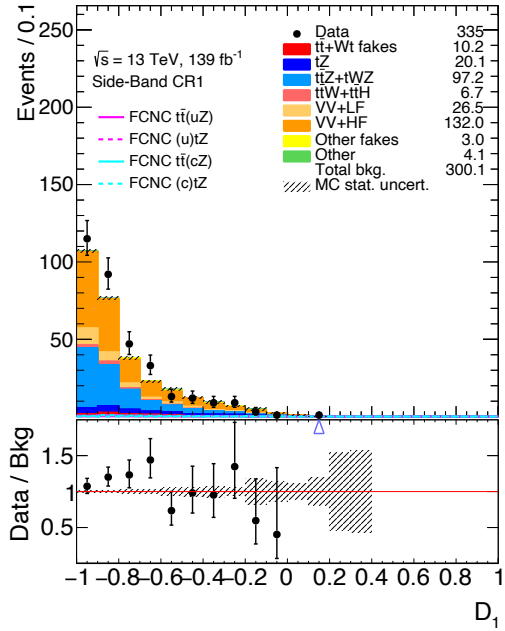
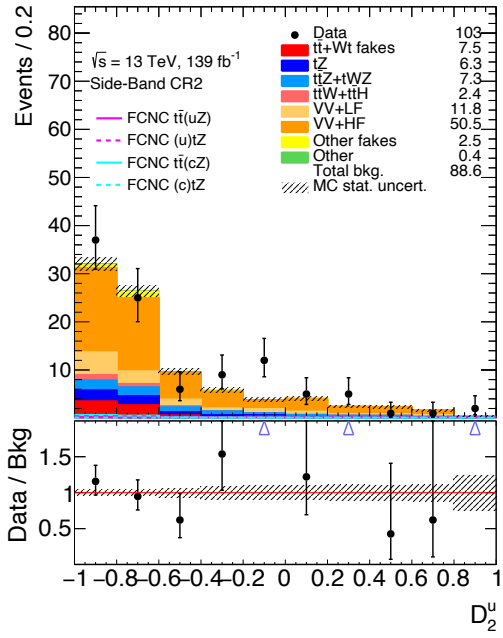
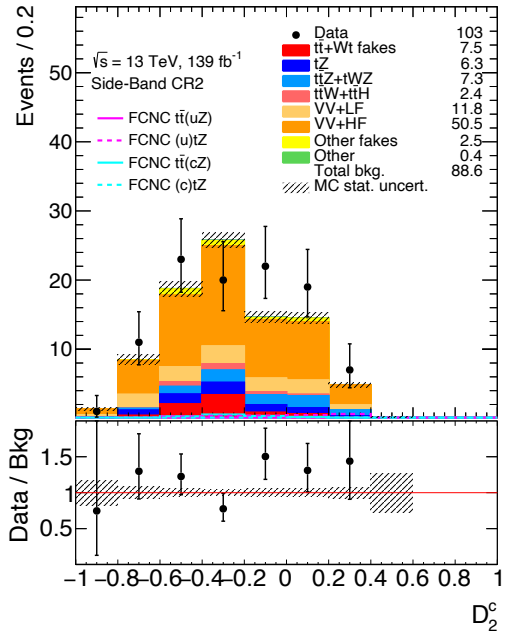

 (a) D_1 discriminant - Side-band control region 1

 (b) D_2^u discriminant - Side-band control region 2

 (c) D_2^c discriminant - Side-band control region 2

Figure 4.24: Pre-fit distributions of the D_1 , D_2^u and D_2^c discriminants in the side-band background control regions. Number of signal events are normalised to the current observed branching ratio limits. The uncertainty band includes only the statistical uncertainty.

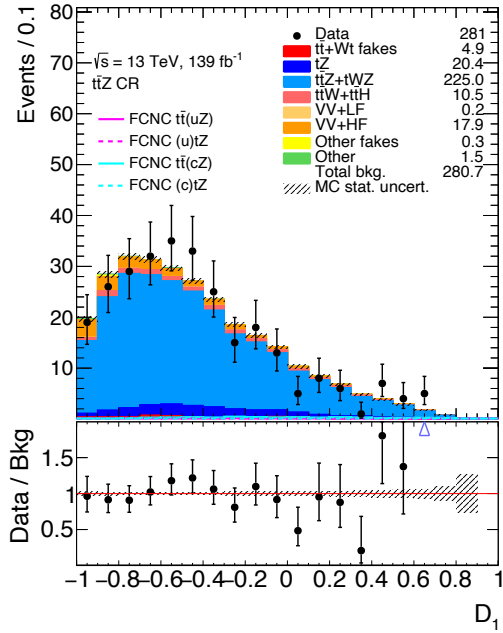
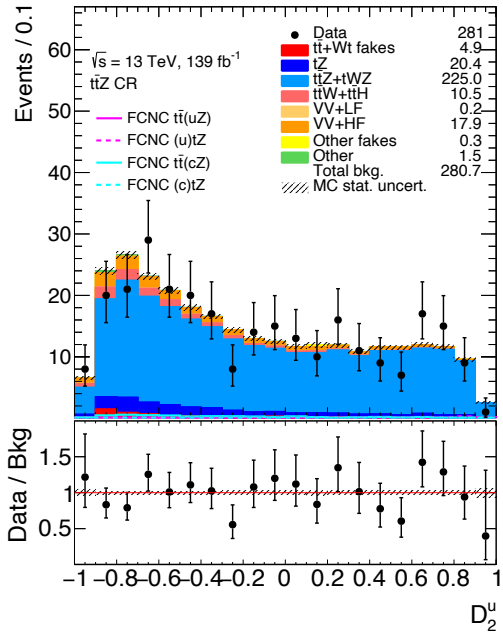
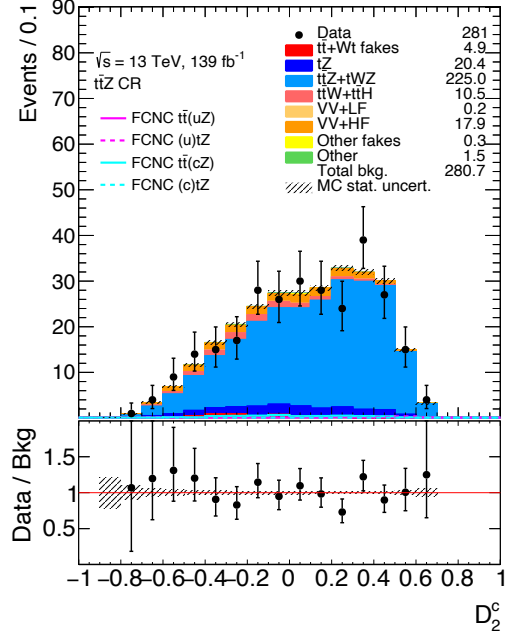

 (a) D_1 discriminant for $t\bar{t}Z$ control region

 (b) D_2^u discriminant for $t\bar{t}Z$ control region

 (c) D_2^c discriminant for $t\bar{t}Z$ control region

Figure 4.25: Pre-fit distributions of the D_1 , D_2^u and D_2^c discriminants in the $t\bar{t}Z$ control region. Number of signal events are normalised to the current observed branching ratio limits. The uncertainty band includes only the statistical uncertainty.

Variable	GBDT #1	GBDT #2	GBDT #3	GBDT #4	GBDT #5
$\Delta R(b, Z)$	0.1793	0.1761	0.1791	0.1809	0.1778
p_T^Z	0.1784	0.1717	0.1736	0.1785	0.181
$m_{b\ell\nu}$	0.1755	0.1819	0.1743	0.173	0.1776
$\Delta R(\ell, Z)$	0.1748	0.1739	0.1776	0.1762	0.166
p_T^b	0.1741	0.1778	0.1658	0.1715	0.1766
χ^2_{tZ}	0.1178	0.1186	0.1296	0.1199	0.121

Table 4.15: Importance of the input variables in each GBDT used to built the D_2^u discriminant.

Variable	GBDT #1	GBDT #2	GBDT #3	GBDT #4	GBDT #5
$\Delta R(b, Z)$	0.1938	0.1932	0.1962	0.188	0.1889
p_T^Z	0.1889	0.1869	0.19	0.1774	0.1857
$m_{b\ell\nu}$	0.1787	0.1805	0.1737	0.1826	0.183
$\Delta R(\ell, Z)$	0.1596	0.159	0.1496	0.1584	0.1639
p_T^b	0.152	0.1508	0.1557	0.1508	0.157
χ^2_{tZ}	0.127	0.1296	0.1347	0.1427	0.1216

Table 4.16: Importance of the input variables in each GBDT used to built the D_2^c discriminant.

4.6.5 Hyper-parameters optimisation

Once the final set of input variables are defined, the BDT hyper-parameters optimisation is performed. The following BDT parameters [167] and values are considered with total of 144 combinations: NTrees = [400, 600, 800, 1000], minNodSize = [2.0, 4.0, 6.0], shrinkage = [0.025, 0.05, 0.1], maxDepth = [1, 2, 3, 4]. Figure 4.26 presents the maximum value of $S_{\text{eff}} / \sqrt{B_{\text{eff}}}$ by cutting the BDT output score, and the ROC integral, averaged over the validation folds, as a function of BDT hyper-parameters combination for the D_2^u discriminant. The difference between highest and lowest values of $S_{\text{eff}} / \sqrt{B_{\text{eff}}}$ and ROC integral, with the different BDT hyper-parameters combinations, is $\sim 12\%$ and $\sim 2\%$, respectively. These results indicate that the BDT performance is stable and not much can be improved with the hyper-parameters. The average ROC integral (0.8486 with RMS of 0.0053) obtained with the reference BDT parameters is almost identical to the highest value of ROC integral (0.8502 with RMS of 0.0050) obtained from the hyper-parameters optimisation. However, the agreement between results with training and test samples are better for reference BDT parameters, so that these parameters are used to build the final BDT discriminant. Similar studies were performed for the D_1 and D_2^c discriminants and documented in Appendix A, concluding that the BDT performance is stable and optimal for the reference parameters.

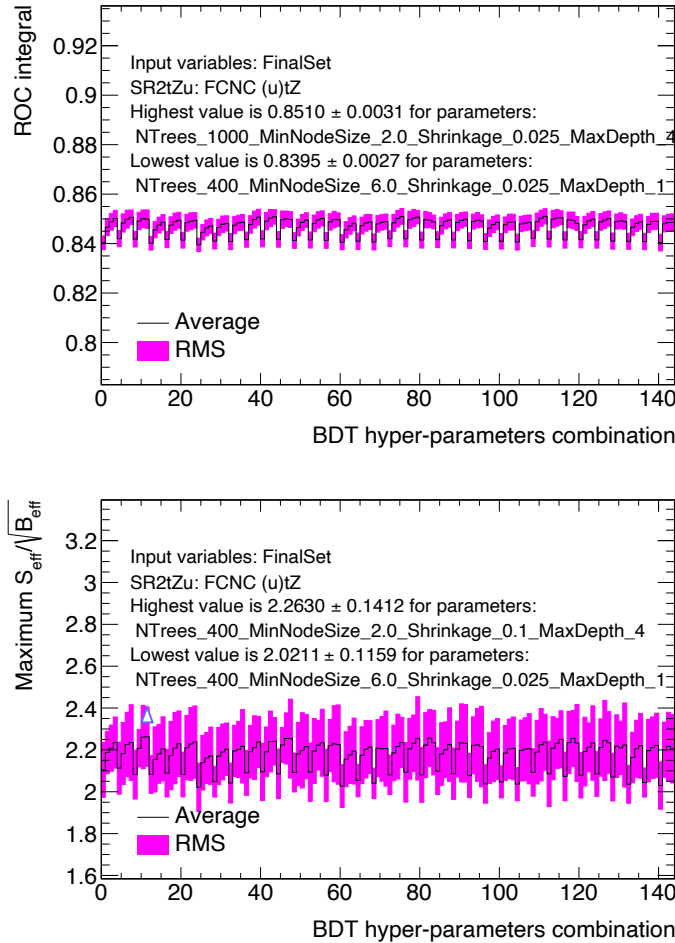


Figure 4.26: The maximum value of $S_{\text{eff}}/\sqrt{B_{\text{eff}}}$ by cutting the BDT output score (top) and the ROC integral (bottom), averaged over the validation folds, as a function of BDT hyper-parameters combination in the SR2 utZ . The highest and lowest values of $S_{\text{eff}}/\sqrt{B_{\text{eff}}}$ and ROC integral are presented on the plots as well as the corresponding BDT parameters values.

4.6.6 Validation regions definition

The validation regions are used to check the modelling of background sources. Two validation regions are defined from the full signal regions (see Table 4.4), applying cuts on the GBDT discriminants described in Table 4.9. The event selection of the validation regions is summarised in Table 4.17.

Validation Region	Defined from	Applied cut
VR1	Full SR1	$D_1 < -0.6$
VR2	Full SR2	$D_2^u < -0.7$ and $D_2^c < -0.4$

Table 4.17: Summary of the event selection applied to the GBDT discriminant variables in the full signal regions to define the validation regions.

The fraction of signal events that ends in the validation regions from the full signal regions ranges from 2 % to 5 %, depending on the signal region. With the given normalisation of signal samples, the signal contamination in the validation regions is at most 2 %. The subtraction of events from the full signal regions (in order to define the validation regions) has an effect on the expected search sensitivity (i.e. in the signal-to-background ratio of the signal regions) of below 1 %. Figure 4.27 presents the comparison of pre-fit GBDT output score distributions in the validation regions. The distributions from data and pre-fit backgrounds agree within the statistical and systematic uncertainties.

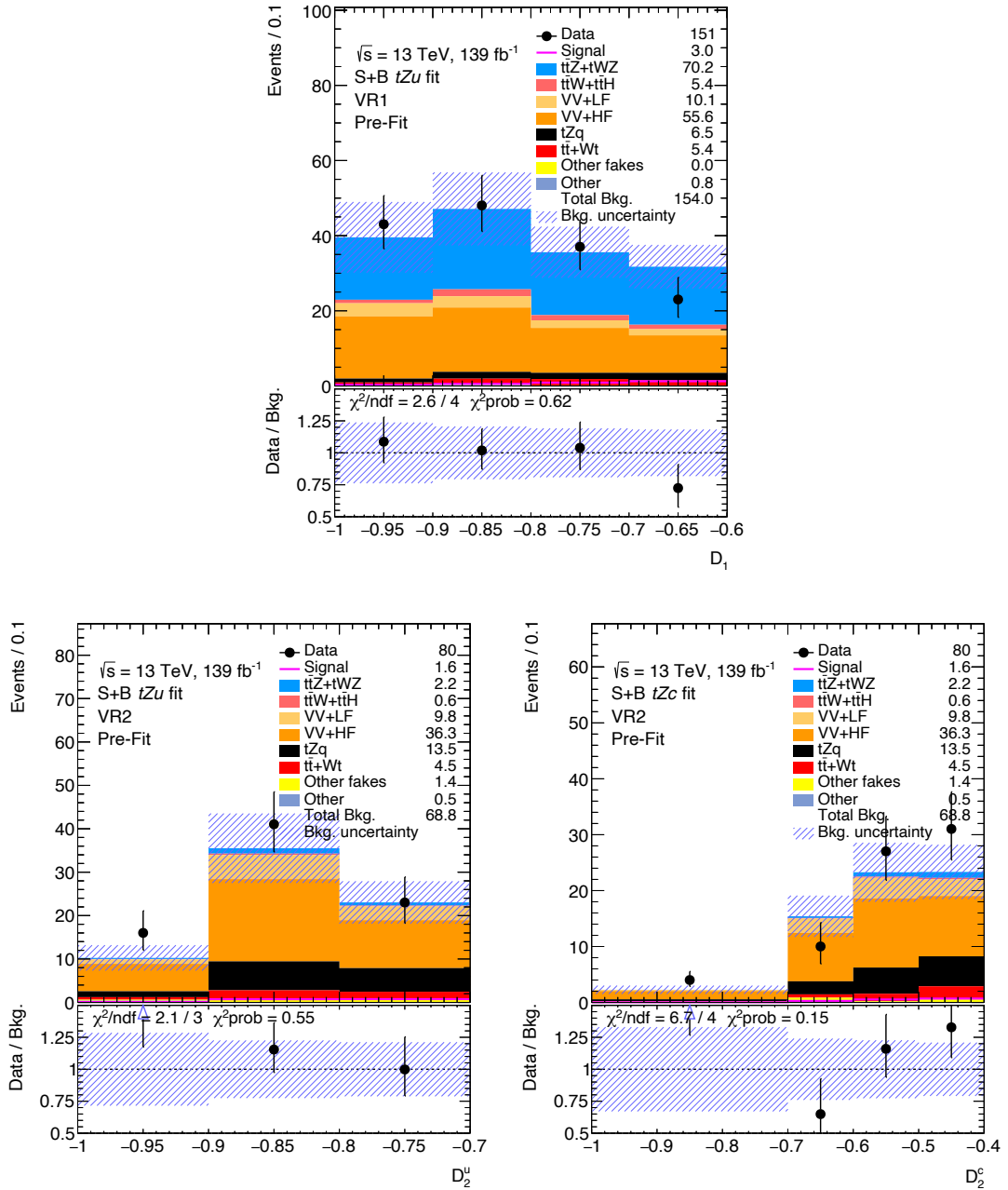


Figure 4.27: Pre-fit distributions of the D_1 , D_2^u and D_2^c discriminants in the validation regions. Number of signal events are normalised to the current observed branching ratio limits. The uncertainty band includes only the statistical uncertainty.

4.7 Systematic uncertainties

Many sources of systematic uncertainties are considered in the search for FCNC tZq interactions. The systematic uncertainties are evaluated using the common Top Working Group prescriptions and the standard ATLAS procedures. Systematics uncertainties are considered for the normalisation and shape of the individual backgrounds from various sources.

Object energy scale/resolution and efficiencies

Systematic uncertainties due to residual differences between data and Monte Carlo simulations, for jet, electron and muon reconstruction after calibration, as well as uncertainties on the calibration scale factors are propagated to the event yields and observables.

- **Lepton reconstruction:** The mis-modelling of muon (electron) trigger, reconstruction, identification and also from the Prompt Lepton Veto tool isolation efficiencies in simulation is corrected by introducing scale factors derived from measured efficiencies in data. The decays of $Z \rightarrow \mu^+ \mu^-$ ($Z \rightarrow e^+ e^-$) are used to obtain scale factors as functions of the lepton kinematics. The uncertainties are evaluated by varying the lepton and signal selections and from the uncertainties in the backgrounds evaluation.
- **Lepton momentum scale and resolution:** The $Z \rightarrow \ell\ell$ processes are used to measure the lepton momentum scale and resolution. Calibration factors and associated uncertainties are derived to match the simulation to observed distributions in collision data. The effect of momentum scale uncertainties is evaluated by repeating the event selection after varying the lepton momentum up by 1σ and down by 1σ . For the momentum resolution uncertainties, the event selection is repeated by smearing the lepton momentum [168].
- **Jet energy scale:** The JES was derived using information from test-beam data, LHC collision data and simulation. The JES calibration consists of several steps that account for detector problems, jet reconstruction algorithms, jet fragmentation models, dense data-taking environment from high pile-up conditions and response difference between data and MC simulation. The fractional uncertainty decreases with the p_T of the reconstructed jet and is rather stable in η . The JES uncertainty has various components according to the factors it accounts for and the different steps used to compute it. The jet calibration procedure is described in Ref. [169]. The sources of the JES uncertainties with different effective number of parameters are: BJES response, detector, mixed, modelling, statistical, eta intercalibration, flavour composition, pile-up and relative non-closure.
- **Jet energy resolution:** The impact of the uncertainty on the jet energy resolution is evaluated by smearing the jet energy in the MC samples.

- **Jet Vertex Tagger efficiency:** The uncertainty related to the Jet Vertex Tagger scaling factors applied to the MC simulation includes the statistical uncertainty, which is a 30% uncertainty on the estimation of the residual contamination from pile-up jets after pile-up suppression [170]. Such uncertainty is considered in the fit as a nuisance parameter (NP) named *jvt*.
- **Missing transverse momentum:** Uncertainties of the soft-track component are derived from the level of agreement between data and MC simulation of the p_T balance between the hard and soft E_T^{miss} components. Three different uncertainties are considered: an offset along the p_T (hard) axis, as well as the smearing resolution along and perpendicular to the p_T (hard) axis.
- ***b*-tagging efficiency:** The *b*-tagging efficiencies and mis-tag rate for the taggers have been measured in data using the same methods as described in [171, 172]. The number of NP used for the *b*-tagging data/MC scale factors is evaluated separately for *b*, *c* and light-flavour quark jets in the MC samples.

Monte Carlo modelling

Systematic effects from MC modelling are estimated by comparing different generators and varying parameters for the event generation.

- **Signal:** Scale uncertainties are included for the signal, following the latest prescriptions. In particular, the scale variations μ_r and μ_f are included and the envelope of the variations is added. Corresponding NP name is *Signal* μ_r and μ_f . An additional uncertainty focusing on the parton shower is included, through the comparison of the signal samples produced using Herwig7 and Pythia8 (NP called *Signal PS*).
- **$t\bar{t}$:** The effect of changing the parton shower (PS) for $t\bar{t}$ events is included as an uncertainty. The difference between Pythia8 and Herwig7.13 prediction is taken as the $t\bar{t}$ PS uncertainty (NP called *t \bar{t} PS*). The Var3c A14 tune variation [137], that largely corresponds to the variation of α_s for Initial State Radiation (ISR) in the A14 tune, is considered (NP called *t \bar{t} A14 tune (ISR)*). The impact of Final State Radiation (FSR) is evaluated (NP called *t \bar{t} FSR*) using PS weights which vary the renormalisation scale for QCD emission in the FSR by a factor of 0.5 and 2.0, respectively. Additionally, the uncertainty associated to the h_{damp} parameter is evaluated (NP called *t \bar{t} hdamp*) using the alternative sample with the h_{damp} value increased to 3.0 m_t . Scale and PDF uncertainties are also included, following the latest prescriptions. In particular, the μ_r and μ_f variations are included and the envelope of the variations is added (NP called *t \bar{t} μ_r and μ_f*). The PDF uncertainty (NP called *t \bar{t} PDF*) is evaluated using alternative PDF weights (PDF260100). Last but not least, as mentioned in Section 4.5.1, uncertainties are added to take into account the differences in the fractions of fake leptons originate from photon conversion and *b*-hadron decay in the signal regions

with respect to the $t\bar{t}$ control region, where the $t\bar{t}$ background is controlled. These uncertainties are obtained by taking the maximum difference in the fractions between the signal and $t\bar{t}$ control regions in the different jet multiplicity bins. Obtained values are summarised in Table 4.18. The two uncertainties are called $t\bar{t}$ non-prompt lep. (photon conv.) and $t\bar{t}$ non-prompt lep. (b -decay), each having 5 NPs corresponding to the jet multiplicity bins ($= 1, = 2, = 3, = 4, \geq 5$ jets).

Jet multiplicity	Photon conversion	B -meson decay
$= 1$	23 %	5 %
$= 2$	35 %	23 %
$= 3$	9 %	0.6 %
$= 4$	33 %	27 %
≥ 5	23 %	56 %

Table 4.18: Uncertainties applied to the $t\bar{t}$ sample with fake leptons originated from photon conversion and B -meson decay in the different jet multiplicity bins.

- **$t\bar{t}Z$:** The effect of changing the parton shower for $t\bar{t}Z$ events was investigated. The difference between Pythia8 and Herwig7 prediction is taken as the $t\bar{t}Z$ PS uncertainty. A scale uncertainty systematic is also included, following the latest prescriptions. In particular, the μ_r and μ_f variations are included and the envelope of the variations is added. Additionally, the effects of QCD radiation for this sample are also taken into account through alternative samples with up/down variation of Var3c parameter in the A14 tune [137] (NP called $t\bar{t}Z$ QCD).
- **tWZ :** The effect of changing the diagram removal used for tWZ events was investigated and the difference between the two diagram removals prediction is included as tWZ DR systematic uncertainty.
- **tZq :** Also for SM tZq background, the differences by using variation of Var3c parameter in the A14 tune are accounted and considered in the fit (called tZ QCD).
- **Diboson:** The effect of changing the MC generator for diboson events was also investigated and the difference between Sherpa and PowhegBox prediction is included as diboson generator uncertainty. This uncertainty is split into two components: light- and heavy-flavour (called $VV + LF$ Generator and $VV + HF$ Generator). These uncertainties are evaluated independently in different jet multiplicity bins each of them resulting 5 NPs corresponding to the number of jets: $= 1, = 2, = 3, = 4, \geq 5$. An uncertainty depending on the jet multiplicity (so-called Berends scaling [173, 174]) is also included for the diboson samples with the separation by light- and heavy-flavour as well. Therefore, an uncertainty of 25 % (called $VV + LF$ Berends scaling and similarly for $VV + HF$) is added in quadrature per jet in each jet multiplicity resulting into 5 NPs ($= 1, = 2, = 3, = 4, \geq 5$ jets).

Process	Rate uncertainty
$t\bar{t}+Wt$	–
$t\bar{t}Z$	12 %
$t\bar{t}W$	50 %
tWZ	30 %
tZq	15 %
$VV+LF$	20 %
$VV+HF$	30 %
$Z+\text{jets}$	100 %
$t\bar{t}H$	15 %
Other ($t\bar{t}t, t\bar{t}\bar{t}, VVV, VH$ and $t\bar{t}WW$)	50 %

Table 4.19: Rate uncertainties applied on the normalisation of the background processes.

- **MC statistics:** The uncertainty due to the limited size of the MC samples is also included.

Rate uncertainty

Additional uncertainties on the normalisation of the different backgrounds considered in this analysis are used. Motivated by theoretical calculations and past measurements in particle physics analyses targeting the specific processes, the uncertainties applied on the background rate are summarised in Table 4.19.

Luminosity

The uncertainty in the combined 2015-2018 integrated luminosity is 1.7 %. It is derived, following a methodology similar to that detailed in Ref. [175], from the calibration of the luminosity scale using $x - y$ beam-separation scans.

Pile-up reweighting

An uncertainty related to the scaling factor applied in MC samples to account for differences in pile-up distributions between MC simulation and data is considered.

4.7.1 Acceptance and shape uncertainties

The systematic uncertainties discussed above cause variations on the signal acceptance, the background rates, and the shape of the distributions that are fed to the fit. The MC statistics is related to the statistical uncertainty in each bin of the distributions that are used in the fit, so it can change the shape of the distributions. For all systematics listed, rate and shape differences are taken into account.

Symmetrisation of uncertainties: Symmetrisation is applied to all systematic uncertainties, as implemented in the `TRExFitter` package.

Smoothing: Some fluctuations in individual bins can be caused by the low statistics shape systematic uncertainties. A smoothing of systematic shape uncertainties is performed using the default smoothing algorithm available through the `TRExFitter` package to average adjacent bins to remove statistical

fluctuations.

Pruning: To prevent statistical fluctuations increasing the systematic uncertainties and wasted computation on fitting insignificant NPs, systematic uncertainties are pruned from the fit. A value of 1 % and 0.5 % are used for normalisation and shape, respectively. Therefore, if a given systematic uncertainty does not change any bin by more than 1 % (0.5 %) from the nominal value, then the normalisation (shape) component of that systematic for that sample in that region is ignored. This analysis uses different levels of pruning with 1 % and 0.5 % applied on the normalisation and shape uncertainties, respectively. Studies with different values for these parameters were performed presenting a negligible difference on the expected limits with respect with the reference parameters (being documented in Appendix B).

4.8 Statistical analysis and results

All analysis regions are combined in a statistical model using a profile likelihood fit in order to test for the presence of a FCNC $t \rightarrow qZ$ (with $q = u, c$) signal. The profile likelihood function is described in Section 4.8.1, where the impact of the systematic uncertainties is propagated through the so-called nuisance parameters in the fit. The details of the fit model for the FCNC $t \rightarrow qZ$ signal hypothesis are described in Section 4.8.2. Finally, Section 4.8.3 presents the results obtained from the fit to data and Section 4.8.4 explains the procedure leading to the determination of the upper limit of the signal strength of $t \rightarrow qZ$ processes.

4.8.1 Profile likelihood fit

The distributions of the discriminant variables from each of the analysis regions are combined in a profile likelihood fit to test for the presence of a FCNC $t \rightarrow qZ$ signal and to constrain the background predictions. For each bin i of the input distribution of each region r , the number of data events $N_{r,i}^{data}$ are compared to the expected bin content $N_{r,i}^{expected}$. The expected bin content $N_{r,i}^{expected}$ is expressed as the following:

$$N_{r,i}^{expected}(\mu, k_1, \dots, k_m, \theta_1, \dots, \theta_n) = \mu \cdot N_{r,i,sig}^{expected}(\theta_1, \dots, \theta_{n_{sig}}) + \sum_{b \in bkg} k_b \cdot N_{r,i,b}^{expected}(\theta_1, \dots, \theta_{n_b}) \quad (4.4)$$

where n is the total number of nuisance parameters, $(\theta_1, \dots, \theta_n)$ is the set of n_i nuisance parameters related to the sample i being signal (sig) or background (bkg), k_b is the normalisation factor on the background b , m is the number of backgrounds, and μ is the signal strength. For every systematic variation described in Section 4.7, there is a nuisance parameter θ_i that modifies the shape and/or the normalisation of the templates depending on the parametrised systematic uncertainty. The templates are formed from the expected distributions where the nuisance parameters are varied. The normalisation factors (k -factors) and

the signal strength (μ) modify only the normalisation of the template distributions. The data content of each bin is expected to follow a Poisson probability. Therefore, the primary likelihood function is constructed as the product of a Poisson probability terms for each bin. By construction, the value $\theta = 0$ corresponds to the best knowledge of a specific parameter (nominal value). Uncertainty variations up to $\pm 1\sigma$ correspond to the 1σ uncertainty. The nuisance parameters are defined by the extrapolation ($|\theta| > 1$) and interpolation ($|\theta| < 1$) functions with constraints that $\theta = 0$ corresponds to no corrections and $\theta = \pm 1$ shifts the distribution by $\pm 1\sigma$ systematic uncertainty. A linear and exponential extrapolations for the shape and normalisation components of the systematic uncertainties are used, respectively. Consequently, two polynomial functions are defined, one for the shape and one for the normalisation components of the systematic uncertainties. The deviation of the nuisance parameters, the normalisation factors or the signal strength are referred to as a pull. Nuisance parameters are implemented using Gaussian constraints reflecting the prior knowledge of the systematic uncertainty. To understand the impact of the nuisance parameters on the extracted μ the following procedure is used: the fit is re-run several times, separately for each nuisance parameter, changing the central value of each nuisance parameter up and down by the pre-fit (post-fit) $\pm 1\sigma$ uncertainties, fixing it to that value and re-running the fit to μ . The difference between this μ and the one extracted from the standard fit, $\Delta\mu$, is the pre-fit (post-fit) impact on μ . The values of $\Delta\mu$ are shown in the so called ranking plot presented in next sections. The reference scale for this information in the ranking plot is the top x -axis, labelled $\Delta\mu$. The global likelihood function describing the agreement between data and prediction as a function of the parameter of interest (POI) and the set of nuisance parameters describing the effect of the corresponding systematic uncertainty sources is constructed and fitted. The POI is the signal strength parameter, μ , a multiplicative factor for the number of signal events normalised to a reference branching ratio ($BR_{\text{ref}}(t \rightarrow uZ) = 0.017\%$ for the tZu case and $BR_{\text{ref}}(t \rightarrow cZ) = 0.024\%$ for the tZc case). The relationship between μ and the corresponding $BR(t \rightarrow qZ)$ is:

$$\mu = \frac{BR(t \rightarrow qZ)(1 - BR(t \rightarrow qZ))}{BR_{\text{ref}}(t \rightarrow qZ)(1 - BR_{\text{ref}}(t \rightarrow qZ))}. \quad (4.5)$$

Technically, the software framework used for the fit is TRExFitter [176], which combines the functionalities of RooFit [177] and RooStats [178] and is designed to build probability density functions that are automatically fit to data and interpreted with statistical tests.

4.8.2 The fit model

The fit model is described by the chosen variables to build the template distributions, and the list of systematics uncertainties and their correlations across the defined analysis regions. The distributions of the discriminant variable from each of the signal regions of the analysis are combined in the profile likelihood fit to test for the presence of a FCNC $t \rightarrow qZ$ signal, while simultaneously determining the normalisation and constraining the different distributions of the dominant background components. Since

two signal hypotheses were tested, two independent fits were performed for FCNC $t \rightarrow uZ$ and $t \rightarrow cZ$ signals with the same approach considering all analysis regions defined. Similarly to the signal regions, the input distributions of the multivariate discriminant is considered for the side-band control regions. In the $t\bar{t}$ and $t\bar{t}Z$ control regions, only the event yield is used as input for the fit. Additionally, for each MC sample, separate templates that take into account the systematic variations discussed in Section 4.7 are created and included in the fit. The regions included in the fit, as well as the distributions that are fit, are summarised in Table 4.20. The selection of the various regions are shown in Table 4.4 for the signal regions and in Table 4.7 for the control regions. In addition, as mentioned in Section 4.6.6, further cuts are applied to the GBDT discriminants in the full signal regions to create validation regions.

tZu coupling extraction		
Region	Distribution	Additional info
SR1	D_1	$D_1 > -0.6$
SR2	D_2^u	$D_2^u > -0.7$ or $D_2^c > -0.4$
Side-band CR1	D_1	
Side-band CR2	D_2^u	
$t\bar{t}Z$ CR	–	Single bin
$t\bar{t}$ CR	–	Single bin

tZc coupling extraction		
Region	Distribution	Additional info
SR1	D_1	$D_1 > -0.6$
SR2	D_2^c	$D_2^u > -0.7$ or $D_2^c > -0.4$
Side-band CR1	D_1	
Side-band CR2	D_2^c	
$t\bar{t}Z$ CR	–	Single bin
$t\bar{t}$ CR	–	Single bin

Table 4.20: Overview of the variables used in the combined fit for the signal and control regions.

Concerning the background treatment in the fit, the $t\bar{t}Z$ and tWZ backgrounds are merged in one template as well as $t\bar{t}$ and Wt . The dilepton samples other than $t\bar{t}$ and Wt ($Z+jets$, $t\bar{t}Z$ (2ℓ), VV (2ℓ)) are also merged as well as templates for rare processes ($t\bar{t}t$, $t\bar{t}t\bar{t}$, VVV , VH , $t\bar{t}WW$). Two templates are included in the fit for diboson process that correspond to the heavy and light components ($VV + HF$ and $VV + LF$). Separate templates are used for the remaining background sources. The signal strength is considered as a freely floating parameter, applied without any prior in the fit, along with the normalisation factors of the $t\bar{t}$ and Wt backgrounds. The normalisation of $t\bar{t} + Wt$ background is free-floating in the fit means that an unconstrained NP is associated to the corresponding template, namely $\mu_{t\bar{t}+Wt}$. For all other background processes, the normalisation is controlled through specific nuisance parameters

that reflect the theoretical knowledge of the respective cross-sections or the uncertainty on the estimate methods, as discussed in Section 4.7.

4.8.3 Fit to data

4.8.3.1 Likelihood fit using Asimov data

The study of the expected behaviour of the fit is performed through simultaneous likelihood fits under the background-only (with $\mu = 0$) and signal-plus-background hypothesis using an artificial dataset known as Asimov dataset in the signal regions. The Asimov dataset is defined as the one where the pseudo-data is equal (within data statistical uncertainties) to the expectation value, i.e to the sum of background predictions [179]. While this pseudo-data is used in the signal regions, all the defined background control regions are considered in the fits using the real data. The approach implemented in the presented analysis was the following:

- First, a background-only fit with real data in the control regions is performed;
- From the results of the background-only fit, a realistic Asimov dataset is build taking into account the predictions of the normalisation factors studied. A signal-plus-background fit is executed then, using real data in the control regions and the realistic Asimov data set in the signal regions.

4.8.3.2 Signal-plus-background fit for tZu coupling in the signal and control regions with realistic Asimov data from the control regions

The list of the systematic shapes that are dropped from the fit for each sample and for each region due to the pruning is shown in Figure 4.28. Several fits with different pruning thresholds were compared and summarised in Appendix B. This study concluded that the pruning levels used in this analysis do not affect the expected limits on the signal processes. The pull distributions of the all nuisance parameters considered in this analysis can be seen in Figure 4.29. The normalisation factor for $t\bar{t} + Wt$ background processes is found to be 0.91 ± 0.24 . The fit constrains the free-floating background normalisation factor being those processes overestimated in the pre-fit predictions. In the pre-fit plots, the normalisation factors are set to 1, which corresponds to considering the prediction from the $t\bar{t}$ and Wt background processes. Figures 4.33 and 4.34 show comparisons of the observed data and the prediction for the discriminant variable used for each control region before and after applying the corrections from the fit (pre-fit and post-fit). The fit corrects the normalisation mismodeling of the $t\bar{t}$ and Wt backgrounds in these regions. Similarly, Figure 4.32 show comparisons for the observed data to the prediction of the GBDT score in the two signal regions. The shape of the GBDT is modeled within the assigned uncertainties and the fit mainly corrects for the MC overestimated normalisation in these regions. Some fluctuations due to low statistics in some of the bins of these distributions show a 1σ deviations of data from the MC predictions. As expected, the uncertainty is

reduced due to the constraints on the nuisance parameters and the overall agreement between data and prediction is also improved. Additionally, a clear trend of a shape mismodeling or normalisation offset is not observed in the post-fit distributions. Pre-fit and post-fit event yields in the signal and control regions are presented in Tables 4.21 and 4.22, respectively. In all analysis regions, the data agrees with the corrected prediction within the total uncertainty. The nuisance parameters are included in the maximum likelihood fit as uncorrelated parameters. However, the fit creates correlations between complementary nuisance parameters. Figure 4.30 shows the linear correlation coefficients of a selection of the most important systematic uncertainties (being some of them reported in the ranking plot in Figure 4.31) obtained by the full fit to data. The normalisation of the background processes represent the systematics with higher correlation to the signal strength with 19% for tZq normalisation and 9.1% for $t\bar{t}Z$ normalisation. Such correlations are predicted since those processes have a significant contribution for both signal regions along with diboson production. Therefore, some strong correlations between diboson related nuisance parameters are also present, as expected. The ranking of the nuisance parameters is shown in Figure 4.31. Similarly to the correlation matrix, the systematics highly ranked are the ones related to the normalisation of tZq and $t\bar{t}Z$ production processes. As expected, the behaviour of the fit with the realistic Asimov dataset is almost identical to the results of the background-only fit in the control regions. One thing that can be noticed is that the tZq background normalisation is slightly constrained. The most pulled nuisance parameters (e.g. $VV + HF$ and the other fake normalisations) are not among the highest ranked (Figure 4.31). In order to validate the fit procedure on the background predictions, the fitted nuisance parameters are propagated to the validation regions. Pre-fit and post-fit distributions of the GBDT discriminant in the validation regions are shown in Figure 4.35. Event yields pre-fit and post-fit in the validation regions are shown in Table 4.23. For both validation regions, an increase on the $VV + HF$ contribution can be seen in the post-fit background and an agreement between data and prediction within one sigma is observed for the majority of the bins.

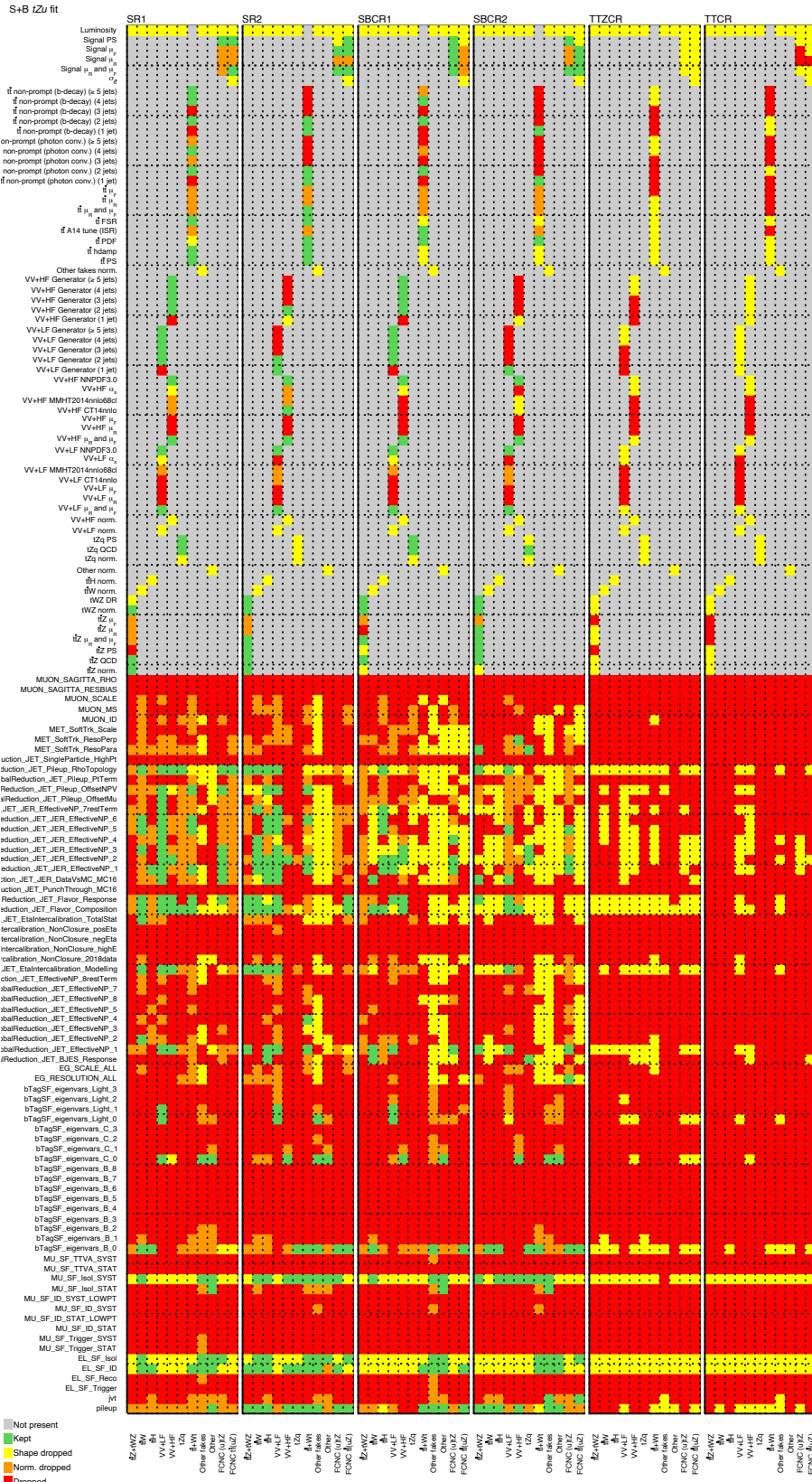


Figure 4.28: Pruning of the nuisance parameters for the signal-plus-background tZu fit in the signal and control regions with realistic Asimov data from the control regions.

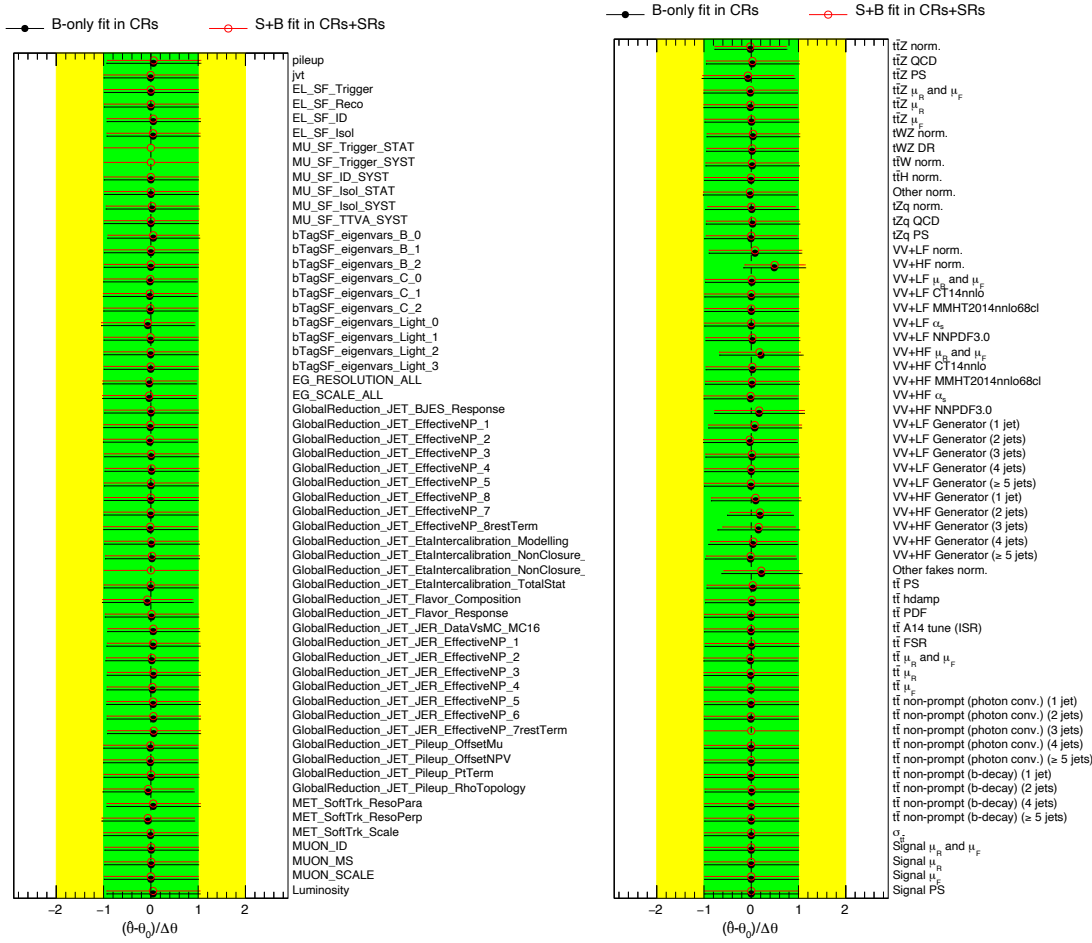


Figure 4.29: Pulls and constraints of the instrumental (left) and the theoretical and modeling (right) nuisance parameters for the signal-plus-background tZu fit in the signal and control regions with realistic Asimov data from the control regions (in red). Results for the background-only tZu fit in the control regions with real data are also shown (in black).

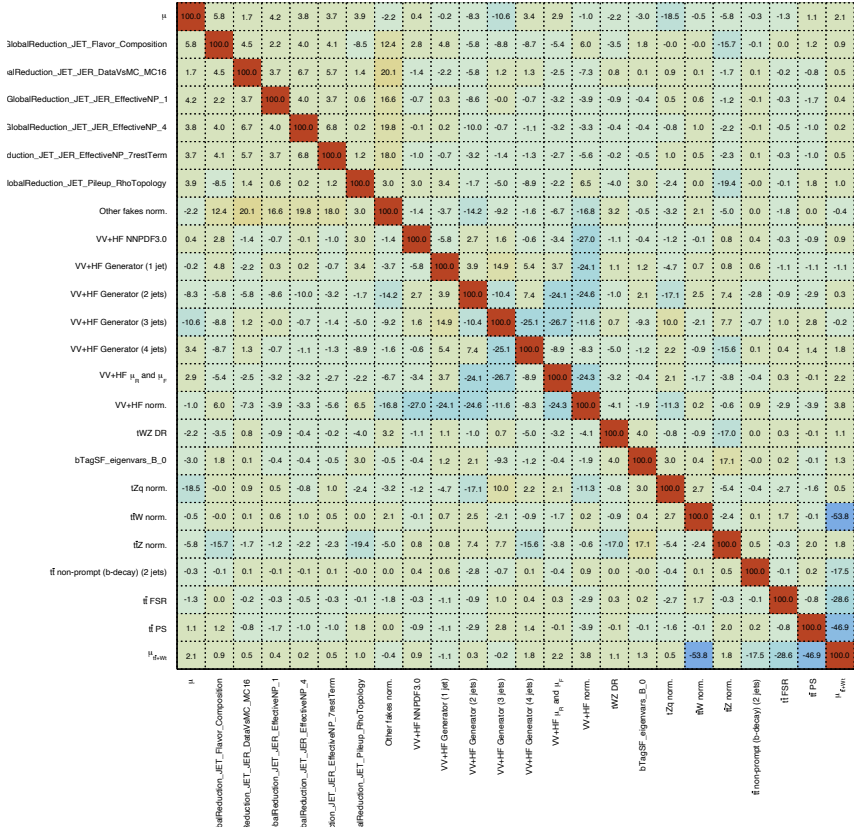


Figure 4.30: Correlation matrix of the nuisance parameters for the signal-plus-background tZu fit in the signal and control regions with realistic Asimov data from the control regions.

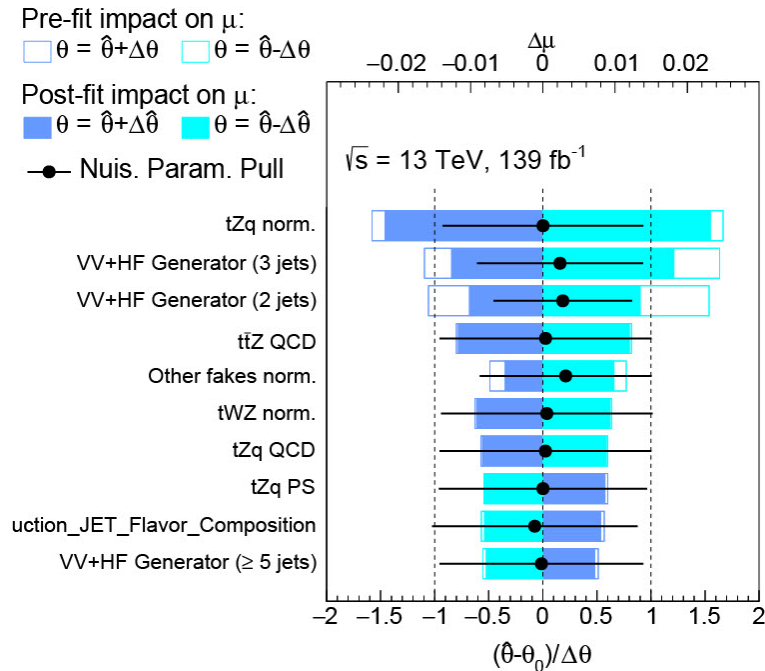


Figure 4.31: Ranking of the nuisance parameters for the signal-plus-background tZu fit in the signal and control regions with realistic Asimov data from the control regions.

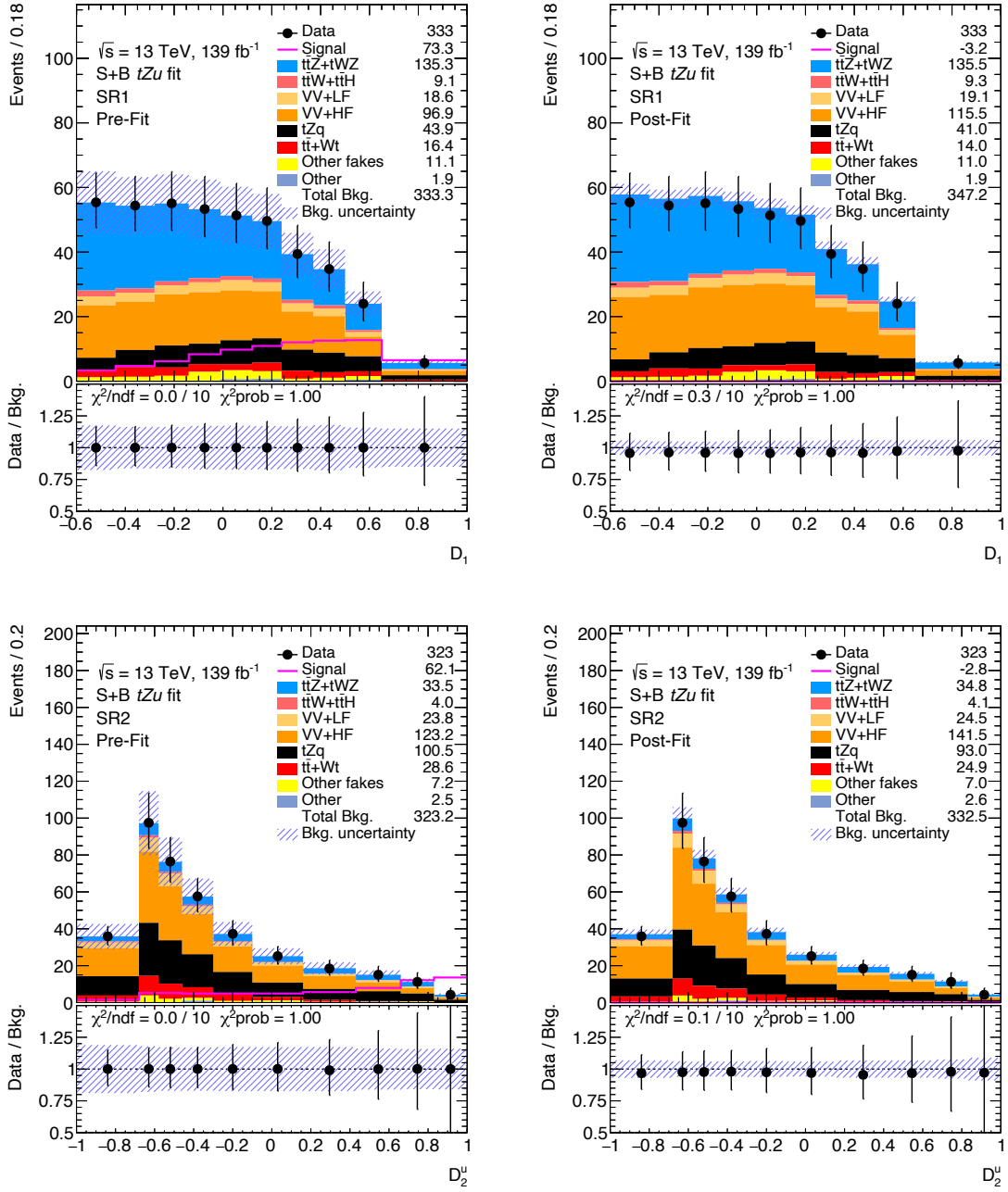


Figure 4.32: Pre-fit (left) and post-fit (right) BDTG output distributions in the signal regions for the signal-plus-background $t\bar{t}Zu$ fit in the signal and control regions with realistic Asimov data from the control regions. The uncertainty band includes both statistical and systematic uncertainties.

Pre-fit	SR1	SR2	Side-band CR1	Side-band CR2	$t\bar{t} Z$ CR	$t\bar{t}$ CR
$t\bar{t} Z + tWZ$	135 ± 17	33 ± 6	97 ± 16	7.6 ± 1.4	229 ± 31	15.0 ± 2.0
$t\bar{t} W$	4.4 ± 2.2	3.1 ± 1.6	4.6 ± 2.3	2.2 ± 1.1	3.2 ± 1.6	2.7 ± 14
$t\bar{t} H$	4.8 ± 0.8	0.85 ± 0.17	2.5 ± 0.4	0.31 ± 0.07	7.6 ± 1.2	14.1 ± 2.2
VV + LF	19 ± 8	24 ± 8	27 ± 11	12 ± 4	0.25 ± 0.21	0.40 ± 0.28
VV + HF	100 ± 50	120 ± 50	130 ± 60	51 ± 17	18 ± 12	2.3 ± 1.0
tZq	44 ± 8	101 ± 19	21 ± 4	6.2 ± 1.4	20 ± 5	0.90 ± 0.21
$t\bar{t} + W$	16 ± 4	29 ± 10	10.2 ± 3.3	7.8 ± 2.5	4.8 ± 1.2	1.05 ± 18
Other fakes	11 ± 11	7 ± 8	4 ± 5	2.8 ± 3.5	0.24 ± 0.32	0.12 ± 0.14
Other	1.9 ± 1.2	2.5 ± 2.7	3.2 ± 2.8	0.7 ± 0.6	1.8 ± 1.0	3.0 ± 1.5
FCNC ($u\bar{t}Z$)	12.2 ± 1.9	52.0 ± 3.0	5.1 ± 0.6	2.27 ± 0.27	1.2 ± 0.4	0.66 ± 0.10
FCNC $t\bar{t}$ ($u\bar{Z}$)	61 ± 5	10.0 ± 1.4	1.8 ± 0.5	0.45 ± 0.19	1.43 ± 0.26	0.24 ± 0.05
Total background	330 ± 50	320 ± 50	300 ± 70	91 ± 19	280 ± 40	168 ± 23
Data	333	323	343	104	286	157
Data / Bkg.	1.00 ± 0.17	1.00 ± 0.18	1.14 ± 0.26	1.00 ± 0.14	0.94 ± 0.15	

Table 4.21: Pre-fit event yields in the signal-plus-background tZu fit in the signal and control regions with realistic Asimov data from the control regions. The error includes both statistical and systematic uncertainties.

Post-fit	SR1	SR2	Side-band CR1	Side-band CR2	$t\bar{t} Z$ CR	$t\bar{t}$ CR
$t\bar{t} Z + tWZ$	135 ± 12	35 ± 6	101 ± 14	8.0 ± 1.3	228 ± 18	15.3 ± 1.5
$t\bar{t} W$	4.5 ± 2.1	3.3 ± 1.6	4.8 ± 2.3	2.4 ± 1.2	3.2 ± 1.6	28 ± 13
$t\bar{t} H$	4.7 ± 0.7	0.87 ± 0.16	2.6 ± 0.4	0.31 ± 0.07	7.5 ± 1.2	14.0 ± 2.2
VV + LF	19 ± 8	25 ± 8	28 ± 11	12 ± 4	0.26 ± 0.20	0.41 ± 0.27
VV + HF	115 ± 20	141 ± 23	160 ± 25	60 ± 9	21 ± 9	2.7 ± 0.5
tZq	41 ± 7	93 ± 16	20 ± 4	5.9 ± 1.2	19 ± 5	0.86 ± 0.18
$t\bar{t} + W$	14.0 ± 3.4	25 ± 7	8.9 ± 2.4	6.8 ± 1.9	4.1 ± 1.3	91 ± 18
Other fakes	11 ± 10	7 ± 6	5 ± 8	3 ± 4	0.24 ± 0.23	0.12 ± 0.11
Other	1.9 ± 1.0	2.6 ± 2.6	2.9 ± 2.5	0.7 ± 0.4	1.8 ± 0.9	3.0 ± 1.5
FCNC ($u\bar{t}Z$)	0.5 ± 1.4	2 ± 6	0.2 ± 0.6	-0.10 ± 0.26	-0.05 ± 0.14	-0.03 ± 0.08
FCNC $t\bar{t}$ ($u\bar{Z}$)	-3 ± 7	-0.5 ± 1.2	-0.08 ± 0.21	-0.02 ± 0.06	-0.06 ± 0.16	-0.010 ± 0.027
Total background	347 ± 15	332 ± 18	332 ± 17	99 ± 8	285 ± 16	156 ± 13
Data	333	323	343	104	286	157
Data / Bkg.	0.96 ± 0.04	0.97 ± 0.05	1.03 ± 0.05	1.05 ± 0.09	1.00 ± 0.06	1.00 ± 0.08

Table 4.22: Post-fit event yields in the signal-plus-background tZu fit in the signal and control regions with realistic Asimov data from the control regions. The error includes both statistical and systematic uncertainties.

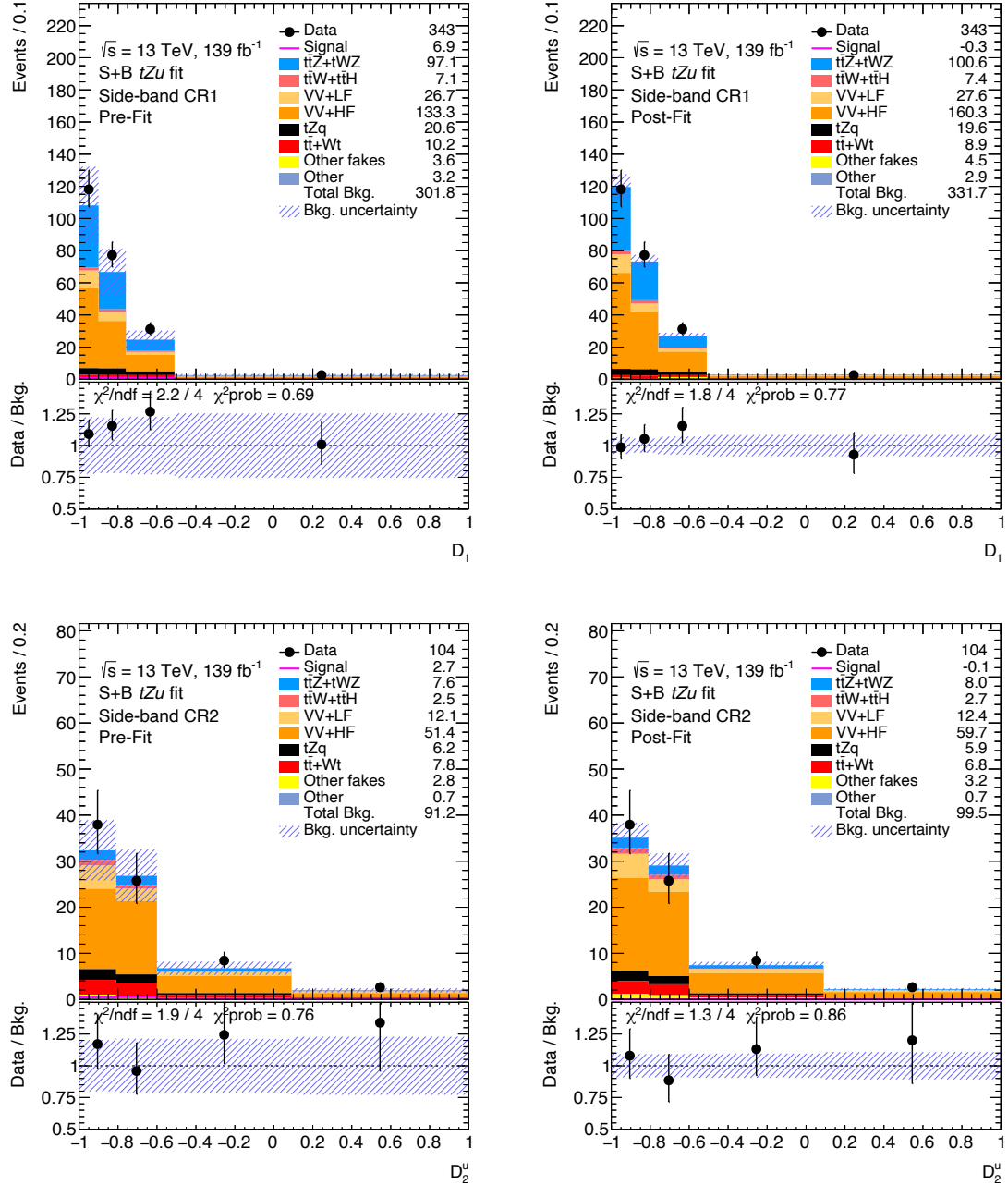


Figure 4.33: Pre-fit (left) and post-fit (right) BDTG output distributions in the side-band control regions for the signal-plus-background tZu fit in the signal and control regions with realistic Asimov data from the control regions. The uncertainty band includes both statistical and systematic uncertainties.

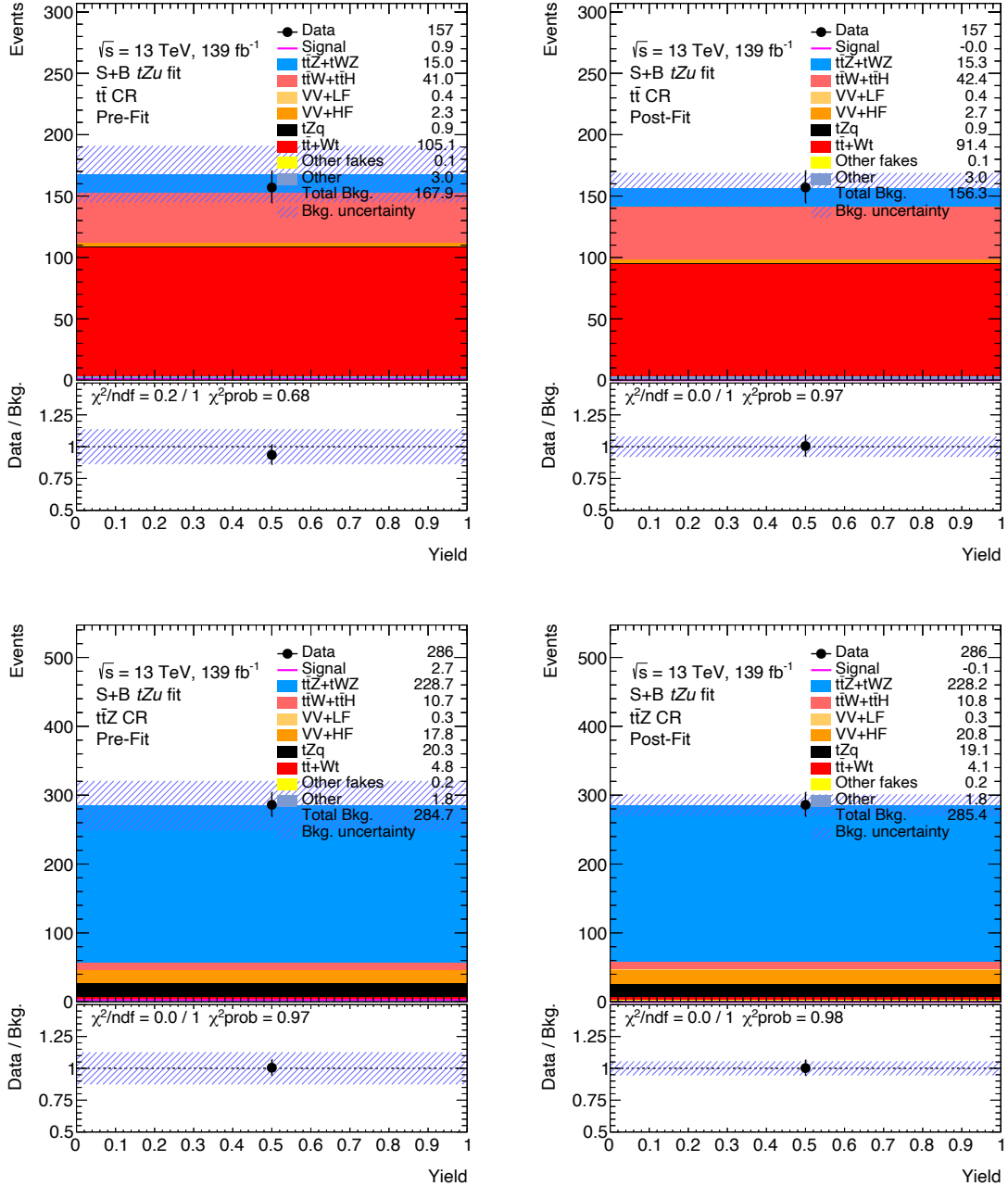


Figure 4.34: Pre-fit (left) and post-fit (right) event yield distributions in the $t\bar{t}$ and $t\bar{t}Z$ control regions for the signal-plus-background tZu fit in the signal and control regions with realistic Asimov data from the control regions. The uncertainty band includes both statistical and systematic uncertainties.

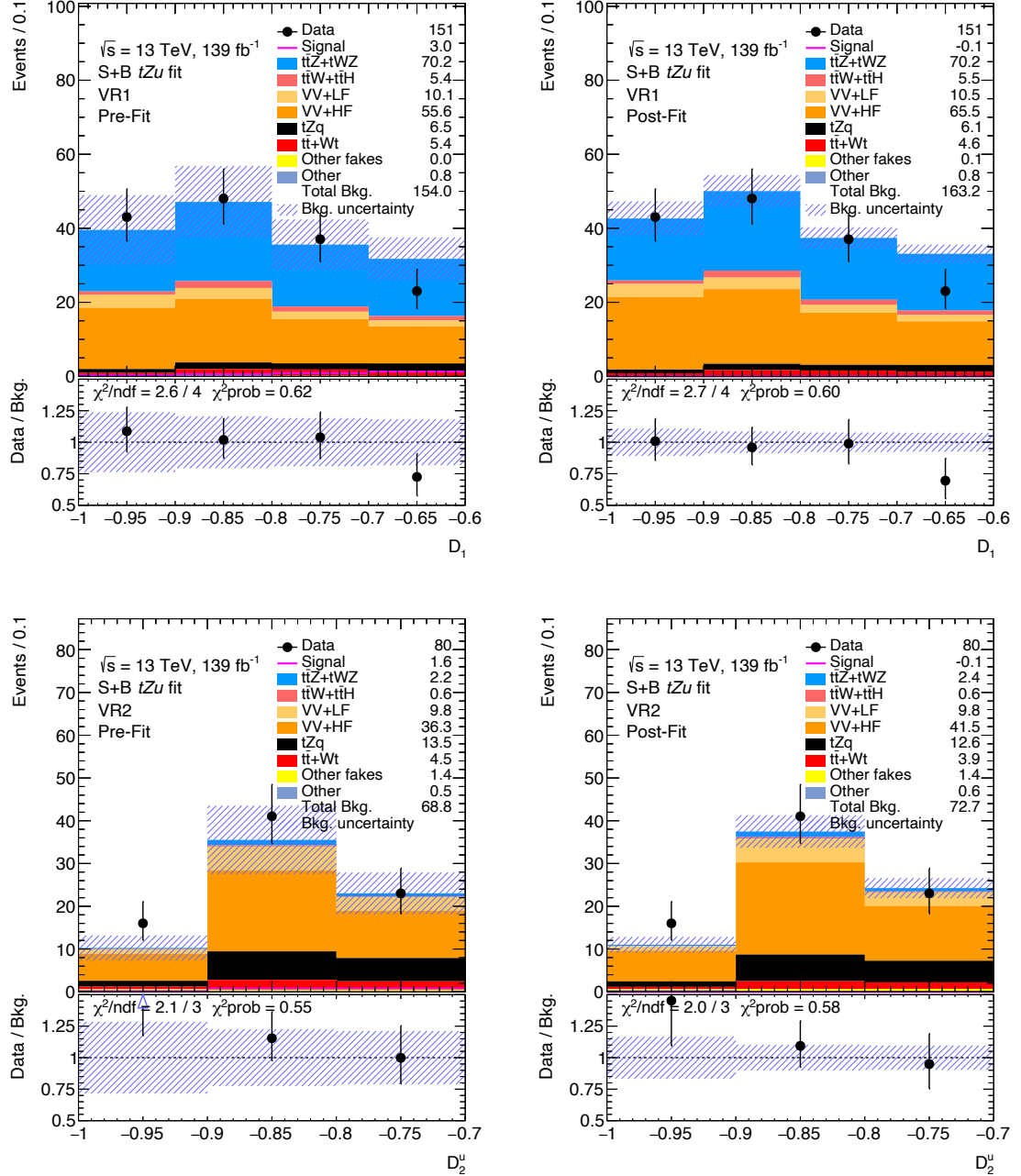


Figure 4.35: Pre-fit (left) and post-fit (right) BDTG output distributions in the validation regions for the signal-plus-background tZu fit in the signal and control regions with realistic Asimov data from the control regions. The uncertainty band includes both statistical and systematic uncertainties.

Pre-fit	VR1	VR2	Post-fit	VR1	VR2
$t\bar{t}Z + tWZ$	70 ± 10	2.2 ± 0.6	$t\bar{t}Z + tWZ$	70 ± 7	2.3 ± 0.5
$t\bar{t}W$	2.3 ± 1.2	0.48 ± 0.26	$t\bar{t}W$	2.4 ± 1.2	0.48 ± 0.25
$t\bar{t}H$	3.0 ± 0.5	0.101 ± 0.032	$t\bar{t}H$	3.0 ± 0.5	0.105 ± 0.030
$VV + LF$	10 ± 5	9.8 ± 3.4	$VV + LF$	10 ± 5	9.9 ± 3.1
$VV + HF$	56 ± 28	36 ± 14	$VV + HF$	69 ± 16	44 ± 7
tZq	6.5 ± 1.6	13.5 ± 2.7	tZq	6.5 ± 1.5	13.5 ± 2.4
$t\bar{t} + Wt$	5.4 ± 2.6	4.5 ± 1.7	$t\bar{t} + Wt$	4.8 ± 2.2	3.9 ± 1.4
Other fakes	0.0 ± 0.6	1.4 ± 1.9	Other fakes	0.1 ± 0.6	1.7 ± 1.7
Other	0.8 ± 0.4	0.5 ± 0.7	Other	0.8 ± 0.4	0.5 ± 0.6
FCNC ($u\bar{t}Z$)	1.14 ± 0.23	0.91 ± 0.16	FCNC ($u\bar{t}Z$)	0.00 ± 0.15	0.00 ± 0.12
FCNC $t\bar{t}$ ($u\bar{Z}$)	1.91 ± 0.34	0.69 ± 0.12	FCNC $t\bar{t}$ ($u\bar{Z}$)	0.00 ± 0.24	0.00 ± 0.09
Total background	154 ± 31	69 ± 15	Total background	167 ± 14	77 ± 7
Data	151	80	Data	151	80
Data / Bkg.	0.98 ± 0.22	1.16 ± 0.29	Data / Bkg.	0.90 ± 0.08	1.04 ± 0.10
S / \sqrt{B}	0.020	0.023	S / \sqrt{B}	0.000	0.000

Table 4.23: Pre-fit (left) and post-fit (right) event yields in the signal-plus-background tZu fit in the validation regions with realistic Asimov data from the control regions. The error includes both statistical and systematic uncertainties.

4.8.3.3 Signal-plus-background fit for tZc coupling in the signal and control regions with realistic Asimov data from the control regions

The result of the pruning applied on the fit for each sample and for each region is shown in Figure 4.36. The fitted nuisance parameters for the signal-plus-background hypothesis are represented in Figure 4.37. The normalisation factor for $t\bar{t} + Wt$ background processes is found to be 0.89 ± 0.23 , being similar to the correspondent value obtained for the tZu fit. The corresponding correlation matrix of the nuisance parameters can be found in Figure 4.38. The nuisance parameters with highest correlation to the signal strength are the following: $VV + HF$ generator (3 jets) with 18.9%, tZq normalisation with 17.1% and $t\bar{t}Z$ normalisation with 11.3%. The ranking of the ten most important nuisance parameters is shown in Figure 4.39, being mainly composed by the normalisation of the main backgrounds. Pre-fit and post-fit distributions of the fitted distributions in the signal and control regions are shown in Figures 4.40 and 4.41 and section 4.8.3.3. The corresponding pre-fit and post-fit event yields in the signal and control regions are shown in Tables 4.24 and 4.25. Similarly to the tZu fit, the fitted nuisance parameters were propagated to the validation regions. Pre-fit and post-fit event yields in the validation regions are shown in Table 4.26. The pre-fit and post-fit distributions of the GBDT discriminant in the validation regions are shown in Figure 4.42. A better agreement between data and prediction can be seen in the post-fit distributions with most of the bins within one sigma uncertainties, while having some bins with a worst agreement due to the low statistics.



Figure 4.36: Pruning of the nuisance parameters for the signal-plus-background tZc fit in the signal and control regions with realistic Asimov data from the control regions.

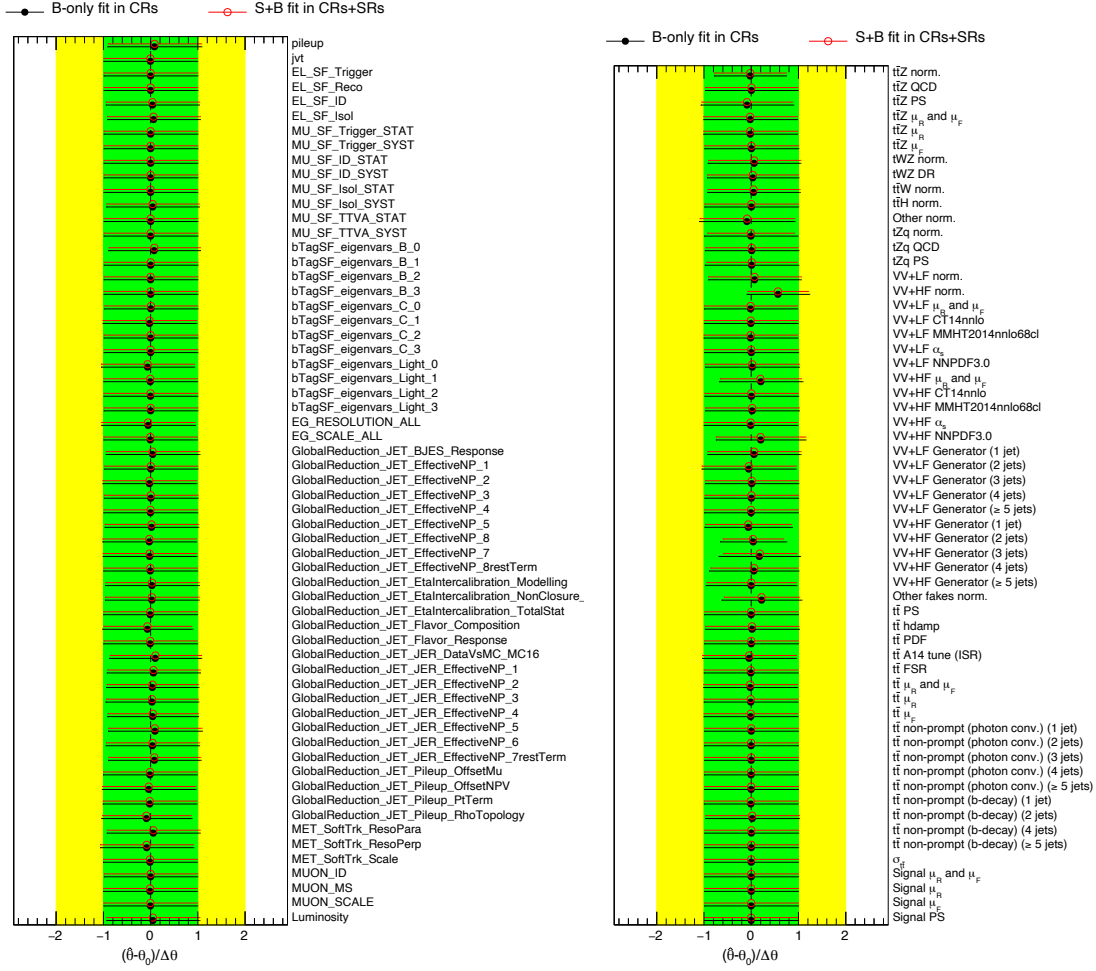


Figure 4.37: Pulls and constraints of the instrumental (left) and the theoretical and modeling (right) nuisance parameters for the signal-plus-background tZc fit in the signal and control regions with realistic Asimov data from the control regions (in red). Results for the background-only tZc fit in the control regions with real data are also shown (in black).

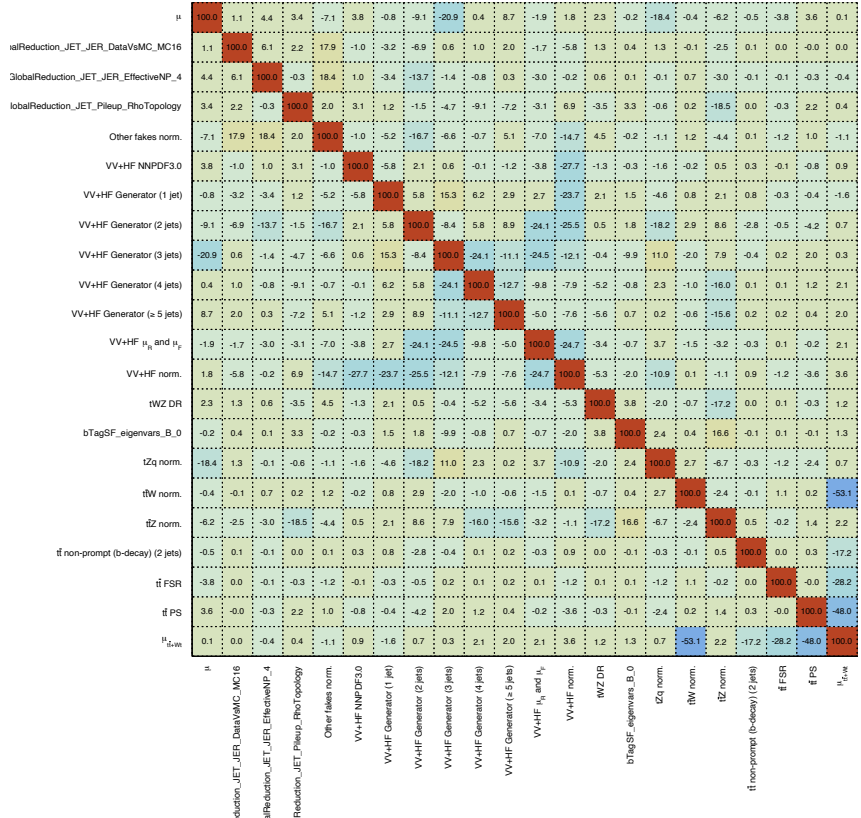


Figure 4.38: Correlation matrix of the nuisance parameters for the signal-plus-background tZc fit in the signal and control regions with realistic Asimov data from the control regions.

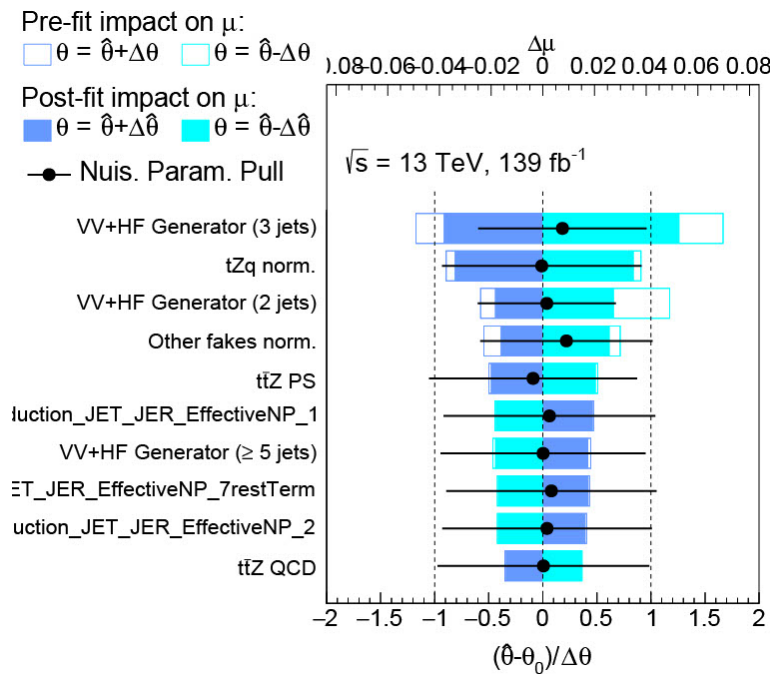


Figure 4.39: Ranking of the nuisance parameters for the signal-plus-background tZc fit in the signal and control regions with realistic Asimov data from the control regions.

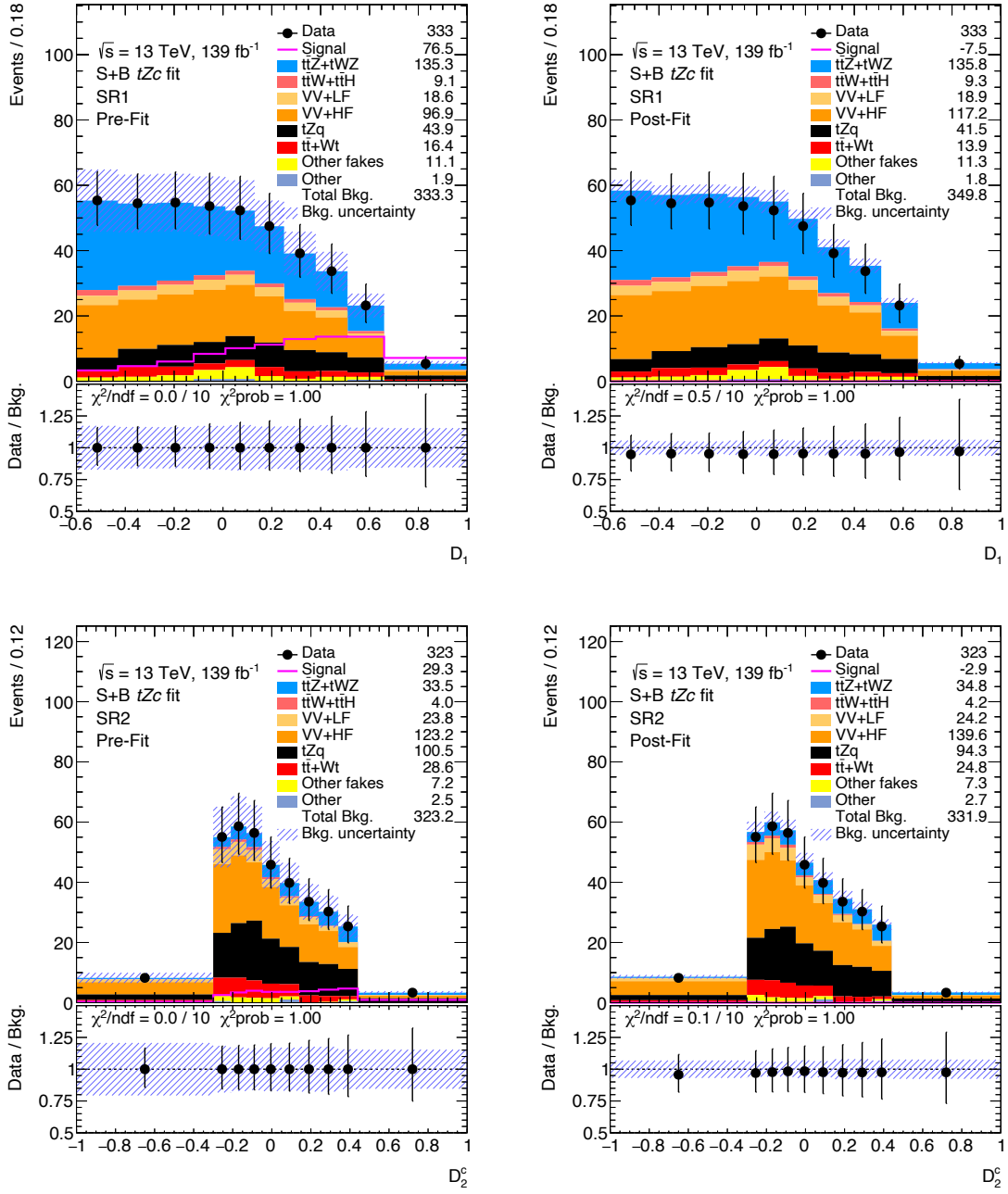


Figure 4.40: Pre-fit (left) and post-fit (right) BDTG output distributions in the signal region for the signal-plus-background tZc fit in the signal and control regions with realistic Asimov data from the control regions. The uncertainty band includes both statistical and systematic uncertainties.

Pre-fit	SR1	SR2	Side-band CR1	Side-band CR2	$t\bar{t}Z$ CR	$t\bar{t}$ CR
$t\bar{t}Z + tWZ$	135 ± 17	33 ± 6	97 ± 16	7.6 ± 1.4	229 ± 31	15.0 ± 2.0
$t\bar{t}W$	4.4 ± 2.2	3.1 ± 1.6	4.6 ± 2.3	2.2 ± 1.1	3.2 ± 1.6	27 ± 14
$t\bar{t}H$	4.8 ± 0.8	0.85 ± 0.17	2.5 ± 0.4	0.31 ± 0.07	7.6 ± 1.2	14.1 ± 2.2
$VV + LF$	19 ± 8	24 ± 8	27 ± 11	12 ± 4	0.25 ± 0.21	0.40 ± 0.28
$VV + HF$	100 ± 50	120 ± 50	130 ± 60	51 ± 17	18 ± 12	2.3 ± 1.0
tZq	44 ± 8	101 ± 19	21 ± 4	6.2 ± 1.3	20 ± 5	0.90 ± 0.21
$t\bar{t} + Wt$	16 ± 4	29 ± 9	10.2 ± 3.3	7.8 ± 2.4	4.8 ± 1.2	1.05 ± 18
Other fakes	11 ± 11	7 ± 8	4 ± 5	2.8 ± 3.5	0.24 ± 0.32	0.12 ± 0.14
Other	1.9 ± 1.2	2.5 ± 2.5	3.2 ± 2.8	0.7 ± 0.5	1.8 ± 1.0	3.0 ± 1.5
FCNC (tZ)	3.3 ± 0.6	12.0 ± 0.8	1.06 ± 0.11	0.55 ± 0.05	0.33 ± 0.07	0.104 ± 0.016
FCNC $t\bar{t}$ (cZ)	73 ± 6	17.4 ± 1.8	4.8 ± 0.5	1.53 ± 0.21	5.1 ± 1.0	0.34 ± 0.08
Total background	330 ± 50	320 ± 50	300 ± 70	91 ± 19	280 ± 40	168 ± 23
Data	333	323	343	104	286	157
Data / Bkg.	1.00 ± 0.17	1.00 ± 0.18	1.14 ± 0.25	1.14 ± 0.26	1.00 ± 0.14	0.94 ± 0.15

Table 4.24: Pre-fit event yields in the signal-plus-background tZc fit in the signal and control regions with realistic Asimov data from the control regions. The error includes both statistical and systematic uncertainties.

Post-fit	SR1	SR2	Side-band CR1	Side-band CR2	$t\bar{t}Z$ CR	$t\bar{t}$ CR
$t\bar{t}Z + tWZ$	136 ± 12	35 ± 6	101 ± 14	8.0 ± 1.3	228 ± 18	15.4 ± 1.5
$t\bar{t}W$	4.6 ± 2.2	3.3 ± 1.6	4.9 ± 2.3	2.4 ± 1.2	3.3 ± 1.6	29 ± 13
$t\bar{t}H$	4.7 ± 0.7	0.87 ± 0.16	2.6 ± 0.4	0.32 ± 0.07	7.5 ± 1.2	14.1 ± 2.2
$VV + LF$	19 ± 7	24 ± 8	27 ± 11	12 ± 4	0.25 ± 0.20	0.40 ± 0.26
$VV + HF$	117 ± 20	140 ± 23	162 ± 25	60 ± 9	21 ± 10	2.7 ± 0.5
tZq	41 ± 7	94 ± 15	20 ± 4	6.0 ± 1.2	19 ± 5	0.87 ± 0.18
$t\bar{t} + Wt$	13.9 ± 3.4	25 ± 7	8.8 ± 2.3	6.7 ± 1.8	4.1 ± 1.3	91 ± 18
Other fakes	11 ± 10	7 ± 6	5 ± 8	3 ± 4	0.25 ± 0.23	0.13 ± 0.11
Other	1.8 ± 1.0	2.7 ± 2.5	2.7 ± 2.2	0.7 ± 0.4	1.8 ± 0.9	2.9 ± 1.5
FCNC (tZ)	-0.3 ± 0.6	-1.2 ± 2.3	-0.11 ± 0.20	-0.05 ± 0.10	-0.03 ± 0.06	-0.010 ± 0.019
FCNC $t\bar{t}$ (cZ)	-7 ± 14	-1.7 ± 3.3	-0.5 ± 0.9	-0.15 ± 0.29	-0.5 ± 0.9	-0.03 ± 0.06
Total background	350 ± 16	332 ± 18	333 ± 17	100 ± 8	286 ± 16	156 ± 13
Data	333	323	343	104	286	157
Data / Bkg.	0.95 ± 0.04	0.97 ± 0.05	1.03 ± 0.05	1.04 ± 0.09	1.00 ± 0.06	1.01 ± 0.08

Table 4.25: Post-fit event yields in the signal-plus-background tZc fit in the signal and control regions with realistic Asimov data from the control regions. The error includes both statistical and systematic uncertainties.

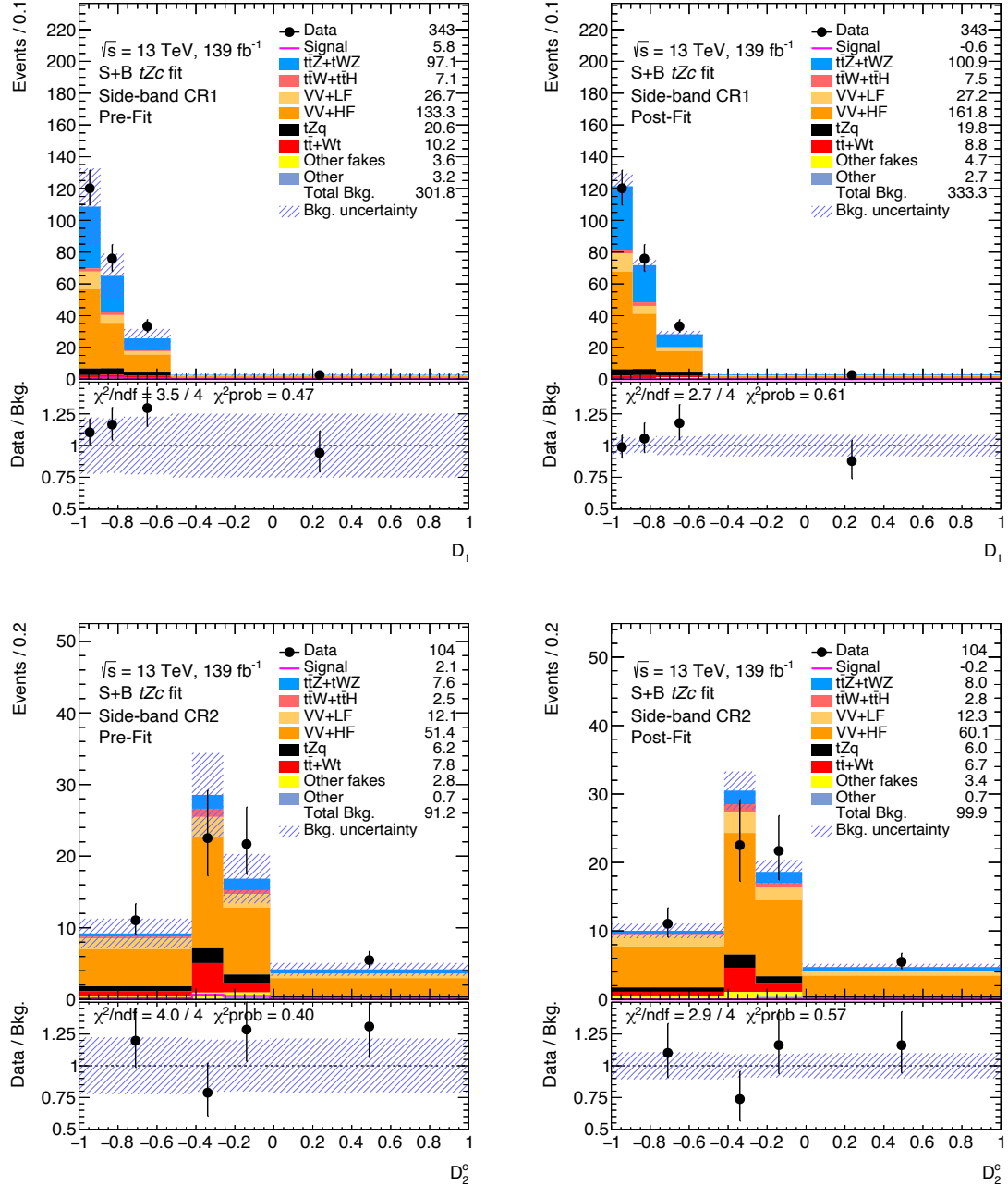
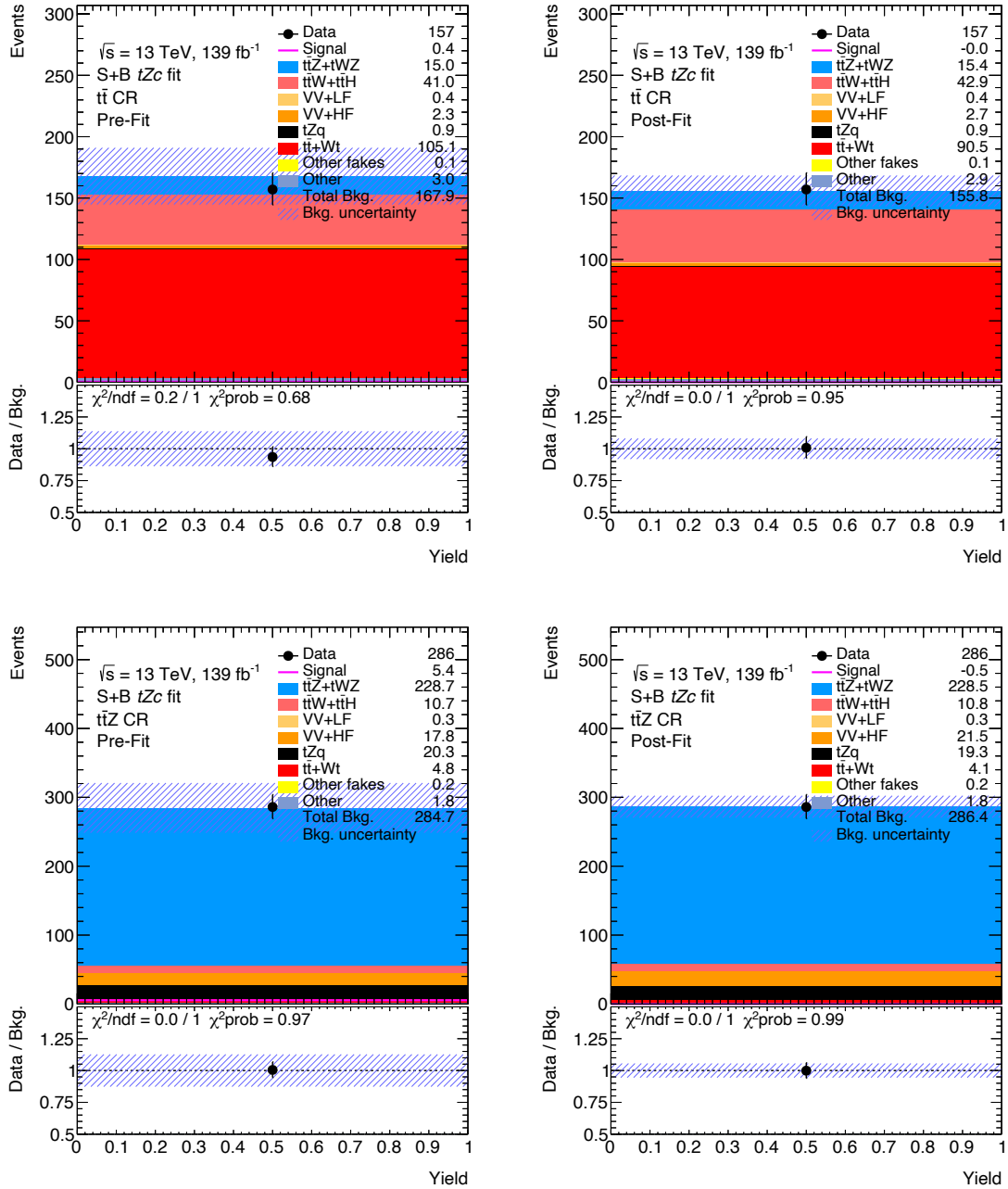


Figure 4.41: Pre-fit (left) and post-fit (right) BDTG output distributions in the side-band control regions for the signal-plus-background tZ_c fit in the signal and control regions with realistic Asimov data from the control regions. The uncertainty band includes both statistical and systematic uncertainties.



and post-fit event yield distributions in the $t\bar{t}$ and $t\bar{t}Z$ control regions for the S+B tZc fit in the SRs+CRs with realistic Asimov data. Pre-fit (left) and post-fit (right) event yield distributions in the $t\bar{t}$ and $t\bar{t}Z$ control regions for the signal-plus-background tZc fit in the signal and control regions with realistic Asimov data from the control regions. The uncertainty band includes both statistical and systematic uncertainties.

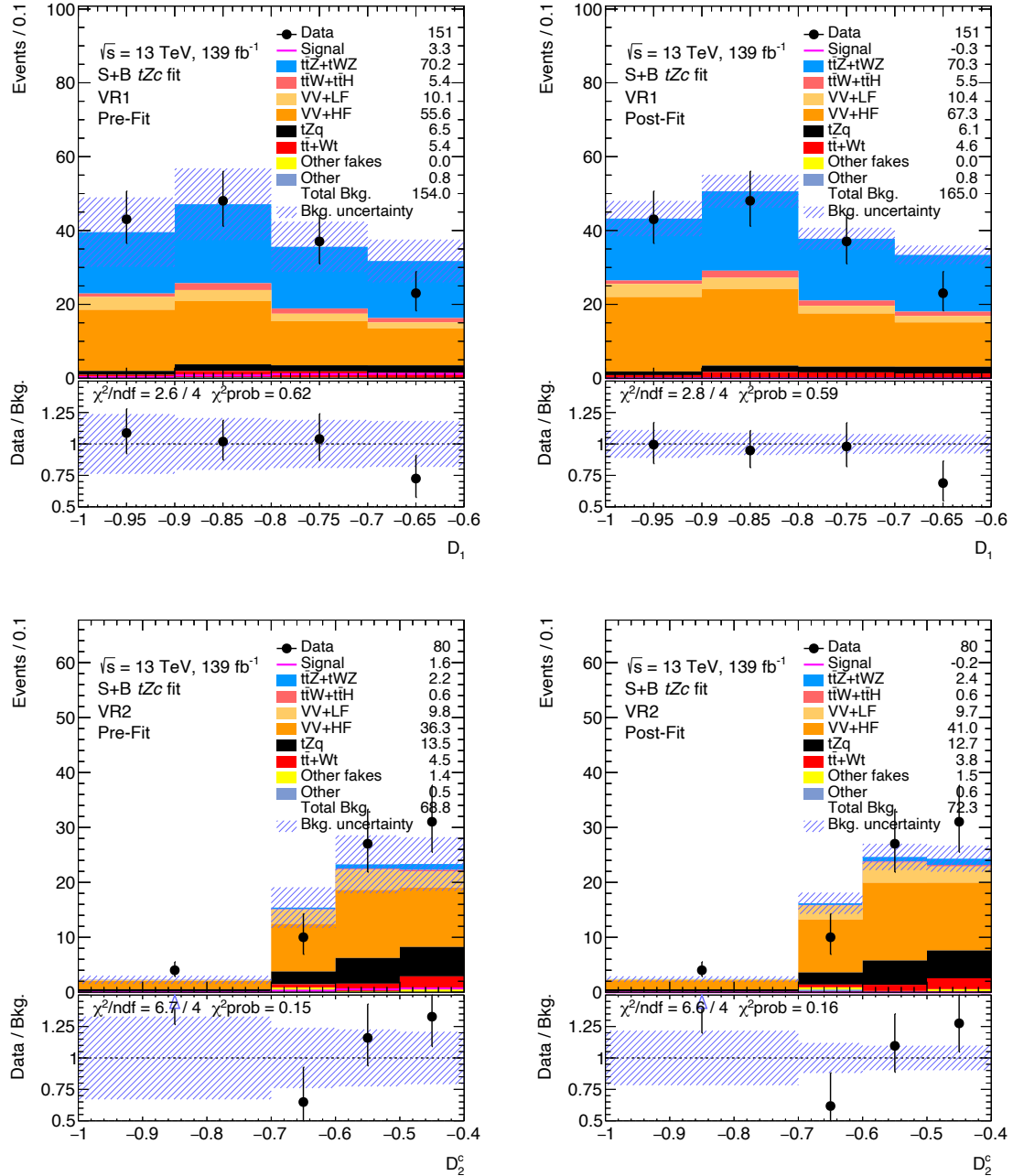


Figure 4.42: Pre-fit (left) and post-fit (right) BDTG output distributions in the validation regions for the signal-plus-background tZc fit in the signal and control regions with realistic Asimov data from the control regions. The uncertainty band includes both statistical and systematic uncertainties.

Pre-fit	VR1	VR2	Post-fit	VR1	VR2
$t\bar{t}Z + tWZ$	70 ± 10	2.2 ± 0.6	$t\bar{t}Z + tWZ$	71 ± 7	2.3 ± 0.6
$t\bar{t}W$	2.3 ± 1.2	0.48 ± 0.26	$t\bar{t}W$	2.4 ± 1.2	0.49 ± 0.25
$t\bar{t}H$	3.0 ± 0.5	0.101 ± 0.032	$t\bar{t}H$	3.0 ± 0.5	0.106 ± 0.031
$VV + LF$	10 ± 5	9.8 ± 3.4	$VV + LF$	10 ± 5	9.8 ± 3.1
$VV + HF$	56 ± 28	36 ± 14	$VV + HF$	71 ± 16	44 ± 7
tZq	6.5 ± 1.6	13.5 ± 2.7	tZq	6.5 ± 1.5	13.5 ± 2.3
$t\bar{t} + Wt$	5.4 ± 2.6	4.5 ± 1.9	$t\bar{t} + Wt$	4.8 ± 2.2	3.8 ± 1.4
Other fakes	0.0 ± 0.6	1.4 ± 1.9	Other fakes	0.1 ± 0.6	1.8 ± 1.7
Other	0.8 ± 0.4	0.5 ± 0.7	Other	0.7 ± 0.4	0.5 ± 0.6
FCNC (c) tZ	0.30 ± 0.07	0.34 ± 0.04	FCNC (c) tZ	-0.00 ± 0.06	-0.00 ± 0.07
FCNC $t\bar{t}$ (cZ)	3.0 ± 0.6	1.23 ± 0.34	FCNC $t\bar{t}$ (cZ)	-0.0 ± 0.6	-0.01 ± 0.26
Total background	154 ± 31	69 ± 15	Total background	169 ± 15	76 ± 7
Data	151	80	Data	151	80
Data / Bkg.	0.98 ± 0.22	1.16 ± 0.29	Data / Bkg.	0.89 ± 0.08	1.05 ± 0.09
S / \sqrt{B}	0.021	0.023	S / \sqrt{B}	-0.000	-0.000

Table 4.26: Pre-fit (left) and post-fit (right) event yields in the signal-plus-background tZc fit in the validation regions with realistic Asimov data from the control regions. The error includes both statistical and systematic uncertainties.

4.8.3.4 Likelihood fit with real data

After detailed studies, the fit was performed with the full measured data and the obtained results for tZu and tZc anomalous couplings are described in the following sections. Since the real data is used for all regions, the validation regions merged with the signal regions resulting in the full signal regions as described in Table 4.4, i.e. without cutting on the multivariate discriminants.

4.8.3.5 Signal-plus-background fit for tZu coupling in the signal and control regions with real data

The profile likelihood fit for the tZu anomalous coupling has been performed in the background control and signal regions with real data under the signal-plus-background hypothesis. The fitted nuisance parameters are represented in Figure 4.43. The fitted values are within their prior uncertainties, which is an indication that the data is well modeled with the MC within the uncertainties. The normalisation factor for $t\bar{t} + Wt$ background processes is found to be 0.85 ± 0.22 in agreement with the correspondent value obtained for the blinded tZu fit. The corresponding correlation matrix for the fitted nuisance parameters under the signal-plus-background hypothesis can be found in Figure 4.44. Similarly to the blinded fit, the uncertainties with highest correlation with the signal strength are the tZq and $VV+HF$ normalisations as expected due to its contribution to the background prediction in the signal regions. Figures 4.45 to 4.47 show the pre-fit and post-fit plots under the signal-plus-background hypothesis for the signal and background control regions. Pre-fit and post-fit event yields in the signal and control regions are presented in Table 4.27 and Table 4.28, respectively. Good agreement between data and background expectations is observed in both signal and control regions within one sigma uncertainties and no evidence for the $t \rightarrow uZ$ processes is found.

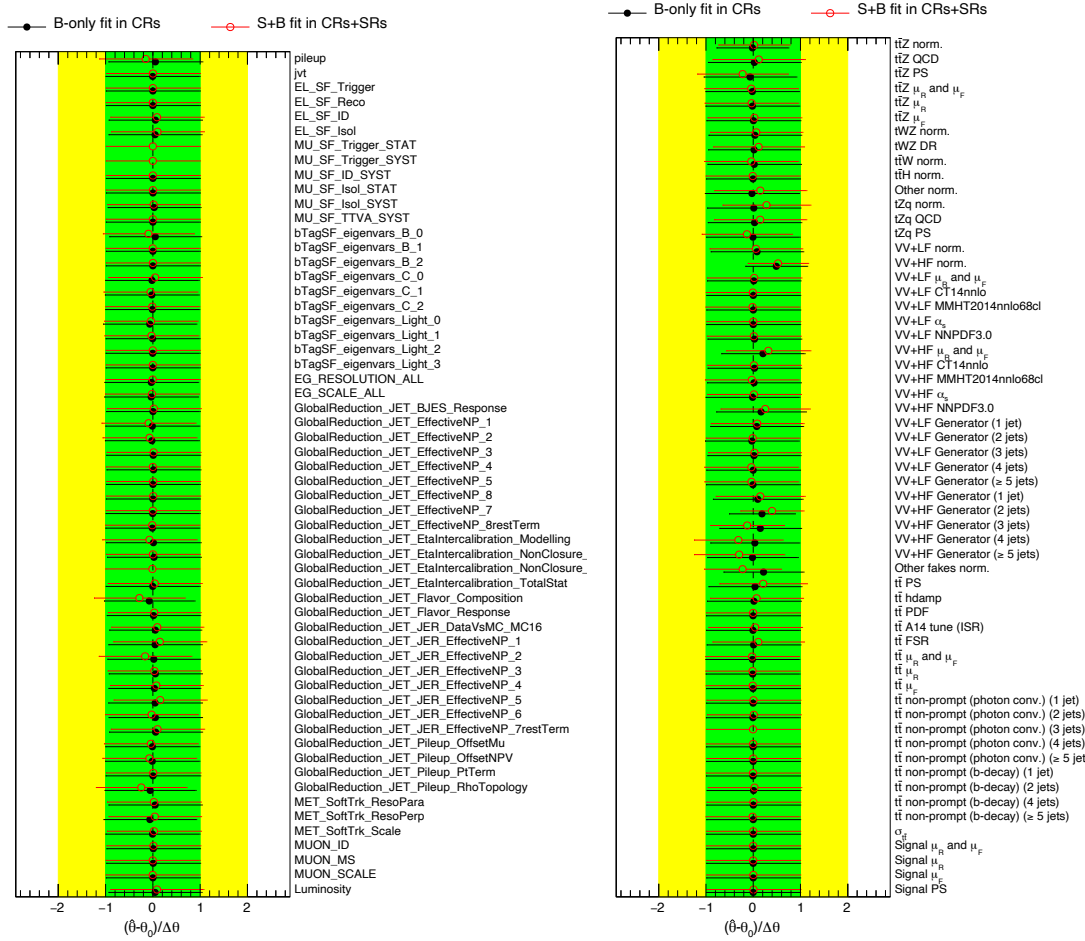


Figure 4.43: Pulls and constraints of the instrumental (left) and the theoretical and modeling (right) nuisance parameters for the signal-plus-background tZu fit in the signal and control regions with real data.

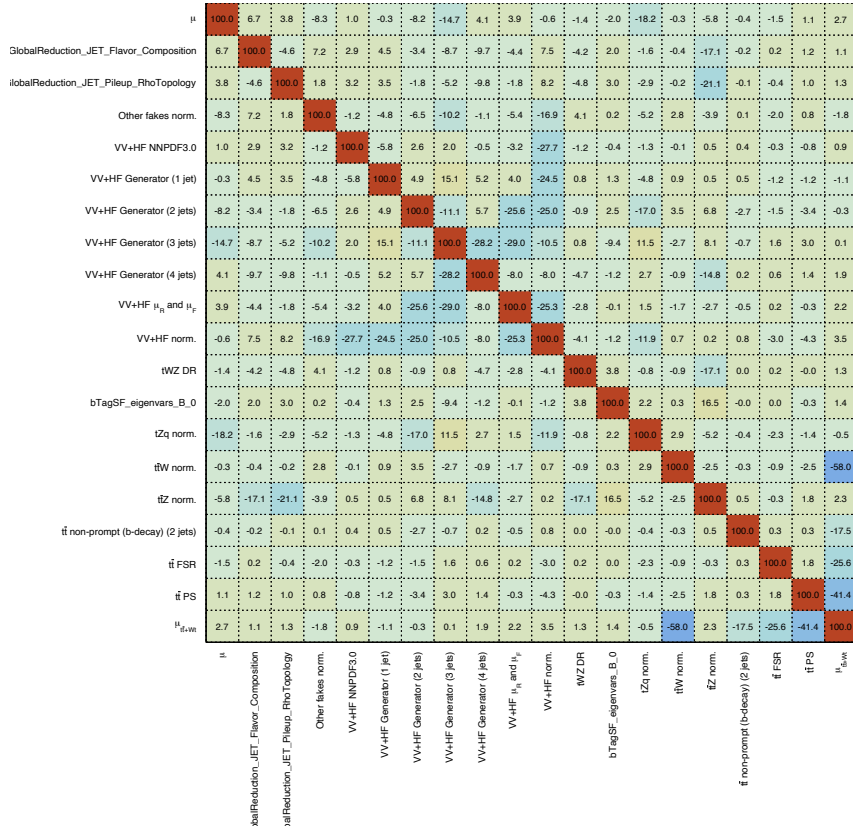


Figure 4.44: Correlation matrix of the nuisance parameters for the signal-plus-background tZu fit in the signal and control regions with real data.

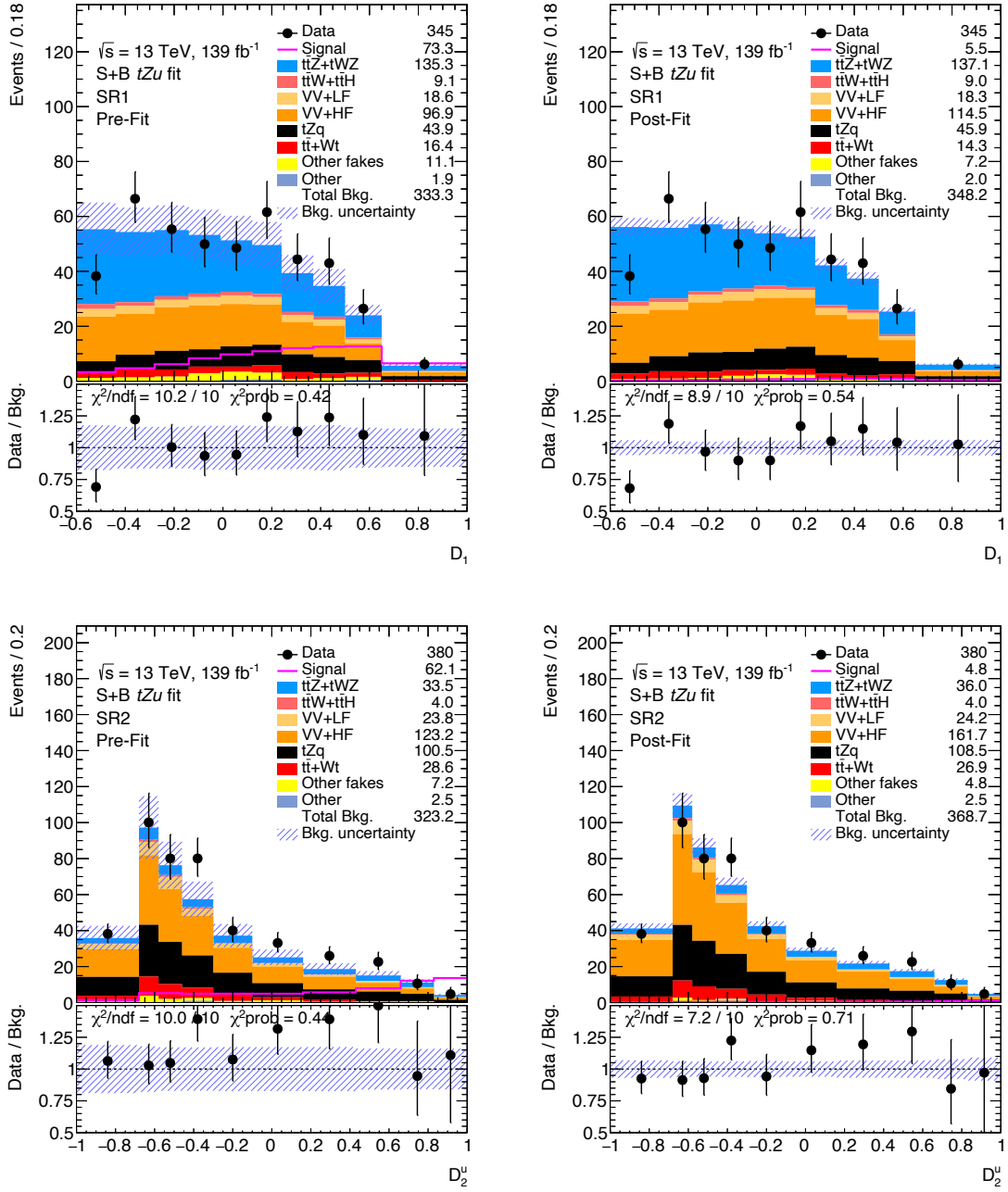


Figure 4.45: Pre-fit (left) and post-fit (right) BDTG output distributions in the signal regions for the signal-plus-background tZu fit in the signal and control regions with real data. The uncertainty band includes both statistical and systematic uncertainties.

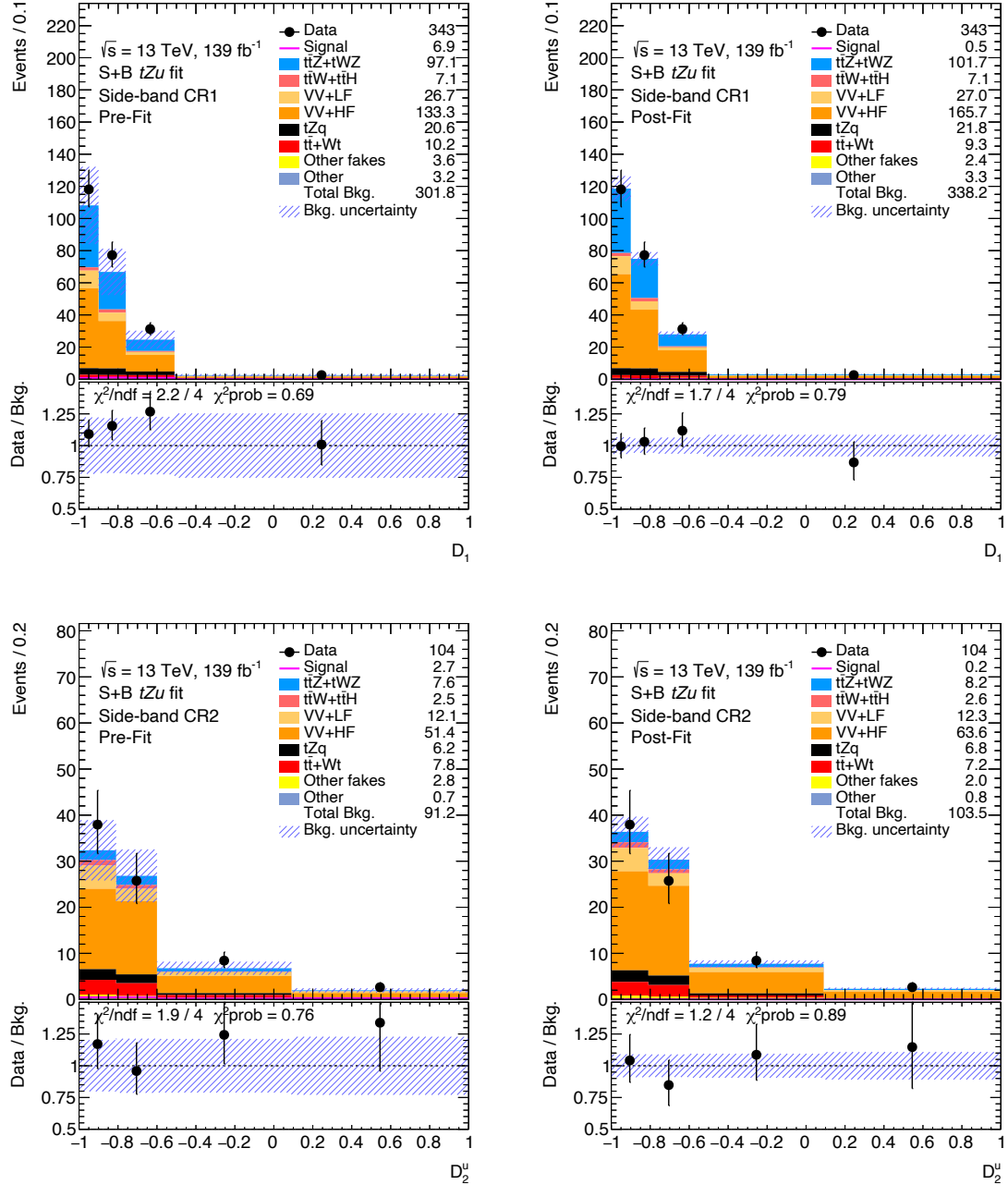


Figure 4.46: Pre-fit (left) and post-fit (right) BDTG output distributions in the side-band control regions for the signal-plus-background tZu fit in the signal and control regions with real data. The uncertainty band includes both statistical and systematic uncertainties.

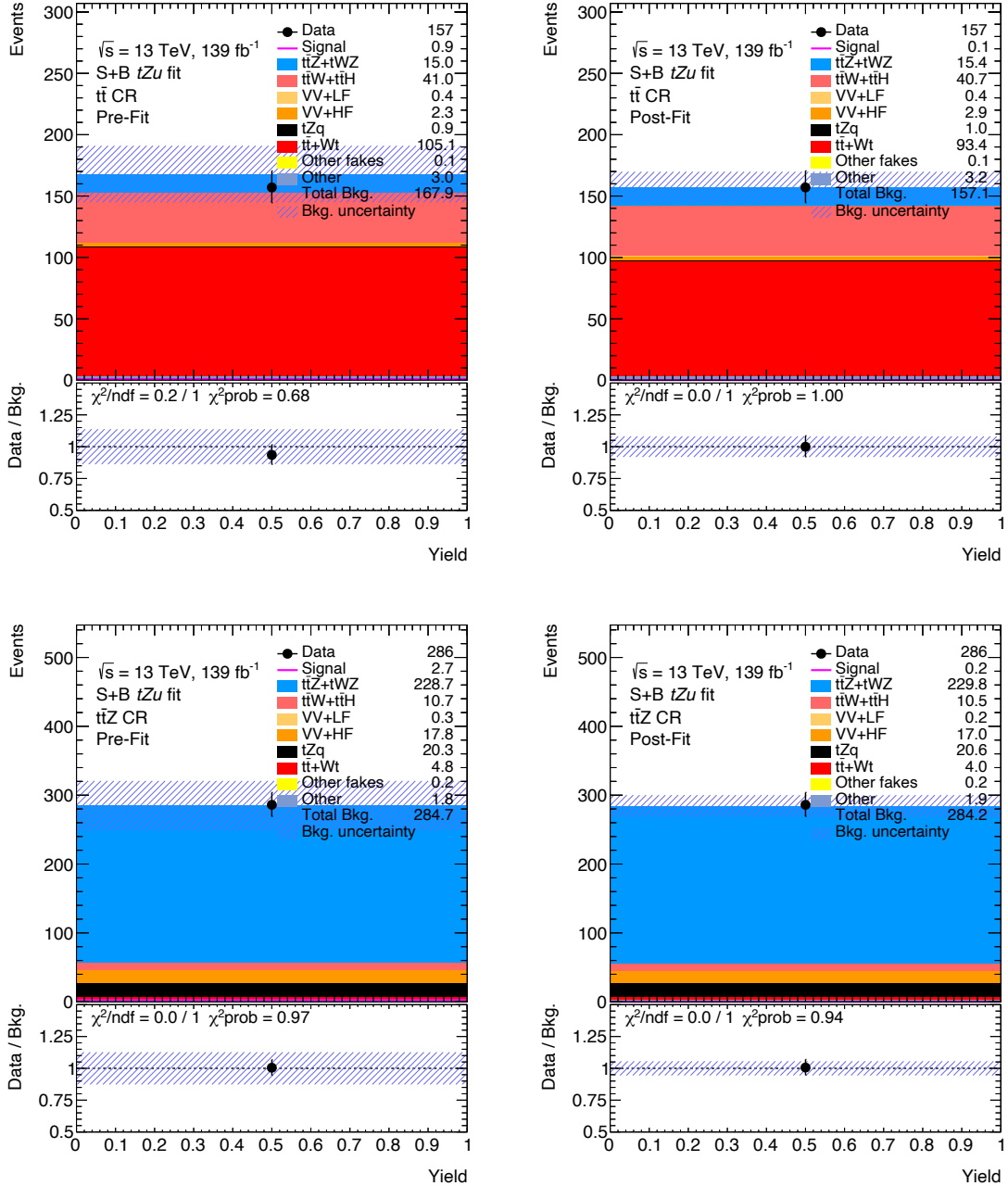


Figure 4.47: Pre-fit (left) and post-fit (right) event yield distributions in the $t\bar{t}$ and $t\bar{t}Z$ control regions for the signal-plus-background tZu fit in the signal and control regions with real data. The uncertainty band includes both statistical and systematic uncertainties.

Pre-fit	SR1	SR2	Side-band CR1	Side-band CR2	$t\bar{t}Z$ CR	$t\bar{t}$ CR
$t\bar{t}Z + tWZ$	135 ± 17	33 ± 6	97 ± 16	7.6 ± 14	229 ± 31	15.0 ± 2.0
$t\bar{t}W$	4.4 ± 2.2	3.1 ± 1.6	4.6 ± 2.3	2.2 ± 1.1	3.2 ± 1.6	27 ± 14
$t\bar{t}H$	4.8 ± 0.8	0.85 ± 0.17	2.5 ± 0.4	0.31 ± 0.07	7.6 ± 1.2	14.1 ± 2.2
VV + LF	19 ± 8	24 ± 8	27 ± 11	12 ± 4	0.25 ± 0.21	0.40 ± 0.28
VV + HF	100 ± 50	120 ± 50	130 ± 60	51 ± 17	1.8 ± 12	2.3 ± 1.0
tZq	44 ± 8	101 ± 19	21 ± 4	6.2 ± 1.4	20 ± 5	0.90 ± 0.21
$t\bar{t} + Wt$	16 ± 4	29 ± 10	10.2 ± 3.3	7.8 ± 2.5	4.8 ± 1.2	$.105 \pm 18$
Other fakes	11 ± 11	7 ± 8	4 ± 5	2.8 ± 3.5	0.24 ± 0.32	0.12 ± 0.14
Other	1.9 ± 1.2	2.5 ± 2.7	3.2 ± 2.8	0.7 ± 0.6	1.8 ± 1.0	3.0 ± 1.5
FCNC ($u\bar{t}Z$)	12.2 ± 1.9	52.0 ± 3.0	51.1 ± 0.6	2.27 ± 0.27	1.2 ± 0.4	0.66 ± 0.10
FCNC ($t\bar{t}$ ($u\bar{Z}$))	61 ± 5	10.0 ± 1.4	1.8 ± 0.5	0.45 ± 0.19	1.43 ± 0.26	0.24 ± 0.05
Total background	330 ± 50	320 ± 50	300 ± 70	91 ± 19	280 ± 40	168 ± 23
Data	345	380	343	104	286	157
Data / Bkg.	1.04 ± 0.18	1.18 ± 0.21	1.14 ± 0.25	1.14 ± 0.26	1.00 ± 0.14	0.94 ± 0.15
S / \sqrt{B}	0.220	0.192	0.023	0.030	0.009	0.005

Table 4.27: Pre-fit event yields in the signal-plus-background tZu fit in the signal and control regions with real data. The error includes both statistical and systematic uncertainties.

Post-fit	SR1	SR2	Side-band CR1	Side-band CR2	$t\bar{t}Z$ CR	$t\bar{t}$ CR
$t\bar{t}Z + tWZ$	137 ± 12	36 ± 6	102 ± 14	8.2 ± 14	230 ± 18	15.4 ± 1.5
$t\bar{t}W$	4.2 ± 2.1	3.1 ± 1.6	4.5 ± 2.3	2.3 ± 1.2	3.0 ± 1.5	27 ± 13
$t\bar{t}H$	4.8 ± 0.7	0.89 ± 0.17	2.6 ± 0.4	0.33 ± 0.07	7.5 ± 1.2	14.1 ± 2.2
VV + LF	18 ± 7	24 ± 8	27 ± 11	12 ± 4	0.23 ± 0.19	0.38 ± 0.25
VV + HF	114 ± 19	162 ± 26	166 ± 25	64 ± 9	17 ± 8	2.9 ± 0.5
tZq	46 ± 7	108 ± 18	22 ± 4	6.8 ± 1.4	21 ± 5	0.96 ± 0.19
$t\bar{t} + Wt$	14 ± 4	27 ± 8	9.3 ± 2.6	7.2 ± 2.1	4.0 ± 1.3	93 ± 19
Other fakes	7 ± 8	5 ± 6	2 ± 4	2.0 ± 2.8	0.15 ± 0.18	0.08 ± 0.09
Other	2.0 ± 1.0	2.5 ± 2.9	3.3 ± 2.5	0.8 ± 0.4	1.9 ± 0.9	3.2 ± 1.5
FCNC ($u\bar{t}Z$)	0.9 ± 1.7	4 ± 8	0.4 ± 0.7	0.17 ± 0.33	0.09 ± 0.18	0.05 ± 0.10
FCNC ($t\bar{t}$ ($u\bar{Z}$))	5 ± 9	0.8 ± 1.5	0.14 ± 0.27	0.04 ± 0.07	0.11 ± 0.20	0.018 ± 0.035
Total background	348 ± 15	369 ± 21	338 ± 18	104 ± 8	284 ± 16	157 ± 13
Data	345	380	343	104	286	157
Data / Bkg.	0.99 ± 0.04	1.03 ± 0.06	1.01 ± 0.05	1.00 ± 0.08	1.01 ± 0.06	1.00 ± 0.08
S / \sqrt{B}	0.016	0.013	0.002	0.002	0.001	0.000

Table 4.28: Post-fit event yields in the signal-plus-background tZu fit in the signal and control regions with real data. The error includes both statistical and systematic uncertainties.

Pre-fit	VR1	VR2	Post-fit	VR1	VR2
$t\bar{t}Z + tWZ$	70 ± 10	2.2 ± 0.6	$t\bar{t}Z + tWZ$	70 ± 7	2.4 ± 0.6
$t\bar{t}W$	2.3 ± 1.2	0.48 ± 0.26	$t\bar{t}W$	2.3 ± 1.2	0.48 ± 0.25
$t\bar{t}H$	3.0 ± 0.5	0.101 ± 0.032	$t\bar{t}H$	3.0 ± 0.5	0.108 ± 0.033
$VV + LF$	10 ± 5	9.8 ± 3.4	$VV + LF$	10 ± 5	9.7 ± 3.0
$VV + HF$	56 ± 28	36 ± 14	$VV + HF$	60 ± 14	47 ± 8
tZq	6.5 ± 1.6	13.5 ± 2.7	tZq	6.6 ± 1.5	14.7 ± 2.6
$t\bar{t} + Wt$	5.4 ± 2.6	4.5 ± 1.7	$t\bar{t} + Wt$	4.8 ± 2.1	3.8 ± 1.4
Other fakes	0.0 ± 0.6	1.4 ± 1.9	Other fakes	0.03 ± 0.24	0.8 ± 1.1
Other	0.8 ± 0.4	0.5 ± 0.7	Other	0.8 ± 0.4	0.5 ± 0.6
FCNC ($u\bar{u}$) tZ	1.14 ± 0.23	0.91 ± 0.16	FCNC ($u\bar{u}$) tZ	0.08 ± 0.16	0.07 ± 0.14
FCNC $t\bar{t}$ ($u\bar{u}$) Z	1.91 ± 0.34	0.69 ± 0.12	FCNC $t\bar{t}$ ($u\bar{u}$) Z	0.14 ± 0.27	0.05 ± 0.10
Total background	154 ± 31	69 ± 15	Total background	158 ± 13	79 ± 7
Data	151	80	Data	151	80
Data / Bkg.	0.98 ± 0.22	1.16 ± 0.29	Data / Bkg.	0.96 ± 0.08	1.01 ± 0.09
S / \sqrt{B}	0.020	0.023	S / \sqrt{B}	0.001	0.002

Table 4.29: Pre-fit (left) and post-fit (right) event yields in the signal-plus-background tZu fit in the validation regions with realistic Asimov from the control regions. The error includes both statistical and systematic uncertainties.

4.8.3.6 Signal-plus-background fit for tZc coupling in the signal and control regions with real data

Similarly to the tZu search, the combined fit for the tZc anomalous coupling was performed with real data in both signal and control regions. The pulls and constraints of the instrumental, theoretical and modeling nuisance parameters are represented in Figure 4.49. No significant pulls and constraints are observed, which is in agreement with the results from the several studies performed on the fit without real data in the signal regions. Similar to the results from the blinded tZc fit, the normalisation factor for $t\bar{t} + Wt$ background processes is found to be 0.86 ± 0.22 . The correlation matrix of the fitted nuisance parameters can be found in Figure 4.50, being the tZq and $VV+HF$ normalisations the systematics with highest correlation with the signal strength. Figures 4.51 to 4.53 show the pre-fit and post-fit distributions of the discriminant variables of the signal and background control regions. The corresponding event yields can be found in Table 4.30 and Table 4.31, respectively. The distributions for the signal and control regions present a reasonable agreement between data and background predictions. On the specific case of the signal regions, there are some bins with significant uncertainty due to the low statistics. However, both signal and background prediction for those bins are also negligible. Finally, no evidence for the $t \rightarrow cZ$ processes is found.

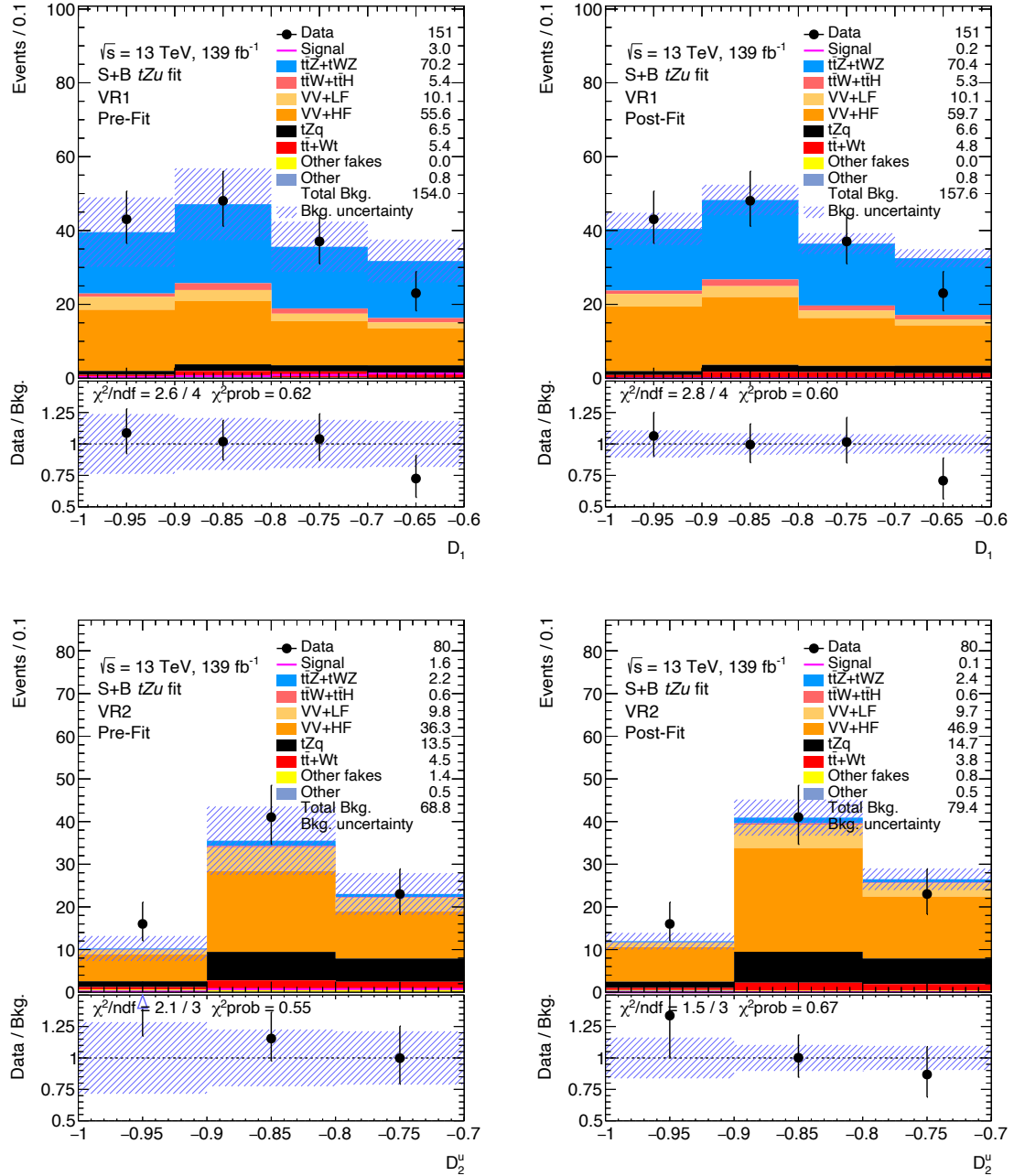


Figure 4.48: Pre-fit (left) and post-fit (right) BDTG output distributions in VR1 and VR2 for the signal-plus-background tZu fit in the signal and control regions with realistic Asimov from the control regions. The uncertainty band includes both statistical and systematic uncertainties.

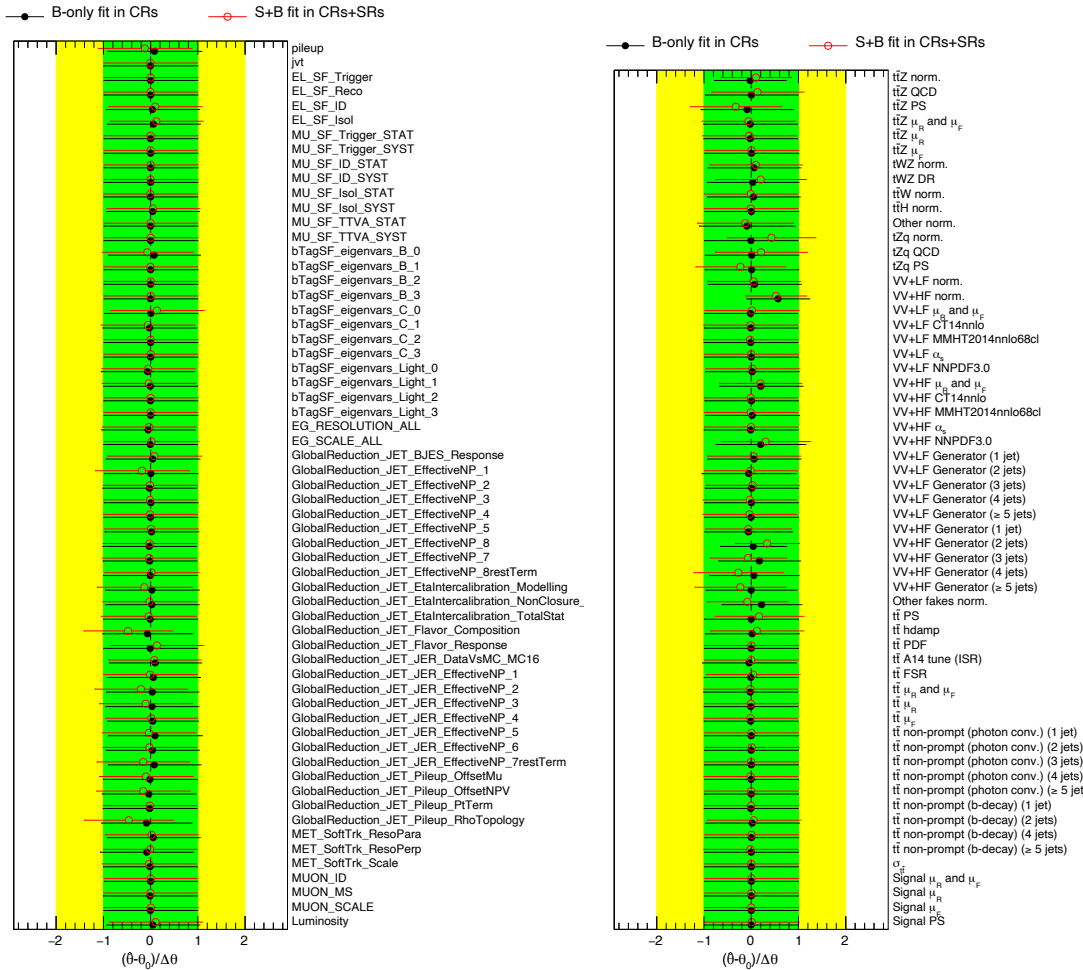


Figure 4.49: Pulls and constraints of the instrumental (left) and the theoretical and modeling (right) nuisance parameters for the signal-plus-background tZc fit in the signal and control regions with real data.

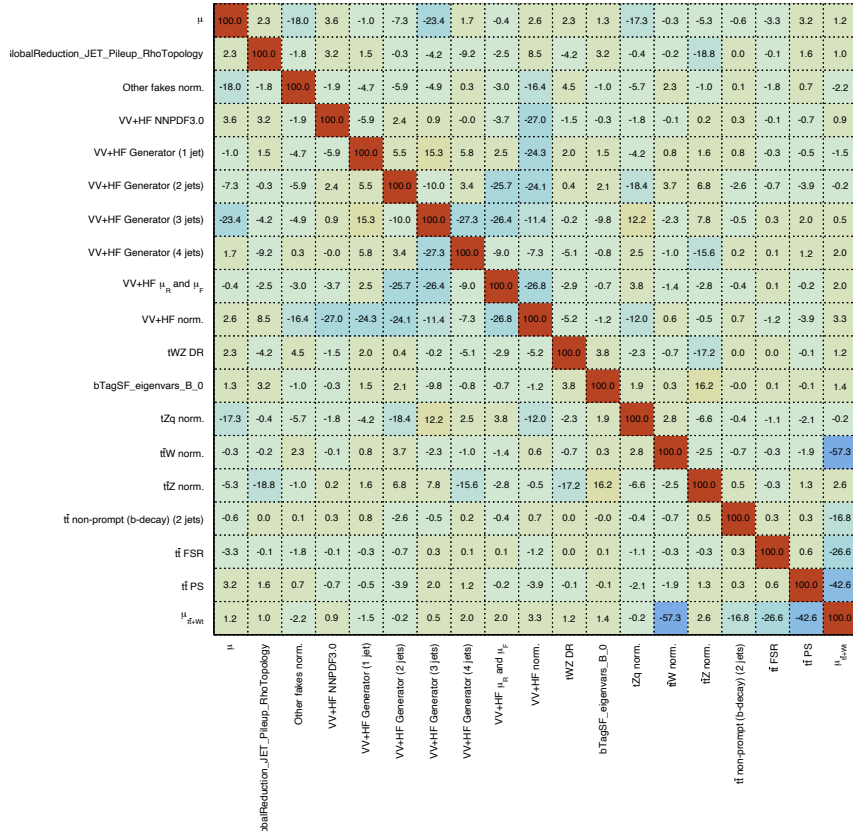


Figure 4.50: Correlation matrix of the nuisance parameters for the signal-plus-background tZc fit in the signal and control regions with real data.

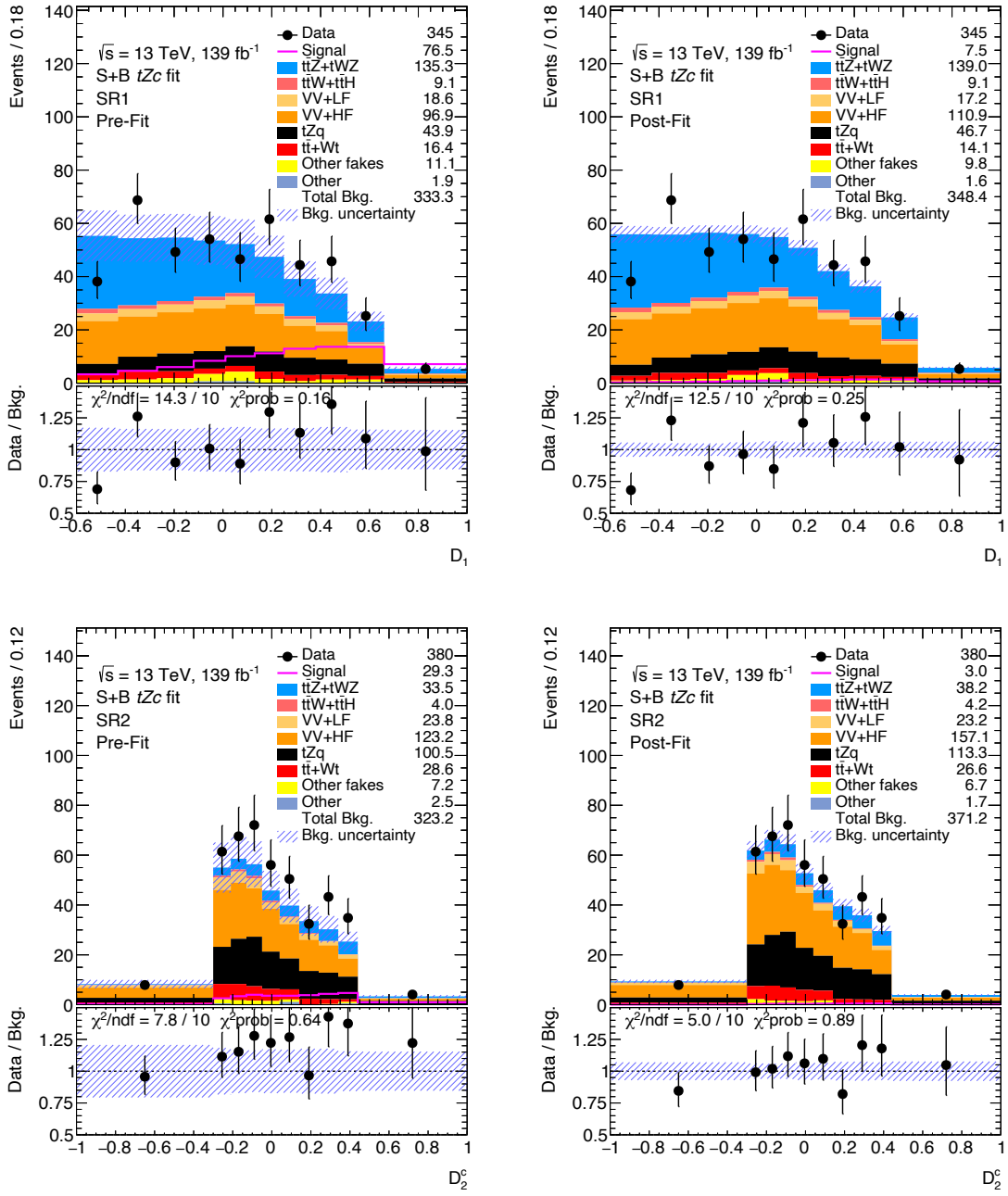


Figure 4.51: Pre-fit (left) and post-fit (right) BDTG output distributions in the signal regions for the signal-plus-background tZc fit in the signal and control regions with real data. The uncertainty band includes both statistical and systematic uncertainties.

Pre-fit	SR1	SR2	Side-band CR1	Side-band CR2	$t\bar{t}Z$ CR	$t\bar{t}$ CR
$t\bar{t}Z + tWZ$	135 ± 17	33 ± 6	97 ± 16	7.6 ± 1.4	229 ± 31	15.0 ± 2.0
$t\bar{t}W$	4.4 ± 2.2	3.1 ± 1.6	4.6 ± 2.3	2.2 ± 1.1	3.2 ± 1.6	27 ± 14
$t\bar{t}H$	4.8 ± 0.8	0.85 ± 0.17	2.5 ± 0.4	0.31 ± 0.07	7.6 ± 1.2	14.1 ± 2.2
VV + LF	19 ± 8	24 ± 8	27 ± 11	12 ± 4	0.25 ± 0.21	0.40 ± 0.28
VV + HF	100 ± 50	120 ± 50	130 ± 60	51 ± 17	18 ± 12	2.3 ± 1.0
tZq	44 ± 8	101 ± 19	21 ± 4	6.2 ± 1.3	20 ± 5	0.90 ± 0.21
$t\bar{t} + Wt$	16 ± 4	29 ± 9	10.2 ± 3.3	7.8 ± 2.4	4.8 ± 1.2	$.05 \pm 18$
Other fakes	11 ± 11	7 ± 8	4 ± 5	2.8 ± 3.5	0.24 ± 0.32	0.12 ± 0.14
Other	1.9 ± 1.2	2.5 ± 2.5	3.2 ± 2.8	0.7 ± 0.5	1.8 ± 1.0	3.0 ± 1.5
FCNC ($c\bar{t}Z$)	3.3 ± 0.6	12.0 ± 0.8	1.06 ± 0.11	0.55 ± 0.05	0.33 ± 0.07	0.104 ± 0.016
FCNC $t\bar{t}$ ($c\bar{Z}$)	73 ± 6	17.4 ± 1.8	4.8 ± 0.5	1.53 ± 0.21	5.1 ± 1.0	0.34 ± 0.08
Total background	330 ± 50	320 ± 50	300 ± 70	91 ± 19	280 ± 40	168 ± 23
Data	345	380	343	104	286	157
Data / Bkg.	1.04 ± 0.18	1.18 ± 0.21	1.14 ± 0.25	1.14 ± 0.26	1.00 ± 0.14	0.94 ± 0.15
S / \sqrt{B}	0.230	0.091	0.019	0.023	0.019	0.003

Table 4.30: Pre-fit event yields in the signal-plus-background tZc fit in the signal and control regions with real data. The error includes both statistical and systematic uncertainties.

Post-fit	SR1	SR2	Side-band CR1	Side-band CR2	$t\bar{t}Z$ CR	$t\bar{t}$ CR
$t\bar{t}Z + tWZ$	139 ± 12	38 ± 6	104 ± 14	8.5 ± 1.4	230 ± 18	15.7 ± 1.5
$t\bar{t}W$	4.3 ± 2.1	3.3 ± 1.6	4.4 ± 2.2	2.3 ± 1.2	3.0 ± 1.5	27 ± 13
$t\bar{t}H$	4.8 ± 0.7	0.93 ± 0.17	2.6 ± 0.4	0.34 ± 0.07	7.4 ± 1.2	14.2 ± 2.2
VV + LF	17 ± 7	23 ± 7	26 ± 11	12 ± 4	0.20 ± 0.16	0.35 ± 0.23
VV + HF	111 ± 19	157 ± 25	160 ± 24	63 ± 9	17 ± 8	2.7 ± 0.5
tZq	47 ± 8	113 ± 19	22 ± 4	6.9 ± 1.3	20 ± 5	0.97 ± 0.20
$t\bar{t} + Wt$	14.1 ± 3.5	27 ± 8	9.2 ± 2.5	7.4 ± 2.0	3.8 ± 1.2	93 ± 19
Other fakes	10 ± 9	7 ± 7	2.2 ± 3.3	2.4 ± 2.8	0.19 ± 0.19	0.10 ± 0.10
Other	1.6 ± 0.9	1.7 ± 1.7	3.3 ± 2.5	0.7 ± 0.4	1.7 ± 0.9	2.8 ± 1.5
FCNC ($c\bar{t}Z$)	0.3 ± 0.7	1.2 ± 2.7	0.10 ± 0.23	0.06 ± 0.13	0.03 ± 0.07	0.010 ± 0.023
FCNC $t\bar{t}$ ($c\bar{Z}$)	7 ± 16	2 ± 4	0.5 ± 1.1	0.16 ± 0.35	0.5 ± 1.0	0.03 ± 0.08
Total background	348 ± 16	371 ± 20	335 ± 18	103 ± 8	283 ± 16	157 ± 13
Data	345	380	343	104	286	157
Data / Bkg.	0.99 ± 0.05	1.02 ± 0.06	1.03 ± 0.05	1.01 ± 0.08	1.01 ± 0.06	1.00 ± 0.08
S / \sqrt{B}	0.021	0.008	0.002	0.002	0.002	0.000

Table 4.31: Post-fit event yields in the signal-plus-background tZc fit in the signal and control regions with real data. The error includes both statistical and systematic uncertainties.

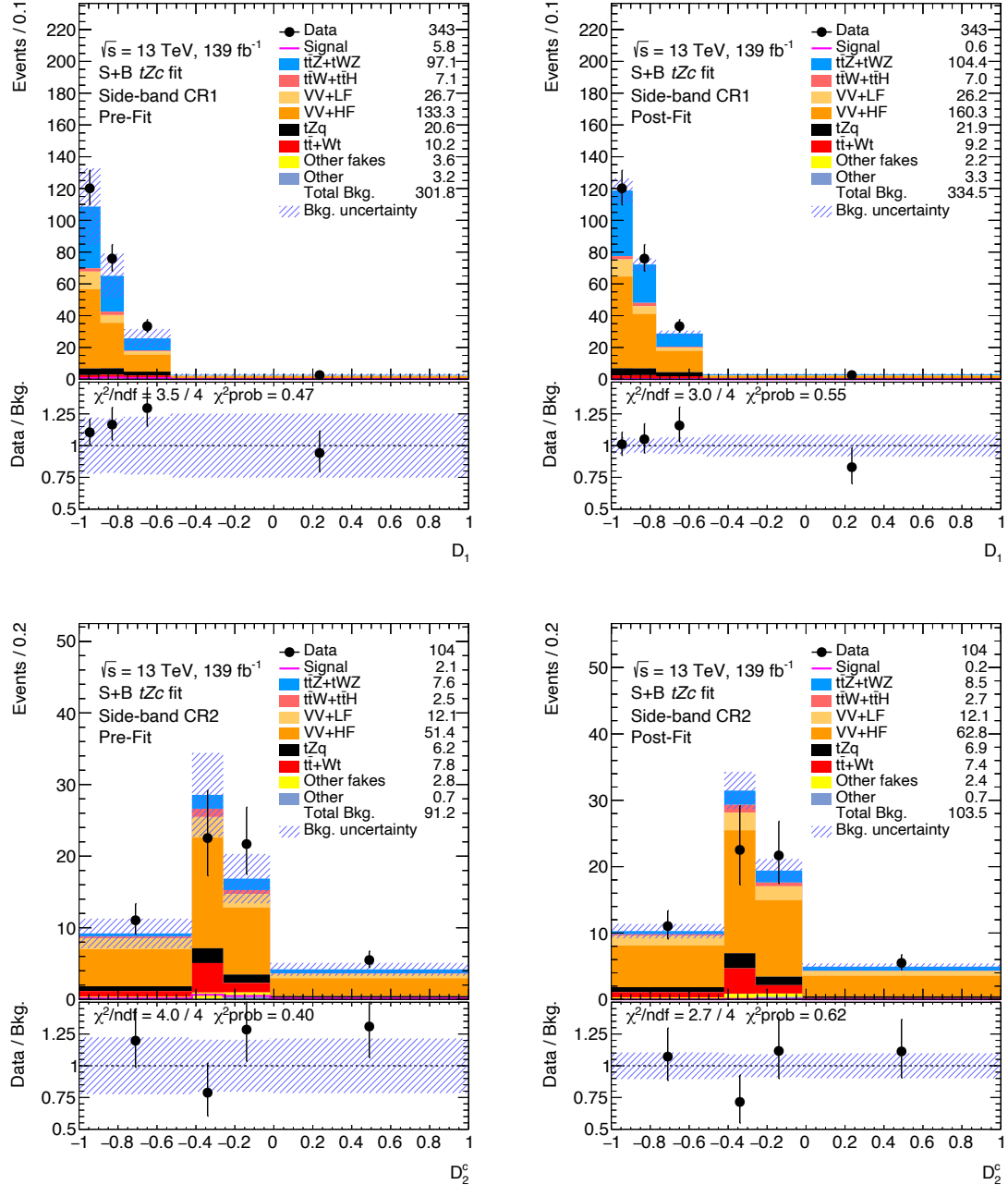


Figure 4.52: Pre-fit (left) and post-fit (right) BDTG output distributions in the side-band control regions for the signal-plus-background tZc fit in the signal and control regions with real data. The uncertainty band includes both statistical and systematic uncertainties.

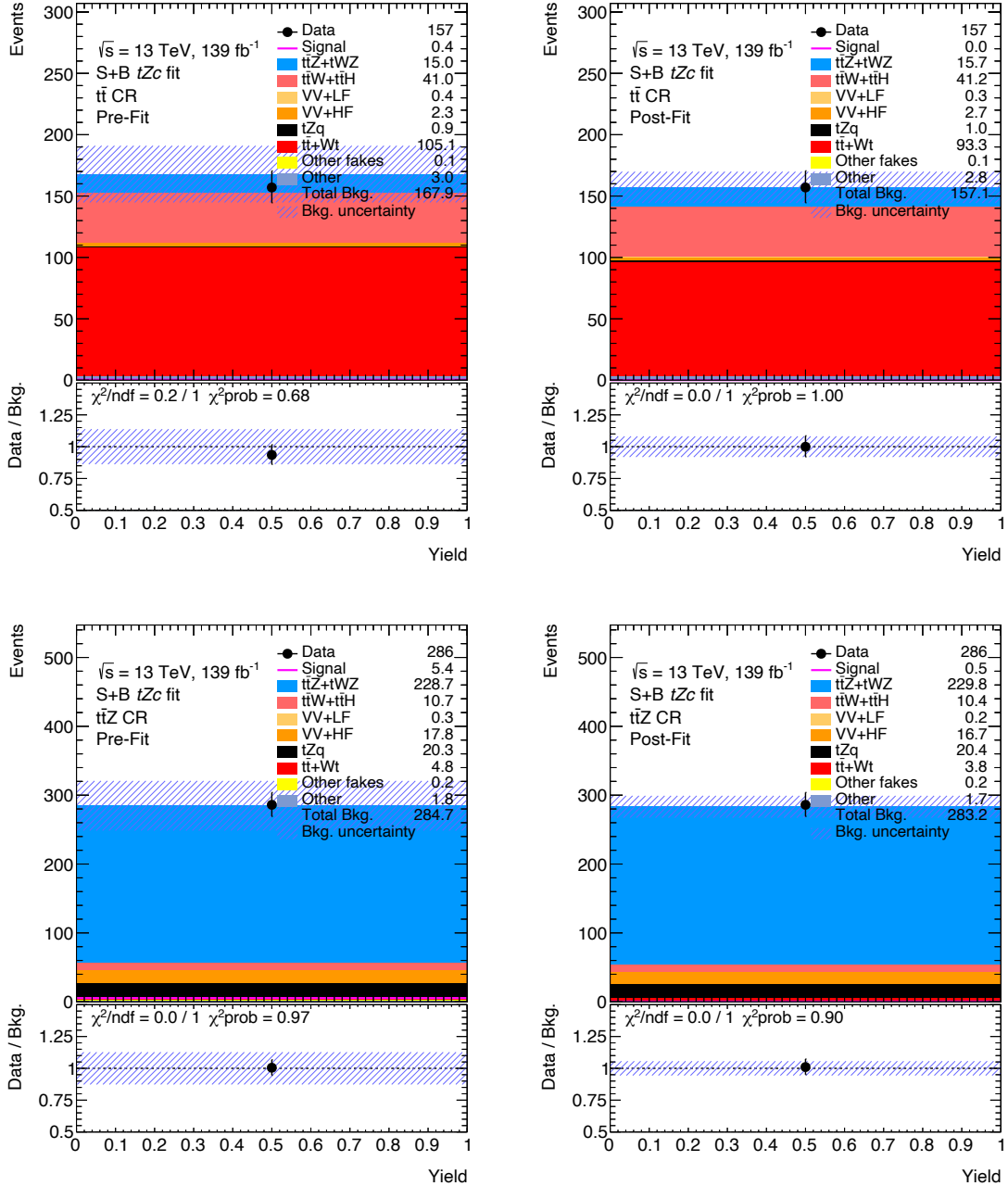


Figure 4.53: Pre-fit (left) and post-fit (right) event yield distributions in the $t\bar{t}$ and $t\bar{t}Z$ control regions for the signal-plus-background tZc fit in the signal and control regions with real data. The uncertainty band includes both statistical and systematic uncertainties.

Pre-fit	VR1	VR2	Post-fit	VR1	VR2
$t\bar{t}Z + tWZ$	70 ± 10	2.2 ± 0.6	$t\bar{t}Z + tWZ$	70 ± 7	2.4 ± 0.6
$t\bar{t}W$	2.3 ± 1.2	0.48 ± 0.26	$t\bar{t}W$	2.3 ± 1.2	0.49 ± 0.25
$t\bar{t}H$	3.0 ± 0.5	0.101 ± 0.032	$t\bar{t}H$	2.9 ± 0.5	0.101 ± 0.030
$VV + LF$	10 ± 5	9.8 ± 3.4	$VV + LF$	10 ± 4	9.3 ± 2.9
$VV + HF$	56 ± 28	36 ± 14	$VV + HF$	58 ± 14	44 ± 7
tZq	6.5 ± 1.6	13.5 ± 2.7	tZq	6.5 ± 1.5	15.4 ± 2.7
$t\bar{t} + Wt$	5.4 ± 2.6	4.5 ± 1.9	$t\bar{t} + Wt$	4.6 ± 2.1	3.8 ± 1.5
Other fakes	0.0 ± 0.6	1.4 ± 1.9	Other fakes	0.01 ± 0.07	1.1 ± 1.3
Other	0.8 ± 0.4	0.5 ± 0.7	Other	0.7 ± 0.4	0.4 ± 0.5
FCNC (c) tZ	0.30 ± 0.07	0.34 ± 0.04	FCNC (c) tZ	0.03 ± 0.06	0.04 ± 0.08
FCNC $t\bar{t}$ (cZ)	3.0 ± 0.6	1.23 ± 0.34	FCNC $t\bar{t}$ (cZ)	0.3 ± 0.6	0.12 ± 0.28
Total background	154 ± 31	69 ± 15	Total background	155 ± 13	78 ± 7
Data	151	80	Data	151	80
Data / Bkg.	0.98 ± 0.22	1.16 ± 0.29	Data / Bkg.	0.97 ± 0.08	1.03 ± 0.09
S / \sqrt{B}	0.021	0.023	S / \sqrt{B}	0.002	0.002

Table 4.32: Pre-fit (left) and post-fit (right) event yields in the signal-plus-background tZc fit in the validation regions with realistic Asimov from the control regions. The error includes both statistical and systematic uncertainties.

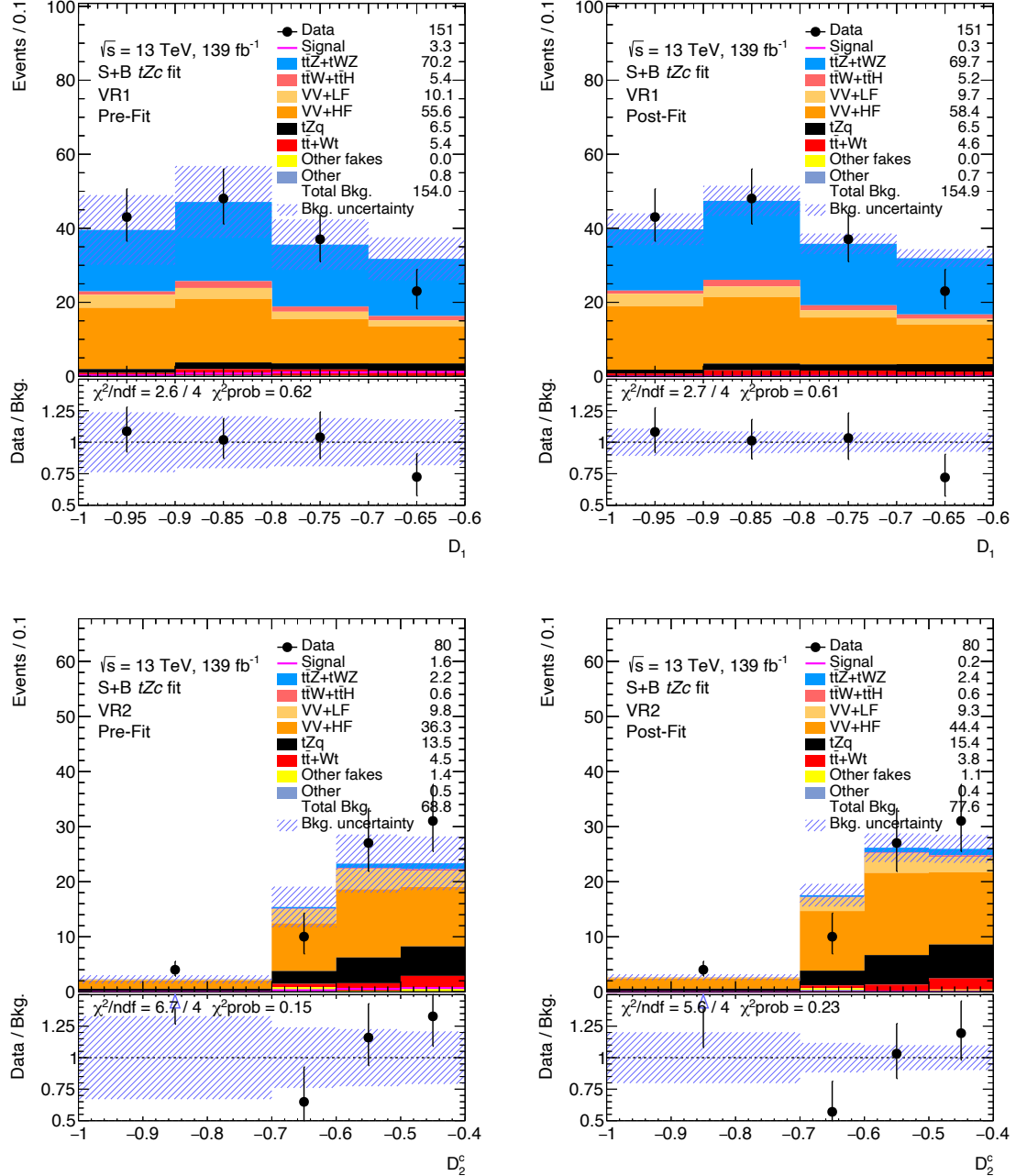


Figure 4.54: Pre-fit (left) and post-fit (right) BDTG output distributions in VR1 and VR2 for the signal-plus-background tZc fit in the signal and control regions with realistic Asimov from the control regions. The uncertainty band includes both statistical and systematic uncertainties.

4.8.4 Limits

In the scenario where the signal strength shows no significant excess with respect to the background-only hypothesis, an upper limit can be set on the branching ratio of the FCNC $t \rightarrow qZ$ ($q = u, c$) processes by performing hypothesis tests based on a frequentist approach. The test statistic q_μ for a hypothesis test is defined as the profile likelihood ratio,

$$q_\mu(x) = -2 \ln \left(\frac{\mathcal{L}(x|\mu, \hat{\theta}_\mu)}{\mathcal{L}(x|\hat{\mu}, \hat{\theta})} \right) \quad (4.6)$$

where \mathcal{L} is the likelihood function of the profile likelihood and x corresponds to the data or pseudo-data. The $\hat{\mu}$ and $\hat{\theta}$ are the parameters that maximise the likelihood (with the constraint $0 \leq \hat{\mu} \leq \mu$), and $\hat{\theta}_\mu$ are the values of the nuisance parameters that maximise the likelihood function for a given value of μ . The test statistic defined in Equation (4.6) is used to evaluate the validity of the background-only hypothesis with $\mu = 0$ and to make statistical inferences about μ , such as upper limits using the CL_s method [180, 181] as implemented in the RooFit package [177, 178].

The compatibility among the observed data (q_{obs}) and a given hypothesis is measured by a p-value:

$$p_{s+b} = P(q \leq q_{obs}|s+b) = \int_{q_{obs}}^{\infty} f(q_\mu|s+b)dq_\mu \quad (4.7)$$

$$1 - p_b = P(q \leq q_{obs}|b) = \int_{q_{obs}}^{\infty} f(q_\mu|b)dq_\mu \quad (4.8)$$

The CL_s variable is obtained by the ratio of those p-values as:

$$CL_s(\mu) = \frac{p_{s+b}}{1 - p_b}. \quad (4.9)$$

The 95% Confidence Level (CL) upper limit on μ , referred to as $\mu^{95\%CL}$, is the value of μ for which $CL_s = 0.05$. Consequently, a value of μ above $\mu^{95\%CL}$ is excluded at 95% confidence level.

The 95% confidence level expected upper limits on the branching ratios of $t \rightarrow Zu$ and $t \rightarrow Zc$ are computed with the CL_s method using the asymptotic properties of the profile likelihood ratio test statistic [177–179] and assuming that only one FCNC anomalous coupling contributes. The likelihood function includes both the signal and control regions with the setup described in Section 4.8.1. The real data are used in all the analysis regions. The expected and observed limits for the branching ratios of $t \rightarrow Zu$ and $t \rightarrow Zc$ are reported in Table 4.33. Limits are obtained separately for the signal with left-handed and right-handed couplings. Corresponding EFT operators are $C_{uB}^{(i3)}, C_{uW}^{(i3)}$ and $C_{uB}^{(3i)}, C_{uW}^{(3i)}$ for the left-handed and right-handed couplings, respectively [59]. The difference between the limits on the branching ratios using left- and right-handed couplings amounts to at most $\sim 7\%$, which is very small compared to the ± 1 standard deviations. Current expected limits are better by a factor of 4.8 and 2.9

than the expected limits from the previous analysis for the tZu and tZc couplings [47], respectively. The expected limits considering statistics only were also obtained. Since the inclusion of the systematics contributes with only 20 % to the final result, it can be concluded that this analysis is statistical limited. The limits on the EFT Wilson coefficients can also be obtained as represented in Table 4.34. For the specific case of the production, limits on the cross-section can also be derived as shown in Table 4.35. The current expected (observed) limits constitute the most stringent limits on the FCNC tZq couplings to date.

Signal coupling	tZu , left-handed	tZu , right-handed	tZc , left-handed	tZc , right-handed
$\mathcal{BR}(t \rightarrow qZ)[10^{-5}]$	$6.16 (4.88^{+2.1}_{-1.4})$	$6.56 (5.05^{+2.1}_{-1.4})$	$13.02 (10.76^{+4.7}_{-3.0})$	$11.73 (10.06^{+4.3}_{-2.8})$

Table 4.33: Observed (expected) upper limits on the branching ratios for the FCNC tZu and tZc vertices.

Signal coupling	Wilson coefficients	95 % CL upper limit
tZu , left-handed	$ C_{uW}^{(13)*} , C_{uB}^{(13)*} $	$0.151 (0.134^{+0.026}_{-0.019})$
tZu , right-handed	$ C_{uW}^{(31)} , C_{uB}^{(31)} $	$0.156 (0.136^{+0.026}_{-0.021})$
tZc , left-handed	$ C_{uW}^{(23)*} , C_{uB}^{(23)*} $	$0.22 (0.20^{+0.04}_{-0.03})$
tZc , right-handed	$ C_{uW}^{(32)} , C_{uB}^{(32)} $	$0.208 (0.194^{+0.038}_{-0.029})$

Table 4.34: Observed (expected) upper limits on the Wilson coefficients for the FCNC tZu and tZc vertices, assuming a scale of new physics of $\Lambda = 1$ TeV.

Signal coupling	tZu , left-handed	tZu , right-handed	tZc , left-handed	tZc , right-handed
$\sigma(pp \rightarrow tZ)[fb]$	$37 (29^{+14}_{-12})$	$33 (27^{+15}_{-11})$	$118 (96^{+12}_{-8})$	$119 (99^{+12}_{-7})$

Table 4.35: Observed (expected) upper limits on the tZ production cross-section for the FCNC tZu and tZc vertices.

Top quark phenomenology as a probe of new interactions with a pseudo-scalar particle

The search for new interactions of the top quark with a Z boson and a light quark was presented in Chapter 4. However, there is also the possibility of searching for top quark decays via neutral currents with new particles instead of the neutral SM bosons. Using an effective field theory approach, the scenario where the production of a new neutral pseudo-scalar particle is produced with a top quark and a light quark was examined through a meticulous study on the sensitivity for such searches at the LHC and future experiments. Arising from New Physics models as the ones introducing composite Higgs bosons, this new particle is assumed to decay to leptons, more specifically to muons or taus. Besides production and decay mechanisms being considered as signal, both the production of one pseudo-scalar and two pseudo-scalars along with the top quark and a light quark were studied. After discussing the details of the model used for this study, the signal and background simulation samples were produced and dedicated analyses for three distinct channels were optimised, taking into account hadronisation and detector simulation. Finally, the obtained upper limits on the cross-section and branching ratios for the respective processes allowed a prediction on how sensitive the experiments at LHC are to these interactions.

5.1 Sensivity on the search for a new scalar S

New pseudo-scalars S with mass m_S close to the electroweak scale, singlets of the SM gauge group, are predicted in very different and well motivated scenarios of new physics. These include, among others, the Next-to-Minimal Supersymmetric Standard Model model [182] as well as a big part of Composite Higgs Models (CHM) developed to the date [183–196]. Moreover, such particles have been showed to be excellent

candidates to accomodate electroweak baryogenesis in which CP is spontaneously broken [191, 196–202] and even to explain the $g - 2$ anomaly of the muon [203]. However, such particles are very difficult to detect since, at the renormalisable level, they only interact with the Higgs boson and the strong constraints on dipole moments [204, 205] also forbids any sizable mixing with the Higgs boson, while other production mechanisms are mediated by higher-dimensional operators and therefore suppressed by the cut-off scale [206, 207]. In ligh of these results, there has been research exploring production mechanisms for new pseudo-scalar singlets. One of the most exciting possibilities is producing such particles in the decay of top quarks via effective interactions. The significant top quark production rate at the LHC can also be exploited by searching for these pseudo-scalars decays. The phenomenological study described here extend previous works in this topic in three ways: considers the rare top decay $t \rightarrow Sq, S \rightarrow l^+l^-$, includes the production of top quarks in addition to the decay mode and predicts the LHC reach to the $t \rightarrow SSq, S \rightarrow l^+l^-$ process [67].

5.1.1 Interactions and constraints

The theoretical formulation for this new particle can be obtained through an EFT approach (as discussed in Chapter 2). The most generic Lagrangian describing the interactions between a scalar singlet S with mass m_S and the SM fields is defined by the following expression:

$$\begin{aligned} \Delta L = & -\frac{1}{2}\lambda_{HS}S^2\left(|H|^2 - \frac{v^2}{2}\right) + c_{HS}\frac{(\partial S)^2}{\Lambda^2}|H|^2 \\ & + \frac{S}{\Lambda}\bar{\mathbf{f_L}}\mathbf{Y}^f_H\mathbf{f_R} + \frac{S^2}{\Lambda^2}\left[c'_{HS}|DH|^2 + \tilde{c}_{HS}\left(|H|^4 - \frac{v^4}{4}\right) + \bar{\mathbf{f_L}}\tilde{\mathbf{Y}}^f_H\mathbf{f_R}\right], \end{aligned} \quad (5.1)$$

where H represents the Higgs doublet, σ_2 the second Pauli matrix and f runs over quarks and leptons ($f = q, l$). The different Wilson coefficients in the expression above are subject to a number of constraints. In particular, the coefficients λ_{HS} , c_{HS} and \tilde{c}_{HS} enter the Higgs width as:

$$\Gamma(h \rightarrow SS) = \frac{1}{32\pi m_h} \sqrt{1 - \frac{4m_S^2}{m_h^2} \left[\lambda_{HS} + c_{HS} \frac{(m_h^2 - 2m_S^2)}{\Lambda^2} - 2\tilde{c}_{HS} \frac{v^2}{\Lambda^2} \right]^2}. \quad (5.2)$$

Therefore, values of $m_S < m_h/2$ are *a priori* constrained by LHC measurements on the Higgs width, $\Gamma_H \lesssim 10$ MeV [208]. Assuming one operator at a time, the bounds on $\lambda_{HS} \lesssim 0.05$; $c_{HS}/\Lambda^2 \lesssim 3(5)$ TeV $^{-2}$ for $m_S = 10(50)$ GeV; and $-\tilde{c}_{HS}/\Lambda^2 \lesssim 0.4$ TeV $^{-2}$ can also be obtained. Additionally, entries in Y^f and \tilde{Y}^f are constrained by direct searches for resonances [209, 210]. One important exception is entries $i3, 3i$ of Y^q since there are no direct limits on these. Moreover, indirect constraints from flavour experiments, as for the $D^0 - \bar{D}^0$ oscillations [57, 211, 212], involve always products of two different Yukawas. Therefore, these Yukawa couplings are negligible in the case where the entry 13 or 23 of Y^q

vanishes [213], being the same for \tilde{Y}^q . After the electroweak symmetry breaking and for $m_t > m_S$ ($2m_S$), the theoretical framework for this new pseudo-scalar particle leads to signatures such as $t \rightarrow qS(S)$ arising from:

$$\Delta L \supset \frac{vS}{\sqrt{2}\Lambda} \left[\mathbf{Y}^q_{i3} \bar{u}_L^i t_R + \mathbf{Y}^q_{3i} \bar{t}_L u_R^i + \frac{S}{\Lambda} \left(\tilde{\mathbf{Y}}^q_{i3} \bar{u}_L^i t_R + \tilde{\mathbf{Y}}^q_{3i} \bar{t}_L u_R^i \right) + \text{h.c.} \right], \quad (5.3)$$

with $i = 1, 2$. The expressions for each decay width can be also obtained:

$$\Gamma(t \rightarrow q^i S) = \frac{v^2}{64\pi\Lambda^2} \left[(\mathbf{Y}^q_{i3})^2 + (\mathbf{Y}^q_{3i})^2 \right] m_t \left(1 - x^2 \right)^2, \quad (5.4)$$

$$\begin{aligned} \Gamma(t \rightarrow q^i SS) = & \frac{v^2}{512\pi^3\Lambda^4} \left[(\tilde{\mathbf{Y}}^q_{i3})^2 + (\tilde{\mathbf{Y}}^q_{3i})^2 \right] m_t^3 \left[\frac{1}{3} \sqrt{1 - 4x^2} (1 + 5x^2 - 6x^4) \right. \\ & \left. + 2(x^2 - 2x^4 + 2x^6) \log \frac{2x^2}{1 - 2x^2 + \sqrt{1 - 4x^2}} \right], \end{aligned} \quad (5.5)$$

where x corresponds to m_S/m_t . Taking the top quark width of $\Gamma_t \sim 1.4$ GeV as reference value, the branching ratio of the top quark into Sq and SSq can be obtained considering $\tilde{Y}_{i3}^q = \tilde{Y}_{3i}^q = Y_{i3}^q = Y_{3i}^q = 1$ and $\Lambda = 1$ TeV for different values of m_S , as represented in the left panel of Figure 5.1. The theoretical formulation above allows the scalar S to decay into fermions, being the study described here focused on the channel $S \rightarrow \ell^+ \ell^-$. Assuming that this decay mode dominates the S width while $t \rightarrow q^i S$ requires that only Y_{i3}^q (and/or Y_{3i}^q) and Y_{jj}^l , $j = 1, 2, 3$, are non vanishing. This scenario does not easily arise in UV models, where diagonal couplings of S to quarks are generally also present, proportional to masses, and $b\bar{b}$ dominates the S width. Even so, the branching ratio to taus is only an order of magnitude smaller. Taking these predictions into account, the unexplored S decay to taus in the context of top FCNCs is pursued being complemented with the dimuon channel due to its clean final state. Prospects are very different in the case of the process $t \rightarrow q^i SS$ instead. From the theory point of view, the $t \rightarrow q^i SS$ case can well be explained by a \mathbb{Z}_2 symmetry $S \rightarrow -S$ that is only (or mostly) broken in the lepton sector. Or even just in the muon and electron side; in which case the dilepton decay of S is dominant. For this specific scenario, the parameter Y_{jj}^f can be defined as $y_{fj} y_{fj}$, where y_{fj} is the fermion Yukawa and $0 < y_{fj} < 1$ parameterises the degree of breaking of the \mathbb{Z}_2 . The branching ratios of S into taus and muons for different assumptions on this parameter are shown in the right panel of Figure 5.1. The interactions above arise very naturally within CHMs [214, 215], where both the Higgs and S are pseudo-Goldstone bosons associated with the spontaneous global symmetry breaking \mathcal{G}/\mathcal{H} driven in a new strong sector at the confinement scale $\Lambda \sim 1$ TeV. In these models, the global symmetry is only approximate; being explicitly broken by the linear mixing between the elementary SM fermions and composite operators. Considering the next-to-minimal CHM based on the coset $SO(6)/SO(5)$ [184], the pseudo Nambu Goldstone Boson matrix can be obtained and, after comparing the final Lagrangian with Equation (5.3), the FCNC processes are introduced for this particular case. The assumption that leptons mix with only one representation of the composite sector

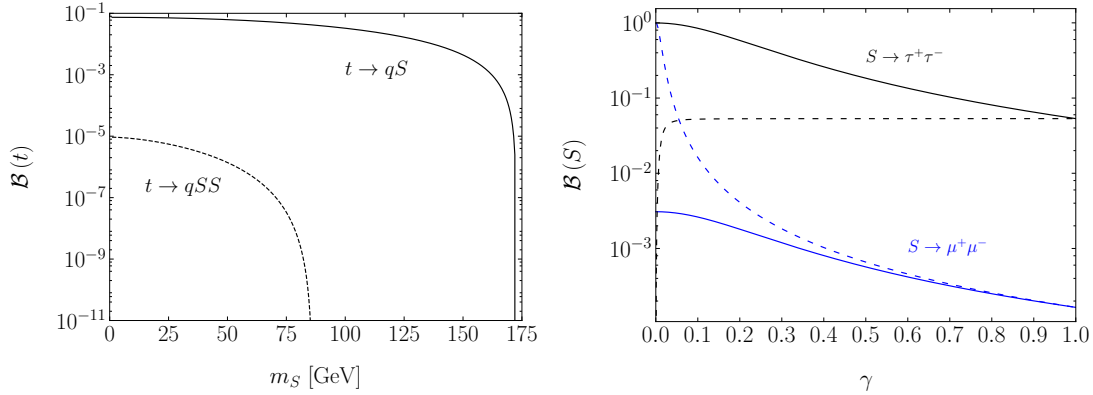


Figure 5.1: Top branching ratios as a function of the mass of S (left). Scalar branching ratios into muons (blue) and taus (black), as a function of the \mathbb{Z}_2 breaking parameter, γ , for $m_S = 100$ GeV (right). Two distinct cases are represented: (in solid lines) $\gamma_\ell = \gamma_\tau = 1$ while $\gamma_q = \gamma$; and (in dashed lines) $\gamma_\ell = 1$ and $\gamma_\tau = \gamma_q = \gamma$.

implies that FCNCs vanish and, simultaneously, Y^l is automatically diagonal in the physical basis, being proportional to the lepton Yukawa matrix. Consequently, the S decay to taus is expected to dominate but the decay to muons should not be neglected. Mainly due to the not dramatically small ratio between the muon and tau masses, i.e. $m_\mu/m_\tau \sim 0.06$, but also because the muon channel dominates the S width in the case of γ_τ being small, as represented in Figure 5.1. Only a few experimental searches are slightly sensitive to the interactions discussed above. The first one is the ATLAS search for the FCNC couplings through the tZq vertex [216], where the event selection from one of the control regions requires exactly three light leptons, exactly one b -tagged jet and at least two more light jets. Related to the leptons, two of them should have the same flavour and opposite sign with an invariant mass within a 15 GeV mass window around the Z boson mass pole (~ 91.2 GeV). Such characteristic imposes that only $t \rightarrow Sq$ events with $m_S \neq m_Z$ are captured in this region. Another analysis sensitive to the proposed top quark interactions is the ATLAS search for SUSY in multilepton final states [217]. After implementing a few cuts from this search, the maximum number of allowed signal events is larger than 20, which arises in the scalar S framework only if FCNC couplings are larger than 1 for $\Lambda = 1$ TeV. In conclusion, there are some searches that can be sensitive to the interactions described above but most of them suffer from being too broad in scope and, consequently, the background processes contribute significantly hiding the signal of interest.

In light of the discussion above, this phenomenological study assumes that $\Lambda \gtrsim 1$ TeV and all Wilson coefficients vanish with the exception of Y_{22}^l (or Y_{33}^l) and either Y_{13}^q or Y_{23}^q or \tilde{Y}_{13}^q (depending on which process is considered). The results are quantified in terms of seven benchmark masses of the pseudo-scalar S : $m_S = 20, 50, 80, 90, 100, 120$ and 150 GeV. Due to the reduced phase space for $t \rightarrow SSq$, the benchmark masses of $m_S = 30, 40, 60$ and 70 GeV are also included. The reach of the dedicated

analyses discussed below will be compared to the following Benchmark Points (BP):

$$\begin{aligned}
 \text{BP 1 : } & \mathbf{Y^q}_{i3} = \mathbf{Y^q}_{3i} = 0.01, \quad \Lambda = 5 \text{ TeV} \implies BR(t \rightarrow Sq) \sim 10^{-8} - 10^{-7}, \\
 \text{BP 2 : } & \mathbf{Y^q}_{i3} = \mathbf{Y^q}_{3i} = 0.10, \quad \Lambda = 5 \text{ TeV} \implies BR(t \rightarrow Sq) \sim 10^{-6} - 10^{-5}, \\
 \text{BP 3 : } & \mathbf{Y^q}_{i3} = \mathbf{Y^q}_{3i} = 0.10, \quad \Lambda = 1 \text{ TeV} \implies BR(t \rightarrow Sq) \sim 10^{-4} - 10^{-3}, \\
 \text{BP 4 : } & \tilde{\mathbf{Y}}_{i3}^q = \tilde{\mathbf{Y}}_{3i}^q = 1.00, \quad \Lambda = 5 \text{ TeV} \implies BR(t \rightarrow SSq) \sim 10^{-11} - 10^{-8}, \\
 \text{BP 5 : } & \tilde{\mathbf{Y}}_{i3}^q = \tilde{\mathbf{Y}}_{3i}^q = 0.20, \quad \Lambda = 1 \text{ TeV} \implies BR(t \rightarrow SSq) \sim 10^{-10} - 10^{-7}, \\
 \text{BP 6 : } & \tilde{\mathbf{Y}}_{i3}^q = \tilde{\mathbf{Y}}_{3i}^q = 1.00, \quad \Lambda = 1 \text{ TeV} \implies BR(t \rightarrow SSq) \sim 10^{-8} - 10^{-5}, \quad (5.6)
 \end{aligned}$$

being $i = 1, 2$ depending if the light quark corresponds to an up or charm quark, respectively. The range in the branching ratio presented considers the wide range of values of m_S .

5.1.2 Search for $t \rightarrow Sq, S \rightarrow \mu^+ \mu^-$

Similarly to top quark decay to a Z boson and a light quark, the singlet S can arise either in the production or in the decay of the top quark, being some examples of the Feynman diagrams represented in Figure 5.2. This leads to a final state with exactly one S , one top quark decaying into Wb and eventually an additional light quark (up or charm quark). The first analysis focus on the scenario where S decays into a pair of muons with a leptonic decay of the top quark. Consequently, it is expected to have three charged leptons, several jets (at least one originated by a B meson) and significant missing energy at the detector level.

The MC simulation of the signal and background events at $\sqrt{s} = 13$ TeV is produced with MadGraph5_aMC@NLO [115], with the signal model being implemented in FeynRules [63]. Subsequently, Pythia8 [64] is used for simulating the initial and final state radiation, the parton shower and the hadronisation. At parton level, only leptons and photons with a transverse momentum higher than 10 GeV are

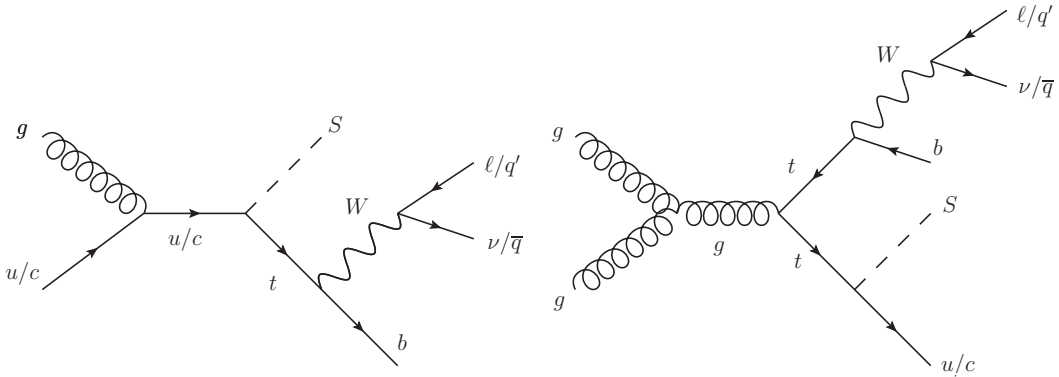


Figure 5.2: Representative Feynman diagrams for the production of a single top quark in association with S via an FCNC interaction (left) and for the top-quark pair production with an FCNC top-quark decay into the extra singlet (right). Similar diagrams but involving two rather than one S in the new physics vertex hold for the production of a top quark in association with SS .

considered. Concerning the jets, this cut rises to 20 GeV. For the absolute pseudo-rapidity $|\eta|$, jets can have a value of this variable lower than 5 while for leptons and photons it should be lower than 2.5. The renormalisation and factorisation scales are set to the default dynamical value from MadGraph and the set NNPDF23L0 [134] of PDFs is used. The background processes considered in these analyses are the following: tW , $t\bar{t}V$, VV , ZVV , $t\bar{t}$, $V + \text{jets}$ and tZ , with $V = W, Z$. The simulation of the detector effects is done using `Delphes` [66] with the default CMS detector card. In respect with the overlap removal, an electron (muon) is considered to be isolated if the sum of the transverse momentum of all particles above $p_T^{\min} = 0.5$ GeV that lie within a cone of radius $R = 0.5$, normalised to the lepton p_T , is smaller than 0.12 (0.25). Concerning the objects definition, jets are defined using the anti- k_t algorithm [105] with a radius parameter of $R = 0.5$. All the jets are required to have $p_T > 25$ GeV and to lie within a pseudo-rapidity range of $|\eta| < 2.5$. Leptons must have $p_T > 15$ GeV and $|\eta| < 2.4$ (2.5) for muons (electrons), where the leading lepton is also required to have $p_T > 25$ GeV. The effect of the previous cuts on the transverse momentum and the pseudo-rapidity on the leptons and jets can be found in the event yields tables labeled as "Basic cuts". The `Delphes` CMS card was also used to parameterise the p_T dependent tagging efficiencies for jets initiated by b -quarks, as well as to account for the mistag probability. As an example, for a b -jet with a transverse momentum of 30 GeV, the tagging efficiency is 55 % and the mistag rate for a c -jet with the same p_T is 12 %.

Due to the targeted trilepton final state of the signal, the most dominant background comes from tZ and $t\bar{t}$ production, where the top quark decays to Wb and all gauge bosons are assumed to decay into muons. The event selection requires exactly three isolated leptons and at least one jet, with one of them being tagged as a bottom quark. The scalar resonance, S , is reconstructed from the hardest $\mu^+\mu^-$ pair. The longitudinal component of the missing neutrino four-momentum, p_ν is reconstructed by demanding $m_W^2 = (p_\ell + p_\nu)^2$, where p_ℓ is the four-momentum of the lepton not used for the scalar S reconstruction and $m_W = 81.2$ GeV is the reference value for the W boson mass. In the case of two possible solutions, the one with smaller absolute value is used. Both p_ℓ and p_ν are then added to the four-momentum of the b -jet in order to reconstruct the SM top quark with the goal of obtaining its invariant mass, m_t^{rec} . Figure 5.3 presents the distributions of the scalar S and top quark reconstructed masses for two signal benchmark points and for the relevant background components. Following the reconstruction of the top quark and the scalar S , the mass of the reconstructed top quark is required to be within a window of 50 GeV from the reference mass (i.e. 172.5 GeV). An additional cut of 1 TeV on maximum invariant mass of the total system is applied to stay in the regime of validity of the effective field theory. Finally, the scalar S candidate invariant mass is required to be within a mass window of ± 30 GeV around the probed mass of m_S . The event yields table for the signal with an up and with a charm quark is given in Table 5.1 and Table 5.2, respectively. The scalar mass-independent yields for the background processes are shown in Table 5.3 and the mass-dependent one is given in Table 5.4. All the dedicated analyses described in this section considered an integrated luminosity of $\mathcal{L} = 150 \text{ fb}^{-1}$. Upper

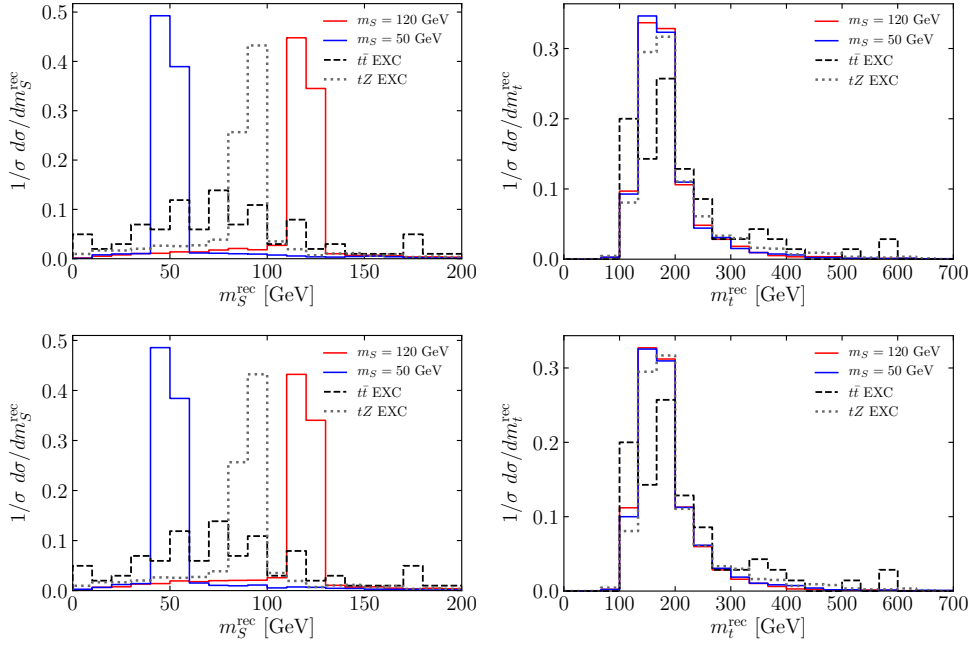


Figure 5.3: The reconstructed scalar (left) and top (right) mass in the analysis proposed for $t \rightarrow Sq$, $S \rightarrow \mu^+ \mu^-$. In the upper (bottom) panel, $q = c$ (u). The distributions represent the two signal benchmark points and the two major background components, after the cut on the particle multiplicities; the background samples are generated exclusively, i.e. only gauge bosons decays into muons are included.

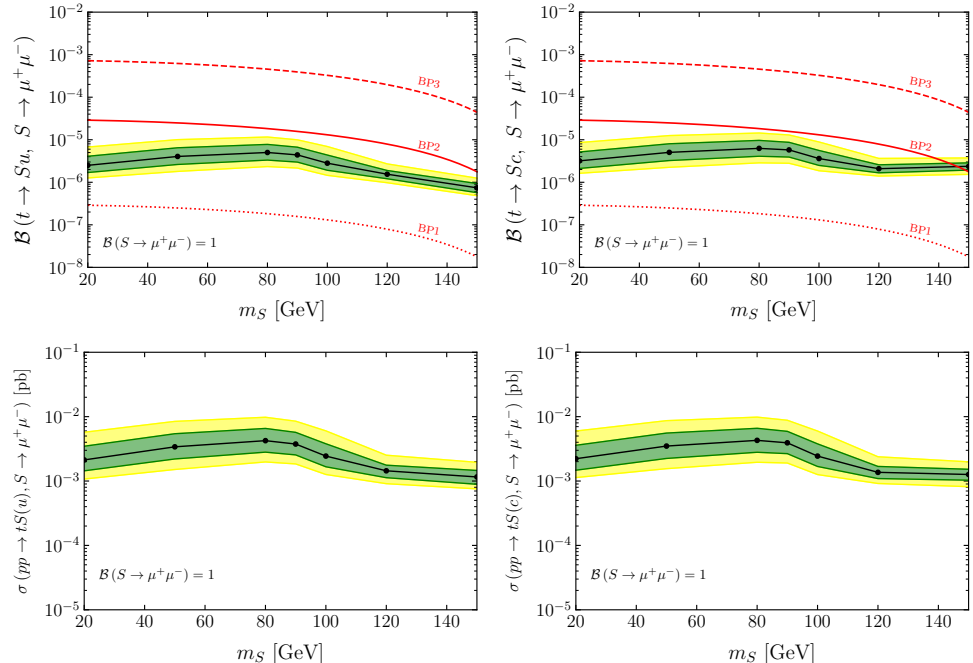


Figure 5.4: In the upper (bottom) panels, the 95% CL limits on the branching ratio (cross-section times branching ratio) that can be tested in the $\mu^+ \mu^-$ channel are shown, in the analysis proposed for $t \rightarrow Sq$, $S \rightarrow \mu^+ \mu^-$, with $q = u$ (c) in the panels on the left (right). The green and yellow bands show the $\pm 1\sigma$ and $\pm 2\sigma$ uncertainty on the limits, respectively. Superimposed are the theoretical expectations in three BPs.

Cuts/ m_S	20 GeV	50 GeV	80 GeV	90 GeV	100 GeV	120 GeV	150 GeV
Basic cuts	29445 ± 133	25065 ± 113	18525 ± 84	16095 ± 73	13623 ± 62	8829 ± 40	3306 ± 15
$n_\ell = 3$	6092 ± 61	5597 ± 54	4769 ± 43	4295 ± 38	3642 ± 32	2416 ± 21	899 ± 8
$n_j > 1$	6033 ± 60	5537 ± 53	4708 ± 42	4249 ± 37	3589 ± 32	2378 ± 21	865 ± 8
$n_b = 1$	3249 ± 44	2961 ± 39	2543 ± 31	2301 ± 27	1914 ± 23	1265 ± 15	479 ± 6
$n_{\mu^+ \mu^-} = 1$	3247 ± 44	2959 ± 39	2542 ± 31	2300 ± 27	1913 ± 23	1265 ± 15	478 ± 6
$ m_t^{\text{rec}} - m_t < 50 \text{ GeV}$	2763 ± 41	2507 ± 36	2152 ± 29	1961 ± 25	1625 ± 21	1075 ± 14	403 ± 5
$m_{\text{total}} < 1 \text{ TeV}$	2713 ± 40	2468 ± 36	2089 ± 28	1893 ± 25	1556 ± 21	1013 ± 13	375 ± 5
$ m_S^{\text{rec}} - m_S < 30 \text{ GeV}$	1908 ± 34	1729 ± 30	1440 ± 23	1297 ± 21	1062 ± 17	690 ± 11	252 ± 4

Table 5.1: Event yields after each cut for the seven benchmark signal points, in the analysis for $t \rightarrow Su, S \rightarrow \mu^+ \mu^-$. The parameters Y_{13} and Y_{31} are fixed to 0.1 with $\Lambda = 1 \text{ TeV}$ and $BR(S \rightarrow \mu^+ \mu^-) = 1$. The event yields presented assume a collected luminosity of $\mathcal{L} = 150 \text{ fb}^{-1}$.

Cuts/ m_S	20 GeV	50 GeV	80 GeV	90 GeV	100 GeV	120 GeV	150 GeV
Basic cuts	24120 ± 109	20655 ± 93	14985 ± 68	12825 ± 58	10597 ± 48	6204 ± 28	1127 ± 5
$n_\ell = 3$	5235 ± 51	4923 ± 46	4070 ± 35	3633 ± 31	3050 ± 26	1836 ± 15	362 ± 3
$n_j > 1$	5214 ± 51	4906 ± 46	4050 ± 35	3616 ± 31	3030 ± 26	1821 ± 15	352 ± 3
$n_b = 1$	2705 ± 37	2520 ± 33	2103 ± 25	1870 ± 22	1571 ± 18	957 ± 11	188 ± 2
$n_{\mu^+ \mu^-} = 1$	2705 ± 37	2520 ± 33	2102 ± 25	1870 ± 22	1571 ± 18	957 ± 11	188 ± 2
$ m_t^{\text{rec}} - m_t < 50 \text{ GeV}$	2229 ± 33	2072 ± 30	1754 ± 23	1551 ± 20	1311 ± 17	801 ± 10	161 ± 2
$m_{\text{total}} < 1 \text{ TeV}$	2194 ± 33	2038 ± 29	1708 ± 23	1488 ± 20	1248 ± 16	749 ± 10	148 ± 2
$ m_S^{\text{rec}} - m_S < 30 \text{ GeV}$	1502 ± 28	1406 ± 24	1166 ± 19	1003 ± 16	829 ± 13	497 ± 8	100 ± 2

Table 5.2: Event yields after each cut for the seven benchmark signal points, in the analysis for $t \rightarrow Sc, S \rightarrow \mu^+ \mu^-$. The parameters Y_{23} and Y_{32} are fixed to 0.1 with $\Lambda = 1 \text{ TeV}$ and $BR(S \rightarrow \mu^+ \mu^-) = 1$. The event yields presented assume a collected luminosity of $\mathcal{L} = 150 \text{ fb}^{-1}$.

limits on the signal cross-section are obtained under the signal absence hypothesis, using the CL_s method [180]. With that goal, the distribution of the invariant mass of the reconstructed scalar S after all selection cuts is fitted with OpTHyLic [218]. A total of 20 bins per signal point are considered and Poissonian statistical uncertainties on each bin of the distributions are included in the fit. An expected upper limit on the signal strength, $\sigma_{95\%}/\sigma_{th}(pp \rightarrow tS(q), S \rightarrow \mu^+ \mu^-)$, at 95% CL is then obtained. The ± 1 and $\pm 2\sigma$ variations are also computed, taking into account the statistical uncertainty coming from finite MC samples. The 95% CL upper limits on the top quark branching ratio ($t \rightarrow Sq, S \rightarrow \mu^+ \mu^-$) and cross-section $\sigma(pp \rightarrow tS(q), S \rightarrow \mu^+ \mu^-)$ are presented in Figure 5.4. For an integrated luminosity of 150 fb^{-1} , the upper limits on the production cross-section were obtained, where $\sigma(pp \rightarrow tS, S \rightarrow \mu^+ \mu^-) > 10^{-3} \text{ pb}$ can be tested at the 95% CL. The highest sensitivity is attained for $m_S \sim 150 \text{ GeV}$, corresponding to a limit on the branching ratio $BR(t \rightarrow Sq) > 5 (15) \times 10^{-7}$ at the 95% CL in the up (charm) channel. In turn, for $O(1)$ couplings in the UV, these results translate into a lower bound on the new physics scale Λ of about 90 TeV , assuming that $BR(S \rightarrow \mu^+ \mu^-) = 1$.

Cuts/Background	tW	$t\bar{t}W/t\bar{t}Z$	ZZZ/WWZ	$ZZ/WZ/WW$	$t\bar{t}$	tZ
Basic cuts	8352000 ± 37351	934 ± 9	1385 ± 6	14835000 ± 66344	852600 ± 1206	1724 ± 8
$n_\ell = 3$	334 ± 236	5.2 ± 0.7	10.1 ± 0.5	16615 ± 2220	348 ± 24	128 ± 2
$n_j > 1$	334 ± 236	5.2 ± 0.7	9.1 ± 0.5	8011 ± 1542	326 ± 24	128 ± 2
$n_b = 1$	334 ± 236	2.2 ± 0.5	1.0 ± 0.2	< 74	172 ± 17	65 ± 1
$n_{\mu^+\mu^-} = 1$	< 42	1.1 ± 0.3	0.7 ± 0.1	—	172 ± 17	39 ± 1
$ m_t^{rec} - m_t < 50 \text{ GeV}$	—	0.7 ± 0.3	0.4 ± 0.1	—	114 ± 14	31 ± 1
$m_{total} < 1 \text{ TeV}$	—	0.3 ± 0.2	0.25 ± 0.08	—	80 ± 12	23.2 ± 0.9

Table 5.3: Event yields after each cut for the dominant backgrounds, in the analysis for $t \rightarrow Sq, S \rightarrow \mu^+ \mu^-$. The $Z + \text{jets}$ sample is reduced to negligible values after the cut on the lepton multiplicity. The event yields presented assume a collected luminosity of $\mathcal{L} = 150 \text{ fb}^{-1}$.

Background/ m_S	20 GeV	50 GeV	80 GeV	90 GeV	100 GeV	120 GeV	150 GeV
$t\bar{t}W/t\bar{t}Z$	< 0.09	< 0.09	0.2 ± 0.1	0.2 ± 0.1	0.2 ± 0.1	0.2 ± 0.1	< 0.09
ZZZ/WWZ	0 ± 0	0.06 ± 0.04	0.22 ± 0.08	0.17 ± 0.07	0.17 ± 0.07	< 0.03	< 0.03
$t\bar{t}(\mu)$	12 ± 4	34 ± 8	39 ± 8	39 ± 8	36 ± 8	15 ± 5	3 ± 2
tZ	1.8 ± 0.2	3.3 ± 0.3	18.6 ± 0.8	18.4 ± 0.8	17.9 ± 0.8	11.4 ± 0.6	0.8 ± 0.2

Table 5.4: Event yields for the last selection cut on m_S^{rec} for the dominant backgrounds, in the analysis for $t \rightarrow Sq, S \rightarrow \mu^+ \mu^-$.

5.1.3 Search for $t \rightarrow Sq, S \rightarrow \tau^+ \tau^-$

The second analysis focus on the scenario where the scalar S decays to a pair of taus, concentrating on the hadronic decays of the latter and the leptonic decay of the top quark. Thus, the event selection requires events to contain exactly one light lepton and at least three jets, from which exactly one must be b -tagged and exactly two must be tagged as taus decaying into hadrons. The efficiency for τ -tagging is 60% while the misidentification rate is 1% without any dependency on the transverse momentum of the jets. The dominant backgrounds for this channel are the exclusive tW and $t\bar{t}$ processes, where the top quark is assumed to decay to Wb and $W \rightarrow \tau\nu$. The scalar S is partially reconstructed from the two tau-jets obtaining its invariant mass. The normalised distribution of this variable, after the basic selection cuts, in two signal benchmark points and in the main backgrounds are represented in the left panels of Figure 5.5. Moreover, the normalised distributions of the transverse mass of the system composed by the lepton, the b -tagged jet, the reconstructed scalar S and the missing energy are represented in the right panels of Figure 5.5. The latter variable is required to be smaller than 500 GeV. Finally, events should have $|m_S - m_S^{\text{rec}}| < 30 \text{ GeV}$, where m_S^{rec} is the mass of the reconstructed scalar candidate S and m_S is the corresponding value being probed. The cut flows for the signal in the up quark and in the charm quark cases are given in Table 5.5 and Table 5.6, respectively. Likewise, Table 5.7 shows the yields independent of the scalar S invariant mass for the distinct background processes, while in Table 5.8 the mass-dependent ones can be found. Similarly to the previous analysis, the expected upper limit on the signal strength, $\sigma_{95\%}/\sigma_{th}(pp \rightarrow tS(q), S \rightarrow \tau^+ \tau^-)$, is obtained using the invariant mass of the scalar S candidate

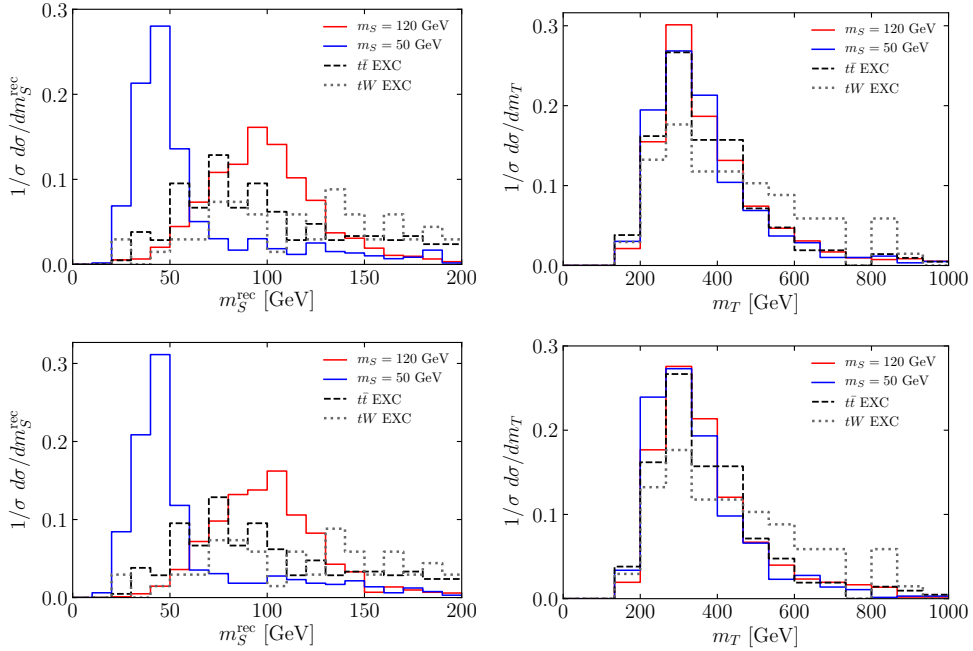


Figure 5.5: The reconstructed scalar mass (left) and the transverse mass of the system composed by the lepton, the b-jet, the reconstructed S and missing energy (right) in the analysis proposed for $t \rightarrow Sq$, $S \rightarrow \tau^+\tau^-$. In the upper (bottom) panel, $q = c$ (u). The distributions represent the two signal benchmark points and the two major background components, after the cut on the particle multiplicities; the background samples are generated exclusively, i.e. only gauge bosons decays into taus are included.

Cuts/ m_S	20 GeV	50 GeV	80 GeV	90 GeV	100 GeV	120 GeV	150 GeV
Basic cuts	29445 ± 133	25065 ± 113	18525 ± 84	16095 ± 73	13608 ± 62	8829 ± 40	3306 ± 15
$n_j > 3$	22290 ± 116	19293 ± 100	14509 ± 74	14698 ± 70	12432 ± 59	6864 ± 35	2439 ± 13
$n_b = 1$	12171 ± 86	10516 ± 73	7910 ± 55	12571 ± 64	10688 ± 55	3723 ± 26	1354 ± 10
$n_\ell = 1$	6148 ± 61	5251 ± 52	3975 ± 39	6804 ± 47	5814 ± 40	1826 ± 18	676 ± 7
$n_{\tau_h} = 2$	118 ± 8	306 ± 12	309 ± 11	3340 ± 33	2877 ± 28	171 ± 6	66 ± 2
$m_T < 500$ GeV	86 ± 7	259 ± 11	256 ± 910	280 ± 10	234 ± 8	143 ± 5	47 ± 2
$ m_S^{\text{rec}} - m_S < 30$ GeV	47 ± 5	220 ± 11	193 ± 9	236 ± 9	195 ± 7	79 ± 4	18 ± 1

Table 5.5: Event yields after each cut for the seven benchmark signal points, in the analysis for $t \rightarrow Su$, $S \rightarrow \tau^+\tau^-$. The parameters Y_{13} and Y_{31} are fixed to 0.1 with $\Lambda = 1$ TeV and $BR(S \rightarrow \tau^+\tau^-) = 1$. The event yields presented assume a collected luminosity of $\mathcal{L} = 150$ fb $^{-1}$.

distributed into 20 bins. The 95% CL upper limits on the branching ratio ($t \rightarrow Sq$, $S \rightarrow \tau^+\tau^-$) and on the cross-section $\sigma(pp \rightarrow tS(q), S \rightarrow \tau^+\tau^-)$ are shown in Figure 5.6. For an integrated luminosity of 150 fb $^{-1}$, an upper limit on the production cross-section $\sigma(pp \rightarrow tS, S \rightarrow \tau^+\tau^-) > 10^{-2}$ pb can be tested at the 95% CL. The highest sensitivity is obtained for $m_S \sim 50$ GeV, where $BR(t \rightarrow Sq) > 11(12) \times 10^{-6}$ can be probed at the 95% CL in the up (charm) channel. Such results translate into a lower bound on the new physics scale Λ of about 75 TeV, assuming that $BR(S \rightarrow \tau^+\tau^-) = 1$.

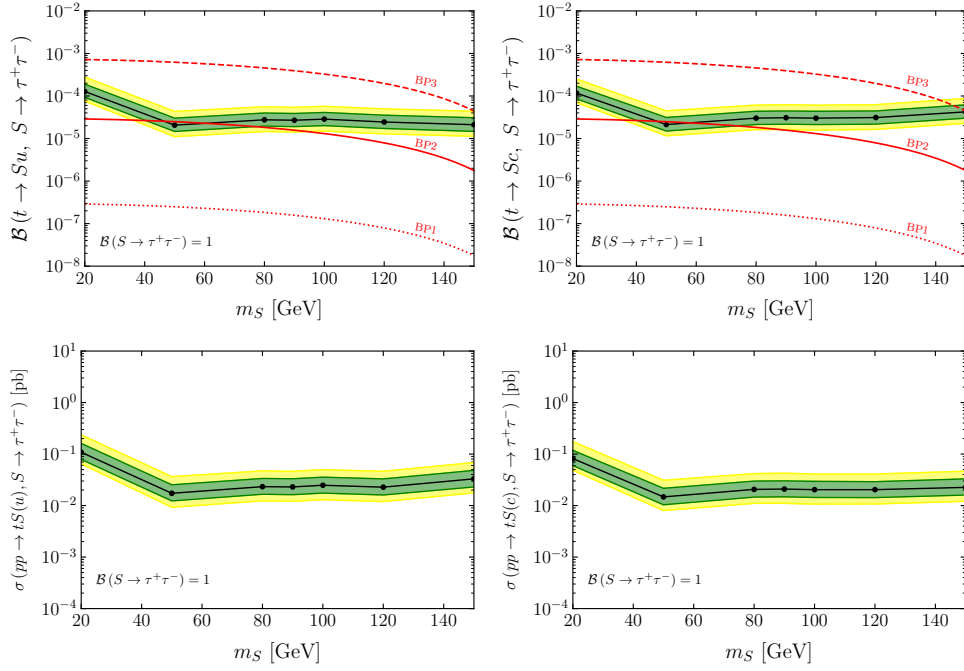


Figure 5.6: In the upper (bottom) panels, the 95% CL limits on the branching ratio (cross-section times branching ratio) that can be tested in the $\tau^+\tau^-$ channel are shown, in the analysis proposed for $t \rightarrow Sq$, $S \rightarrow \tau^+\tau^-$, with $q = u$ (c) in the panels on the left (right). The green and yellow bands show the $\pm 1\sigma$ and $\pm 2\sigma$ uncertainty on the limits, respectively. Superimposed are the theoretical expectations in three BPs.

Cuts/ m_S	20 GeV	50 GeV	80 GeV	90 GeV	100 GeV	120 GeV	150 GeV
Basic cuts	24120 ± 109	20655 ± 93	14985 ± 68	12816 ± 58	10597 ± 48	6204 ± 28	1127 ± 5
$n_j > 3$	19339 ± 98	16636 ± 84	12219 ± 61	11682 ± 55	8679 ± 43	5049 ± 25	873 ± 5
$n_b = 1$	10190 ± 71	8651 ± 60	6398 ± 44	10415 ± 52	4561 ± 31	2653 ± 18	465 ± 3
$n_\ell = 1$	5115 ± 50	4315 ± 43	3172 ± 31	5483 ± 38	2259 ± 22	1325 ± 13	233 ± 2
$n_{\tau_h} = 2$	107 ± 7	276 ± 11	256 ± 9	2730 ± 27	215 ± 7	131 ± 4	27.5 ± 0.8
$m_T < 500$ GeV	91 ± 7	243 ± 10	222 ± 8	244 ± 8	182 ± 6	111 ± 4	22.9 ± 0.7
$ m_S^{rec} - m_S < 30$ GeV	48 ± 5	203 ± 9	171 ± 7	207 ± 7	124 ± 5	62 ± 3	9.0 ± 0.5

Table 5.6: Event yields after each cut for the seven benchmark signal points, in the analysis for $t \rightarrow Sc, S \rightarrow \tau^+\tau^-$. The parameters Y_{23} and Y_{32} are fixed to 0.1 with $\Lambda = 1$ TeV and $BR(S \rightarrow \tau^+\tau^-) = 1$. The event yields presented assume a collected luminosity of $\mathcal{L} = 150$ fb $^{-1}$.

Cuts/Background	$tW(\tau)$	$t\bar{t}W/t\bar{t}Z$	ZZZ/WWZ	$ZZ/WZ/WW$	$t\bar{t}(\tau)$	tZ
Basic cuts	69715 ± 139	934 ± 9	1385 ± 6	14835000 ± 66344	111013 ± 165	1724 ± 8
$n_j > 3$	55080 ± 124	894 ± 9	1160 ± 6	8594806 ± 50498	89367 ± 148	1552 ± 7
$n_b = 1$	28047 ± 88	349 ± 6	264 ± 3	1333073 ± 19888	41365 ± 101	772 ± 5
$n_\ell = 1$	4460 ± 35	80 ± 3	44 ± 1	80406 ± 4884	5041 ± 35	282 ± 3
$n_{\tau_h} = 2$	19 ± 2	0.6 ± 0.2	0.05 ± 0.04	< 74	52 ± 4	0.4 ± 0.1
$m_T < 500$ GeV	11 ± 2	0.4 ± 0.2	0.05 ± 0.04	—	42 ± 3	0.3 ± 0.1

Table 5.7: Event yields after each cut for the dominant backgrounds, in the analysis for $t \rightarrow Sq, S \rightarrow \tau^+\tau^-$. The $Z +$ jets sample is reduced to negligible values after the fifth cut. The event yields presented assume a collected luminosity of $\mathcal{L} = 150$ fb $^{-1}$.

Background/ m_S	20 GeV	50 GeV	80 GeV	90 GeV	100 GeV	120 GeV	150 GeV
$tW(\tau)$	0.6 ± 0.4	3.1 ± 0.9	5 ± 1	5 ± 1	5 ± 1	5 ± 1	4 ± 1
$t\bar{t}W/t\bar{t}Z$	< 0.09	< 0.09	0.3 ± 0.2	0.3 ± 0.2	0.2 ± 0.1	< 0.09	< 0.09
ZZZ/WWZ	< 0.03	< 0.03	< 0.03	< 0.03	< 0.03	< 0.03	< 0.03
$t\bar{t}(\tau)$	3.7 ± 0.9	17 ± 2	24 ± 2	21 ± 2	20 ± 2	14 ± 2	10 ± 1
tZ	< 0.03	0.07 ± 0.05	0.10 ± 0.06	0.10 ± 0.06	0.10 ± 0.06	0.10 ± 0.06	0.14 ± 0.07

Table 5.8: Event yields for the last selection cut on m_S^{rec} of the dominant backgrounds, in the analysis for $t \rightarrow Sq, S \rightarrow \tau^+ \tau^-$. The event yields presented assume a collected luminosity of $\mathcal{L} = 150 \text{ fb}^{-1}$.

5.1.4 Search for $t \rightarrow SSq, S \rightarrow \mu^+ \mu^-$

Finally, the third analysis searches for two singlet scalars produced in association with a top quark (or in the decay of a top quark in pair production), both decaying to a pair of muons and focusing on the hadronic decays of the W boson. Consequently, the targeted final state consists of four isolated leptons and at least three jets, one of them required to be b -tagged. Due to the large lepton and jet multiplicities, all the background components become almost negligible, surviving a few events from the $t\bar{t}V$ and $t\bar{t}$ exclusive samples. The reconstruction of the top quark is performed using the b -tagged and the W boson, which is reconstructed from the two light jets with the invariant mass closest to m_W . The invariant mass of the reconstructed top quark, m_t^{rec} , is then required to be within a window of 50 GeV around the top mass. The two scalars S candidates are reconstructed by requiring two muons with opposite sign, being the event rejected if no such candidates are found. The opposite sign muons reconstructing the two scalars are those minimising $|m_{S_1}^{rec} - m_{S_2}^{rec}|$, with $m_{S_{1,2}}^{rec}$ being the invariant mass of each pair of opposite sign muons. The invariant mass of the total system, composed of the reconstructed top quark and the two scalars, is also required to be smaller than 1 TeV. Finally, the invariant masses $m_{S_{1,2}}^{rec}$ need to be within a window of 30 GeV from the mass of scalar S being probed to survive the event selection. The normalised distributions of each m_S^{rec} , respectively, for two signal benchmark points after the basic selection cuts are shown in Figure 5.7. The event yields for the signal with an up and with a charm quark are given in Table 5.9 and Table 5.10, respectively. Concerning the relevant background processes, the event yields for the scalar S mass-independent can be found in Figure 5.8. With the final cut on $m_{S_{1,2}}^{rec}$, the analysis becomes essentially background-free. As before, expected upper limits on the signal strength, $\sigma_{95\%}/\sigma_{th}(pp \rightarrow tSS(q), S \rightarrow \mu^+ \mu^-)$, are obtained using the invariant mass of the scalar S candidate distributed into 20 bins. The 95% upper limits on the branching ratio ($t \rightarrow SSq, S \rightarrow \mu^+ \mu^-$) and cross-section $\sigma(pp \rightarrow tSS(q), S \rightarrow \mu^+ \mu^-)$ are shown in Figure 5.8, including the $\pm 1\sigma$ (green band) and the $\pm 2\sigma$ (yellow band) uncertainties. For an integrated luminosity of 150 fb^{-1} , the upper limits on the production cross-section $\sigma(pp \rightarrow tSS, S \rightarrow \mu^+ \mu^-) > 10^{-3} \text{ pb}$ are obtained at 95% CL. In the small mass regime, a branching ratio of $BR(t \rightarrow SSq) > 10^{-6}$ can be probed at the 95% CL. The strongest limits in branching ratio are obtained for $m_S \sim 80 \text{ GeV}$, for which $BR(t \rightarrow SSq) > 5 (25) \times 10^{-10}$ can be probed in the up (charm) channel. The branching ratio limits correspond to a lower bound on the new physics scale Λ of about 2 TeV, assuming that $BR(S \rightarrow \mu^+ \mu^-) = 1$.

The dedicated analyses for the three different channels considered an integrated luminosity of $\mathcal{L} = 150 \text{ fb}^{-1}$. However, future particle physics experiments expect to continuously collect more data, where the High-Luminosity LHC effort at CERN is a great example. Consequently, naive prospects for higher luminosities can be obtained by scaling the statistical significance with $\sqrt{\mathcal{L}}$. Considering an integrated luminosity of $\mathcal{L} = 3 \text{ ab}^{-1}$, new physics scales Λ of about 200, 160, and 3 TeV in each of the channels, respectively.

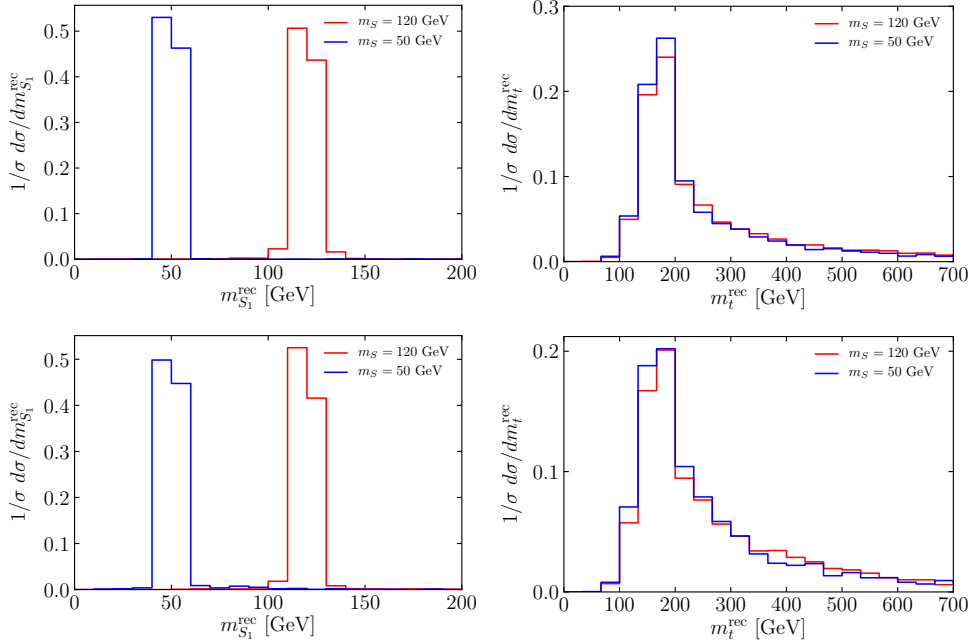


Figure 5.7: The two reconstructed scalar masses, m_{S1}^{rec} and m_{S2}^{rec} , in the analysis proposed for $t \rightarrow SSq$, $S \rightarrow \mu^+ \mu^-$. In the upper (bottom) panel, $q = c$ (u).

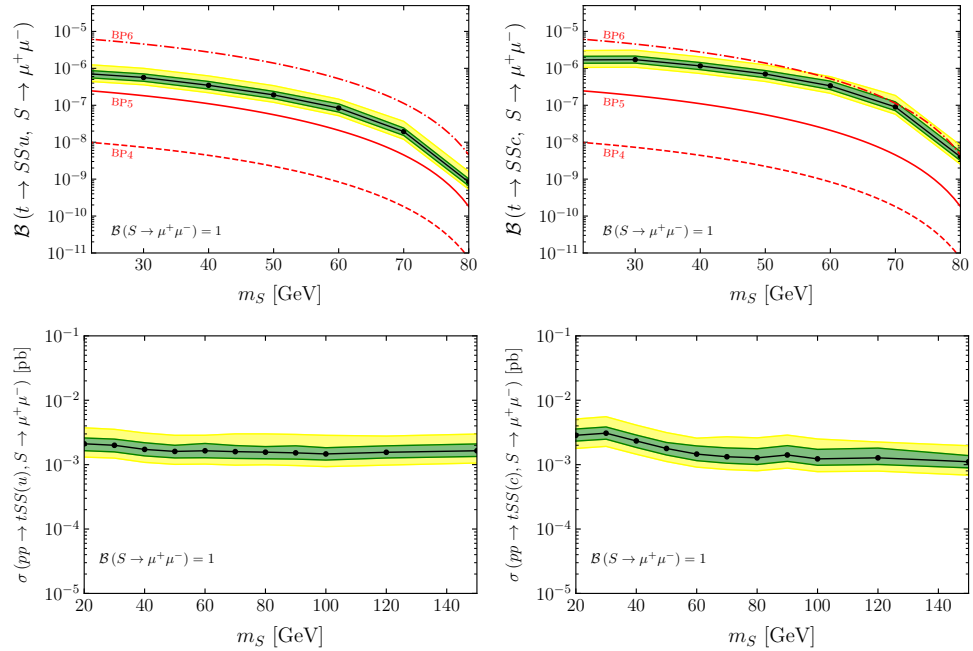


Figure 5.8: In the upper (bottom) panels, the 95% CL limits on the branching ratio (cross-section times branching ratio) that can be tested in the $\mu^+ \mu^-$ channel are shown, in the analysis proposed for $t \rightarrow SSq$, $S \rightarrow \mu^+ \mu^-$, with $q = u$ (c) in the panels on the left (right). The green and yellow bands show the $\pm 1\sigma$ and $\pm 2\sigma$ uncertainty on the limits, respectively. Superimposed are the theoretical expectations in three BPs.

Cuts/ m_S	20 GeV	30 GeV	40 GeV	50 GeV	60 GeV	70 GeV	80 GeV	90 GeV	100 GeV	120 GeV	150 GeV
Basic cuts	17.77 ± 0.08	15.51 ± 0.07	13.36 ± 0.06	11.53 ± 0.05	10.16 ± 0.05	9.21 ± 0.04	8.53 ± 0.04	7.12 ± 0.02	7.35 ± 0.03	6.36 ± 0.03	5.15 ± 0.02
$n_\ell = 4$	2.87 ± 0.03	2.70 ± 0.03	2.58 ± 0.03	2.47 ± 0.02	2.36 ± 0.02	2.27 ± 0.02	2.25 ± 0.02	1.79 ± 0.02	2.10 ± 0.02	1.94 ± 0.02	1.69 ± 0.01
$n_j \geq 3$	2.47 ± 0.03	2.33 ± 0.03	2.21 ± 0.02	2.10 ± 0.02	2.02 ± 0.02	1.91 ± 0.02	1.89 ± 0.02	0.92 ± 0.01	1.77 ± 0.02	1.63 ± 0.01	1.42 ± 0.01
$n_b = 1$	1.32 ± 0.02	1.20 ± 0.02	1.16 ± 0.02	1.11 ± 0.02	1.04 ± 0.01	1.00 ± 0.01	0.99 ± 0.01	0.92 ± 0.01	0.93 ± 0.01	0.86 ± 0.01	0.736 ± 0.009
$ m_t^{rec} - m_t < 50 \text{ GeV}$	0.74 ± 0.02	0.68 ± 0.01	0.65 ± 0.01	0.63 ± 0.01	0.58 ± 0.01	0.56 ± 0.01	0.54 ± 0.01	0.509 ± 0.009	0.504 ± 0.009	0.454 ± 0.008	0.393 ± 0.006
$n_{\mu^+ \mu^-} = 2$	0.74 ± 0.02	0.68 ± 0.01	0.65 ± 0.01	0.63 ± 0.01	0.58 ± 0.01	0.56 ± 0.01	0.54 ± 0.01	0.509 ± 0.009	0.504 ± 0.009	0.454 ± 0.008	0.393 ± 0.006
$m_{total} < 1 \text{ TeV}$	0.43 ± 0.01	0.39 ± 0.01	0.38 ± 0.01	0.349 ± 0.009	0.306 ± 0.008	0.281 ± 0.007	0.262 ± 0.007	0.248 ± 0.006	0.238 ± 0.006	0.197 ± 0.005	0.151 ± 0.004
$ m_{S_{1,2}}^{rec} - m_S < 30 \text{ GeV}$	0.42 ± 0.01	0.39 ± 0.01	0.38 ± 0.01	0.347 ± 0.009	0.301 ± 0.008	0.279 ± 0.007	0.260 ± 0.007	0.245 ± 0.006	0.235 ± 0.006	0.193 ± 0.005	0.146 ± 0.004

Table 5.9: Event yields after each cut for the eleven benchmark signal points, in the analysis for $t \rightarrow SSu, S \rightarrow \mu^+ \mu^-$. The parameters \tilde{Y}_{13} and \tilde{Y}_{31} are fixed to 0.1 with $\Lambda = 1 \text{ TeV}$ and $BR(S \rightarrow \mu^+ \mu^-) = 1$. The event yields presented assume a collected luminosity of $\mathcal{L} = 150 \text{ fb}^{-1}$.

Cuts/ m_S	20 GeV	30 GeV	40 GeV	50 GeV	60 GeV	70 GeV	80 GeV	90 GeV	100 GeV	120 GeV	150 GeV
Basic cuts	10.19 ± 0.05	7.63 ± 0.04	5.26 ± 0.02	3.43 ± 0.02	2.24 ± 0.01	1.656 ± 0.008	1.447 ± 0.007	0.434 ± 0.004	1.201 ± 0.006	1.000 ± 0.005	0.511 ± 0.003
$n_\ell = 4$	0.76 ± 0.01	0.90 ± 0.01	0.85 ± 0.01	0.729 ± 0.008	0.609 ± 0.006	0.526 ± 0.005	0.495 ± 0.004	0.308 ± 0.003	0.445 ± 0.004	0.395 ± 0.003	0.192 ± 0.002
$n_j \geq 3$	0.68 ± 0.01	0.65 ± 0.01	0.624 ± 0.009	0.520 ± 0.006	0.431 ± 0.005	0.369 ± 0.004	0.350 ± 0.003	0.161 ± 0.002	0.315 ± 0.003	0.281 ± 0.003	0.163 ± 0.001
$n_b = 1$	0.347 ± 0.009	0.356 ± 0.008	0.325 ± 0.006	0.274 ± 0.006	0.227 ± 0.003	0.194 ± 0.003	0.183 ± 0.003	0.161 ± 0.002	0.165 ± 0.002	0.145 ± 0.002	0.083 ± 0.001
$ m_t^{rec} - m_t < 50 \text{ GeV}$	0.219 ± 0.007	0.151 ± 0.005	0.145 ± 0.004	0.127 ± 0.003	0.105 ± 0.002	0.090 ± 0.002	0.086 ± 0.002	0.046 ± 0.001	0.075 ± 0.001	0.065 ± 0.001	0.046 ± 0.001
$n_{\mu^+ \mu^-} = 2$	0.219 ± 0.007	0.151 ± 0.005	0.145 ± 0.004	0.127 ± 0.003	0.105 ± 0.002	0.090 ± 0.002	0.086 ± 0.002	0.046 ± 0.001	0.075 ± 0.001	0.065 ± 0.001	0.046 ± 0.001
$m_{total} < 1 \text{ TeV}$	0.186 ± 0.007	0.125 ± 0.005	0.123 ± 0.004	0.101 ± 0.003	0.078 ± 0.002	0.062 ± 0.002	0.057 ± 0.001	0.044 ± 0.001	0.048 ± 0.001	0.039 ± 0.001	0.023 ± 0.001
$ m_{S_{1,2}}^{rec} - m_S < 30 \text{ GeV}$	0.185 ± 0.007	0.121 ± 0.005	0.114 ± 0.004	0.095 ± 0.003	0.074 ± 0.002	0.059 ± 0.002	0.054 ± 0.001	0.044 ± 0.001	0.046 ± 0.001	0.037 ± 0.001	0.022 ± 0.001

Table 5.10: Event yields after each cut for the eleven benchmark signal points, in the analysis for $t \rightarrow SSc, S \rightarrow \mu^+ \mu^-$. The parameters \tilde{Y}_{23} and \tilde{Y}_{32} are fixed to 0.1 with $\Lambda = 1 \text{ TeV}$ and $BR(S \rightarrow \mu^+ \mu^-) = 1$. The event yields presented assume a collected luminosity of $\mathcal{L} = 150 \text{ fb}^{-1}$.

Cuts/Background	tW	$t\bar{t}W/t\bar{t}Z$	ZZZ/WWW	$ZZ/Z/WWW$	$t\bar{t}(p)$	tZ
Basic cuts	8084736 ± 36749	649 ± 2	5.28 ± 0.01	14380159 ± 65319	798347 ± 1167	281 ± 1
$n_\ell = 4$	< 42	8.8 ± 0.2	1.372 ± 0.006	1780 ± 727	17 ± 5	0.07 ± 0.02
$n_j \geq 3$	—	5.6 ± 0.2	0.100 ± 0.002	297 ± 297	7 ± 3	0.03 ± 0.01
$n_b = 1$	—	2.6 ± 0.1	0.010 ± 0.001	< 4	3 ± 2	0.011 ± 0.008
$ m_t^{rec} - m_t < 50 \text{ GeV}$	—	0.62 ± 0.06	0.002 ± 0.001	—	< 2	< 0.006
$n_{\mu^+ \mu^-} = 2$	—	0.62 ± 0.06	0.002 ± 0.001	—	—	—
$m_{total} < 1 \text{ TeV}$	—	0.60 ± 0.06	< 0.0003	—	—	—

Table 5.11: Event yields after each cut for the dominant backgrounds, in the analysis for $t \rightarrow SSq, S \rightarrow \mu^+ \mu^-$. The $Z + \text{jets}$ sample is reduced to negligible values after the second cut. The event yields presented assume a collected luminosity of $\mathcal{L} = 150 \text{ fb}^{-1}$.

Conclusion

The discovery of the top quark was an important step on the knowledge of the building blocks of the world around us. The exciting properties of the top quark opened a new sector of measurements dedicated to the validation of the SM, where the recent discovery of the Higgs boson at the LHC played a major role. So far, all measurements are compatible with the theoretical predictions of the SM. However, several hints of physics beyond it were observed, motivating the search for new horizons within the particle physics field.

To explore some of these shortcomings, a search for FCNC interactions with a top quark, a neutral Z boson and a light-quark has been established using the 13 TeV data collected by the ATLAS detector. As the main analyser for the production mode effort (along with the analysis contact responsibility), the full analysis for this mode was developed, from the validation of the MC simulated signal samples to the setting of the final limits on the signal hypotheses. Events with exactly three charged leptons are considered, assuming the leptonic decays of the Z boson and the top quark. Events are further split into non-overlapping regions based on the number of jets and the reconstructed mass of the top quark candidates, providing regions enriched in the signal and the dominant background processes. Distinct signal regions are defined since the tZ production and the $t\bar{t}$ decay modes were considered. The inclusion of both modes motivated a phenomenological study on the interference effects for the FCNC interaction with a tZq vertex. This estimate was performed for both FCNC tZq and $t\gamma q$ vertices in collaboration with the University of Dortmund (Germany) [67]. A total of three processes (only production, only decay and production and decay modes with interference) were considered, which motivated a detailed investigation on the MC simulation. Interference effects observed in the distribution of the most sensible variables (the transverse momentum of the Z boson/photon for $tZq/t\gamma q$ case) are found to be smaller than variations of the renormalisation and factorisation scales. Returning to the data analysis, the implementation and optimisation of multivariate techniques based on Boosted Decision Trees are performed to improve

the signal-to-background discrimination for the different signal processes. The final results show that no significant deviation from the SM expectation is found for the data analysed. For the FCNC tZq vertex, observed (expected) limits are set at a 95% CL for tZu processes excluding branching ratios above $6.16(4.88) \times 10^{-5}$, and for tZc processes excluding branching ratios above $13.02(10.76) \times 10^{-5}$. These limits were translated into upper limits on the cross-section and the EFT Wilson coefficients as summarised in Table 4.35 and Table 4.34.

The second part of the work of this thesis is the phenomenological study on the top quark interactions with a new pseudo-scalar particle performed in collaboration with the University of Granada (Spain) [219]. In particular, the FCNC processes between a top quark, a new pseudo-scalar and a light quark are considered. MC simulated events for the signal hypotheses of three targeted processes, including both production and decay modes and the decay of the pseudo-scalar particle to muons or tau leptons were generated. The scenario of pair production of the pseudo-scalar particle was also considered. The evaluation of all the non-negligible background processes was pursued and the MC simulation of the dominant processes was executed. After the development of the analysis interface and limits setting tools, an intensive study on the kinematic and angular observables providing the best signal-to-background ratio was performed. Three dedicated searches are proposed and upper limits on the cross-section and branching ratio at a 95% CL are obtained assuming an integrated luminosity of 150 fb^{-1} . For $pp \rightarrow tS, S \rightarrow \mu^+ \mu^-$, the strongest limits on the branching ratio are $5(15) \times 10^{-7}$ for up (charm) quark, with a mass of the pseudo-scalar of 150 GeV . Concerning the $pp \rightarrow tS, S \rightarrow \tau^+ \tau^-$, the strongest limits on the branching ratio are $11(12) \times 10^{-6}$ for up (charm) quark, with a mass of the pseudo-scalar of 50 GeV . Finally, the strongest limits on the branching ratio for $pp \rightarrow tSS, S \rightarrow \mu^+ \mu^-$ are obtained for a mass of the pseudo-scalar of 80 GeV with the values of $5(25) \times 10^{-10}$ for up (charm) quark.

The LHC and the ATLAS experiment will continue to collect data in the coming years. For now, the upper limits on the FCNC tZq vertex present the most stringent limits to date. Future searches with a more significant dataset can shorten the space between the experimental limits and the theoretical expectations of models beyond the SM. Such achievement would not be only important for the FCNC processes but also for the particle physics field in general, since it can exclude or possibly discover new BSM models. In the best scenario, analyses with new sophisticated methods and more data also bring the possibility of an observation of the FCNC processes at a higher rate than the SM predictions, which would be a direct proof of New Physics. Finally, the era of the Higgs physics is only beginning and a better knowledge of the Higgs boson would simultaneously proportionate a stronger comprehension of the top quark.

Bibliography

- [1] S. L. Glashow. “Partial Symmetries of Weak Interactions.” In: *Nucl. Phys.* 22 (1961), pp. 579–588. doi: [10.1016/0029-5582\(61\)90469-2](https://doi.org/10.1016/0029-5582(61)90469-2).
- [2] Particle Data Group. “Review of Particle Physics.” In: *PTEP* 2020.8 (2020), p. 083C01. doi: [10.1093/ptep/ptaa104](https://doi.org/10.1093/ptep/ptaa104).
- [3] ATLAS Collaboration. “Measurement of the Higgs boson mass in the $H \rightarrow ZZ^* \rightarrow 4\ell$ and $H \rightarrow \gamma\gamma$ channels with $\sqrt{s} = 13$ TeV pp collisions using the ATLAS detector.” In: *Phys. Lett. B* 784 (2018), pp. 345–366. doi: [10.1016/j.physletb.2018.07.050](https://doi.org/10.1016/j.physletb.2018.07.050). arXiv: [1806.00242 \[hep-ex\]](https://arxiv.org/abs/1806.00242).
- [4] E. Noether. “Invariant variation problems.” In: *Transport Theory and Statistical Physics* 1.3 (1971), pp. 186–207. issn: 1532-2424. doi: [10.1080/00411457108231446](https://doi.org/10.1080/00411457108231446). url: <http://dx.doi.org/10.1080/00411457108231446>.
- [5] H. Fritzsch, M. Gell-Mann, and H. Leutwyler. “Advantages of the color octet gluon picture.” In: *Physics Letters B* 47.4 (1973), pp. 365 –368. issn: 0370-2693. doi: [http://dx.doi.org/10.1016/0370-2693\(73\)90625-4](http://dx.doi.org/10.1016/0370-2693(73)90625-4). url: <http://www.sciencedirect.com/science/article/pii/0370269373906254>.
- [6] H. Politzer. “Reliable Perturbative Results for Strong Interactions?” In: *Phys. Rev. Lett.* 30 (26 1973), 1346–1349. doi: [{10.1103/PhysRevLett.30.1346}](https://doi.org/10.1103/PhysRevLett.30.1346). url: [{http://link.aps.org/doi/10.1103/PhysRevLett.30.1346}](http://link.aps.org/doi/10.1103/PhysRevLett.30.1346).
- [7] D. J. Gross and F. Wilczek. “Ultraviolet Behavior of Non-Abelian Gauge Theories.” In: *Phys. Rev. Lett.* 30 (26 1973), pp. 1343–1346. doi: [10.1103/PhysRevLett.30.1343](https://doi.org/10.1103/PhysRevLett.30.1343). url: <http://link.aps.org/doi/10.1103/PhysRevLett.30.1343>.
- [8] ATLAS Collaboration. “Jet reconstruction and performance using particle flow with the ATLAS Detector.” In: *Eur. Phys. J. C* 77 (2017), p. 466. doi: [10.1140/epjc/s10052-017-5031-2](https://doi.org/10.1140/epjc/s10052-017-5031-2). arXiv: [1703.10485 \[hep-ex\]](https://arxiv.org/abs/1703.10485).
- [9] S. L. Glashow. “Partial-symmetries of weak interactions.” In: *Nuclear Physics* 22.4 (1961), pp. 579 –588. issn: 0029-5582. doi: [http://dx.doi.org/10.1016/0029-5582\(61\)90469-2](http://dx.doi.org/10.1016/0029-5582(61)90469-2). url: <http://www.sciencedirect.com/science/article/pii/0029558261904692>.

-
- [10] A. Salam. "Weak and Electromagnetic Interactions." In: *Conf. Proc. C680519* (1968), pp. 367–377.
 - [11] S. Weinberg. "A Model of Leptons." In: *Phys. Rev. Lett.* 19 (21 1967), 1264–1266. doi: [10.1103/PhysRevLett.19.1264](https://doi.org/10.1103/PhysRevLett.19.1264). url: <http://link.aps.org/doi/10.1103/PhysRevLett.19.1264>.
 - [12] F. Englert and R. Brout. "Broken Symmetry and the Mass of Gauge Vector Mesons." In: *Phys. Rev. Lett.* 13 (1964), pp. 321–323. doi: [10.1103/PhysRevLett.13.321](https://doi.org/10.1103/PhysRevLett.13.321).
 - [13] P. W. Higgs. "Broken Symmetries and the Masses of Gauge Bosons." In: *Phys. Rev. Lett.* 13 (1964), pp. 508–509. doi: [10.1103/PhysRevLett.13.508](https://doi.org/10.1103/PhysRevLett.13.508).
 - [14] G. Guralnik, C. Hagen and T. Kibble. "Global Conservation Laws and Massless Particles." In: *Phys. Rev. Lett.* 13 (20 1964), 585–587. doi: [10.1103/PhysRevLett.13.585](https://doi.org/10.1103/PhysRevLett.13.585). url: <http://link.aps.org/doi/10.1103/PhysRevLett.13.585>.
 - [15] M. Bustamante, L. Cieri, and J. Ellis. "Beyond the Standard Model for Montaneros." In: *High-energy physics. Proceedings, 5th CERN-Latin-American School, Recinto Quirama, Colombia, March 15-28, 2009*. 2009. arXiv: [0911.4409 \[hep-ph\]](https://arxiv.org/abs/0911.4409). url: <https://inspirehep.net/record/837595/files/arXiv:0911.4409.pdf>.
 - [16] K. Begeman, B. A., and R. Sanders. "Extended rotation curves of spiral galaxies: dark haloes and modified dynamics." In: *Monthly Notices of the Royal Astronomical Society* 249.3 (Apr. 1991), pp. 523–537. issn: 0035-8711. doi: [10.1093/mnras/249.3.523](https://doi.org/10.1093/mnras/249.3.523). eprint: <https://academic.oup.com/mnras/article-pdf/249/3/523/18160929/mnras249-0523.pdf>. url: <https://doi.org/10.1093/mnras/249.3.523>.
 - [17] D. Larson et al. "Seven-Year Wilkinson Microwave Anisotropy Probe (WMAP) Observations: Power Spectra and WMAP-Derived Parameters." In: *The Astrophysical Journal Supplement Series* 192.2 (2011), p. 16. issn: 1538-4365. doi: [10.1088/0067-0049/192/2/16](https://doi.org/10.1088/0067-0049/192/2/16). url: <http://dx.doi.org/10.1088/0067-0049/192/2/16>.
 - [18] P. Ade et al. "Planck 2013 results. XVI. Cosmological parameters." In: *Astron. Astrophys.* 571 (2014), A16. doi: [10.1051/0004-6361/201321591](https://doi.org/10.1051/0004-6361/201321591). arXiv: [1303.5076 \[astro-ph.CO\]](https://arxiv.org/abs/1303.5076).
 - [19] A. D. Sakharov. "Violation of CP Invariance, C asymmetry, and baryon asymmetry of the universe." In: *Pisma Zh. Eksp. Teor. Fiz.* 5 (1967), pp. 32–35. doi: [10.1070/PU1991v034n05ABEH002497](https://doi.org/10.1070/PU1991v034n05ABEH002497).
 - [20] Y. Fukuda et al. "Evidence for oscillation of atmospheric neutrinos." In: *Phys. Rev. Lett.* 81 (1998), pp. 1562–1567. doi: [10.1103/PhysRevLett.81.1562](https://doi.org/10.1103/PhysRevLett.81.1562). arXiv: [hep-ex/9807003](https://arxiv.org/abs/hep-ex/9807003).
 - [21] ATLAS Collaboration. "Measurement of the top quark mass in the $t\bar{t} \rightarrow \text{lepton+jets}$ channel from $\sqrt{s} = 8$ TeV ATLAS data and combination with previous results." In: *Eur. Phys. J. C* 79.4 (2019), p. 290. doi: [10.1140/epjc/s10052-019-6757-9](https://doi.org/10.1140/epjc/s10052-019-6757-9). arXiv: [1810.01772 \[hep-ex\]](https://arxiv.org/abs/1810.01772).

- [22] Y. L. Dokshitzer. “Calculation of the Structure Functions for Deep Inelastic Scattering and $e^+ e^-$ Annihilation by Perturbation Theory in Quantum Chromodynamics.” In: *Sov. Phys. JETP* 46 (1977), pp. 641–653.
- [23] V. N. Gribov and L. N. Lipatov. “Deep inelastic ep scattering in perturbation theory.” In: *Sov. J. Nucl. Phys.* 15 (1972), pp. 438–450.
- [24] G. Altarelli and G. Parisi. “Asymptotic Freedom in Parton Language.” In: *Nucl. Phys. B* 126 (1977), pp. 298–318. doi: [10.1016/0550-3213\(77\)90384-4](https://doi.org/10.1016/0550-3213(77)90384-4).
- [25] NNPDF Collaboration. “Parton distributions from high-precision collider data.” In: *Eur. Phys. J. C* 77.10 (2017), p. 663. doi: [10.1140/epjc/s10052-017-5199-5](https://doi.org/10.1140/epjc/s10052-017-5199-5). arXiv: [1706.00428 \[hep-ph\]](https://arxiv.org/abs/1706.00428).
- [26] CDF Collaboration. “Observation of top quark production in $\bar{p}p$ collisions.” In: *Phys. Rev. Lett.* 74 (1995), pp. 2626–2631. doi: [10.1103/PhysRevLett.74.2626](https://doi.org/10.1103/PhysRevLett.74.2626). arXiv: [hep-ex/9503002 \[hep-ex\]](https://arxiv.org/abs/hep-ex/9503002).
- [27] D0 Collaboration. “Observation of the top quark.” In: *Phys. Rev. Lett.* 74 (1995), pp. 2632–2637. doi: [10.1103/PhysRevLett.74.2632](https://doi.org/10.1103/PhysRevLett.74.2632). arXiv: [hep-ex/9503003 \[hep-ex\]](https://arxiv.org/abs/hep-ex/9503003).
- [28] ATLAS Collaboration. “Measurement of the top quark-pair production cross section with ATLAS in $p\bar{p}$ collisions at $\sqrt{s} = 7$ TeV.” In: *Eur. Phys. J. C* 71 (2011), p. 1577. doi: [10.1140/epjc/s10052-011-1577-6](https://doi.org/10.1140/epjc/s10052-011-1577-6). arXiv: [1012.1792 \[hep-ex\]](https://arxiv.org/abs/1012.1792).
- [29] CMS Collaboration. “First Measurement of the Cross Section for Top-Quark Pair Production in Proton-Proton Collisions at $\sqrt{s} = 7$ TeV.” In: *Phys. Lett. B* 695 (2011), pp. 424–443. doi: [10.1016/j.physletb.2010.11.058](https://doi.org/10.1016/j.physletb.2010.11.058). arXiv: [1010.5994 \[hep-ex\]](https://arxiv.org/abs/1010.5994).
- [30] K. Kröninger, A. B. Meyer, and P. Uwer. “Top-Quark Physics at the LHC.” In: (2015). Ed. by T. Schörner-Sadenius, pp. 259–300. doi: [10.1007/978-3-319-15001-7_7](https://doi.org/10.1007/978-3-319-15001-7_7). arXiv: [1506.02800 \[hep-ex\]](https://arxiv.org/abs/1506.02800). url: <https://inspirehep.net/record/1375310/files/arXiv:1506.02800.pdf>.
- [31] *Feynman diagrams for top quark pair production.* <http://inspirehep.net/record/1103034/plots>. [Online; Accessed: 17-05-2021].
- [32] M. Czakon, P. Fiedler, and A. Mitov. “Total Top-Quark Pair-Production Cross Section at Hadron Colliders Through $O(\alpha_S^4)$.” In: *Phys. Rev. Lett.* 110 (2013), p. 252004. doi: [10.1103/PhysRevLett.110.252004](https://doi.org/10.1103/PhysRevLett.110.252004). arXiv: [1303.6254 \[hep-ph\]](https://arxiv.org/abs/1303.6254).
- [33] N. Kidonakis. “Next-to-next-to-leading-order collinear and soft gluon corrections for t -channel single top quark production.” In: *Phys. Rev. D* 83 (9 2011), p. 091503. doi: [10.1103/PhysRevD.83.091503](https://doi.org/10.1103/PhysRevD.83.091503). url: <https://link.aps.org/doi/10.1103/PhysRevD.83.091503>.

- [34] N. Kidonakis. “Two-loop soft anomalous dimensions for single top quark associated production with a W^- or H^- .” In: *Phys. Rev. D* 82 (5 2010), p. 054018. doi: [10.1103/PhysRevD.82.054018](https://doi.org/10.1103/PhysRevD.82.054018). url: <https://link.aps.org/doi/10.1103/PhysRevD.82.054018>.
- [35] N. Kidonakis. “Next-to-next-to-leading logarithm resummation for s-channel single top quark production.” In: *Phys. Rev. D* 81 (5 2010), p. 054028. doi: [10.1103/PhysRevD.81.054028](https://doi.org/10.1103/PhysRevD.81.054028). url: <https://link.aps.org/doi/10.1103/PhysRevD.81.054028>.
- [36] ATLAS Collaboration. *Top working group cross-section summary plots: Autumn 2020*. Tech. rep. ATL-PHYS-PUB-2020-029. Geneva: CERN, 2020. url: <http://cds.cern.ch/record/2746598>.
- [37] S. L. Glashow, J. Iliopoulos, and L. Maiani. “Weak Interactions with Lepton-Hadron Symmetry.” In: *Phys. Rev. D* 2 (1970), pp. 1285–1292. doi: [10.1103/PhysRevD.2.1285](https://doi.org/10.1103/PhysRevD.2.1285).
- [38] A. Heister et al. “Search for single top production in e^+e^- collisions at \sqrt{s} up to 209-GeV.” In: *Phys. Lett. B* 543 (2002), pp. 173–182. doi: [10.1016/S0370-2693\(02\)02307-9](https://doi.org/10.1016/S0370-2693(02)02307-9). arXiv: [hep-ex/0206070](https://arxiv.org/abs/hep-ex/0206070).
- [39] DELPHI Collaboration. “Search for single top production via FCNC at LEP at $\sqrt{s} = 189$ -GeV to 208-GeV.” In: *Phys. Lett. B* 590 (2004), pp. 21–34. doi: [10.1016/j.physletb.2004.03.051](https://doi.org/10.1016/j.physletb.2004.03.051). arXiv: [hep-ex/0404014](https://arxiv.org/abs/hep-ex/0404014).
- [40] OPAL Collaboration. “Search for single top quark production at LEP-2.” In: *Phys. Lett. B* 521 (2001), pp. 181–194. doi: [10.1016/S0370-2693\(01\)01195-9](https://doi.org/10.1016/S0370-2693(01)01195-9). arXiv: [hep-ex/0110009](https://arxiv.org/abs/hep-ex/0110009).
- [41] L3 Collaboration. “Search for single top production at LEP.” In: *Phys. Lett. B* 549 (2002), pp. 290–300. doi: [10.1016/S0370-2693\(02\)02933-7](https://doi.org/10.1016/S0370-2693(02)02933-7). arXiv: [hep-ex/0210041](https://arxiv.org/abs/hep-ex/0210041).
- [42] LEP Exotica Working Group and DELPHI, ALEPH, L3 and OPAL Collaborations. “Search for single top production via flavour changing neutral currents: preliminary combined results of the LEP experiments.” In: (2001). url: <https://cds.cern.ch/record/1006392>.
- [43] ZEUS Collaboration. “Search for single-top production in ep collisions at HERA.” In: *Phys. Lett. B* 708 (2012), pp. 27–36. doi: [10.1016/j.physletb.2012.01.025](https://doi.org/10.1016/j.physletb.2012.01.025). arXiv: [1111.3901 \[hep-ex\]](https://arxiv.org/abs/1111.3901).
- [44] CDF Collaboration. “Search for the Flavor Changing Neutral Current Decay $t \rightarrow Zq$ in $p\bar{p}$ Collisions at $\sqrt{s} = 1.96$ TeV.” In: *Phys. Rev. Lett.* 101 (2008), p. 192002. doi: [10.1103/PhysRevLett.101.192002](https://doi.org/10.1103/PhysRevLett.101.192002). arXiv: [0805.2109 \[hep-ex\]](https://arxiv.org/abs/0805.2109).
- [45] D0 Collaboration. “Search for Flavor Changing Neutral Currents in Decays of Top Quarks.” In: *Phys. Lett. B* 701 (2011), pp. 313–320. doi: [10.1016/j.physletb.2011.06.014](https://doi.org/10.1016/j.physletb.2011.06.014). arXiv: [1103.4574 \[hep-ex\]](https://arxiv.org/abs/1103.4574).

- [46] J. A. Aguilar-Saavedra. “Top flavor-changing neutral interactions: Theoretical expectations and experimental detection.” In: *Acta Phys. Polon.* B35 (2004), pp. 2695–2710. arXiv: [hep-ph/0409342 \[hep-ph\]](#).
- [47] ATLAS Collaboration. “Search for flavour-changing neutral current top-quark decays $t \rightarrow qZ$ in proton–proton collisions at $\sqrt{s} = 13$ TeV with the ATLAS detector.” In: *JHEP* 07 (2018), p. 176. doi: [10.1007/JHEP07\(2018\)176](#). arXiv: [1803.09923 \[hep-ex\]](#).
- [48] CMS Collaboration. “Search for associated production of a Z boson with a single top quark and for tZ flavour-changing interactions in pp collisions at $\sqrt{s} = 8$ TeV.” In: *JHEP* 07 (2017), p. 003. doi: [10.1007/JHEP07\(2017\)003](#). arXiv: [1702.01404 \[hep-ex\]](#).
- [49] CMS Collaboration. “Search for flavour changing neutral currents in top quark production and decays with three-lepton final state using the data collected at $\sqrt{s} = 13$ TeV.” In: CMS-PAS-TOP-17-017 (2017). url: <https://cds.cern.ch/record/2292045>.
- [50] ATLAS Collaboration. “Search for single top-quark production via flavour-changing neutral currents at 8 TeV with the ATLAS detector.” In: *Eur. Phys. J. C* 76.2 (2016), p. 55. doi: [10.1140/epjc/s10052-016-3876-4](#). arXiv: [1509.00294 \[hep-ex\]](#).
- [51] CMS Collaboration. “Search for anomalous Wtb couplings and flavour-changing neutral currents in t-channel single top quark production in pp collisions at $\sqrt{s} = 7$ and 8 TeV.” In: *JHEP* 02 (2017), p. 028. doi: [10.1007/JHEP02\(2017\)028](#). arXiv: [1610.03545 \[hep-ex\]](#).
- [52] ATLAS Collaboration. “Search for flavour-changing neutral currents in processes with one top quark and a photon using 81 fb^{-1} of pp collisions at $\sqrt{s} = 13$ TeV with the ATLAS experiment.” In: *Phys. Lett. B* 800 (2020), p. 135082. doi: [10.1016/j.physletb.2019.135082](#). arXiv: [1908.08461 \[hep-ex\]](#).
- [53] CMS Collaboration. “Search for Anomalous Single Top Quark Production in Association with a Photon in pp Collisions at $\sqrt{s} = 8$ TeV.” In: *JHEP* 04 (2016), p. 035. doi: [10.1007/JHEP04\(2016\)035](#). arXiv: [1511.03951 \[hep-ex\]](#).
- [54] ATLAS Collaboration. “Search for top-quark decays $t \rightarrow Hq$ with 36 fb^{-1} of pp collision data at $\sqrt{s} = 13$ TeV with the ATLAS detector.” In: *JHEP* 05 (2019), p. 123. doi: [10.1007/JHEP05\(2019\)123](#). arXiv: [1812.11568 \[hep-ex\]](#).
- [55] CMS Collaboration. “Search for the flavor-changing neutral current interactions of the top quark and the Higgs boson which decays into a pair of b quarks at $\sqrt{s} = 13$ TeV.” In: *JHEP* 06 (2018), p. 102. doi: [10.1007/JHEP06\(2018\)102](#). arXiv: [1712.02399 \[hep-ex\]](#).
- [56] CMS Collaboration. “Search for top quark decays via Higgs-boson-mediated flavor-changing neutral currents in pp collisions at $\sqrt{s} = 8$ TeV.” In: *JHEP* 02 (2017), p. 079. doi: [10.1007/JHEP02\(2017\)079](#). arXiv: [1610.04857 \[hep-ex\]](#).

-
- [57] Top Quark Working Group. “Working Group Report: Top Quark.” In: *Community Summer Study 2013: Snowmass on the Mississippi*. Nov. 2013. arXiv: [1311.2028 \[hep-ph\]](#).
 - [58] C. Zhang and S. Willenbrock. “Effective-Field-Theory Approach to Top-Quark Production and Decay.” In: *Phys. Rev.* D83 (2011), p. 034006. doi: [10.1103/PhysRevD.83.034006](#). arXiv: [1008.3869 \[hep-ph\]](#).
 - [59] B. Grzadkowski, M. Iskrzynski, M. Misiak, and J. Rosiek. “Dimension-Six Terms in the Standard Model Lagrangian.” In: *JHEP* 10 (2010), p. 085. doi: [10.1007/JHEP10\(2010\)085](#). arXiv: [1008.4884 \[hep-ph\]](#).
 - [60] C. Degrande, F. Maltoni, J. Wang, and C. Zhang. “Automatic computations at next-to-leading order in QCD for top-quark flavor-changing neutral processes.” In: *Phys. Rev.* D91 (2015), p. 034024. doi: [10.1103/PhysRevD.91.034024](#). arXiv: [1412.5594 \[hep-ph\]](#).
 - [61] G. Durieux, F. Maltoni, and C. Zhang. “Global approach to top-quark flavor-changing interactions.” In: *Phys. Rev.* D91.7 (2015), p. 074017. doi: [10.1103/PhysRevD.91.074017](#). arXiv: [1412.7166 \[hep-ph\]](#).
 - [62] ATLAS Collaboration. “Probing the quantum interference between singly and doubly resonant top-quark production in pp collisions at $\sqrt{s} = 13$ TeV with the ATLAS detector.” In: *Phys. Rev. Lett.* 121.15 (2018), p. 152002. doi: [10.1103/PhysRevLett.121.152002](#). arXiv: [1806.04667 \[hep-ex\]](#).
 - [63] A. Alloul, N. D. Christensen, C. Degrande, C. Duhr, and B. Fuks. “FeynRules 2.0 – A complete toolbox for tree-level phenomenology.” In: *Comput. Phys. Commun.* 185 (2014), pp. 2250–2300. doi: [10.1016/j.cpc.2014.04.012](#). arXiv: [1310.1921 \[hep-ph\]](#).
 - [64] T. Sjöstrand, S. Mrenna, and P. Skands. “A brief introduction to PYTHIA 8.1.” In: *Comput. Phys. Commun.* 178 (2008), pp. 852–867. doi: [10.1016/j.cpc.2008.01.036](#). arXiv: [0710.3820 \[hep-ph\]](#).
 - [65] M. L. Mangano, M. Moretti, F. Piccinini, and M. Treccani. “Matching matrix elements and shower evolution for top-quark production in hadronic collisions.” In: *JHEP* 01 (2007), p. 013. doi: [10.1088/1126-6708/2007/01/013](#). arXiv: [hep-ph/0611129](#).
 - [66] J. de Favereau, C. Delaere, P. Demin, A. Giannanco, V. Lemaître, A. Mertens, and M. Selvaggi. “DELPHES 3: a modular framework for fast simulation of a generic collider experiment.” In: *Journal of High Energy Physics* 2014.2 (2014). issn: 1029-8479. doi: [10.1007/jhep02\(2014\)057](#). url: [http://dx.doi.org/10.1007/JHEP02\(2014\)057](http://dx.doi.org/10.1007/JHEP02(2014)057).

-
- [67] M. Barros, N. F. Castro, J. Erdmann, G. Geßner, K. Kröninger, S. La Cagnina, and A. Peixoto. "Study of interference effects in the search for flavour-changing neutral current interactions involving the top quark and a photon or a Z boson at the LHC." In: *Eur. Phys. J. Plus* 135.3 (2020), p. 339. doi: [10.1140/epjp/s13360-020-00346-3](https://doi.org/10.1140/epjp/s13360-020-00346-3). arXiv: [1909.08443 \[hep-ph\]](https://arxiv.org/abs/1909.08443).
 - [68] *CERN accelerator complex*. <https://cds.cern.ch/record/2684277>. [Online; Accessed: 17-05-2021].
 - [69] F. Hasert, S. Kabe, W. Krenz, J. V. Krogh], D. Lanske, J. Morfin, K. Schultze, and H. Weerts. "Observation of neutrino-like interactions without muon or electron in the gargamelle neutrino experiment." In: *Physics Letters B* 46.1 (1973), pp. 138 –140. issn: 0370-2693. doi: [https://doi.org/10.1016/0370-2693\(73\)90499-1](https://doi.org/10.1016/0370-2693(73)90499-1). url: <http://www.sciencedirect.com/science/article/pii/0370269373904991>.
 - [70] G. Arnison, A. Astbury, B. Aubert, C. Bacci, G. Bauer, A. Bézaguet, R. Böck, and T. Bowcock. "Experimental observation of isolated large transverse energy electrons with associated missing energy at $s=540$ GeV." In: *Physics Letters B* 122.1 (1983), pp. 103 –116. issn: 0370-2693. doi: [https://doi.org/10.1016/0370-2693\(83\)91177-2](https://doi.org/10.1016/0370-2693(83)91177-2). url: <http://www.sciencedirect.com/science/article/pii/0370269383911772>.
 - [71] M. Banner et al. "Observation of Single Isolated Electrons of High Transverse Momentum in Events with Missing Transverse Energy at the CERN anti-p p Collider." In: *Phys. Lett. B* 122 (1983), pp. 476–485. doi: [10.1016/0370-2693\(83\)91605-2](https://doi.org/10.1016/0370-2693(83)91605-2).
 - [72] S. Schael et al. "Precision electroweak measurements on the Z resonance." In: *Phys. Rept.* 427 (2006), pp. 257–454. doi: [10.1016/j.physrep.2005.12.006](https://doi.org/10.1016/j.physrep.2005.12.006). arXiv: [hep-ex/0509008](https://arxiv.org/abs/hep-ex/0509008).
 - [73] V. Fanti, A. Lai, D. Marras, L. Musa, A. Bevan, T. Gershon, B. Hay, R. Moore, K. Moore, and D. Munday. "A new measurement of direct CP violation in two pion decays of the neutral kaon." In: *Physics Letters B* 465.1 (1999), pp. 335 –348. issn: 0370-2693. doi: [https://doi.org/10.1016/S0370-2693\(99\)01030-8](https://doi.org/10.1016/S0370-2693(99)01030-8). url: <http://www.sciencedirect.com/science/article/pii/S0370269399010308>.
 - [74] ATLAS Collaboration. "Observation of a new particle in the search for the Standard Model Higgs boson with the ATLAS detector at the LHC." In: *Physics Letters B* 716.1 (2012), pp. 1 –29. issn: 0370-2693. doi: <https://doi.org/10.1016/j.physletb.2012.08.020>. url: <http://www.sciencedirect.com/science/article/pii/S037026931200857X>.
 - [75] CMS Collaboration. "Observation of a New Boson at a Mass of 125 GeV with the CMS Experiment at the LHC." In: *Phys. Lett. B* 716 (2012), pp. 30–61. doi: [10.1016/j.physletb.2012.08.021](https://doi.org/10.1016/j.physletb.2012.08.021). arXiv: [1207.7235 \[hep-ex\]](https://arxiv.org/abs/1207.7235).

-
- [76] *Diagram of an LHC dipole magnet.* <https://cds.cern.ch/record/40524>. [Online; Accessed: 17-05-2021].
 - [77] T. Kawamoto, S. Vlachos, L. Pontecorvo, J. Dubbert, G. Mikenberg, P. Iengo, C. Dallapiccola, C. Amelung, L. Levinson, R. Richter, and D. Lellouch. *New Small Wheel Technical Design Report*. Tech. rep. CERN-LHCC-2013-006. ATLAS-TDR-020. ATLAS New Small Wheel Technical Design Report. 2013. url: <https://cds.cern.ch/record/1552862>.
 - [78] M. Aleksi, W. Cleland, Y. Enari, M. Fincke-Keeler, L. Hervas, F. Lanni, S. Majewski, C. Marino, and I. Wingerter-Seez. *ATLAS Liquid Argon Calorimeter Phase-I Upgrade Technical Design Report*. Tech. rep. CERN-LHCC-2013-017. ATLAS-TDR-022. Final version presented to December 2013 LHCC. 2013. url: <https://cds.cern.ch/record/1602230>.
 - [79] ALICE Collaboration. “The ALICE experiment at the CERN LHC.” In: *JINST* 3 (2008), S08002. doi: [10.1088/1748-0221/3/08/S08002](https://doi.org/10.1088/1748-0221/3/08/S08002).
 - [80] ATLAS Collaboration. “The ATLAS Experiment at the CERN Large Hadron Collider.” In: *JINST* 3 (2008), S08003. doi: [10.1088/1748-0221/3/08/S08003](https://doi.org/10.1088/1748-0221/3/08/S08003).
 - [81] CMS Collaboration. “The CMS Experiment at the CERN LHC.” In: *JINST* 3 (2008), S08004. doi: [10.1088/1748-0221/3/08/S08004](https://doi.org/10.1088/1748-0221/3/08/S08004).
 - [82] LHCb Collaboration. “The LHCb Detector at the LHC.” In: *JINST* 3 (2008), S08005. doi: [10.1088/1748-0221/3/08/S08005](https://doi.org/10.1088/1748-0221/3/08/S08005).
 - [83] ATLAS Collaboration. “Luminosity determination in $p\bar{p}$ collisions at $\sqrt{s} = 13$ TeV using the ATLAS detector at the LHC.” In: ATLAS-CONF-2019-021 (2019). url: <http://cds.cern.ch/record/2677054>.
 - [84] *Mean number of interactions per crossing during LHC Run-2.* https://atlas.web.cern.ch/Atlas/GROUPS/DATAPREPARATION/PublicPlots/2018/DataSummary/figs/mu_2015_2018.png. [Online; Accessed: 17-05-2021].
 - [85] *Computer generated image of the central ATLAS detector.* <https://cds.cern.ch/images/CERN-GE-0803012-01>. [Online; Accessed: 17-05-2021].
 - [86] *Computer generated image of the ATLAS inner detector.* <https://cds.cern.ch/images/CERN-GE-0803014-01>. [Online; Accessed: 17-05-2021].
 - [87] *Computer Generated image of the ATLAS calorimeter.* <https://cds.cern.ch/record/1095927>. [Online; Accessed: 17-05-2021].
 - [88] *Computer generated image of the ATLAS muon subsystem.* <https://cds.cern.ch/record/1095929>. [Online; Accessed: 17-05-2021].

- [89] ATLAS Collaboration. *The ATLAS Data Acquisition System in LHC Run 2*. Tech. rep. ATL-DAQ-PROC-2017-043. Geneva, 2017. url: <https://cds.cern.ch/record/2292434>.
- [90] *Total integrated luminosity recorded by ATLAS during Run-2*. <https://atlas.web.cern.ch/Atlas/GROUPS/DATAPREPARATION/PublicPlots/2018/DataSummary/figs/intlumivstimeRun2DQall.png>. [Online; Accessed: 17-05-2021].
- [91] L. Adamczyk, E. Bana, A. Brandt, M. Bruschi, S. Grinstein, J. Lange, M. Rijssenbeek, P. Sicho, R. Staszewski, T. Sykora, M. Trzebiski, J. Chwastowski, and K. Korcyl. “Technical Design Report for the ATLAS Forward Proton Detector.” In: (2015). url: <https://cds.cern.ch/record/2017378>.
- [92] *Pictures of the AFP sub-detectors assembled in the roman pot*. https://twiki.cern.ch/twiki/bin/view/Atlas/AFP_Figures. [Online; Accessed: 17-05-2021].
- [93] L. Basso and J. Andrea. “Discovery potential for $T' \rightarrow t\bar{Z}$ in the trilepton channel at the LHC.” In: *JHEP* 02 (2015), p. 032. doi: [10.1007/JHEP02\(2015\)032](https://doi.org/10.1007/JHEP02(2015)032). arXiv: [1411.7587 \[hep-ph\]](https://arxiv.org/abs/1411.7587).
- [94] ATLAS Collaboration. *Luminosity determination in pp collisions at $\sqrt{s} = 13$ TeV using the ATLAS detector at the LHC*. ATLAS-CONF-2019-021. 2019. url: <https://cds.cern.ch/record/2677054>.
- [95] ATLAS Collaboration. “Electron and photon performance measurements with the ATLAS detector using the 2015–2017 LHC proton-proton collision data.” In: *JINST* 14.12 (2019), P12006. doi: [10.1088/1748-0221/14/12/P12006](https://doi.org/10.1088/1748-0221/14/12/P12006). arXiv: [1908.00005 \[hep-ex\]](https://arxiv.org/abs/1908.00005).
- [96] ATLAS Collaboration. “Muon reconstruction performance of the ATLAS detector in proton–proton collision data at $\sqrt{s} = 13$ TeV.” In: *Eur. Phys. J. C* 76.5 (2016), p. 292. doi: [10.1140/epjc/s10052-016-4120-y](https://doi.org/10.1140/epjc/s10052-016-4120-y). arXiv: [1603.05598 \[hep-ex\]](https://arxiv.org/abs/1603.05598).
- [97] ATLAS Collaboration. “Performance of electron and photon triggers in ATLAS during LHC Run 2.” In: *Eur. Phys. J. C* 80.1 (2020), p. 47. doi: [10.1140/epjc/s10052-019-7500-2](https://doi.org/10.1140/epjc/s10052-019-7500-2). arXiv: [1909.00761 \[hep-ex\]](https://arxiv.org/abs/1909.00761).
- [98] ATLAS Collaboration. “Performance of the ATLAS muon triggers in Run 2.” In: *JINST* 15.09 (2020), P09015. doi: [10.1088/1748-0221/15/09/p09015](https://doi.org/10.1088/1748-0221/15/09/p09015). arXiv: [2004.13447 \[physics.ins-det\]](https://arxiv.org/abs/2004.13447).
- [99] ATLAS Collaboration. *Electron identification measurements in ATLAS using $\sqrt{s} = 13$ TeV data with 50 ns bunch spacing*. ATL-PHYS-PUB-2015-041. 2015. url: <https://cds.cern.ch/record/2048202>.
- [100] ATLAS Collaboration. *Electron and photon energy calibration with the ATLAS detector using data collected in 2015 at $\sqrt{s} = 13$ TeV*. ATL-PHYS-PUB-2016-015. 2016. url: <https://cds.cern.ch/record/2203514>.

-
- [101] ATLAS Collaboration. *Electron efficiency measurements with the ATLAS detector using the 2015 LHC proton–proton collision data*. ATLAS-CONF-2016-024. 2016. url: <https://cds.cern.ch/record/2157687>.
 - [102] ATLAS Collaboration. “Electron reconstruction and identification in the ATLAS experiment using the 2015 and 2016 LHC proton–proton collision data at $\sqrt{s} = 13$ TeV.” In: *Eur. Phys. J. C* 79 (2019), p. 639. doi: [10.1140/epjc/s10052-019-7140-6](https://doi.org/10.1140/epjc/s10052-019-7140-6). arXiv: [1902.04655 \[hep-ex\]](https://arxiv.org/abs/1902.04655).
 - [103] ATLAS Collaboration. “Muon reconstruction performance of the ATLAS detector in proton–proton collision data at $\sqrt{s} = 13$ TeV.” In: *Eur. Phys. J. C* 76 (2016), p. 292. doi: [10.1140/epjc/s10052-016-4120-y](https://doi.org/10.1140/epjc/s10052-016-4120-y). arXiv: [1603.05598 \[hep-ex\]](https://arxiv.org/abs/1603.05598).
 - [104] ATLAS Collaboration. “Muon reconstruction and identification efficiency in ATLAS using the full Run 2 pp collision data set at $\sqrt{s} = 13$ TeV.” In: (Dec. 2020). arXiv: [2012.00578 \[hep-ex\]](https://arxiv.org/abs/2012.00578).
 - [105] M. Cacciari, G. P. Salam, and G. Soyez. “The Anti- k_t Jet Clustering Algorithm.” In: *JHEP* 0804 (2008), p. 063. doi: [10.1088/1126-6708/2008/04/063](https://doi.org/10.1088/1126-6708/2008/04/063). arXiv: [0802.1189 \[hep-ph\]](https://arxiv.org/abs/0802.1189).
 - [106] ATLAS Collaboration. *Tagging and suppression of pile-up jets with the ATLAS detector*. ATLAS-CONF-2014-018. 2014. url: <https://cds.cern.ch/record/1700870>.
 - [107] ATLAS Collaboration. “ATLAS b -jet identification performance and efficiency measurement with $t\bar{t}$ events in pp collisions at $\sqrt{s} = 13$ TeV.” In: *Eur. Phys. J. C* 79.11 (2019), p. 970. doi: [10.1140/epjc/s10052-019-7450-8](https://doi.org/10.1140/epjc/s10052-019-7450-8). arXiv: [1907.05120 \[hep-ex\]](https://arxiv.org/abs/1907.05120).
 - [108] ATLAS Collaboration. “Performance of algorithms that reconstruct missing transverse momentum in $\sqrt{s} = 8$ TeV proton–proton collisions in the ATLAS detector.” In: *Eur. Phys. J. C* 77.4 (2017), p. 241. doi: [10.1140/epjc/s10052-017-4780-2](https://doi.org/10.1140/epjc/s10052-017-4780-2). arXiv: [1609.09324 \[hep-ex\]](https://arxiv.org/abs/1609.09324).
 - [109] ATLAS Collaboration. “Performance of algorithms that reconstruct missing transverse momentum in $\sqrt{s} = 8$ TeV proton–proton collisions in the ATLAS detector.” In: *The European Physical Journal C* 77.4 (2017), p. 241. issn: 1434-6052. doi: [10.1140/epjc/s10052-017-4780-2](https://doi.org/10.1140/epjc/s10052-017-4780-2). url: <https://doi.org/10.1140/epjc/s10052-017-4780-2>.
 - [110] ATLAS Collaboration. “Performance of missing transverse momentum reconstruction in proton–proton collisions at $\sqrt{s} = 7$ TeV with ATLAS.” In: *Eur. Phys. J. C* 72 (2012), p. 1844. doi: [10.1140/epjc/s10052-011-1844-6](https://doi.org/10.1140/epjc/s10052-011-1844-6). arXiv: [1108.5602 \[hep-ex\]](https://arxiv.org/abs/1108.5602).
 - [111] ATLAS Collaboration. “Performance of algorithms that reconstruct missing transverse momentum in $\sqrt{s} = 8$ TeV proton–proton collisions in the ATLAS detector.” In: *Eur. Phys. J. C* 77 (2017), p. 241. doi: [10.1140/epjc/s10052-017-4780-2](https://doi.org/10.1140/epjc/s10052-017-4780-2). arXiv: [1609.09324 \[hep-ex\]](https://arxiv.org/abs/1609.09324).
 - [112] ATLAS Collaboration. *Performance of missing transverse momentum reconstruction with the ATLAS detector in the first proton–proton collisions at $\sqrt{s} = 13$ TeV*. ATL-PHYS-PUB-2015-027. 2015. url: <https://cds.cern.ch/record/2037904>.

-
- [113] ATLAS Collaboration. “The ATLAS Simulation Infrastructure.” In: *Eur. Phys. J. C* 70 (2010), pp. 823–874. doi: [10.1140/epjc/s10052-010-1429-9](https://doi.org/10.1140/epjc/s10052-010-1429-9). arXiv: [1005.4568 \[physics.ins-det\]](https://arxiv.org/abs/1005.4568).
 - [114] S. Agostinelli et al. “GEANT4—a simulation toolkit.” In: *Nucl. Instrum. Meth. A* 506 (2003), pp. 250–303. doi: [10.1016/S0168-9002\(03\)01368-8](https://doi.org/10.1016/S0168-9002(03)01368-8).
 - [115] J. Alwall, R. Frederix, S. Frixione, V. Hirschi, F. Maltoni, O. Mattelaer, H. S. Shao, T. Stelzer, P. Torrielli, and M. Zaro. “The automated computation of tree-level and next-to-leading order differential cross sections, and their matching to parton shower simulations.” In: *JHEP* 07 (2014), p. 079. doi: [10.1007/JHEP07\(2014\)079](https://doi.org/10.1007/JHEP07(2014)079). arXiv: [1405.0301 \[hep-ph\]](https://arxiv.org/abs/1405.0301).
 - [116] P. Z. Skands. “Tuning Monte Carlo Generators: The Perugia Tunes.” In: *Phys. Rev.* D82 (2010), p. 074018. doi: [10.1103/PhysRevD.82.074018](https://doi.org/10.1103/PhysRevD.82.074018). arXiv: [1005.3457 \[hep-ph\]](https://arxiv.org/abs/1005.3457).
 - [117] M. Beneke, P. Falgari, S. Klein, and C. Schwinn. “Hadronic top-quark pair production with NNLL threshold resummation.” In: *Nucl. Phys. B* 855 (2012), pp. 695–741. doi: [10.1016/j.nuclphysb.2011.10.021](https://doi.org/10.1016/j.nuclphysb.2011.10.021). arXiv: [1109.1536 \[hep-ph\]](https://arxiv.org/abs/1109.1536).
 - [118] M. Cacciari, M. Czakon, M. Mangano, A. Mitov, and P. Nason. “Top-pair production at hadron colliders with next-to-next-to-leading logarithmic soft-gluon resummation.” In: *Phys. Lett. B* 710 (2012), pp. 612–622. doi: [10.1016/j.physletb.2012.03.013](https://doi.org/10.1016/j.physletb.2012.03.013). arXiv: [1111.5869 \[hep-ph\]](https://arxiv.org/abs/1111.5869).
 - [119] P. Bärnreuther, M. Czakon, and A. Mitov. “Percent-Level-Precision Physics at the Tevatron: Next-to-Next-to-Leading Order QCD Corrections to $q\bar{q} \rightarrow t\bar{t} + X$.” In: *Phys. Rev. Lett.* 109 (2012), p. 132001. doi: [10.1103/PhysRevLett.109.132001](https://doi.org/10.1103/PhysRevLett.109.132001). arXiv: [1204.5201 \[hep-ph\]](https://arxiv.org/abs/1204.5201).
 - [120] M. Czakon and A. Mitov. “NNLO corrections to top-pair production at hadron colliders: the all-fermionic scattering channels.” In: *JHEP* 12 (2012), p. 054. doi: [10.1007/JHEP12\(2012\)054](https://doi.org/10.1007/JHEP12(2012)054). arXiv: [1207.0236 \[hep-ph\]](https://arxiv.org/abs/1207.0236).
 - [121] M. Czakon and A. Mitov. “NNLO corrections to top pair production at hadron colliders: the quark-gluon reaction.” In: *JHEP* 01 (2013), p. 080. doi: [10.1007/JHEP01\(2013\)080](https://doi.org/10.1007/JHEP01(2013)080). arXiv: [1210.6832 \[hep-ph\]](https://arxiv.org/abs/1210.6832).
 - [122] M. Czakon, P. Fiedler, and A. Mitov. “Total Top-Quark Pair-Production Cross Section at Hadron Colliders Through $O(\alpha_S^4)$.” In: *Phys. Rev. Lett.* 110 (2013), p. 252004. doi: [10.1103/PhysRevLett.110.252004](https://doi.org/10.1103/PhysRevLett.110.252004). arXiv: [1303.6254 \[hep-ph\]](https://arxiv.org/abs/1303.6254).
 - [123] M. Czakon and A. Mitov. “Top++: A program for the calculation of the top-pair cross-section at hadron colliders.” In: *Comput. Phys. Commun.* 185 (2014), p. 2930. doi: [10.1016/j.cpc.2014.06.021](https://doi.org/10.1016/j.cpc.2014.06.021). arXiv: [1112.5675 \[hep-ph\]](https://arxiv.org/abs/1112.5675).
 - [124] M. Botje et al. “The PDF4LHC Working Group Interim Recommendations.” In: (2011). arXiv: [1101.0538 \[hep-ph\]](https://arxiv.org/abs/1101.0538).

- [125] A. D. Martin, W. J. Stirling, R. S. Thorne, and G. Watt. “Parton distributions for the LHC.” In: *Eur. Phys. J. C* 63 (2009), pp. 189–285. doi: [10.1140/epjc/s10052-009-1072-5](https://doi.org/10.1140/epjc/s10052-009-1072-5). arXiv: [0901.0002 \[hep-ph\]](https://arxiv.org/abs/0901.0002).
- [126] A. D. Martin, W. Stirling, R. Thorne, and G. Watt. “Uncertainties on α_S in global PDF analyses and implications for predicted hadronic cross sections.” In: *Eur. Phys. J. C* 64 (2009), pp. 653–680. doi: [10.1140/epjc/s10052-009-1164-2](https://doi.org/10.1140/epjc/s10052-009-1164-2). arXiv: [0905.3531 \[hep-ph\]](https://arxiv.org/abs/0905.3531).
- [127] H. Lai, M. Guzzi, J. Huston, Z. Li, P. Nadolsky, et al. “New parton distributions for collider physics.” In: *Phys. Rev. D* 82 (2010), p. 074024. doi: [10.1103/PhysRevD.82.074024](https://doi.org/10.1103/PhysRevD.82.074024). arXiv: [1007.2241 \[hep-ph\]](https://arxiv.org/abs/1007.2241).
- [128] J. Gao, M. Guzzi, J. Huston, H.-L. Lai, Z. Li, et al. “CT10 next-to-next-to-leading order global analysis of QCD.” In: *Phys. Rev. D* 89 (2014), p. 033009. doi: [10.1103/PhysRevD.89.033009](https://doi.org/10.1103/PhysRevD.89.033009). arXiv: [1302.6246 \[hep-ph\]](https://arxiv.org/abs/1302.6246).
- [129] NNPDF Collaboration. “Parton distributions with LHC data.” In: *Nucl. Phys. B* 867 (2013), pp. 244–289. doi: [10.1016/j.nuclphysb.2012.10.003](https://doi.org/10.1016/j.nuclphysb.2012.10.003). arXiv: [1207.1303 \[hep-ph\]](https://arxiv.org/abs/1207.1303).
- [130] S. Frixione, P. Nason, and G. Ridolfi. “A Positive-weight next-to-leading-order Monte Carlo for heavy flavour hadroproduction.” In: *JHEP* 09 (2007), p. 126. doi: [10.1088/1126-6708/2007/09/126](https://doi.org/10.1088/1126-6708/2007/09/126). arXiv: [0707.3088 \[hep-ph\]](https://arxiv.org/abs/0707.3088).
- [131] P. Nason. “A new method for combining NLO QCD with shower Monte Carlo algorithms.” In: *JHEP* 11 (2004), p. 040. doi: [10.1088/1126-6708/2004/11/040](https://doi.org/10.1088/1126-6708/2004/11/040). arXiv: [hep-ph/0409146](https://arxiv.org/abs/hep-ph/0409146).
- [132] S. Frixione, P. Nason, and C. Oleari. “Matching NLO QCD computations with Parton Shower simulations: the POWHEG method.” In: *JHEP* 11 (2007), p. 070. doi: [10.1088/1126-6708/2007/11/070](https://doi.org/10.1088/1126-6708/2007/11/070). arXiv: [0709.2092 \[hep-ph\]](https://arxiv.org/abs/0709.2092).
- [133] S. Alioli, P. Nason, C. Oleari, and E. Re. “A general framework for implementing NLO calculations in shower Monte Carlo programs: the POWHEG BOX.” In: *JHEP* 06 (2010), p. 043. doi: [10.1007/JHEP06\(2010\)043](https://doi.org/10.1007/JHEP06(2010)043). arXiv: [1002.2581 \[hep-ph\]](https://arxiv.org/abs/1002.2581).
- [134] NNPDF Collaboration. “Parton distributions for the LHC Run II.” In: *JHEP* 04 (2015), p. 040. doi: [10.1007/JHEP04\(2015\)040](https://doi.org/10.1007/JHEP04(2015)040). arXiv: [1410.8849 \[hep-ph\]](https://arxiv.org/abs/1410.8849).
- [135] ATLAS Collaboration. *Studies on top-quark Monte Carlo modelling for Top2016*. ATL-PHYS-PUB-2016-020. 2016. url: <https://cds.cern.ch/record/2216168>.
- [136] T. Sjöstrand, S. Ask, J. R. Christiansen, R. Corke, N. Desai, P. Ilten, S. Mrenna, S. Prestel, C. O. Rasmussen, and P. Z. Skands. “An introduction to PYTHIA 8.2.” In: *Comput. Phys. Commun.* 191 (2015), pp. 159–177. doi: [10.1016/j.cpc.2015.01.024](https://doi.org/10.1016/j.cpc.2015.01.024). arXiv: [1410.3012 \[hep-ph\]](https://arxiv.org/abs/1410.3012).

- [137] ATLAS Collaboration. *ATLAS Pythia 8 tunes to 7 TeV data*. ATL-PHYS-PUB-2014-021. 2014. url: <https://cds.cern.ch/record/1966419>.
- [138] D. J. Lange. “The EvtGen particle decay simulation package.” In: *Nucl. Instrum. Meth.* A462 (2001), pp. 152–155. doi: [10.1016/S0168-9002\(01\)00089-4](https://doi.org/10.1016/S0168-9002(01)00089-4).
- [139] M. Bahr et al. “Herwig++ physics and manual.” In: *Eur. Phys. J. C* 58 (2008), pp. 639–707. doi: [10.1140/epjc/s10052-008-0798-9](https://doi.org/10.1140/epjc/s10052-008-0798-9). arXiv: [0803.0883 \[hep-ph\]](https://arxiv.org/abs/0803.0883).
- [140] J. Bellm et al. “Herwig 7.0/Herwig++ 3.0 release note.” In: *Eur. Phys. J. C* 76.4 (2016), p. 196. doi: [10.1140/epjc/s10052-016-4018-8](https://doi.org/10.1140/epjc/s10052-016-4018-8). arXiv: [1512.01178 \[hep-ph\]](https://arxiv.org/abs/1512.01178).
- [141] J. Bellm et al. “Herwig 7.1 Release Note.” In: (2017). arXiv: [1705.06919 \[hep-ph\]](https://arxiv.org/abs/1705.06919).
- [142] L. Harland-Lang, A. Martin, P. Motylinski, and R. Thorne. “Parton distributions in the LHC era: MMHT 2014 PDFs.” In: *Eur. Phys. J. C* 75.5 (2015), p. 204. doi: [10.1140/epjc/s10052-015-3397-6](https://doi.org/10.1140/epjc/s10052-015-3397-6). arXiv: [1412.3989 \[hep-ph\]](https://arxiv.org/abs/1412.3989).
- [143] E. Re. “Single-top Wt-channel production matched with parton showers using the POWHEG method.” In: *Eur. Phys. J. C* 71 (2011), p. 1547. doi: [10.1140/epjc/s10052-011-1547-z](https://doi.org/10.1140/epjc/s10052-011-1547-z). arXiv: [1009.2450 \[hep-ph\]](https://arxiv.org/abs/1009.2450).
- [144] S. Frixione, E. Laenen, P. Motylinski, B. R. Webber, and C. D. White. “Single-top hadroproduction in association with a W boson.” In: *JHEP* 07 (2008), p. 029. doi: [10.1088/1126-6708/2008/07/029](https://doi.org/10.1088/1126-6708/2008/07/029). arXiv: [0805.3067 \[hep-ph\]](https://arxiv.org/abs/0805.3067).
- [145] E. Bothmann et al. “Event Generation with Sherpa 2.2.” In: (2019). arXiv: [1905.09127 \[hep-ph\]](https://arxiv.org/abs/1905.09127).
- [146] T. Gleisberg and S. Höche. “Comix, a new matrix element generator.” In: *JHEP* 12 (2008), p. 039. doi: [10.1088/1126-6708/2008/12/039](https://doi.org/10.1088/1126-6708/2008/12/039). arXiv: [0808.3674 \[hep-ph\]](https://arxiv.org/abs/0808.3674).
- [147] S. Schumann and F. Krauss. “A Parton shower algorithm based on Catani-Seymour dipole factorisation.” In: *JHEP* 03 (2008), p. 038. doi: [10.1088/1126-6708/2008/03/038](https://doi.org/10.1088/1126-6708/2008/03/038). arXiv: [0709.1027 \[hep-ph\]](https://arxiv.org/abs/0709.1027).
- [148] S. Höche, F. Krauss, M. Schönher, and F. Siegert. “A critical appraisal of NLO+PS matching methods.” In: *JHEP* 09 (2012), p. 049. doi: [10.1007/JHEP09\(2012\)049](https://doi.org/10.1007/JHEP09(2012)049). arXiv: [1111.1220 \[hep-ph\]](https://arxiv.org/abs/1111.1220).
- [149] S. Höche, F. Krauss, M. Schönher, and F. Siegert. “QCD matrix elements + parton showers. The NLO case.” In: *JHEP* 04 (2013), p. 027. doi: [10.1007/JHEP04\(2013\)027](https://doi.org/10.1007/JHEP04(2013)027). arXiv: [1207.5030 \[hep-ph\]](https://arxiv.org/abs/1207.5030).
- [150] S. Catani, F. Krauss, R. Kuhn, and B. R. Webber. “QCD Matrix Elements + Parton Showers.” In: *JHEP* 11 (2001), p. 063. doi: [10.1088/1126-6708/2001/11/063](https://doi.org/10.1088/1126-6708/2001/11/063). arXiv: [hep-ph/0109231](https://arxiv.org/abs/hep-ph/0109231).

- [151] S. Höche, F. Krauss, S. Schumann, and F. Siegert. “QCD matrix elements and truncated showers.” In: *JHEP* 05 (2009), p. 053. doi: [10.1088/1126-6708/2009/05/053](https://doi.org/10.1088/1126-6708/2009/05/053). arXiv: [0903.1219](https://arxiv.org/abs/0903.1219) [hep-ph].
- [152] F. Cascioli, P. Maierhofer, and S. Pozzorini. “Scattering Amplitudes with Open Loops.” In: *Phys. Rev. Lett.* 108 (2012), p. 111601. doi: [10.1103/PhysRevLett.108.111601](https://doi.org/10.1103/PhysRevLett.108.111601). arXiv: [1111.5206](https://arxiv.org/abs/1111.5206) [hep-ph].
- [153] A. Denner, S. Dittmaier, and L. Hofer. “Collier: A fortran-based complex one-loop library in extended regularizations.” In: *Comput. Phys. Commun.* 212 (2017), pp. 220–238. doi: [10.1016/j.cpc.2016.10.013](https://doi.org/10.1016/j.cpc.2016.10.013). arXiv: [1604.06792](https://arxiv.org/abs/1604.06792) [hep-ph].
- [154] P. Nason and G. Zanderighi. “ W^+W^- , WZ and ZZ production in the POWHEG-BOX-V2.” In: *Eur. Phys. J. C* 74.1 (2014), p. 2702. doi: [10.1140/epjc/s10052-013-2702-5](https://doi.org/10.1140/epjc/s10052-013-2702-5). arXiv: [1311.1365](https://arxiv.org/abs/1311.1365) [hep-ph].
- [155] ATLAS Collaboration. “Measurement of the Z/γ^* boson transverse momentum distribution in pp collisions at $\sqrt{s} = 7$ TeV with the ATLAS detector.” In: *JHEP* 09 (2014), p. 145. doi: [10.1007/JHEP09\(2014\)145](https://doi.org/10.1007/JHEP09(2014)145). arXiv: [1406.3660](https://arxiv.org/abs/1406.3660) [hep-ex].
- [156] J. Pumplin et al. “New Generation of Parton Distributions with Uncertainties From Global QCD Analysis.” In: *JHEP* 07 (2002), p. 012. doi: [10.1088/1126-6708/2002/07/012](https://doi.org/10.1088/1126-6708/2002/07/012). arXiv: [hep-ph/0201195](https://arxiv.org/abs/hep-ph/0201195).
- [157] S. Alioli, P. Nason, C. Oleari, and E. Re. “NLO vector-boson production matched with shower in POWHEG.” In: *JHEP* 07 (2008), p. 060. doi: [10.1088/1126-6708/2008/07/060](https://doi.org/10.1088/1126-6708/2008/07/060). arXiv: [0805.4802](https://arxiv.org/abs/0805.4802) [hep-ph].
- [158] P. Gononka and Z. Was. “PHOTOS Monte Carlo: A Precision tool for QED corrections in Z and W decays.” In: *Eur. Phys. J. C* 45 (2006), pp. 97–107. doi: [10.1140/epjc/s2005-02396-4](https://doi.org/10.1140/epjc/s2005-02396-4). arXiv: [hep-ph/0506026](https://arxiv.org/abs/hep-ph/0506026).
- [159] N. Davidson, T. Przedzinski, and Z. Was. “PHOTOS interface in C++: Technical and physics documentation.” In: *Comput. Phys. Commun.* 199 (2016), pp. 86–101. doi: [10.1016/j.cpc.2015.09.013](https://doi.org/10.1016/j.cpc.2015.09.013). arXiv: [1011.0937](https://arxiv.org/abs/1011.0937) [hep-ph].
- [160] H. B. Hartanto, B. Jäger, L. Reina, and D. Wackerlo. “Higgs boson production in association with top quarks in the POWHEG BOX.” In: *Phys. Rev. D* 91.9 (2015), p. 094003. doi: [10.1103/PhysRevD.91.094003](https://doi.org/10.1103/PhysRevD.91.094003). arXiv: [1501.04498](https://arxiv.org/abs/1501.04498) [hep-ph].
- [161] R. Frederix, S. Frixione, V. Hirschi, F. Maltoni, R. Pittau, and P. Torrielli. “Scalar and pseudoscalar Higgs production in association with a top–antitop pair.” In: *Phys. Lett. B* 701 (2011), pp. 427–433. doi: [10.1016/j.physletb.2011.06.012](https://doi.org/10.1016/j.physletb.2011.06.012). arXiv: [1104.5613](https://arxiv.org/abs/1104.5613) [hep-ph].

- [162] F. Buccioni, J.-N. Lang, J. M. Lindert, P. Maierhöfer, S. Pozzorini, H. Zhang, and M. F. Zoller. “OpenLoops 2.” In: *Eur. Phys. J. C* 79.10 (2019), p. 866. doi: [10.1140/epjc/s10052-019-7306-2](https://doi.org/10.1140/epjc/s10052-019-7306-2). arXiv: [1907.13071 \[hep-ph\]](https://arxiv.org/abs/1907.13071).
- [163] A. D. Bukin. *Fitting function for asymmetric peaks*. 2007. arXiv: [0711.4449 \[physics.data-an\]](https://arxiv.org/abs/0711.4449).
- [164] ATLAS Collaboration. *MCTruthClassifier tool*. <https://ucatlas.github.io/RootCoreDocumentation/2.4.28/d6/d4a/classMCTruthClassifier.html>. [Online; Accessed: 17-05-2021].
- [165] L. Breiman, J. Friedman, R. Olshen, and C. Stone. *Classification And Regression Trees*. Oct. 2017, pp. 1–358. isbn: 9781315139470. doi: [10.1201/9781315139470](https://doi.org/10.1201/9781315139470).
- [166] J. Friedman. *Stochastic gradient boosting*. 2002, p. 367.
- [167] A. Hoecker et al. *TMVA - Toolkit for Multivariate Data Analysis*. 2007. arXiv: [physics/0703039 \[physics.data-an\]](https://arxiv.org/abs/physics/0703039).
- [168] ATLAS Collaboration. “Electron and photon energy calibration with the ATLAS detector using LHC Run 1 data.” In: *Eur. Phys. J. C* 74 (2014), p. 3071. doi: [10.1140/epjc/s10052-014-3071-4](https://doi.org/10.1140/epjc/s10052-014-3071-4). arXiv: [1407.5063 \[hep-ex\]](https://arxiv.org/abs/1407.5063).
- [169] ATLAS Collaboration. “Jet energy scale measurements and their systematic uncertainties in proton–proton collisions at $\sqrt{s} = 13\text{ TeV}$ with the ATLAS detector.” In: *Phys. Rev. D* 96 (2017), p. 072002. doi: [10.1103/PhysRevD.96.072002](https://doi.org/10.1103/PhysRevD.96.072002). arXiv: [1703.09665 \[hep-ex\]](https://arxiv.org/abs/1703.09665).
- [170] ATLAS Collaboration. “Performance of pile-up mitigation techniques for jets in $p\bar{p}$ collisions at $\sqrt{s} = 8\text{ TeV}$ using the ATLAS detector.” In: *Eur. Phys. J. C* 76.11 (2016), p. 581. doi: [10.1140/epjc/s10052-016-4395-z](https://doi.org/10.1140/epjc/s10052-016-4395-z). arXiv: [1510.03823 \[hep-ex\]](https://arxiv.org/abs/1510.03823).
- [171] ATLAS Collaboration. *Calibration of the performance of b -tagging for c and light-flavour jets in the 2012 ATLAS data*. ATLAS-CONF-2014-046. 2014. url: <https://cds.cern.ch/record/1741020>.
- [172] ATLAS Collaboration. *Calibration of b -tagging using dileptonic top pair events in a combinatorial likelihood approach with the ATLAS experiment*. ATLAS-CONF-2014-004. 2014. url: <https://cds.cern.ch/record/1664335>.
- [173] S. Ellis, R. Kleiss, and W. J. Stirling. “W’s, Z’s and Jets.” In: *Phys. Lett. B* 154 (1985), p. 435. doi: [10.1016/0370-2693\(85\)90425-3](https://doi.org/10.1016/0370-2693(85)90425-3).
- [174] F. A. Berends, H. Kuijf, B. Tausk, and W. Giele. “On the Production of a W and Jets at Hadron Colliders.” In: *Nucl. Phys. B* 357 (1991), pp. 32–64. doi: [10.1016/0550-3213\(91\)90458-A](https://doi.org/10.1016/0550-3213(91)90458-A).
- [175] ATLAS Collaboration. “Luminosity determination in $p\bar{p}$ collisions at $\sqrt{s} = 8\text{ TeV}$ using the ATLAS detector at the LHC.” In: *Eur. Phys. J. C* 76 (2016), p. 653. doi: [10.1140/epjc/s10052-016-4466-1](https://doi.org/10.1140/epjc/s10052-016-4466-1). arXiv: [1608.03953 \[hep-ex\]](https://arxiv.org/abs/1608.03953).

- [176] *TRExFitter tool*. [Online; Accessed: 10-06-2021]. url: <https://gitlab.cern.ch/TRExStats>.
- [177] W. Verkerke and D. P. Kirkby. “The RooFit Toolkit for Data Modeling.” In: *eConf C0303241* (2003), MOLT007. arXiv: [physics/0306116 \[physics\]](#).
- [178] L. Moneta, K. Belasco, K. S. Cranmer, S. Kreiss, A. Lazzaro, et al. “The RooStats Project.” In: *PoS ACAT2010* (2010), p. 057. arXiv: [1009.1003 \[physics.data-an\]](#).
- [179] G. Cowan, K. Cranmer, E. Gross, and O. Vitells. “Asymptotic formulae for likelihood-based tests of new physics.” In: *Eur. Phys. J. C* 71 (2011). [Erratum: *Eur. Phys. J. C* 73, 2501 (2013)], p. 1554. doi: [10.1140/epjc/s10052-011-1554-0](#), [10.1140/epjc/s10052-013-2501-z](#). arXiv: [1007.1727 \[physics.data-an\]](#).
- [180] A. L. Read. “Presentation of search results: The CL(s) technique.” In: *J. Phys.* G28 (2002), [,11(2002)], pp. 2693–2704. doi: [10.1088/0954-3899/28/10/313](#).
- [181] T. Junk. “Confidence level computation for combining searches with small statistics.” In: *Nucl. Instrum. Meth.* A434 (1999), pp. 435–443. doi: [10.1016/S0168-9002\(99\)00498-2](#). arXiv: [hep-ex/9902006 \[hep-ex\]](#).
- [182] U. Ellwanger, C. Hugonie, and A. M. Teixeira. “The Next-to-Minimal Supersymmetric Standard Model.” In: *Phys. Rept.* 496 (2010), pp. 1–77. doi: [10.1016/j.physrep.2010.07.001](#). arXiv: [0910.1785 \[hep-ph\]](#).
- [183] R. Contino, Y. Nomura, and A. Pomarol. “Higgs as a holographic pseudoGoldstone boson.” In: *Nucl. Phys. B* 671 (2003), pp. 148–174. doi: [10.1016/j.nuclphysb.2003.08.027](#). arXiv: [hep-ph/0306259](#).
- [184] B. Gripaios, A. Pomarol, F. Riva, and J. Serra. “Beyond the Minimal Composite Higgs Model.” In: *JHEP* 04 (2009), p. 070. doi: [10.1088/1126-6708/2009/04/070](#). arXiv: [0902.1483 \[hep-ph\]](#).
- [185] M. Chala. “ $h \rightarrow \gamma\gamma$ excess and Dark Matter from Composite Higgs Models.” In: *JHEP* 01 (2013), p. 122. doi: [10.1007/JHEP01\(2013\)122](#). arXiv: [1210.6208 \[hep-ph\]](#).
- [186] L. Vecchi. “The Natural Composite Higgs.” In: (2013). arXiv: [1304.4579 \[hep-ph\]](#).
- [187] B. Bellazzini, C. Csáki, and J. Serra. “Composite Higgses.” In: *Eur. Phys. J. C* 74.5 (2014), p. 2766. doi: [10.1140/epjc/s10052-014-2766-x](#). arXiv: [1401.2457 \[hep-ph\]](#).
- [188] V. Sanz and J. Setford. “Composite Higgses with seesaw EWSB.” In: *JHEP* 12 (2015), p. 154. doi: [10.1007/JHEP12\(2015\)154](#). arXiv: [1508.06133 \[hep-ph\]](#).
- [189] T. Ma and G. Cacciapaglia. “Fundamental Composite 2HDM: SU(N) with 4 flavours.” In: *JHEP* 03 (2016), p. 211. doi: [10.1007/JHEP03\(2016\)211](#). arXiv: [1508.07014 \[hep-ph\]](#).

- [190] A. Belyaev, G. Cacciapaglia, H. Cai, T. Flacke, A. Parolini, and H. Serôdio. “Singlets in composite Higgs models in light of the LHC 750 GeV diphoton excess.” In: *Phys. Rev. D* 94.1 (2016), p. 015004. doi: [10.1103/PhysRevD.94.015004](https://doi.org/10.1103/PhysRevD.94.015004). arXiv: [1512.07242 \[hep-ph\]](https://arxiv.org/abs/1512.07242).
- [191] M. Chala, G. Nardini, and I. Sobolev. “Unified explanation for dark matter and electroweak baryogenesis with direct detection and gravitational wave signatures.” In: *Phys. Rev. D* 94.5 (2016), p. 055006. doi: [10.1103/PhysRevD.94.055006](https://doi.org/10.1103/PhysRevD.94.055006). arXiv: [1605.08663 \[hep-ph\]](https://arxiv.org/abs/1605.08663).
- [192] B. Gripaios, M. Nardecchia, and T. You. “On the Structure of Anomalous Composite Higgs Models.” In: *Eur. Phys. J. C* 77.1 (2017), p. 28. doi: [10.1140/epjc/s10052-017-4603-5](https://doi.org/10.1140/epjc/s10052-017-4603-5). arXiv: [1605.09647 \[hep-ph\]](https://arxiv.org/abs/1605.09647).
- [193] M. Chala, R. Grober, and M. Spannowsky. “Searches for vector-like quarks at future colliders and implications for composite Higgs models with dark matter.” In: *JHEP* 03 (2018), p. 040. doi: [10.1007/JHEP03\(2018\)040](https://doi.org/10.1007/JHEP03(2018)040). arXiv: [1801.06537 \[hep-ph\]](https://arxiv.org/abs/1801.06537).
- [194] M. Chala, R. Grober, and M. Spannowsky. “Interplay between collider searches for vector-like quarks and dark matter searches in composite Higgs models.” In: *Int. J. Mod. Phys. A* 34.13n14 (2019), p. 1940011. doi: [10.1142/S0217751X19400116](https://doi.org/10.1142/S0217751X19400116).
- [195] G. Cacciapaglia, G. Ferretti, T. Flacke, and H. Serôdio. “Light scalars in composite Higgs models.” In: *Front. in Phys.* 7 (2019), p. 22. doi: [10.3389/fphy.2019.00022](https://doi.org/10.3389/fphy.2019.00022). arXiv: [1902.06890 \[hep-ph\]](https://arxiv.org/abs/1902.06890).
- [196] M. Ramos. “Non-Minimal Composite Dark Matter.” In: (Dec. 2019). arXiv: [1912.11061 \[hep-ph\]](https://arxiv.org/abs/1912.11061).
- [197] J. R. Espinosa, B. Gripaios, T. Konstandin, and F. Riva. “Electroweak Baryogenesis in Non-minimal Composite Higgs Models.” In: *JCAP*01 (2012), p. 012. doi: [10.1088/1475-7516/2012/01/012](https://doi.org/10.1088/1475-7516/2012/01/012). arXiv: [1110.2876 \[hep-ph\]](https://arxiv.org/abs/1110.2876).
- [198] V. Vaskonen. “Electroweak baryogenesis and gravitational waves from a real scalar singlet.” In: *Phys. Rev. D* 95.12 (2017), p. 123515. doi: [10.1103/PhysRevD.95.123515](https://doi.org/10.1103/PhysRevD.95.123515). arXiv: [1611.02073 \[hep-ph\]](https://arxiv.org/abs/1611.02073).
- [199] A. Beniwal, M. Lewicki, J. D. Wells, M. White, and A. G. Williams. “Gravitational wave, collider and dark matter signals from a scalar singlet electroweak baryogenesis.” In: *JHEP* 08 (2017), p. 108. doi: [10.1007/JHEP08\(2017\)108](https://doi.org/10.1007/JHEP08(2017)108). arXiv: [1702.06124 \[hep-ph\]](https://arxiv.org/abs/1702.06124).
- [200] Z. Kang, P. Ko, and T. Matsui. “Strong first order EWPT & strong gravitational waves in Z_3 -symmetric singlet scalar extension.” In: *JHEP* 02 (2018), p. 115. doi: [10.1007/JHEP02\(2018\)115](https://doi.org/10.1007/JHEP02(2018)115). arXiv: [1706.09721 \[hep-ph\]](https://arxiv.org/abs/1706.09721).
- [201] B. Grzadkowski and D. Huang. “Spontaneous CP -Violating Electroweak Baryogenesis and Dark Matter from a Complex Singlet Scalar.” In: *JHEP* 08 (2018), p. 135. doi: [10.1007/JHEP08\(2018\)135](https://doi.org/10.1007/JHEP08(2018)135). arXiv: [1807.06987 \[hep-ph\]](https://arxiv.org/abs/1807.06987).

-
- [202] S. De Curtis, L. Delle Rose, and G. Panico. “Composite Dynamics in the Early Universe.” In: *JHEP* 12 (2019), p. 149. doi: [10.1007/JHEP12\(2019\)149](https://doi.org/10.1007/JHEP12(2019)149). arXiv: [1909.07894 \[hep-ph\]](https://arxiv.org/abs/1909.07894).
 - [203] J. Liu, C. E. M. Wagner, and X.-P. Wang. “A light complex scalar for the electron and muon anomalous magnetic moments.” In: *JHEP* 03 (2019), p. 008. doi: [10.1007/JHEP03\(2019\)008](https://doi.org/10.1007/JHEP03(2019)008). arXiv: [1810.11028 \[hep-ph\]](https://arxiv.org/abs/1810.11028).
 - [204] C. Baker et al. “An Improved experimental limit on the electric dipole moment of the neutron.” In: *Phys. Rev. Lett.* 97 (2006), p. 131801. doi: [10.1103/PhysRevLett.97.131801](https://doi.org/10.1103/PhysRevLett.97.131801). arXiv: [hep-ex/0602020](https://arxiv.org/abs/hep-ex/0602020).
 - [205] V. Andreev et al. “Improved limit on the electric dipole moment of the electron.” In: *Nature* 562.7727 (2018), pp. 355–360. doi: [10.1038/s41586-018-0599-8](https://doi.org/10.1038/s41586-018-0599-8).
 - [206] R. Franceschini, G. F. Giudice, J. F. Kamenik, M. McCullough, F. Riva, A. Strumia, and R. Torre. “Digamma, what next?” In: *JHEP* 07 (2016), p. 150. doi: [10.1007/JHEP07\(2016\)150](https://doi.org/10.1007/JHEP07(2016)150). arXiv: [1604.06446 \[hep-ph\]](https://arxiv.org/abs/1604.06446).
 - [207] B. Gripaios and D. Sutherland. “An operator basis for the Standard Model with an added scalar singlet.” In: *JHEP* 08 (2016), p. 103. doi: [10.1007/JHEP08\(2016\)103](https://doi.org/10.1007/JHEP08(2016)103). arXiv: [1604.07365 \[hep-ph\]](https://arxiv.org/abs/1604.07365).
 - [208] CMS Collaboration. “Search for Higgs boson off-shell production in proton-proton collisions at 7 and 8 TeV and derivation of constraints on its total decay width.” In: *JHEP* 09 (2016), p. 051. doi: [10.1007/JHEP09\(2016\)051](https://doi.org/10.1007/JHEP09(2016)051). arXiv: [1605.02329 \[hep-ex\]](https://arxiv.org/abs/1605.02329).
 - [209] CMS Collaboration. “Search for low-mass resonances decaying into bottom quark-antiquark pairs in proton-proton collisions at $\sqrt{s} = 13$ TeV.” In: *Phys. Rev. D* 99.1 (2019), p. 012005. doi: [10.1103/PhysRevD.99.012005](https://doi.org/10.1103/PhysRevD.99.012005). arXiv: [1810.11822 \[hep-ex\]](https://arxiv.org/abs/1810.11822).
 - [210] CMS Collaboration. “Search for high mass dijet resonances with a new background prediction method in proton-proton collisions at $\sqrt{s} = 13$ TeV.” In: *JHEP* 05 (2020), p. 033. doi: [10.1007/JHEP05\(2020\)033](https://doi.org/10.1007/JHEP05(2020)033). arXiv: [1911.03947 \[hep-ex\]](https://arxiv.org/abs/1911.03947).
 - [211] R. Harnik, J. Kopp, and J. Zupan. “Flavor Violating Higgs Decays.” In: *JHEP* 03 (2013), p. 026. doi: [10.1007/JHEP03\(2013\)026](https://doi.org/10.1007/JHEP03(2013)026). arXiv: [1209.1397 \[hep-ph\]](https://arxiv.org/abs/1209.1397).
 - [212] M. Bona et al. “Model-independent constraints on $\Delta F = 2$ operators and the scale of new physics.” In: *JHEP* 03 (2008), p. 049. doi: [10.1088/1126-6708/2008/03/049](https://doi.org/10.1088/1126-6708/2008/03/049). arXiv: [0707.0636 \[hep-ph\]](https://arxiv.org/abs/0707.0636).
 - [213] S. Banerjee, M. Chala, and M. Spannowsky. “Top quark FCNCs in extended Higgs sectors.” In: *Eur. Phys. J. C* 78.8 (2018), p. 683. doi: [10.1140/epjc/s10052-018-6150-0](https://doi.org/10.1140/epjc/s10052-018-6150-0). arXiv: [1806.02836 \[hep-ph\]](https://arxiv.org/abs/1806.02836).

- [214] D. B. Kaplan and H. Georgi. “ $SU(2) \times U(1)$ Breaking by Vacuum Misalignment.” In: *Phys. Lett. B* 136 (1984), pp. 183–186. doi: [10.1016/0370-2693\(84\)91177-8](https://doi.org/10.1016/0370-2693(84)91177-8).
- [215] D. B. Kaplan, H. Georgi, and S. Dimopoulos. “Composite Higgs Scalars.” In: *Phys. Lett. B* 136 (1984), pp. 187–190. doi: [10.1016/0370-2693\(84\)91178-X](https://doi.org/10.1016/0370-2693(84)91178-X).
- [216] ATLAS Collaboration. “Search for flavour-changing neutral current top-quark decays $t \rightarrow qZ$ in proton-proton collisions at $\sqrt{s} = 13$ TeV with the ATLAS detector.” In: *JHEP* 07 (2018), p. 176. doi: [10.1007/JHEP07\(2018\)176](https://doi.org/10.1007/JHEP07(2018)176). arXiv: [1803.09923 \[hep-ex\]](https://arxiv.org/abs/1803.09923).
- [217] ATLAS Collaboration. “Search for supersymmetry in events with four or more leptons in $\sqrt{s} = 13$ TeV pp collisions with ATLAS.” In: *Phys. Rev. D* 98.3 (2018), p. 032009. doi: [10.1103/PhysRevD.98.032009](https://doi.org/10.1103/PhysRevD.98.032009). arXiv: [1804.03602 \[hep-ex\]](https://arxiv.org/abs/1804.03602).
- [218] E. Busato, D. Calvet, and T. Theveneaux-Pelzer. “OpTHyLiC: an Optimised Tool for Hybrid Limits Computation.” In: *Comput. Phys. Commun.* 226 (2018), pp. 136–150. doi: [10.1016/j.cpc.2018.01.009](https://doi.org/10.1016/j.cpc.2018.01.009). arXiv: [1502.02610 \[hep-ex\]](https://arxiv.org/abs/1502.02610).
- [219] N. Castro, M. Chala, A. Peixoto, and M. Ramos. “Novel flavour-changing neutral currents in the top quark sector.” In: *JHEP* 10 (2020), p. 038. doi: [10.1007/JHEP10\(2020\)038](https://doi.org/10.1007/JHEP10(2020)038). arXiv: [2005.09594 \[hep-ph\]](https://arxiv.org/abs/2005.09594).



Optimisation studies for the multivariate discriminants

A.0.1 Study of the BDT in SR1

A.0.1.1 Input variables

Input variables considered for the D_1 discriminant in SR1 are presented in Table A.1, that includes invariant mass of the reconstructed objects as well as transverse momentum, pseudo-rapidity and ΔR between them in (η, ϕ) plane. Separation values are presented in the same table, while correlations are shown in Figure A.1. Input variables that have separation value below 0.02 are removed from the final set of input variables. The χ^2_{tt} and $m_{\ell\nu}$ variables present high correlations with $m_{b\ell\nu}$ which has better separation value, so that they are removed as well as E_T^{miss} which is highly correlated with p_T^W and having lower separation value. The final set of input variables are presented in Table A.2. With the full set (initial set) of input variables, the GBDT output score distributions in each fold for the signal and background samples are presented in Figure A.2 and Figure A.3, respectively, while for the final (reduced) set of input variables in Figure A.4 and Figure A.5. The ROC integral, averaged over the validation folds, for the BDT trained with the full set of input variables is 0.8162 with RMS of 0.0058, while for the BDT with final set of input variables: 0.8025 with RMS of 0.0025. Figure A.6 shows the $S_{\text{eff}}/\sqrt{B_{\text{eff}}}$ value averaged over the validation folds as a function of the cut on the GBDT output score, with full set and final set of input variables. The $S_{\text{eff}}/\sqrt{B_{\text{eff}}}$ values are calculated only if S_{eff} and B_{eff} are above 1% to avoid statistically unstable results. The maximum value of $S_{\text{eff}}/\sqrt{B_{\text{eff}}}$ is 1.507 with RMS of 0.063 for the full set of input variables, while 1.407 with RMS of 0.016 for the final set of input variables. Results show that the final set of input variables for the BDT gives slightly worse performance than the full set, however the $S_{\text{eff}}/\sqrt{B_{\text{eff}}}$ values tend to have

smaller RMS (as can be seen in fig. A.6), which indicates a better stability of BDT output.

Variable	$\langle s^2 \rangle$	Definition
$m_{b\ell\nu}$	0.1364	SM top-quark candidate mass
$\chi^2_{t\bar{t}}$	0.07668	χ^2 from the kinematic fit under the FCNC $t\bar{t}$ decay signal hypothesis
p_T^q	0.07345	u/c -quark candidate transverse momentum
N_{jets}	0.05747	Jet multiplicity
$m_{q\ell\ell}$	0.04173	FCNC top-quark candidate mass
$\Delta R(t_{\text{SM}}, t_{\text{FCNC}})$	0.04109	ΔR between SM and FCNC top-quark candidates
$m_{\ell\nu}$	0.03923	W boson candidate mass
$\Delta R(q, Z)$	0.03546	ΔR between u/c -quark and Z boson candidates
$\Delta R(\ell, Z)$	0.02441	ΔR between W boson lepton and Z boson candidates
p_T^b	0.01702	b -quark candidate transverse momentum
$p_T^{\ell 1}$	0.01409	Leading lepton p_T
E_T^{miss}	0.01021	Missing transverse energy
p_T^W	0.009453	W boson candidate transverse momentum
$\Delta R(b, Z)$	0.005482	ΔR between b -quark and Z boson candidates
$p_T^{\ell 2}$	0.004546	Sub-leading lepton p_T
η^q	0.004271	u/c -quark candidate pseudorapidity
p_T^Z	0.004052	Z boson candidate transverse momentum
$p_T^{\ell 3}$	0.002776	Third lepton p_T
η^b	0.002333	b -quark candidate pseudorapidity
$\eta^{\ell 3}$	0.001055	Third lepton η
$\eta^{\ell 2}$	0.0006566	Sub-leading lepton η
$\eta^{\ell 1}$	0.0005999	Leading lepton η

Table A.1: Initial (full) set of input variables considered in the training of the GBDT in SR1 to built the D_1 discriminant for both tZu and tZc couplings searches. Variables are ordered by the separation $\langle s^2 \rangle$ value.

Variable	$\langle s^2 \rangle$	Definition
$m_{b\ell\nu}$	0.1364	SM top-quark candidate mass
p_T^q	0.07345	u/c -quark candidate transverse momentum
N_{jets}	0.05747	Jet multiplicity
$m_{q\ell\ell}$	0.04173	FCNC top-quark candidate mass
$\Delta R(t_{\text{SM}}, t_{\text{FCNC}})$	0.04109	ΔR between SM and FCNC top-quark candidates
$\Delta R(\ell, Z)$	0.02441	ΔR between W boson lepton and Z boson candidates

Table A.2: Final set of input variables considered in the training of the GBDT in SR1 to built the D_1 discriminant used in both tZu and tZc couplings searches. Variables are ordered by the separation $\langle s^2 \rangle$ value.

A.0.1.2 Hyper-parameters optimisation

Similarly to the SR2 tZu case, the BDT hyper-parameters optimisation is performed. The following BDT parameters [167] and values are considered with total of 144 combinations: NTrees=[400,600,800,1000],

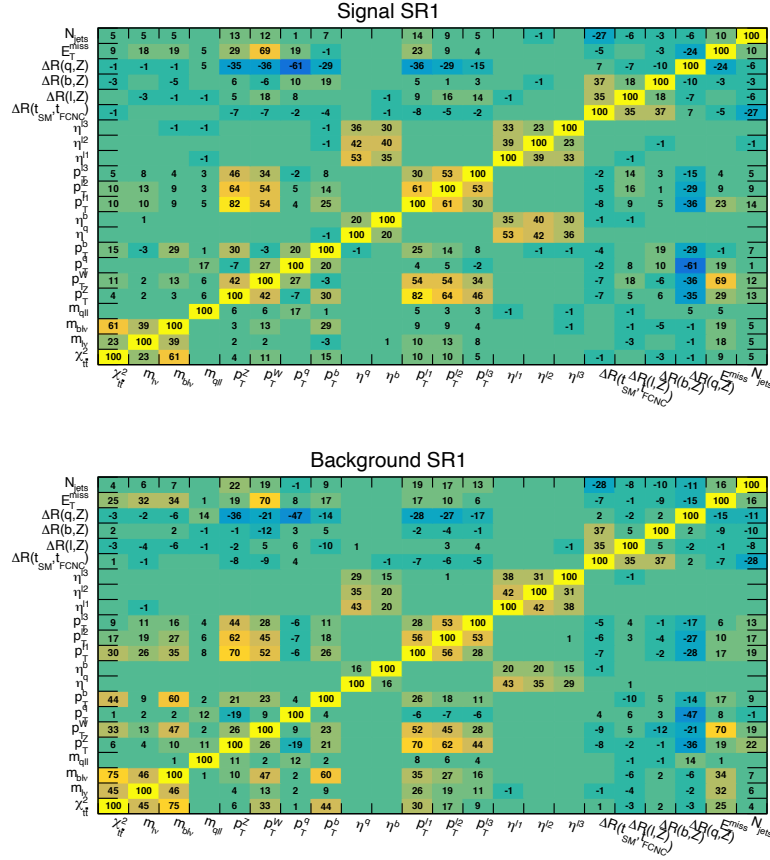


Figure A.1: Correlation matrix of the input variables from signal (top) and background (bottom) samples considered in the training of the GBDT in SR1 to built the D_1 discriminant for both tZu and tZc couplings searches.

`minNodeSize=[2.0,4.0,6.0]`, `shrinkage=[0.025,0.05,0.1]`, `maxDepth=[1,2,3,4]`. Figure A.7 presents the maximum value of $S_{\text{eff}}/\sqrt{B_{\text{eff}}}$ by cutting the GBDT output score, and the ROC integral, averaged over the validation folds, as a function of BDT hyper-parameters combination. The difference between highest and lowest values of $S_{\text{eff}}/\sqrt{B_{\text{eff}}}$ and ROC integral, with the different BDT hyper-parameters combinations, is $\sim 5\%$ and $\sim 2\%$, respectively. These results indicate that the BDT performance is stable and not much can be improved with the hyper-parameters. The average ROC integral (0.8025 with RMS of 0.0025) obtained with the reference BDT parameters is almost identical to the highest value of ROC integral (0.8039 with RMS of 0.0023) obtained from the hyper-parameters optimisation.

A.0.2 Study of the BDT in SR2 ctZ

A.0.2.1 Input variables

Input variables considered for the D_2^C discriminant in SR2 ctZ are presented in Table A.3, that includes invariant mass of the reconstructed objects as well as transverse momentum, pseudo-rapidity and ΔR

APPENDIX A. OPTIMISATION STUDIES FOR THE MULTIVARIATE DISCRIMINANTS

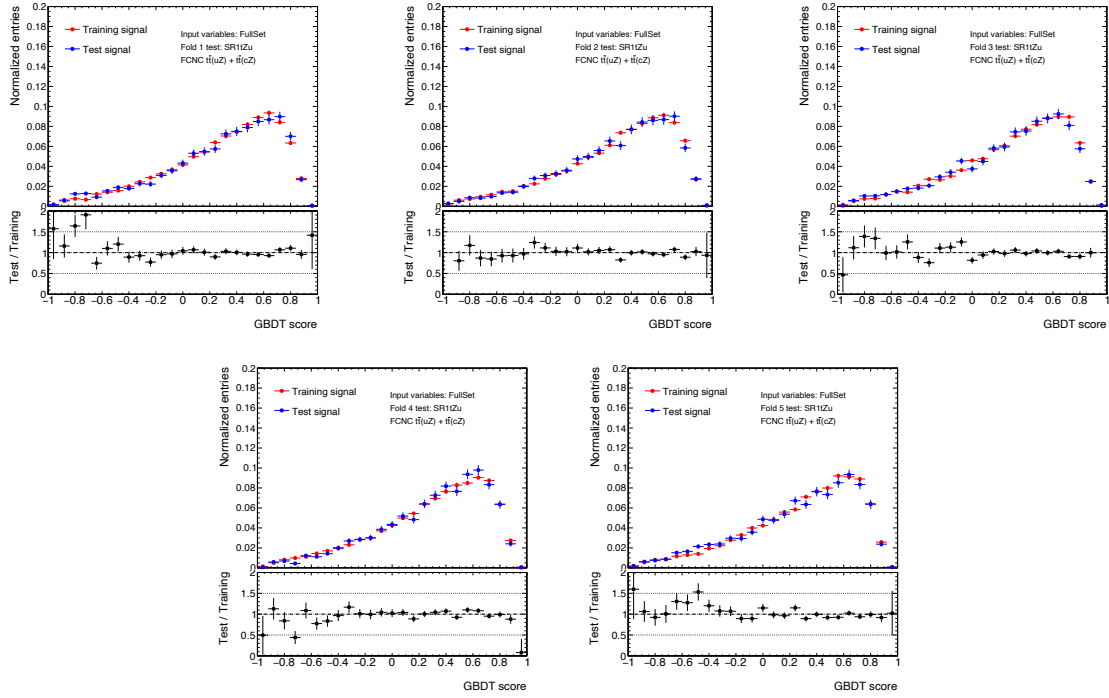


Figure A.2: The FCNC $t\bar{t}$ decay signal GBDT output score distribution for each of five GBDTs trained in SR1 for the D_1 discriminant. Initial (full) set of input variables is used in the training. Comparison of results between training and test samples.

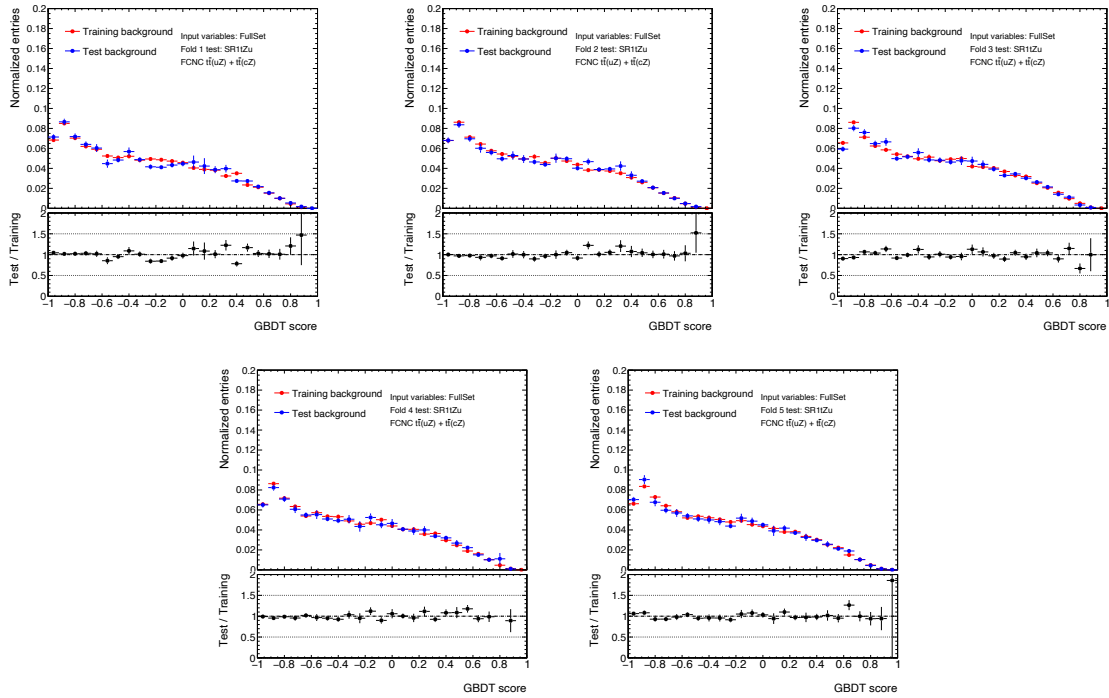


Figure A.3: The background GBDT output score distribution for each of five GBDTs trained in SR1 to built the D_1 discriminant. Initial (full) set of input variables is used in the training. Comparison of results between training and test samples.

APPENDIX A. OPTIMISATION STUDIES FOR THE MULTIVARIATE DISCRIMINANTS

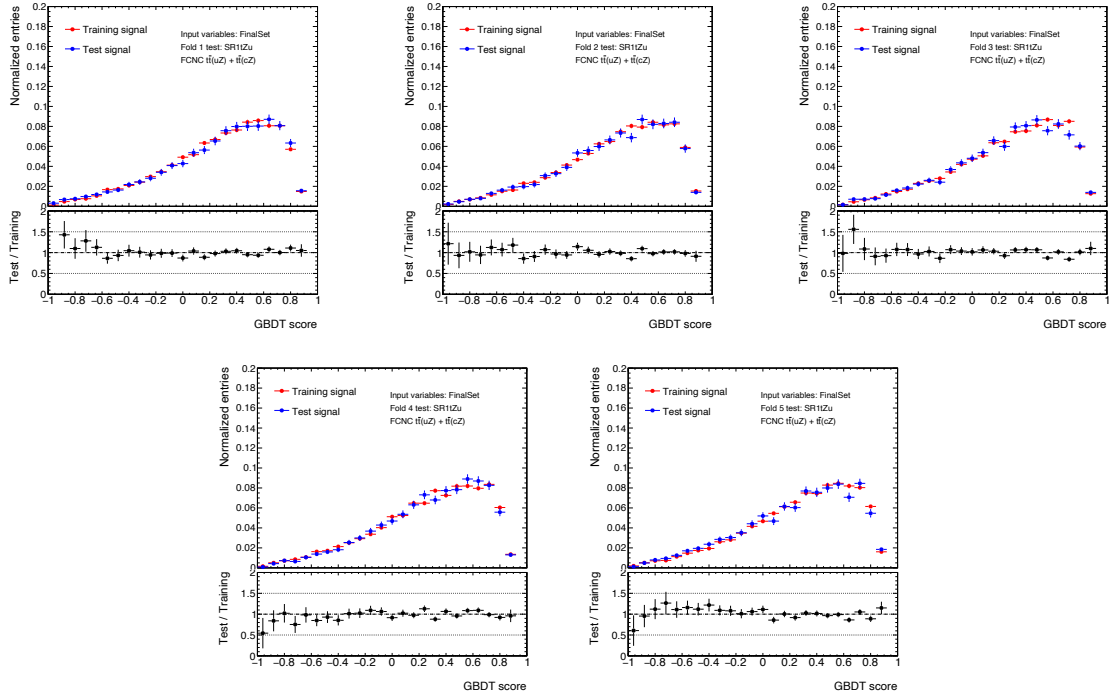


Figure A.4: The FCNC $t\bar{t}$ decay signal GBDT output score distribution for each of five GBDTs trained in SR1 for the D_1 discriminant. Final set of input variables is used in the training. Comparison of results between training and test samples.

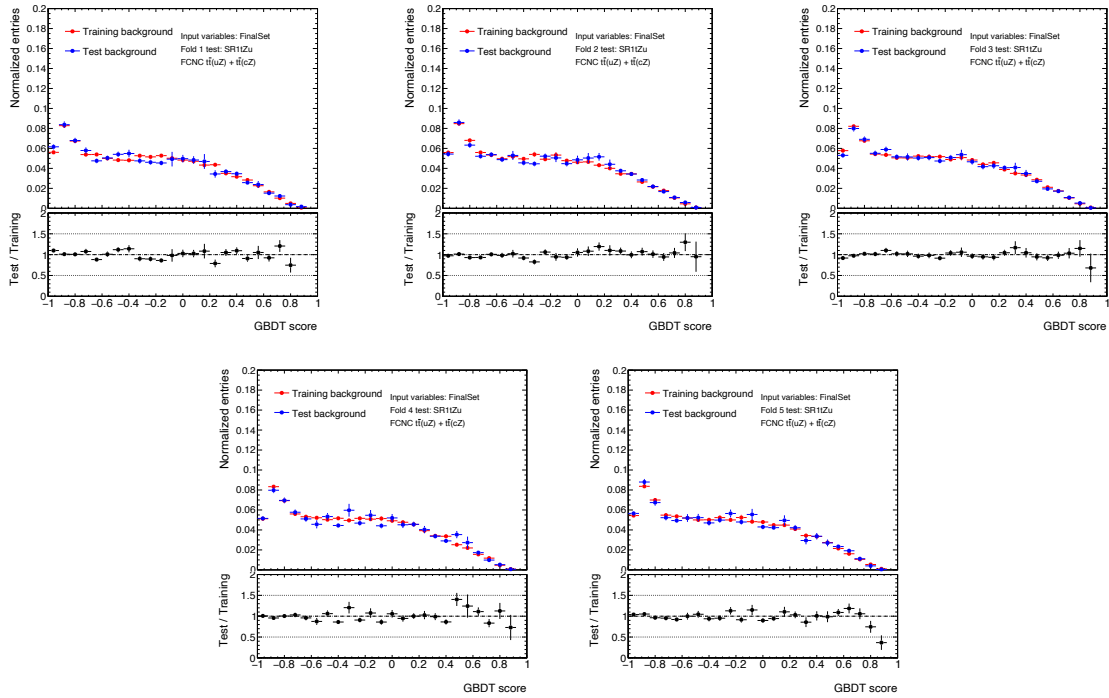


Figure A.5: The background GBDT output score distribution for each of five GBDTs trained in SR1 for the D_1 discriminant. Final set of input variables is used in the training. Comparison of results between training and test samples.

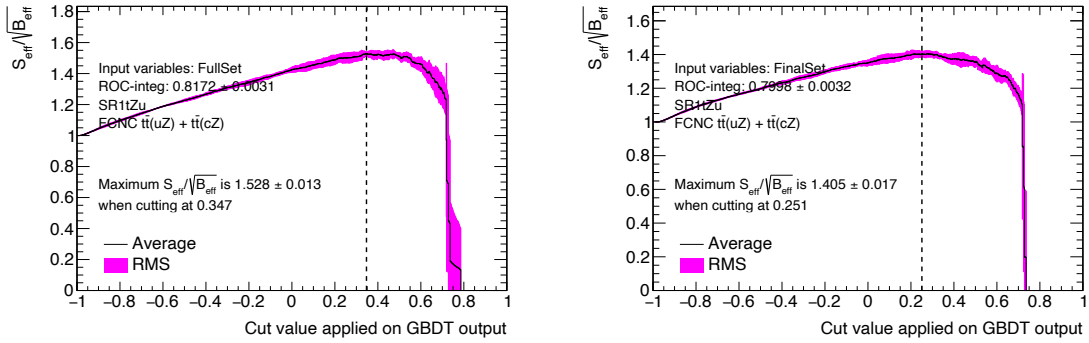


Figure A.6: The $S_{\text{eff}}/\sqrt{B_{\text{eff}}}$ value averaged over the validation folds as a function of the cut on the GBDT output score with full set (left) and final set (right) of input variables in the SR1. Values are calculated only if S_{eff} and B_{eff} are above 1% to avoid statistically unstable results.

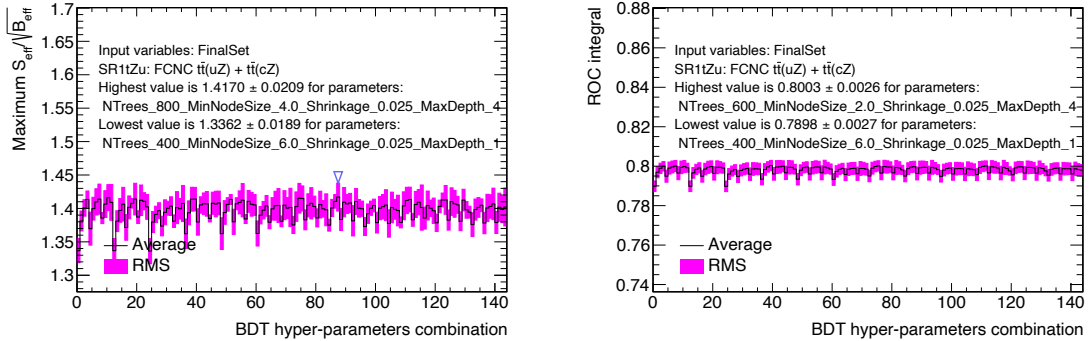


Figure A.7: The maximum value of $S_{\text{eff}}/\sqrt{B_{\text{eff}}}$ by cutting the GBDT output score (left) and the ROC integral (right), averaged over the validation folds, as a function of BDT hyper-parameters combination in the SR1. The highest and lowest values of $S_{\text{eff}}/\sqrt{B_{\text{eff}}}$ and ROC integral are presented on the plots as well as the corresponding BDT parameters values. Final set of input variables is used in the training.

between them in (η, ϕ) plane. Separation values are presented in the same table, while correlations are shown in fig. A.8. Input variables that have separation value below 0.01 are removed from the final set of input variables. The final set of input variables are presented in Table A.4. With the full set (initial set) of input variables, the GBDT output score distributions in each fold for the signal and background samples are presented in Figure A.9 and Figure A.10, respectively, while for the final (reduced) set of input variables in Figure A.11 and Figure A.12. The ROC integral, averaged over the validation folds, for the BDT trained with the full set of input variables is 0.7220 with RMS of 0.0047, while for the BDT with final set of input variables: 0.6986 with RMS of 0.0053. Figure A.13 shows the $S_{\text{eff}}/\sqrt{B_{\text{eff}}}$ value averaged over the validation folds as a function of the cut on the GBDT output score, with full set and final set of input variables. The $S_{\text{eff}}/\sqrt{B_{\text{eff}}}$ values are calculated only if S_{eff} and B_{eff} are above 1% to avoid statistically unstable results. The maximum value of $S_{\text{eff}}/\sqrt{B_{\text{eff}}}$ is 1.131 with RMS of 0.014 for the full set of input variables, while 1.088 with RMS of 0.010 for the final set of input variables. Results show that the final set of input variables for

the BDT gives slightly worse performance than the full set, however the $S_{\text{eff}}/\sqrt{B_{\text{eff}}}$ values tend to have smaller RMS (as can be seen in Figure A.13), which indicates a better stability of BDT output.

Variable	$\langle s^2 \rangle$	Definition
p_T^Z	0.07408	Z boson candidate transverse momentum
p_T^b	0.05261	b -quark candidate transverse momentum
$p_T^{\ell 1}$	0.04809	Leading lepton p_T
$H_T(l, j)$	0.04568	Sum of p_T of leptons and jets
p_T^W	0.02487	W boson candidate transverse momentum
$p_T^{\ell 2}$	0.02362	Sub-leading lepton p_T
$m_{b\ell\nu}$	0.02282	SM top-quark candidate mass
$\Delta R(b, Z)$	0.02143	ΔR between b -quark and Z boson candidates
E_T^{miss}	0.02039	Missing transverse energy
$p_T^{\ell 3}$	0.01843	Third lepton p_T
χ^2_{tZ}	0.01561	χ^2 from the kinematic fit under the FCNC tZ production signal hypothesis
$m_{\ell\nu}$	0.008803	W boson candidate mass
$\Delta R(\ell, Z)$	0.008783	ΔR between W boson lepton and Z boson candidates
η^b	0.005338	b -quark candidate pseudorapidity
$\eta^{\ell 1}$	0.002856	Leading lepton η
$\eta^{\ell 2}$	0.001887	Sub-leading lepton η
$\eta^{\ell 3}$	0.001372	Third lepton η

Table A.3: Initial (full) set of input variables considered in the training of the GBDT in SR2 to built the D_2^c discriminant used in tZc coupling search. Variables are ordered by the separation $\langle s^2 \rangle$ value.

Variable	$\langle s^2 \rangle$	Definition
p_T^Z	0.07408	Z boson candidate transverse momentum
p_T^b	0.05261	b -quark candidate transverse momentum
$m_{b\ell\nu}$	0.02282	SM top-quark candidate mass
$\Delta R(b, Z)$	0.02143	ΔR between b -quark and Z boson candidates
χ^2_{tZ}	0.01561	χ^2 from the kinematic fit under the FCNC tZ production signal hypothesis
$\Delta R(\ell, Z)$	0.008783	ΔR between W boson lepton and Z boson candidates

Table A.4: Final set of input variables considered in the training of the GBDT in SR2 to built the D_2^c discriminant used in tZc coupling search. Variables are ordered by the separation $\langle s^2 \rangle$ value.

A.0.2.2 Hyper-parameters optimisation

Similarly to the SR2 tZu case, the BDT hyper-parameters optimisation is performed. The following BDT parameters [167] and values are considered with total of 144 combinations: NTrees=[400,600,800,1000], minNodeSize=[2.0,4.0,6.0], shrinkage=[0.025,0.05,0.1], maxDepth=[1,2,3,4]. Figure A.14 presents the maximum value of $S_{\text{eff}}/\sqrt{B_{\text{eff}}}$ by cutting the GBDT output score, and the ROC integral, averaged over

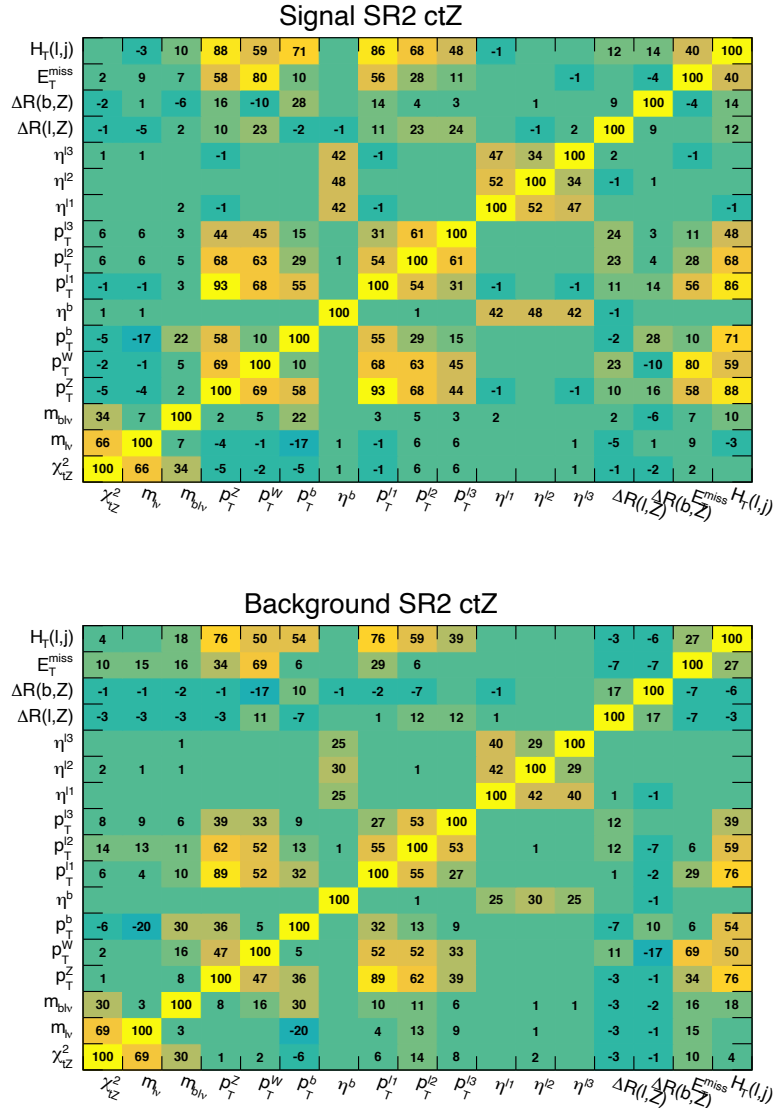


Figure A.8: Correlation matrix of the input variables from signal (top) and background (bottom) samples considered in the training of the GBDT in SR2 to built the D_2^C discriminant used in tZc coupling search.

APPENDIX A. OPTIMISATION STUDIES FOR THE MULTIVARIATE DISCRIMINANTS

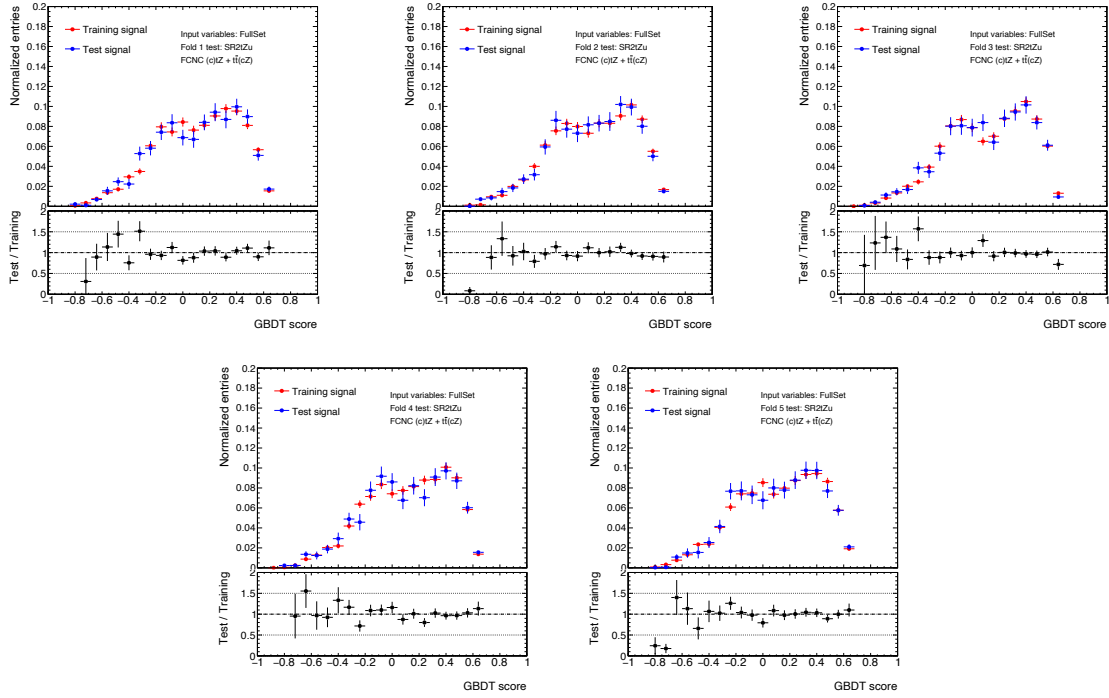


Figure A.9: The FCNC tZ production signal GBDT output score distribution for each of five GBDTs trained in SR2 ctZ for the D_2^c discriminant. Initial (full) set of input variables is used in the training. Comparison of results between training and test samples.

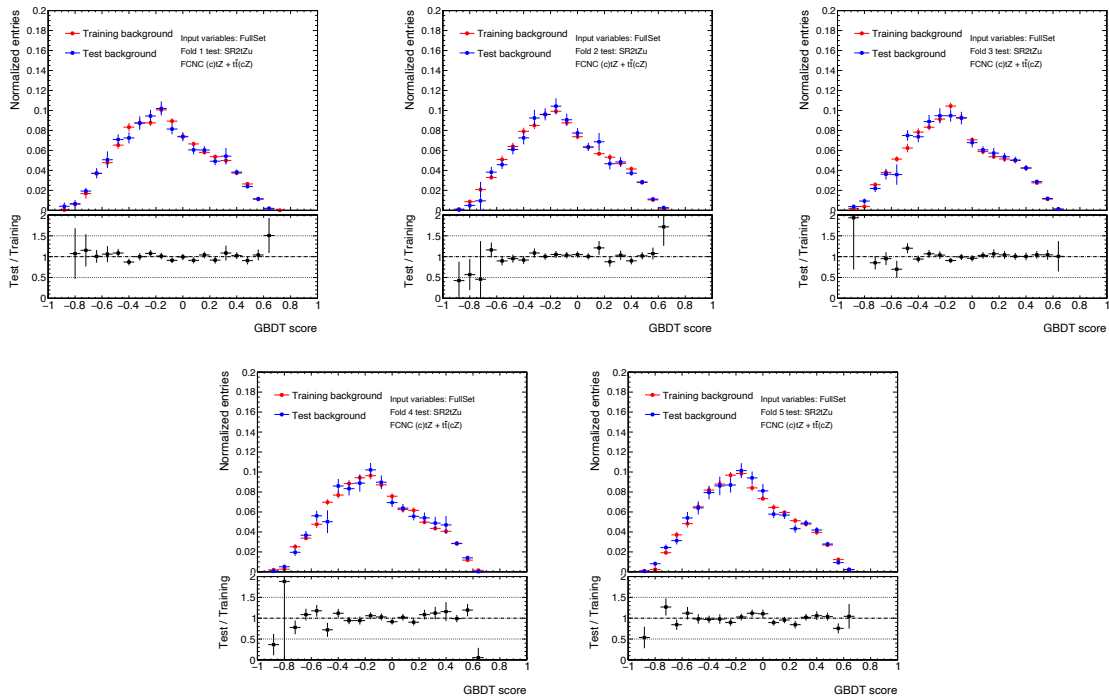


Figure A.10: The background GBDT output score distribution for each of five GBDTs trained in SR2 ctZ to built the D_2^c discriminant. Initial (full) set of input variables is used in the training. Comparison of results between training and test samples.

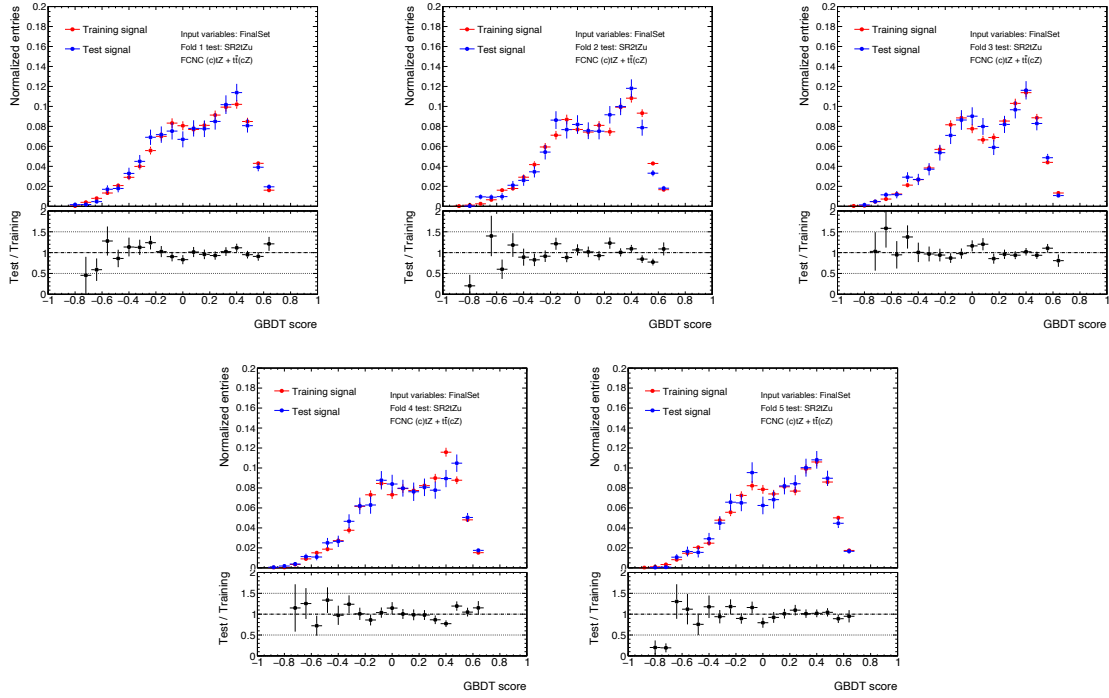


Figure A.11: The FCNC tZ production signal GBDT output score distribution for each of five GBDTs trained in SR2 ctZ for the D_2^C discriminant. Final set of input variables is used in the training. Comparison of results between training and test samples.

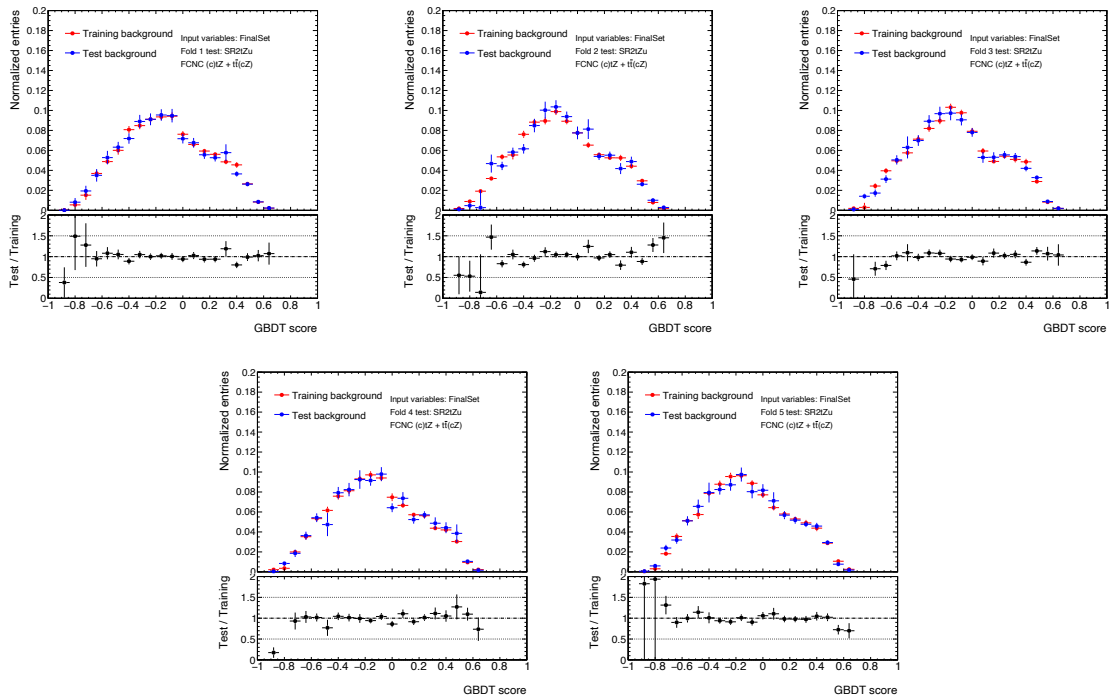


Figure A.12: The background GBDT output score distribution for each of five GBDTs trained in SR2 ctZ for the D_2^C discriminant. Final set of input variables is used in the training. Comparison of results between training and test samples.

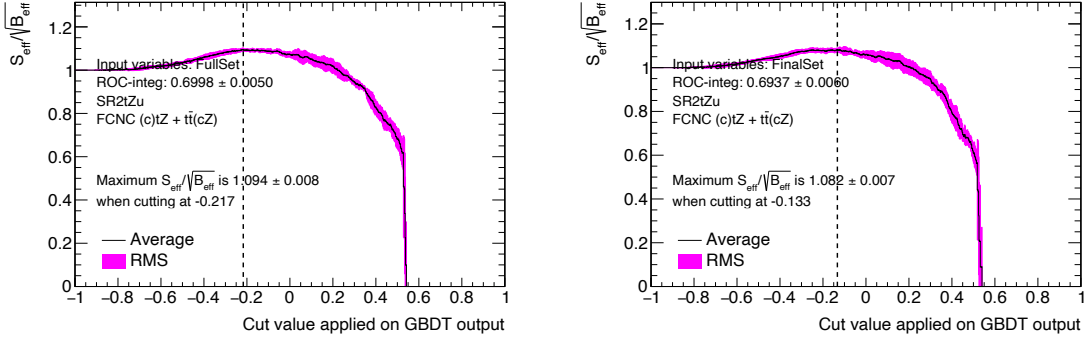


Figure A.13: The $S_{\text{eff}}/\sqrt{B_{\text{eff}}}$ value averaged over the validation folds as a function of the cut on the GBDT output score with full set (left) and final set (right) of input variables in the SR2 $c\bar{t}Z$. Values are calculated only if S_{eff} and B_{eff} are above 1% to avoid statistically unstable results.

the validation folds, as a function of BDT hyper-parameters combination. The difference between highest and lowest values of $S_{\text{eff}}/\sqrt{B_{\text{eff}}}$ and ROC integral, with the different BDT hyper-parameters combinations, is $\sim 2\%$ and $\sim 2\%$, respectively. These results indicate that the BDT performance is stable and not much can be improved with the hyper-parameters. The average ROC integral (0.6986 with RMS of 0.0053) obtained with the reference BDT parameters is almost identical to the highest value of ROC integral (0.7110 with RMS of 0.0065) obtained from the hyper-parameters optimisation. However, the agreement between results with training and test samples are better for reference BDT parameters, so that these parameters were chosen to build the final BDT discriminant.

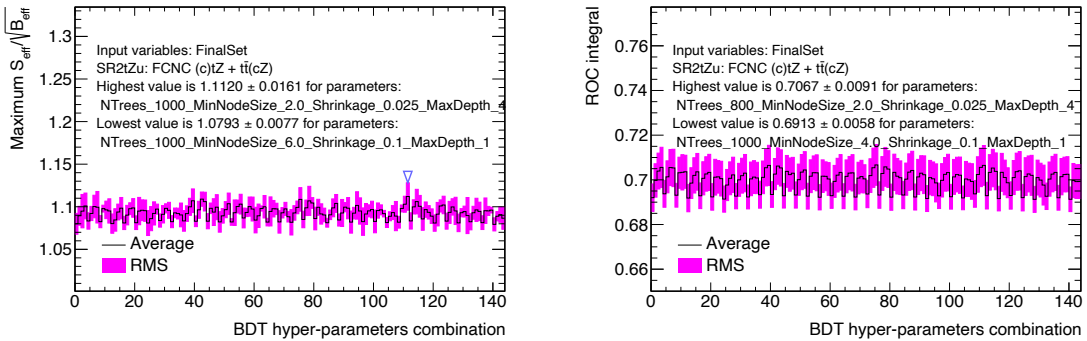


Figure A.14: The maximum value of $S_{\text{eff}}/\sqrt{B_{\text{eff}}}$ by cutting the GBDT output score (left) and the ROC integral (right), averaged over the validation folds, as a function of BDT hyper-parameters combination in the SR2 $c\bar{t}Z$. The highest and lowest values of $S_{\text{eff}}/\sqrt{B_{\text{eff}}}$ and ROC integral are presented on the plots as well as the corresponding BDT parameters values. Final set of input variables is used in the training.

Effect of the pruning on the branching ratio upper limits

This appendix summarises the results of various fits with different levels of pruning, for both normalisations and shapes. As mentioned in Section 4.7, a value of 1 % is used to prune the normalisation of systematic uncertainties and a value of 0.5 % is used to prune the shape. The aim of the present studies is to check the impact of these thresholds on the final results. Therefore, the strategy is to compare various fits with different pruning levels. Table B.1 shows the values that were tested. The final expected limits on the FCNC tZu and tZc branching ratios are compared. The pulls of the different nuisance parameters are also checked and compared.

Setup	Normalisation	Shape
Default	1 %	0.5 %
Scenario 1	1 %	1 %
Scenario 2	2 %	1 %
Scenario 3	0.5 %	0.25 %
No pruning	-	-

Table B.1: Summary of normalisation and shape pruning levels that were tested.

FCNC tZu fit Figures B.1 and B.4 show the NP pulls and constraints for the default and the other pruning threshold scenarios. As expected, the lower the pruning thresholds are (e.g. as in Scenario 3), the more NPs are retained in the fit, especially for the instrumental NPs. Table B.2 shows the expected limits in the default and in the varied scenarios. It can be noticed that the expected limits are stable under the

change of the pruning thresholds, with differences lower than 2 %. This gives confidence that the pruning levels applied in the analysis are adequate.

Limits BR $t \rightarrow Zu$	-1σ	Expected	$+1\sigma$
Default	3.49×10^{-5}	4.84×10^{-5}	6.91×10^{-5}
Scenario 1	3.49×10^{-5}	4.84×10^{-5}	6.92×10^{-5}
Scenario 2	3.47×10^{-5}	4.81×10^{-5}	6.84×10^{-5}
Scenario 3	3.51×10^{-5}	4.87×10^{-5}	6.96×10^{-5}
No pruning	3.53×10^{-5}	4.90×10^{-5}	7.01×10^{-5}

Table B.2: Expected limits on the branching ratios of $t \rightarrow Zu$ for the default and the other pruning threshold scenarios listed in table B.1.

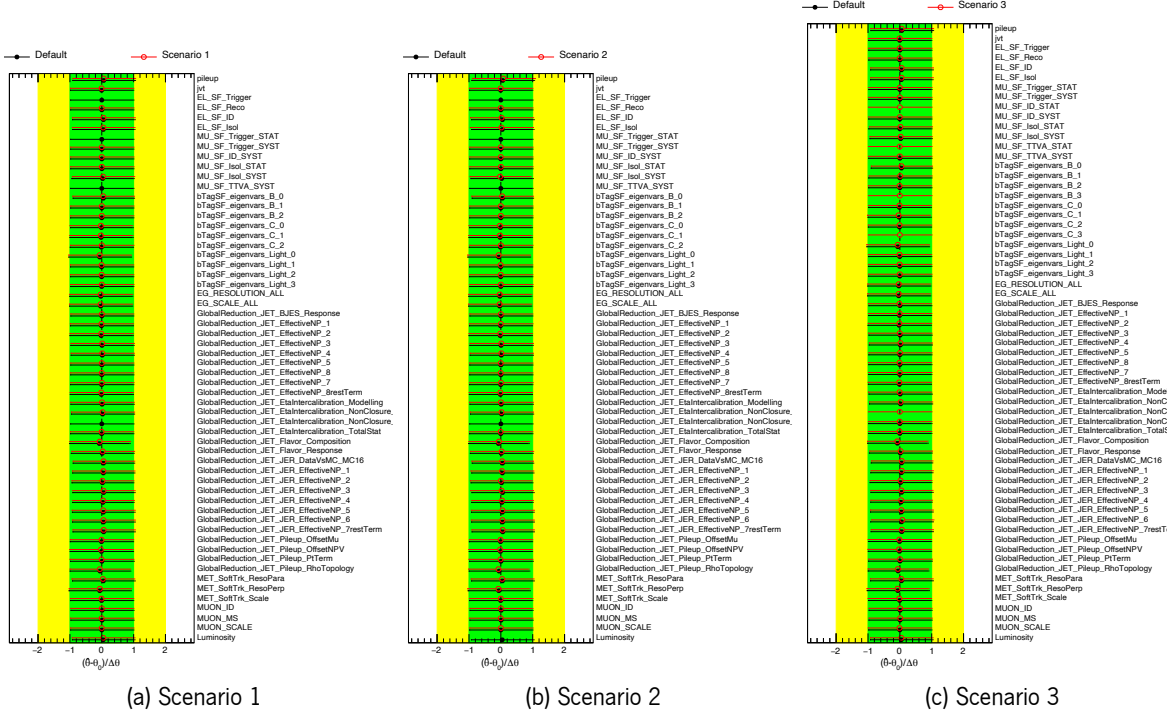


Figure B.1: Pulls and constraints of the instrumental nuisance parameters for the signal-plus-background tZu fit in the signal and control regions with realistic Asimov dataset, for the default (black) and the other pruning threshold scenarios (red).

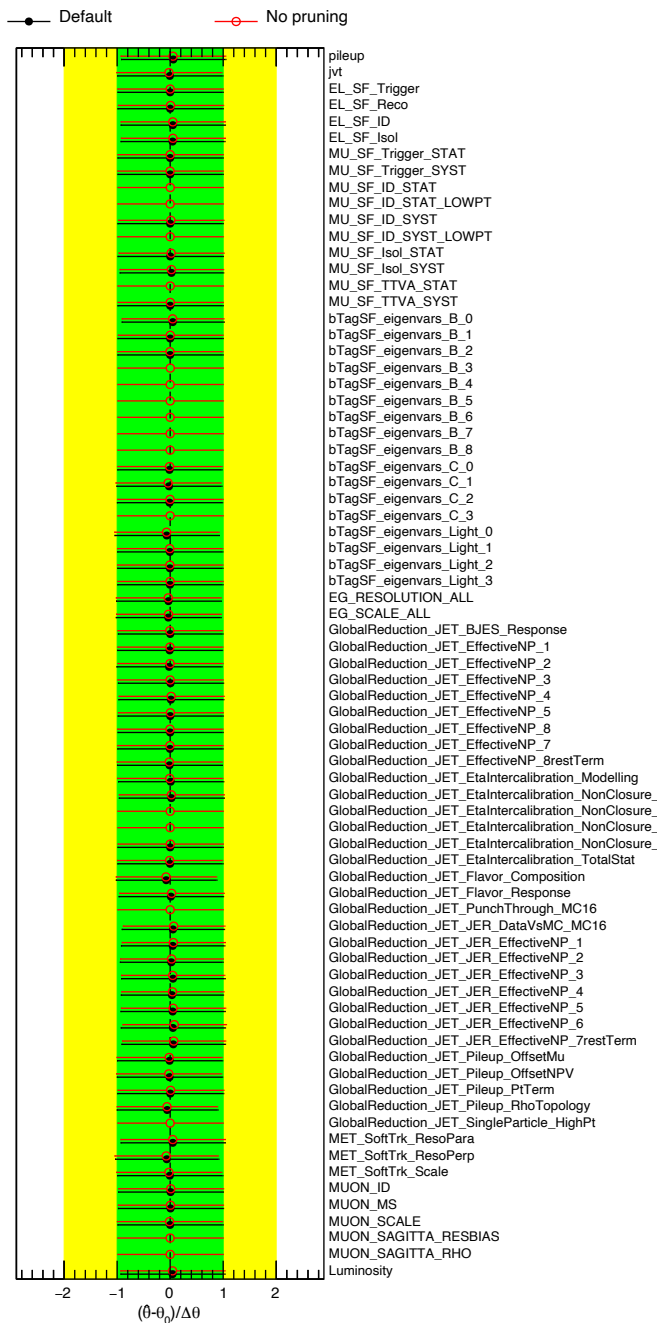


Figure B.2: Pulls and constraints of the instrumental nuisance parameters for the signal-plus-background tZu fit in the signal and control regions with realistic Asimov dataset, for the default setup (black) and no pruning setup (red).

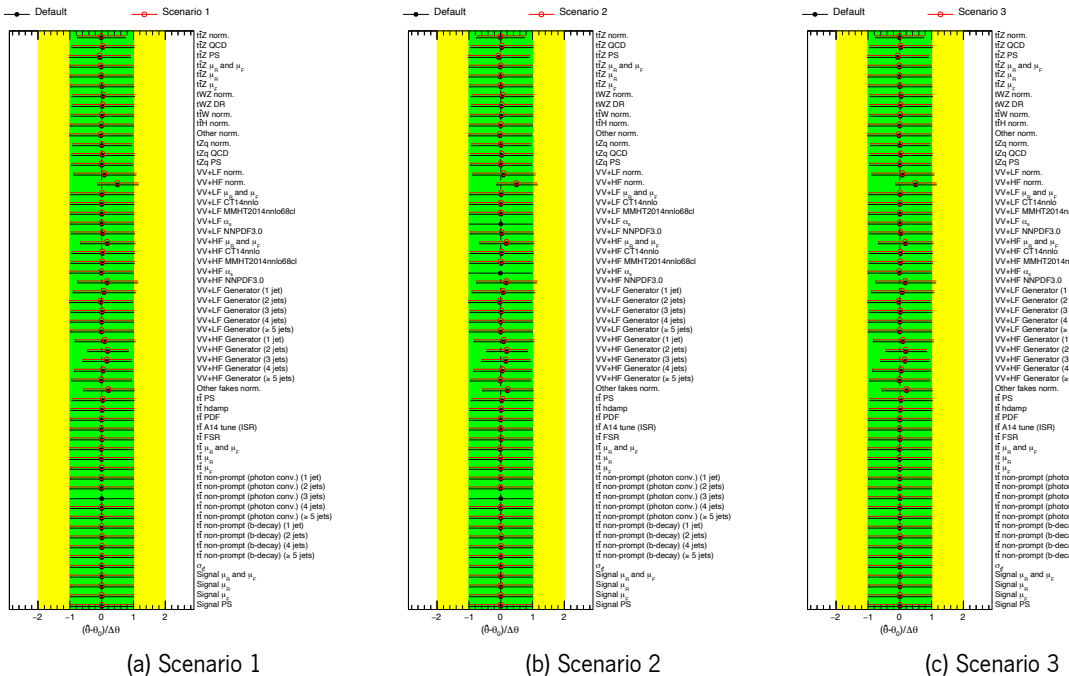


Figure B.3: Pulls and constraints of the theoretical and modelling nuisance parameters for the signal-plus-background tZu fit in the signal and control regions with realistic Asimov dataset, for the default (black) and the other pruning threshold scenarios (red).

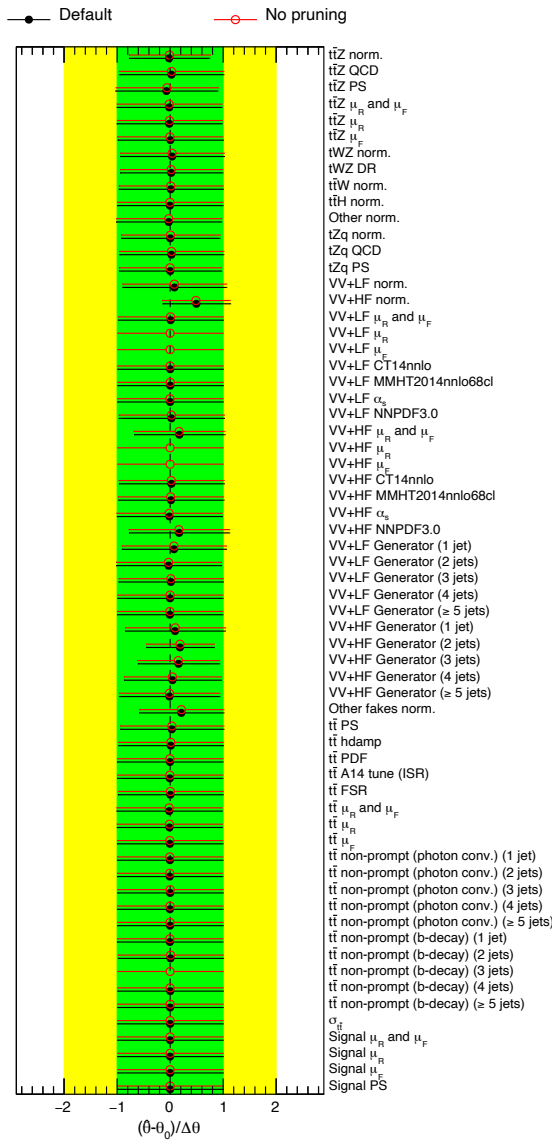


Figure B.4: Pulls and constraints of the theoretical and modelling nuisance parameters for the signal-plus-background tZu fit in the signal and control regions with realistic Asimov dataset, for the default setup (black) and no pruning setup (red).

FCNC tZc fit Figures B.5 and B.8 show the NP pulls and constraints for the default and the other pruning threshold scenarios. As expected, the lower the pruning thresholds are (e.g. as in Scenario 3), the more NPs are retained in the fit, especially for the instrumental NPs. Table B.3 shows the expected limits in the default and in the varied scenarios. It can be noticed that the expected limits are stable under the change of the pruning thresholds, with differences lower than 2 %. This gives confidence that the pruning levels applied in the analysis are adequate.

Limits	-1σ	Expected	$+1\sigma$
BR $t \rightarrow Zc$			
Default	7.78×10^{-5}	10.80×10^{-5}	15.48×10^{-5}
Scenario 1	7.75×10^{-5}	10.76×10^{-5}	15.42×10^{-5}
Scenario 2	7.72×10^{-5}	10.71×10^{-5}	15.30×10^{-5}
Scenario 3	7.90×10^{-5}	10.96×10^{-5}	15.77×10^{-5}
No pruning	7.97×10^{-5}	11.06×10^{-5}	15.93×10^{-5}

Table B.3: Expected limits on the branching ratios of $t \rightarrow Zc$ for the default and the other pruning threshold scenarios listed in table B.1.

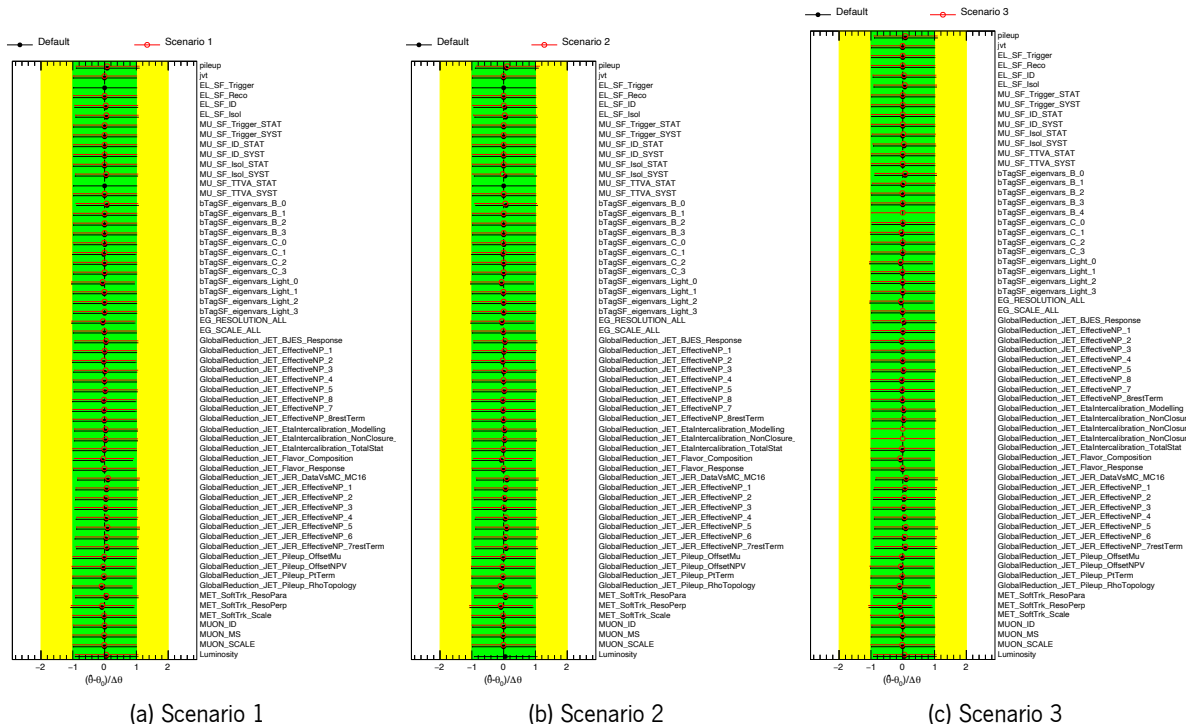


Figure B.5: Pulls and constraints of the instrumental nuisance parameters for the signal-plus-background tZc fit in the signal and control regions with realistic Asimov dataset, for the default (black) and the other pruning threshold scenarios (red).

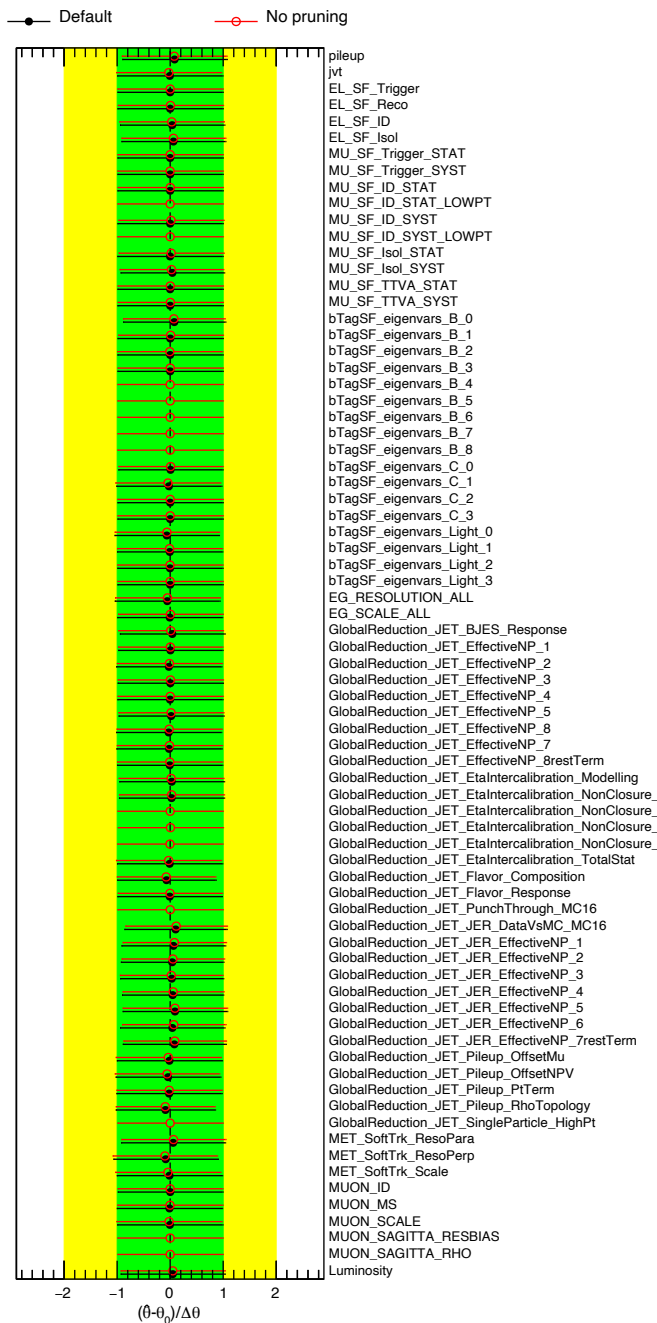


Figure B.6: Pulls and constraints of the instrumental nuisance parameters for the signal-plus-background tZc fit in the signal and control regions with realistic Asimov dataset, for the default setup (black) and no pruning setup (red).

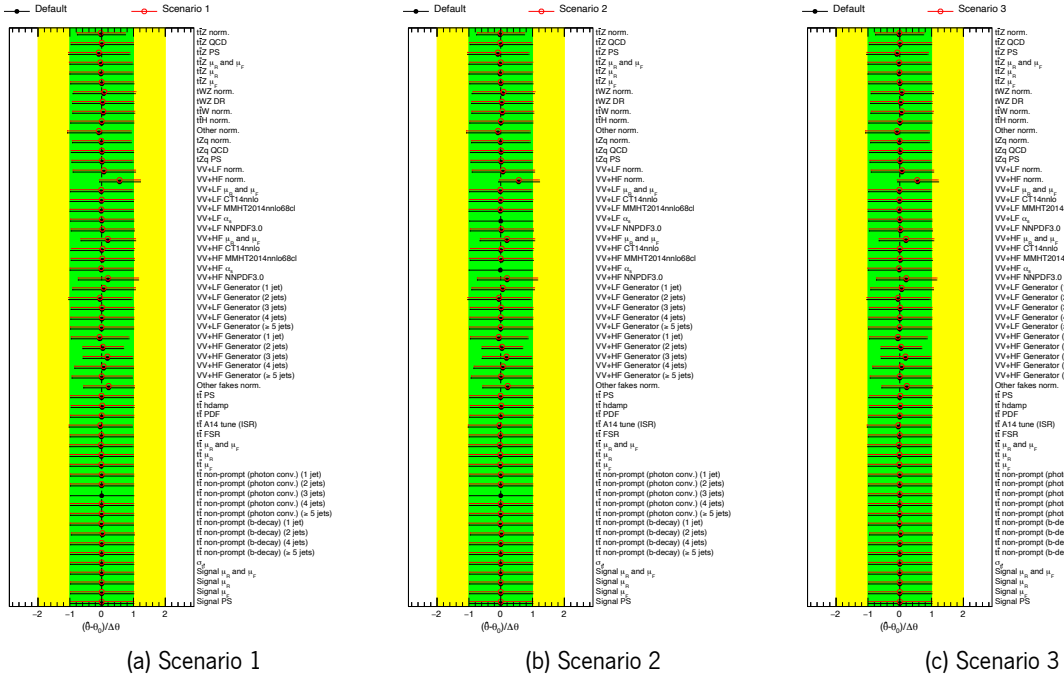


Figure B.7: Pulls and constraints of the theoretical and modelling nuisance parameters for the signal-plus-background tZc fit in the signal and control regions with realistic Asimov dataset, for the default (black) and the other pruning threshold scenarios (red).

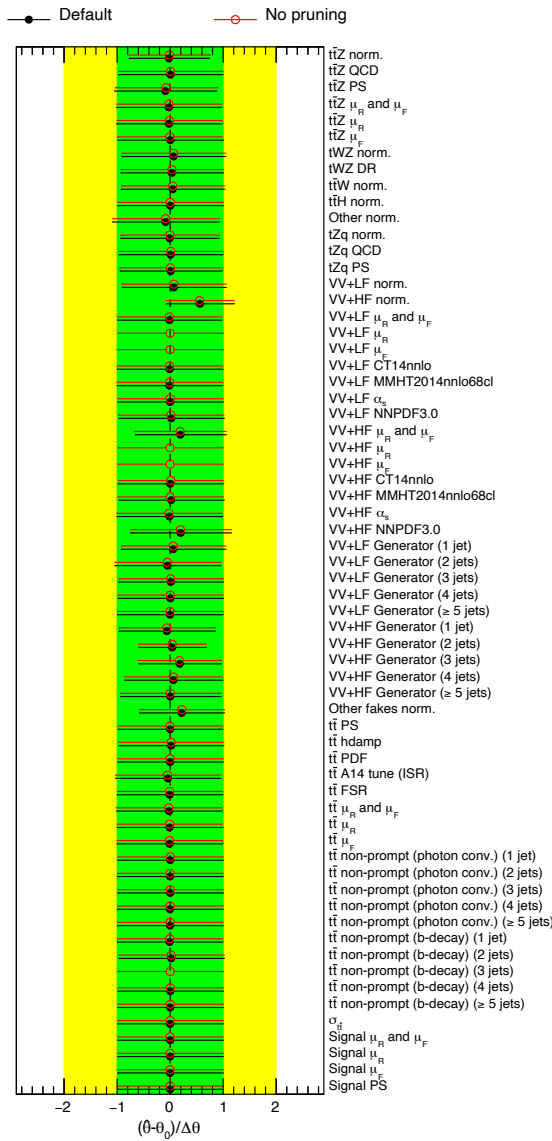


Figure B.8: Pulls and constraints of the theoretical and modelling nuisance parameters for the signal-plus-background tZc fit in the signal and control regions with realistic Asimov dataset, for the default setup (black) and no pruning setup (red).